



THE HONG KONG  
POLYTECHNIC UNIVERSITY

香港理工大學

Pao Yue-kong Library

包玉剛圖書館

---

## Copyright Undertaking

This thesis is protected by copyright, with all rights reserved.

**By reading and using the thesis, the reader understands and agrees to the following terms:**

1. The reader will abide by the rules and legal ordinances governing copyright regarding the use of the thesis.
2. The reader will use the thesis for the purpose of research or private study only and not for distribution or further reproduction or any other purpose.
3. The reader agrees to indemnify and hold the University harmless from and against any loss, damage, cost, liability or expenses arising from copyright infringement or unauthorized usage.

### IMPORTANT

If you have reasons to believe that any materials in this thesis are deemed not suitable to be distributed in this form, or a copyright owner having difficulty with the material being included in our database, please contact [lbsys@polyu.edu.hk](mailto:lbsys@polyu.edu.hk) providing details. The Library will look into your claim and consider taking remedial action upon receipt of the written requests.

CFD SIMULATION AND EXPERIMENTS ON  
OPTIMIZATION DESIGN OF  
VERTICAL AXIS WIND TURBINES (VAWTs)

CHEN JIAN

Ph.D

The Hong Kong Polytechnic University

2013

**The Hong Kong Polytechnic University**

**Department of Building Services Engineering**

**CFD Simulation and Experiments on Optimization  
Design of Vertical Axis Wind Turbines (VAWTs)**

**Chen Jian**

**A thesis submitted in partial fulfillment of the requirements for the  
Degree of Doctor of Philosophy**

July 2013

## **CERTIFICATE OF ORIGINALITY**

I hereby declare that this thesis is my own work and that, to the best of my knowledge and belief, it reproduces no material previously published or written, nor material that has been accepted for the award of any other degree or diploma, except where due acknowledgement has been made in the text.

I also declare that the intellectual content of this thesis is the product of my own work, even though I may have received assistance from others on style, presentation and language expression.

\_\_\_\_\_ (Signed)

Chen Jian (Name of student)

Department of Building Services Engineering

The Hong Kong Polytechnic University

Hong Kong SAR, China

## **ABSTRACT**

Abstract of thesis entitled:

### **CFD Simulation and Experiments on Optimization Design of Vertical Axis Wind Turbines (VAWTs)**

Submitted by:                      Chen Jian

For the degree of:                Doctor of Philosophy

at The Hong Kong Polytechnic University

Unlike horizontal-axis wind turbines (HAWTs), vertical-axis wind turbines (VAWTs) are still not popular for wind power generation in large scale although a lot of researches have been conducted in an effort to improve the performance of the VAWTs. The VAWTs can take wind from any direction, and they also have been proved to be a promising candidate for power generation in urban environment. However, the current fact is that the Savonius rotor (drag-type VAWT) has a good starting ability, but low power coefficient (CP), and the Darrieus rotor (lift-type VAWT) has a high power coefficient, but poor reputation of self-starting, which highly limits the utilization of the VAWTs in an open area or urban area where the more complex wind environment exists. Thus, the objective of this thesis is to improve the starting ability and the CP of the VAWTs, especially for the Darrieus

rotor, through the computational fluid dynamic (CFD) method and experiments.

In order to improve the starting ability of the lift-type VAWTs, three methods are proposed and studied in this thesis. These three methods are the usage of two-stage Savonius rotors, an opening at the blade tip and the two sets of blades.

Wind tunnel test was conducted to study the two-stage Savonius rotors with two and three blades (first method) which improve the starting ability of Darrieus rotor. The experimental tests of the Savonius rotor find that the two-stage rotors can be a good assistant to improve the self-starting ability of the Darrieus rotors, especially the two-stage rotor with three blades due to the fact that the CTs of the two-stage rotor with three blades is higher than that of the two-stage rotor with two blades. It also demonstrates that although the two-stage rotors produce lower power than that of the one-stage rotor, the two-stage rotors have fairly higher and smoother static torque coefficient (CTs) than that of the one-stage rotor. This makes the Darrieus rotor has the better starting ability.

A novel method is proposed as the second method to improve the starting ability of the Darrieus rotor. This novel method is the Darrieus rotor with opening at the blade tips which has not been studied and mentioned in public literatures. The finding shows that the opening at the blade tip can improve the starting ability of the Darrieus rotor. It is also found that the CP loss of the Darrieus rotor with an opening is less than the hybrid Savonius and Darrieus rotor. This new design is a promising device for the standing alone system.

The third method proposed to improve the starting ability of the Darrieus rotor is the Darrieus rotors with two sets of blades. This method has been rarely studied. The

effect of the distance between two sets of blades, and the effect of the offset angle between two sets of blades have been evaluated. It is found that the CP of the Darrieus rotors with two sets of blades is generally lower than that of the rotor with one set of blades. This conclusion is different from the statement in literature. In addition, a remarkable finding is that the Darrieus rotors with two sets of blades do increase the CTs which make the rotors start easily.

In order to improve the CP of the Darrieus rotor, a novel airfoil selection method based on an automatic CFD process and design of experiment has been established in this thesis. By using this novel method, not only can the impact weight of each factor be found, but also an optimal airfoil has been found to improve the CP of the Darrieus rotors. This airfoil selection method not only extended the Darrieus rotor's airfoil selection from one-factor to three factors, but also laid down the fundamentals of the parametric airfoil design process for Darrieus rotors, which is the original intention of the author for doing this project. An optimal airfoil was found. It can produce 9.7% more energy than that of the NACA 0015 airfoil which is widely used before.

In the end, a real 1.5 kW Darrieus rotor turbine with an opening at the blade tip and optimal airfoil gained from the novel airfoil optimal design process has been built for the future testing. Five construction processes of this 1.5kW Darrieus rotor are summarized. An axial flux permanent-magnet synchronous generator (AFPMSG) and a magnetic bearing are integrated into this 1.5kW Darrieus rotor to reduce the starting torque of this system.

**Keywords:** Vertical axis wind turbines (VAWTs), Drag-type, Lift-type, Savonius rotor, Darrieus rotor, Hybrid Savonius-Darrieus rotor, Starting ability, Power coefficient (CP), Static torque coefficient (CTs), Two-stage Savonius rotor, Opening, Two sets of blades, Airfoil selection, Wind tunnel test, Computational fluid dynamics (CFD), Turbulence model, NACA airfoil

## PUBLICATIONS DURING PHD STUDY

### Journal papers during PhD study:

1. Jan Kumbernuss, **Chen Jian**, Junhua Wang, H.X. Yang and W.N. Fu. A novel magnetic levitated bearing system for Vertical Axis Wind Turbines (VAWT), *Applied Energy*, 2012; 90(1).148-153.
2. **Chen Jian**, Jan Kumbernuss, Zhang Linhua, Lu Lin and Yang Hongxing. Influence of phase-shift and overlap ratio on Savonius wind turbine's performance, *Journal of Solar Energy Engineering-ASME*. 2011; 134(1): 011016-1-011016-9.
3. Jan Kumbernussa , **Chen Jian**, H. X. Yang and Lu Lin. Investigation into the relationship of the overlap ratio and shift angle of double stage three bladed vertical axis wind turbine (VAWT), *Journal of Wind Engineering and Industrial Aerodynamics*.2012; 107-108(0), 57-75.
4. **J. Chen**, C P Liu, Edmond C H LAU, M Lo and H X Yang. A novel vertical axis water turbine for power generation from water pipelines, *Energy*. 2013; 54(1), 184–193.

### Conference papers during PhD study:

1. **Chen Jian**, Jan Kumbernuss, H. X. Yang, X.Y.Wang. Influences of helix blade and unsymmetrical airfoil on the performance of the Darrieus wind rotor,

International Conference on Applied Energy. Perugia, Italy. May 12-18, 2010.

2. **Chen Jian**, Yang Hongxing. Simulation and Experimental Studies on the Two-Stage Savonius Rotors for Wind Power Generation, 9th International Conference on Sustainable Energy Technologies. Shanghai, China. August 24-27, 2010.
3. **J. Chen**, C P Liu, Edmond C H LAU, M Lo and HX Yang. Development of a Novel Hydro Power Harness Device for Power Generation from Water Pipelines, The 4th IWA-ASPIRE Conference & Exhibition, Tokyo, Japan. October 2-6, 2012.

## **PATENT AND AWARD**

### **PATENT:**

Patent No.: HK1150355--An Inline Hydroelectric Generating System in Confined  
Condition.

### **AWARDS:**

1. Silver Medal from the 40th International Exhibition of Inventions in Geneva, Geneva, 2012.
2. Merit Award of the Innovation Award for the Engineering Industry from the Hong Kong Institution of Engineers (HKIE), Hong Kong, 2013.

## **ACKNOWLEDGEMENT**

I hereby extend my hearty thanks to my chief-supervisor, Prof. Hongxing Yang for his specialized guidance, continuous encouragement and unstinting support throughout the last four years of my post-graduate study. His profound specialized knowledge, rigorous scholarship, optimistic open spirit and indefatigable noble quality have great influence on my future career and life.

Furthermore, I would like to offer my sincere gratitude to my co-supervisor, Dr. Lin Lu, Vivien, Associate Professor from the BSE Department, for her patient guidance and kind support.

Thanks also go to my colleagues in the Renewable Energy Research Group and technicians in the Building Services Department, for their assistance in laboratory work.

A special appreciation is given to Dr. Ke Sun for his generous assistance and valuable information provided in the area of CFD simulation. I would also like to thank Dr. Jan Kumbernuss for his selfless assistance during the testing period in Shang Dong Jianzhu University and the construction of the wind turbine. I am also grateful to Micky Lo and Maggie Cui at the PolyU Technology & Consultancy Company Limited for sharing with me their expertise in the development of the water turbines for water pipelines.

I also appreciate The Hong Kong Polytechnic University for providing me with a studentship and research assistant. Without this financial support, it would not have

been possible to complete my PhD study in Hong Kong. The financial supports from the grant of the Sun Hung Kai Properties Group (Project No: ZZ1T), and Green Building System Designs for the New Dormitory at Gaoming (Sub-project) (Project No.: H-ZG94) for the project are also acknowledged.

I also appreciate for Mr Nie Long, Associate Professor from ZheJiang University City College, for his guidance on my English writing.

Finally, I wish to dedicate this thesis to my parents, Chen Xiaoliang and Cheng Changmei, and my sisters, Chen Zihong and Chen Zijuan to them for their love, patience, and support.

# TABLE OF CONTENT

<b>CERTIFICATE OF ORIGINALITY</b>	<b>I</b>
<b>ABSTRACT</b>	<b>II</b>
<b>PUBLICATIONS DURING PHD STUDY</b>	<b>VI</b>
<b>PATENT AND AWARD</b>	<b>VIII</b>
<b>ACKNOWLEDGEMENT</b>	<b>IX</b>
<b>TABLE OF CONTENT</b>	<b>XI</b>
<b>LIST OF FIGURES</b>	<b>XVIII</b>
<b>LIST OF TABLES</b>	<b>XXVIII</b>
<b>NOMENCLATURE</b>	<b>XXXI</b>
<b>CHAPTER 1 INTRODUCTION</b>	<b>1</b>
1.1 WHY DO WE USE VERTICAL AXIS WIND TURBINES (VAWTS)	1
1.2 AIMS AND OBJECTIVES OF THIS THESIS	3
1.3 ORGANIZATION OF THIS THESIS	4
<b>CHAPTER 2 LITERATURE REVIEW OF THE VAWTS</b>	<b>9</b>

<b>2.1</b>	<b>REVIEW OF THE DRAG TYPE VAWTS -SAVONIUS ROTOR</b>	<b>9</b>
2.1.1	REVIEW OF THE RESEARCH FOCUS RELATED TO DRAG TYPE VAWTS	9
2.1.2	REVIEW OF THE RESEARCH METHODOLOGY RELATED TO DRAG TYPE VAWTS	45
2.1.3	CURRENT SHORTCOMING OF DRAG-TYPE VAWTS	53
<b>2.2</b>	<b>REVIEW OF THE FIXED PITCH LIFT-TYPE VAWTS -DARRIEUS ROTOR</b>	<b>56</b>
2.2.1	REVIEW OF THE RESEARCH FOCUS RELATED TO LIFT TYPE VAWTS	60
2.2.2	REVIEW OF THE RESEARCH METHODOLOGY	90
2.2.3	CURRENT INSUFFICIENCY OF THE FIXED PITCH LIFT-TYPE VAWTS	96
<b>2.3</b>	<b>REVIEW OF HYBRID VAWTS-SAVONIUS-DARRIEUS ROTOR</b>	<b>96</b>
<b>2.4</b>	<b>SUMMARY</b>	<b>99</b>
<b><u>CHAPTER 3 SIMULATION AND WIND TUNNEL TEST OF THE TWO-STAGE SAVONIUS</u></b>		
<b><u>ROTOR</u></b>		
<hr/>		
<b>3.1</b>	<b>INTRODUCTION</b>	<b>101</b>
<b>3.2</b>	<b>RESEARCH METHODOLOGY OF THE TWO-STAGE SAVONIUS ROTOR</b>	<b>101</b>
<b>3.3</b>	<b>2D AND 3D SIMULATIONS OF THE SAVONIUS ROTOR</b>	<b>102</b>
3.3.1	SIMULATION MODELS AND SIMULATION SETUP	102
3.3.2	2D SIMULATION AND RESULTS	103
3.3.3	3D SIMULATION AND RESULTS	105
3.3.4	DISCUSSIONS ON THE SIMULATION OF THE SAVONIUS ROTOR	108

<b>3.4</b>	<b>WIND TUNNEL TESTING OF ONE-STAGE AND TWO-STAGE SAVONIUS ROTORS</b>	<b>110</b>
3.4.1	INTRODUCTION OF AN ENVIRONMENTAL WIND TUNNEL (EWT)	110
3.4.2	INTRODUCTION OF THE TESTING RIG	112
3.4.3	WIND TUNNEL CORRECTION	114
3.4.4	MEASUREMNT UNCERTAINTY	115
3.4.5	DIMENSIONS AND ABBREVIATIONS OF THE TESTED SAVONIUS ROTORS	116
3.4.6	EXPERIMENTAL RESULTS OF THE TWO-BLADE SAVONIUS ROTORS	121
3.4.7	EXPERIMENTAL RESULTS OF THE THREE-BLADE SAVONIUS ROTORS	139
<b>3.5</b>	<b>SUMMARY</b>	<b>149</b>
 <b><u>CHAPTER 4 THE CFD SIMULAITON PROCESSES AND STRATEGIES OF DARRIEUS ROTOR</u></b>		
		<b>151</b>
<hr/>		
<b>4.1</b>	<b>INTRODUCTION</b>	<b>151</b>
<b>4.2</b>	<b>CFD SIMULATION PROCESSES FOR THE DARRIEUS ROTOR</b>	<b>151</b>
<b>4.3</b>	<b>COMPUTATIONAL DOMAIN</b>	<b>156</b>
<b>4.4</b>	<b>CFD STRATEGIES AND VALIDATION</b>	<b>157</b>
4.4.1	DOMAIN SIZE	157
4.4.2	MESH NUMBER	159
4.4.3	NUMBER OF MESH NODE ON THE BLADE SURFACE	160
4.4.4	TURBULENCE MODELS	162

4.4.5	INFLUENCE OF TIME STEP SIZE AND NUMBER OF TURNS	164
4.4.6	VALIDATION	168
4.5	SUMMARY	169
<b>CHAPTER 5 THE DARRIEUS ROTOR WITH AN OPENING AT THE BLADE TIP</b>		<b>171</b>
5.1	INTRODUCTION	171
5.2	GEOMETRY OF THE INVESTIGATED ROTORS	172
5.3	THE EFFECT OF THE MOUNTING RATIO	175
5.4	THE EFFECT OF THE CENTER SHAFT	176
5.5	COMPARISON BETWEEN THE NACA 0015 AND NACA 4415 AIRFOIL	177
5.6	THE EFFECT OF THE OPENING FOR THE NACA 4415 AIRFOIL	179
5.7	THE EFFECT OF THE OPENING FOR THE NACA 0015 AIRFOIL	184
5.8	STARTING ABILITY COMPARISON BETWEEN THE DARRIEUS ROTOR WITH AN OPENING AND THE HYBRID SAVONIUS-DARRIEUS ROTOR	189
5.9	POWER COEFFICIENT EQUATION TO EVALUATE THE DARRIEUS TURBINE WITH AN OPENING	190
5.10	SUMMARY	192
<b>CHAPTER 6 THE DARRIEUS ROTOR WITH TWO SETS OF BLADES</b>		<b>195</b>
6.1	INTRODUCTION	195
6.2	GEOMETRY PARAMETERS OF THE INVESTIGATED ROTORS	195

<b>6.3</b>	<b>THE EFFECT OF DISTANCE BETWEEN TWO SETS OF BLADES</b>	<b>198</b>
<b>6.4</b>	<b>THE EFFECT OF THE OFFSET ANGLE BETWEEN TWO SETS OF BLADES</b>	<b>201</b>
<b>6.5</b>	<b>SUMMARY</b>	<b>204</b>
<b><u>CHAPTER 7 A NOVEL AIRFOIL OPTIMAL DESIGN PROCESS FOR THE DARRIEUS ROTOR</u></b>		<b>207</b>
<b>7.1</b>	<b>INTRODUCTION</b>	<b>207</b>
<b>7.2</b>	<b>INTRODUCTION OF THE NACA 4-DIGIT-SERIES AND NACA 4-DIGIT-MODIFIED-SERIES</b>	<b>208</b>
<b>7.3</b>	<b>ONE FACTOR SELECTION FOR NACA 4-DIGIT-SERIES</b>	<b>212</b>
<b>7.4</b>	<b>A NOVEL AIRFOIL OPTIMAL DESIGN PROCESS</b>	<b>214</b>
7.4.1	SELECTION USING THE ORTHOGONAL METHOD FOR NACA 4-MODIFIED-DIGIT-SERIES	214
7.4.2	SELECTION METHOD CHANGES ONE FACTOR EACH TIME BASED ON THE ORTHOGONAL METHOD FOR NACA 4-MODIFIED-DIGIT-SERIES	224
<b>7.5</b>	<b>SUMMARY</b>	<b>229</b>
<b><u>CHAPTER 8 SUMMARY AND FUTURE WORKS</u></b>		<b>231</b>
<b>8.1</b>	<b>SUMMARY OF THIS THESIS</b>	<b>231</b>
<b>8.2</b>	<b>FUTURE WORK</b>	<b>234</b>
<b><u>APPENDIX A THE CONSTRUCTION OF AN 1.5KW DARRIEUS ROTOR</u></b>		<b>237</b>
<b>APPENDIX A 1. INTRODUCTION</b>		<b>237</b>

<b>APPENDIX A 2. CONSTRUCTION OF THE BLADES AND THEIR COMPONENTS</b>	<b>238</b>
A 2.1 CONSTRUCTION OF THE BLADES	238
A 2.2 CONSTRUCTION OF THE COMPONENTS RELATED TO THE BLADES	244
<b>APPENDIX A 3. DESIGN OF THE STRUTS</b>	<b>246</b>
<b>APPENDIX A 4. MAGNETIC BEARING AND THE CENTRAL COLUMN</b>	<b>247</b>
<b>APPENDIX A 5. SELECTION OF THE GENERATOR</b>	<b>251</b>
<b>APPENDIX A 6. ON-SITE INSTALLATION</b>	<b>253</b>
<b>APPENDIX A 7. SUMMARY OF THE DESIGN AND CONSTRUCTION PROCESS</b>	<b>255</b>
<b><u>APPENDIX B APPLICATION OF VAWT FOR DEVELOPING A VERTICAL AXIS WATER TURBINE</u></b>	<b>259</b>
<hr/>	
<b>APPENDIX B 1. INTRODUCTION</b>	<b>259</b>
<b>APPENDIX B 2. REVIEW OF THE CURRENT POWER SUPPLY TO THE PIPELINE MONITORING SYSTEM</b>	<b>263</b>
B 2.1 LOW POWER CONSUMPTION METHODS	263
B 2.2 POWER GENERATED FROM THE AMBIENT ENVIRONMENT	263
<b>APPENDIX B 3. HYDROPOWER HARVEST INSIDE THE PIPELINE</b>	<b>266</b>
<b>APPENDIX B 4. DESIGN METHODOLOGY</b>	<b>270</b>
B 4.1 DESIGN PROCESS	270
B 4.2 CFD SETTINGS	271
B 4.3 PROTOTYPES AND EXPERIMENT SETUP	274

<b>APPENDIX B 5. EXPERIMENTAL AND SIMULATION RESULTS OF THE THREE EVOLUTIONS OF HYDROPOWER SYSTEM</b>	<b>277</b>
B 5.1 FIRST GENERATION OF THE HYDROPOWER SYSTEM	277
B 5.2 SECOND GENERATION OF THE HYDROPOWER SYSTEM	284
B 5.3 THIRD GENERATION OF THE HYDROPOWER SYSTEM	292
B 5.4 SUMMARY OF THREE GENERATIONS	295
B 5.5 CONCLUSION	297
B 5.6 DISCUSSION	298
B 5.7 ACKNOWLEDGEMENTS	299
<b>APPENDIX C (AWARD AND PATNET)</b>	<b>301</b>
<b>PATENT</b>	<b>301</b>
<b>GENEVA AWARD</b>	<b>303</b>
<b>HKIE AWARD</b>	<b>304</b>
<b>REFERENCE</b>	<b>305</b>

## LIST OF FIGURES

<i>Figure 2.1 A traditional Savonius rotor</i> .....	10
<i>Figure 2.2 A semicircular blade</i> .....	14
<i>Figure 2.3 The Bach’s blade profile</i> .....	15
<i>Figure 2.4 The blade profile proposed by Sivasegaram</i> .....	16
<i>Figure 2.5 Different profiles tested by Khan</i> .....	17
<i>Figure 2.6 Five different profiles tested by Fleming</i> .....	19
<i>Figure 2.7 The swinging blades</i> .....	19
<i>Figure 2.8 The cranfield slatted rotor</i> .....	21
<i>Figure 2.9 The twisted rotor and blade (Saha and Rajumar, 2006)</i> .....	22
<i>Figure 2.10 The Savonius rotor tested by Nemoto</i> .....	22
<i>Figure 2.11 A helical Savonius rotor tested by Kamoji</i> .....	23
<i>Figure 2.12 The evolutionary algorithm optimization of the blade (Moharmed et al)</i> .....	25
<i>Figure 2.13 The two- and three-blade rotors tested by Blackwell</i> .....	25
<i>Figure 2.14 The effect of the endplate shapes (Sivasegaram, 1978)</i> .....	28
<i>Figure 2.15 The impact of aspect ratio on acceleration ability (Ushiyama et al.,1986)</i> .....	29
<i>Figure 2.16 A ducted augmentation system (Sabzevari, 1977)</i> .....	32
<i>Figure 2.17 The straight-vane augmentation systems (Ogawa and Yoshida, 1986)</i> .....	33
<i>Figure 2.18 Two straight vanes tested (Altan et al, 2005)</i> .....	34

<i>Figure 2.19 An augmentation system with one straight vane (Mohamed et al, 2011)</i> .....	35
<i>Figure 2.20 A guide-box tunnel augmentation system</i> .....	36
<i>Figure 2.21 The coupled rotors tested by Bowden and McAleese (1984)</i> .....	37
<i>Figure 2.22 The coupled rotors tested by Aldoss and Najjar (1987)</i> .....	37
<i>Figure 2.23 The coupled rotors tested by Shigetomi et al. (2011)</i> .....	38
<i>Figure 2.24 Flow in and around a Savonius rotor (Fujisawa and Gotoh, 1992)</i> .....	41
<i>Figure 2.25 The vortices generated by the Savonius rotor (Benghrib et al, 1998)</i> .....	42
<i>Figure 2.26 The flow field visualized through PIV (Murai et al. 2007)</i> .....	42
<i>Figure 2.27 The flow patterns summarized by Nakajima et al (2008)</i> .....	43
<i>Figure 2.28 A vertical testing rig</i> .....	47
<i>Figure 2.29 A horizontal testing rig</i> .....	47
<i>Figure 2.30 The <math>m</math> values of the square plate and Savonius rotor (Alexander, 1978)</i> .....	49
<i>Figure 2.31 The working principle of the VAWTs</i> .....	57
<i>Figure 2.32 The V-VAWT</i> .....	62
<i>Figure 2.33 The rotor with double blades (Ljungstrom 1982)</i> .....	63
<i>Figure 2.34 The Darrieus rotor with double blades</i> .....	64
<i>Figure 2.35 The arrowhead Darrieus (Morcos and Abdel-Hafez 1996)</i> .....	65
<i>Figure 2.36 Helix or helical Darrieus tested by the Gorlov (2001)</i> .....	66
<i>Figure 2.37 The helical rotor and the inclined angle <math>\phi</math> from Shiono (2002)</i> .....	66
<i>Figure 2.38 The straight and helical Darrieus rotors tested by the Kirke (2011)</i> .....	67

<i>Figure 2.39 The Achard turbine (by courtesy of LEGI).....</i>	<i>70</i>
<i>Figure 2.40 The blade type simulated by the Zanette et al. (2010) .....</i>	<i>70</i>
<i>Figure 2.41 The canted blade (Armstrong and Tullis 2011).....</i>	<i>71</i>
<i>Figure 2.42 The effect of the blade solidity (Templin 1974) .....</i>	<i>73</i>
<i>Figure 2.43 Effects of the solidity (Strickland 1975) <math>Re = 0.3 \times 10^6</math> .....</i>	<i>74</i>
<i>Figure 2.44 Effects of the solidity (Strickland 1975) <math>Re = 3 \times 10^6</math> .....</i>	<i>74</i>
<i>Figure 2.45 Three types of horizontal supporting systems .....</i>	<i>78</i>
<i>Figure 2.46 The drag coefficient of various typical bodies (Talay 1975).....</i>	<i>79</i>
<i>Figure 2.47 The supporting struts (Li and Calisal 2010).....</i>	<i>80</i>
<i>Figure 2.48 The supporting system with inclined supporting struts .....</i>	<i>80</i>
<i>Figure 2.49 The mounting location and pitch angle .....</i>	<i>81</i>
<i>Figure 2.50 The pitch angle definition (Klimas and Worstell 1981) .....</i>	<i>82</i>
<i>Figure 2.51 Lift coefficient vs. angle of attack .....</i>	<i>85</i>
<i>Figure 2.52 AoA (<math>\alpha</math>) vs. azimuth angle (<math>\theta</math>) for dynamic stall .....</i>	<i>86</i>
<i>Figure 2.53 AOA vs. TSR .....</i>	<i>87</i>
<i>Figure 2.54 The dynamic stall on a NACA 0012 airfoil at low free-stream Mach number (Carr 1985).....</i>	<i>88</i>
<i>Figure 2.55 The blade tip vortex (Ferreira et al. 2006) .....</i>	<i>89</i>
<i>Figure 2.56 Two types of hybrid rotors tested by NAL and a Waded turbine tested by NAL(a) A hybrid rotor called Waded turbine tested by NAL (Shankar 1979) (b).....</i>	<i>97</i>
<i>Figure 2.57 Two types of hybrid rotors (Wakui et al. 2005) .....</i>	<i>98</i>

<i>Figure 2.58 The definition of attached angle (Kyozuka 2008)</i> .....	98
<i>Figure 2.59 Comparison of the power coefficient (Kyozuka 2008)</i> .....	99
<i>Figure 3.1 Three meshing methods</i> .....	102
<i>Figure 3.2 The 2D simulation results of three different mesh methods</i> .....	103
<i>Figure 3.3 The effect of the turbulence models</i> .....	104
<i>Figure 3.4 The 3D simulation results of the Savonius rotor</i> .....	106
<i>Figure 3.5 The 3D simulation results of the Savonius rotor</i> .....	106
<i>Figure 3.6 The 3D simulation results of the Savonius rotor</i> .....	107
<i>Figure 3.7 The velocity field and vorticity magnitude distribution in and around the Savonius rotor: (a) velocity field distribution; (b) vorticity magnitude distribution</i> .....	108
<i>Figure 3.8 The velocity distributions in and around the stationary Savonius rotor (<math>\theta = 0^\circ</math>): (a) 3D simulation; (b) 2D simulation</i> .....	109
<i>Figure 3.9 The velocity distributions in and around the stationary Savonius rotor (<math>\theta = 90^\circ</math>): (a) 3D simulation; (b) 2D simulation</i> .....	109
<i>Figure 3.10 The environmental wind tunnel</i> .....	110
<i>Figure 3.11 The wind speed distribution of the wind tunnel</i> .....	111
<i>Figure 3.12 The test rig in the wind tunnel</i> .....	113
<i>Figure 3.13 The relationship of <math>m</math> vs. <math>A/C</math> for a square plate and Savonius rotor [14]</i> .....	114
<i>Figure 3.14 The parameters and configuration of the tested two-blade Savonius rotor</i> .....	117
<i>Figure 3.15 The real rotors with two and three blades</i> .....	118
<i>Figure 3.16 The CTs of the two-stage rotor</i> .....	121

Figure 3.17 The $C_T$ s of one-stage rotor at wind velocity 8m/s .....	121
Figure 3.18 The $C_P$ of the one-stage Savonius rotor at wind velocity 8m/s.....	123
Figure 3.19 The $C_i$ of the one-stage Savonius rotor at wind velocity 8m/s .....	123
Figure 3.20 The $C_T$ s of the one-stage and two-stage Savonius rotors at 8m/s .....	125
Figure 3.21 The $C_T$ s of the one-stage and two-stage Savonius rotors at 8m/s .....	125
Figure 3.22 The $C_T$ s of the one-stage and two-stage Savonius rotors at 8m/s .....	126
Figure 3.23 The $C_T$ s of the one-stage and two-stage Savonius rotors at 8m/s .....	126
Figure 3.24 The comparisons between one-stage and two-stage rotors for gap rates 0.....	127
Figure 3.25 The comparisons between one-stage and two-stage rotors for gap rates 0.167.....	127
Figure 3.26 The comparisons between one-stage and two-stage rotors for gap rate 0.333 .....	128
Figure 3.27 The $C_P$ and $C_i$ of the two-stage Savonius rotor with $PSA=0^\circ$ .....	129
Figure 3.28 The $C_P$ and $C_i$ of the two-stage Savonius rotor at $PSA=45^\circ$ .....	130
Figure 3.29 The $C_P$ and $C_i$ of the two-stage Savonius rotor at $PSA=90^\circ$ .....	131
Figure 3.30 The $C_T$ s of the two-stage Savonius rotor at wind velocity 8m/s.....	133
Figure 3.31 The $C_T$ s of the two-stage Savonius rotor at wind velocity 8m/s.....	134
Figure 3.32 The $C_P$ and $C_i$ of the two-stage Savonius rotor with $\beta=0$ .....	136
Figure 3.33 The $C_P$ and $C_i$ of the two-stage Savonius rotor with $\beta=0.167$ .....	137
Figure 3.34 The $C_P$ and $C_i$ of the two-stage Savonius rotor with $\beta=0.333$ .....	138
Figure 3.35 The static torque coefficient of one-stage three-blade rotors.....	140

<i>Figure 3.36 The power coefficient of one-stage three-blade rotors .....</i>	<i>141</i>
<i>Figure 3.37 The effect of gap rate on CP at PSA=0.....</i>	<i>142</i>
<i>Figure 3.38 The effect of gap rate on CP at PSA=15.....</i>	<i>143</i>
<i>Figure 3.39 The effect of gap rate on CP at PSA=30.....</i>	<i>143</i>
<i>Figure 3.40 The effect of gap rate on CP at PSA=45.....</i>	<i>144</i>
<i>Figure 3.41 The effect of gap rate on CP at PSA=60.....</i>	<i>144</i>
<i>Figure 3.42 The effect of gap rate and PSA on CTs at 8m/s .....</i>	<i>145</i>
<i>Figure 3.43 The effect of gap rate and PSA on CTs at 8m/s .....</i>	<i>146</i>
<i>Figure 3.44 The effect of gap rate and PSA on CTs at 8m/s .....</i>	<i>146</i>
<i>Figure 3.45 The effect of phase-shift angle at gap rate is 0.....</i>	<i>148</i>
<i>Figure 3.46 The effect of phase-shift angle at gap rate is 0.166.....</i>	<i>148</i>
<i>Figure 3.47 The effect of phase-shift angle at gap rate is 0.333.....</i>	<i>149</i>
<i>Figure 4.1 The three steps of common CFD simulation process of VAWTs.....</i>	<i>152</i>
<i>Figure 4.2 An automatic CFD analysis process .....</i>	<i>154</i>
<i>Figure 4.3 The parametric optimization CFD process.....</i>	<i>155</i>
<i>Figure 4.4 The computational domain .....</i>	<i>156</i>
<i>Figure 4.5 The effect of the diameter ratio on the torque coefficient.....</i>	<i>158</i>
<i>Figure 4.6 The effect of the mesh number on the torque coefficient .....</i>	<i>160</i>
<i>Figure 4.7 The aspect ratio of a quadrilateral element.....</i>	<i>161</i>
<i>Figure 4.8 The effect of the mesh node number on the airfoil surface .....</i>	<i>162</i>

<i>Figure 4.9 Comparison between six turbulence models .....</i>	<i>163</i>
<i>Figure 4.10 The effect of the time step size .....</i>	<i>165</i>
<i>Figure 4.11 CP varies with number of turns .....</i>	<i>167</i>
<i>Figure 4.12 The validation of simulation .....</i>	<i>168</i>
<i>Figure 5.1 Four kinds of VAWTs .....</i>	<i>172</i>
<i>Figure 5.2 The airfoils used for the Darrieus rotor with an opening .....</i>	<i>173</i>
<i>Figure 5.3 Design parameters of the H-Darrieus turbines .....</i>	<i>174</i>
<i>Figure 5.4 The effect of the mounting ratio .....</i>	<i>175</i>
<i>Figure 5.5 The effect of the shaft on the torque and power coefficient of the rotor .....</i>	<i>176</i>
<i>Figure 5.6 The difference between the rotors with and without shaft at TSR=3 .....</i>	<i>177</i>
<i>Figure 5.7 Comparison between NACA 0015 airfoil and NACA 4415 airfoil .....</i>	<i>178</i>
<i>Figure 5.8 Comparison for the entire azimuth angle .....</i>	<i>179</i>
<i>Figure 5.9 The NACA 4415 airfoil with inside opening .....</i>	<i>180</i>
<i>Figure 5.10 The NACA 4415 airfoil with outside opening .....</i>	<i>181</i>
<i>Figure 5.11 The effect of the opening ratio and opening location on the CTs .....</i>	<i>183</i>
<i>Figure 5.12 The increase percentage of CTs and decrease percentage of CP .....</i>	<i>183</i>
<i>Figure 5.13 Effect of the opening ratio on the airfoil (inside opening) .....</i>	<i>184</i>
<i>Figure 5.14 Effect of the opening ratio on the airfoil (outside opening) .....</i>	<i>185</i>
<i>Figure 5.15 Effect of the opening ratio and location on the CTs .....</i>	<i>187</i>
<i>Figure 5.16 The increase percentage of CTs and decrease percentage of CP .....</i>	<i>188</i>

<i>Figure 6.1 Geometry of rotor with two sets of blades.....</i>	<i>196</i>
<i>Figure 6.2 Power output of the rotors with two sets of blades for different distance ratios .....</i>	<i>199</i>
<i>Figure 6.3 CTs of rotors with two sets of blades.....</i>	<i>201</i>
<i>Figure 6.4 Power output curves of the rotor for different offset angle .....</i>	<i>203</i>
<i>Figure 6.5 CTs values of the rotor for different offset angle .....</i>	<i>203</i>
<i>Figure 7.1 Effect of the thickness-chord ratio on the performance of the rotor .....</i>	<i>213</i>
<i>Figure 7.2 The power curves of all cases .....</i>	<i>217</i>
<i>Figure 7.3 Maximum power coefficient for 16 different cases.....</i>	<i>221</i>
<i>Figure 7.4 Static torque coefficient for 16 different cases.....</i>	<i>223</i>
<i>Figure 7.5 The effect of the maximum thickness in tenths of chord.....</i>	<i>226</i>
<i>Figure 7.6 Effect of the leading-edge number.....</i>	<i>227</i>
<i>Figure 7.7 Effect of Thickness-chord ratio .....</i>	<i>228</i>
<i>Figure 0.1 Ribs and spars of the rotor blades (Appendix A) .....</i>	<i>239</i>
<i>Figure 0.2 The blade design of the wing method (Appendix A).....</i>	<i>240</i>
<i>Figure 0.3 The extrusion of the blades (Appendix A).....</i>	<i>240</i>
<i>Figure 0.4 The strain and displacement analysis (Appendix A) .....</i>	<i>242</i>
<i>Figure 0.5 The extruded blades in the factory (Appendix A) .....</i>	<i>243</i>
<i>Figure 0.6 Comparison between the real airfoil profile to the designed airfoil profile (Appendix A) .</i>	<i>244</i>
<i>Figure 0.7 Components related to the blades (Appendix A).....</i>	<i>245</i>
<i>Figure 0.8 Pre-assembling of blades in the factory (Appendix A).....</i>	<i>245</i>

<i>Figure 0.9 Inclined and horizontal struts (Appendix A)</i> .....	246
<i>Figure 0.10 Three parts of the struts (Appendix A)</i> .....	247
<i>Figure 0.11 Lower disk, upper disk, base and center column (Appendix A)</i> .....	248
<i>Figure 0.12 The settlement of main components (Appendix A)</i> .....	249
<i>Figure 0.13 The braking system of the H-Darrieus (Appendix A)</i> .....	250
<i>Figure 0.14 An outer-rotor axial flux permanent-magnet synchronous generator (Appendix A)</i> .....	252
<i>Figure 0.15 Match of the power curves (Appendix A)</i> .....	253
<i>Figure 0.16 Installed site (Appendix A)</i> .....	254
<i>Figure 0.17 One blade set (Appendix A)</i> .....	254
<i>Figure 0.18 The finished installation (Appendix A)</i> .....	255
<i>Figure 0.1 Turbine application chart (Appendix B)</i> .....	267
<i>Figure 0.2 The proposed system for the water pipeline (Appendix B)</i> .....	268
<i>Figure 0.3 LucidEnergy lift-type turbines from LucidEnergy (Appendix B)</i> .....	269
<i>Figure 0.4 Design methodology of the hydropower system (Appendix B)</i> .....	271
<i>Figure 0.5 Mesh of the simulated models (Appendix B)</i> .....	272
<i>Figure 0.6 CNC turbine models (Appendix B)</i> .....	275
<i>Figure 0.7 Whole testing rig (Appendix B)</i> .....	276
<i>Figure 0.8 Initial proposed designs (Appendix B)</i> .....	277
<i>Figure 0.9 The solid and hollow drag-type turbines (Appendix B)</i> .....	278
<i>Figure 0.10 The working principle of the drag-type turbine (Appendix B)</i> .....	285

*Figure 0.11 Four forms of block (Appendix B) ..... 286*

*Figure 0.12 Two different combinations (Appendix B) ..... 292*

*Figure 0.13 The hydropower system is running on the site (Appendix B)..... 297*

## LIST OF TABLES

<i>Table 2.1 The research focus of the Savonius rotors .....</i>	11
<i>Table 2.2 The multi-stage rotors tested by Kamoji .....</i>	30
<i>Table 2.3 The double-stage rotors tested by Nakajima .....</i>	31
<i>Table 2.4 Three two-straight vanes tested by Altan .....</i>	34
<i>Table 2.5 A brief review of the CFD works conducted by different authors.....</i>	52
<i>Table 2.6 A brief review of the CFD simulation of VAWTs .....</i>	94
<i>Table 3.1 Percentage of the measurement uncertainty .....</i>	116
<i>Table 3.2 Detailed dimensions of the tested rotors with two blades.....</i>	119
<i>Table 3.3 Abbreviations of the rotor with two-blade.....</i>	120
<i>Table 3.4 Abbreviations of the rotor with three-blade .....</i>	120
<i>Table 3.5 The average <math>C_{ts}</math> and <math>C_p</math> of the two-stage Savonius rotor .....</i>	139
<i>Table 4.1 The aspect ratio of the first boundary layer attached to the airfoil surface .....</i>	162
<i>Table 4.2 Detailed time step for different tip speed ratio at 10m/s .....</i>	164
<i>Table 4.3 The percentage of chord length moved per time step .....</i>	164
<i>Table 4.4 The Effect of the number of turns .....</i>	167
<i>Table 5.1 The maximum power coefficient for NACA 4415 airfoil .....</i>	181
<i>Table 5.2 The maximum CP for NACA 0015 airfoil (inside opening).....</i>	186
<i>Table 5.3 The maximum CP for NACA 0015 airfoil (outside opening).....</i>	186

<i>Table 6.1 Dimensions and abbreviations of the tested rotors.....</i>	<i>196</i>
<i>Table 6.2 The loss percentage of CP and increase percentage of CTs.....</i>	<i>201</i>
<i>Table 6.3 The loss percentage of power and increase percentage of CTs.....</i>	<i>204</i>
<i>Table 7.1 The relationship between values of <math>d_1</math> and values of <math>m</math> .....</i>	<i>211</i>
<i>Table 7.2 The relationship between leading-edge index number and values of <math>a_0</math> .....</i>	<i>211</i>
<i>Table 7.3 The factors and levels investigated .....</i>	<i>215</i>
<i>Table 7.4 Orthogonal list <math>L_{16}(4^5)</math> .....</i>	<i>216</i>
<i>Table 7.5 The maximum CP results of the orthogonal method .....</i>	<i>219</i>
<i>Table 7.6 The CTs results of the orthogonal method.....</i>	<i>222</i>
<i>Table 7.7 The maximum and average CP for maximum thickness in tenths of chord.....</i>	<i>225</i>
<i>Table 0.1 Simulation and testing results of lift-type model at 1.5m/s: (Appendix B).....</i>	<i>279</i>
<i>Table 0.2 Simulation and testing results of drag type models at 1.5m/s: influence of rotor size on the turbine performance (Appendix B).....</i>	<i>281</i>
<i>Table 0.3 Simulation and testing results of drag type models at 1.5m/s: influence of blade number on the turbine performance (Appendix B).....</i>	<i>282</i>
<i>Table 0.4 Simulation and testing results of drag type models at 1.5m/s: influence of diameter of the center hollow on the turbine performance (Appendix B).....</i>	<i>283</i>
<i>Table 0.5 Simulation results of drag type models at 1.5m/s (Appendix B).....</i>	<i>288</i>
<i>Table 0.6 testing results of drag type models at 1.5 m/s (Appendix B).....</i>	<i>289</i>
<i>Table 0.7 Testing results of drag type models with long slanted block (Appendix B) .....</i>	<i>290</i>
<i>Table 0.8 Testing results of drag type models with short slanted block (Appendix B) .....</i>	<i>291</i>

*Table 0.9 Simulation results of drag type models (Appendix B) .....293*

*Table 0.10 Testing results of drag type models (Appendix B).....295*

*Table 0.11 Summary of the development of hydropower turbine (Appendix B) .....296*

## NOMENCLATURE

$A$	maixmum frontal area
BN	blade number
$C$	testing section area of wind tunnel
CP	power coefficient
CT	torque coefficient
CTs	static torque coefficient
CFD	computational fluid dynamic
$d$	diameter of the blade
H	height of the rotor
$a$	diameter of central column
$b$	separation gap distance
BT	blade thickness
D0	diameter of endplate
RAR	rotor aspect ratio
SAR	stage aspect ratio
PSA	phase shift angle

GA	genetic algorithms	
m	swept area of Savonius rotor	
$x$	variable	
$x_{ave}$	average of variable	
$x_{SD}$	standard deviation of variable	
$V_{\infty}$	undisturbed velocity	
$V_a$	induced velocity	
$W$	relative velocity	Equation 2.9
R	radius of the Darrieus rotor	
$V_c$	tangential velocity	Equation 2.10
$V_n$	normal velocity	Equation 2.11
$C_T$	tangential force coefficient	Equation 2.15
$C_N$	normal force coefficient	Equation 2.16
$L$	lift force	Equation 2.17
$D$	drag force	Equation 2.18
T	tangential force	Equation 2.19
N	normal force	Equation 2.20

$F_{ta}$	total force	Equation 2.21
$F_{av}$	average force	Equation 2.22
$Q$	total torque	Equation 1.23
$P = Q\omega$	power	Equation 1.24
TSR	tip speed ratio	
OLR	opening length ratio	
$r_{out}$	radius of outer blades	
$r_{in}$	radius of inner blades	
$c_{out}$	chord length of the outer blades	
$c_{in}$	chord length of the inner blades	
$c$	chord length of airfoil	
$t$	thickness-chord ratio	
$a_0, a_1, a_2, a_3, a_4$	constats of NACA 4-digit-series	Equation 7.1
$d_0, d_1, d_2, d_3$	constats of NACA 4-digit-modifed-series	Equation 7.7

### **Greek symbols**

$\varepsilon$	turbulence dissipation rate
---------------	-----------------------------

$\rho$	air density	
$\beta$	gap rate	
$\alpha = \text{AOA}$	angle of attack	Equation 2.12
$\omega$	rotational speed	
$\theta$	azimuth angle	
$\eta$	offset angle between two sets of blades	

# CHAPTER 1 INTRODUCTION

## 1.1 Why do we use vertical axis wind turbines (VAWTs)

The global energy consumption from buildings, including residential and commercial buildings, has increased steadily and ranges between 20% and 40% of the total energy delivered in developed countries (Perez-Lombard et al. 2008). This increase will continue due to the growth in population, the requirement of better living and working condition and the rise of the GDP in developing countries. According to the assessment of the U.S. Energy Information Administration (EIA), the residential and commercial energy use will grow at an average rate between 1.1 and 1.5 percent per year, respectively from 2008 to 2035 (Conti and Holtberg 2011). On the other hand, the rapid growing of the world energy use results in depletion of energy resources and serious environmental problems. Thus, the use of renewable energies will lead to a sustainable development of the future energy supply to buildings. The most commonly used renewable energies in buildings are solar and wind power. Many small solar systems (Littlefair 1998, Hestnes 1999), wind systems (Blanch 2002, Ferreira et al. 2006) and wind-solar hybrid systems (Yang et al. 2007, Nema et al. 2009) have been integrated into buildings in urban areas and in the countryside. Recently, the utilization of small or micro wind turbines working in the urban environment is attracting more and more attention of the researchers.

There are several advantages of integrating a wind turbine into a building. The power generated from the wind turbine can be fed directly into the building's own electrical

circuits, and this avoids the connection costs of the distribution network to the local utility and prevents energy transport losses from large wind farms to the consumer. Using the electricity generated from the wind turbine not only saves the electricity consumption bill of the owner, but may get profit by selling superfluous electricity to the grid. The utility of the wind turbine is also a visible green education device for the whole residents. Last, it is obvious that using the wind power will reduce CO<sub>2</sub> emission and fossil fuel resource consumption.

Based on the advantages mentioned above, it seems that the application of wind turbines in buildings has a promising future, but there are many problems remaining to be settled. The wind speed in an urban environment is generally less than that in an open area. The efficiency of the wind turbine at low wind speed is always less than that at high wind speed. Meanwhile, buildings may cause turbulence. Wind shear in an urban environment is also greater than that in an open area. Therefore, the most important characteristics of the wind turbine in an urban environment are to withstand the turbulence flow, take the wind from all directions, and especially produce high annual energy output under relatively low wind speed. The research about the micro wind turbines in the British domestic sector shows that the development of the turbines which can produce power at low cut-in speeds is an alternative approach to make the micro wind turbines suit for the urban terrain (Peacock et al. 2008). A simple supporting structure, easy maintenance, low noise and vibration levels are also required in the urban environment.

Considering the requirements mentioned above, the VAWT appears to be the most promising turbine in the building environment due to the advantages of the VAWT

which is independent of wind direction, low noise and vibration level. Recent researches have shown that the H-Darrieus, one type of the VAWTs, can produce an increased power output in skewed flow, while a horizontal wind turbine, on the contrary, suffers from a power decrease (Mertens et al. 2003).

## **1.2 Aims and objectives of this thesis**

Generally, there are two kinds of VAWTs. They are drag-type and lift-type VAWTs. The representative of the drag-type and lift-type is Savonius rotor and Darrieus, respectively. The Savonius rotors have relatively lower power coefficient and better starting ability. Although the Darrieus rotors have a relatively high power coefficient, the Darrieus turbine typically generates very little starting torque and they may fail to accelerate beyond a “dead band” even when they do begin to move (Kirke 1998), which limited the utilization of such VAWTs in the urban environment.

Thus, the main objective of this thesis is to improve the starting ability and the CP of the VAWTs, especially for the Darrieus rotor, through the computational fluid dynamic (CFD) method and experiments.

Three methods are proposed to improve the starting ability of the Darrieus rotor. A novel airfoil optimal design process is established to improve the CP of the Darrieus rotor. A general realization way of each objective is summarized as follows:

- a) To gain the objective of the improvement of the starting ability of the Darrieus rotor, three methods are proposed and studied in this thesis. These three methods are the use of two-stage Savonius rotors, an opening at the blade tip

and adoption of two sets of blades. The wind tunnel test is conducted for the research of the two-stage Savonius rotor. And the CFD simulation research is carried out for the Darrieus rotor with an opening at the blade tip, the Darrieus rotor with two sets of blades and the airfoil optimal design process.

- b) To use the wind tunnel to test the two-stage rotor, a test rig is built. The upper part of this test rig is located inside of the wind tunnel, the lower part of this test rig is located outside of the wind tunnel
- c) To use the CFD to simulate the Darrieus rotor with an opening at the blade tip and two sets of blades and to establish the airfoil optimal design process, a detailed investigation of the CFD simulation process and strategies is carried out to find the reliable and efficient CFD process and strategies for the simulation of the Darrieus.
- d) To improve the CP of the Darrieus rotor, a novel airfoil optimal design process based on an automatic CFD process and design of the experiment is established in this thesis.
- e) Finally, a real 1.5 kW Darrieus rotor turbine with an opening at the blade tip is built to test the real performance of the rotor with an opening at the blade tip and optimal airfoil based on CFD simulation studies mentioned above for future study.

### **1.3 Organization of this thesis**

The objective of this thesis is to improve the starting ability and the CP of the

Darrieus rotor. Hence, the research works of this thesis center around three starting ability improvement methods and one airfoil optimal design process. A brief introduction of the organization of this thesis is presented below:

The first chapter of this thesis mainly presents the advantages and problems of the VAWTs used in the urban environment or open areas. In order to solve the aforementioned problems, three methods are proposed to improve the starting ability of the Darrieus rotors, i.e. the usage of two-stage Savonius rotors, an opening at the blade tip and adoption of two sets of blades. To improve the CP of the Darrieus rotor, a novel airfoil design process is proposed and established.

The second chapter is a detailed literature review of the VAWT research and development. This literature review includes the research focus related to the VAWTs, research methodology of the VAWTs and research insufficiency of the VAWTs. The aim of this review is to depict a general outline of the development of the VAWTs, types of the VAWTs, effect of geometry parameters and research methodologies for the VAWTs. This review can offer a valuable guidance for author to find the method to improve the starting ability and the CP of the Darrieus rotor.

In Chapter 3, wind tunnel tests were conducted for the first method, two-stage Savonius rotors, widely used to assist the starting of the Darrieus rotors. It was found in the review that the studies of the two-stage Savonius rotors are not sufficient for starting purpose. The two-stage Savonius rotors with two and three blades were tested to evaluate the ability of the Savonius rotor for starting device, and the effect of three typical design parameters on rotor's performance. And some of CFD simulation works about the Savonius rotor are also presented in this chapter.

In Chapter 4, CFD simulation processes and strategies are discussed to find the right CFD simulation process and strategies for the study of second and third starting ability improvement methods and the study of a novel airfoil optimal design process. It is very important to discuss three kinds of CFD design process and their ability as well as the CFD strategies which are suitable for the simulation of the Darrieus rotor.

In Chapter 5, the second starting ability improvement method is studied based on the CFD discussion in Chapter 4. An opening is created at the blade tip. This is a new Darrieus rotor which has not been studied and mentioned in public literatures. The effect of the opening ratio, the opening location and mounting location are also studied for the Darrieus rotor with symmetrical NACA 0015 airfoil and camber NACA 4415 airfoil.

Chapter 6 presents the investigation of the third starting ability improvement method for the Darrieus based on the CFD discussion in Chapter 4. This third method is the Darrieus rotor with two sets of blades. The effect of the distance between the two sets of blades, and the effect of the offset angle between the two sets of blades on the CP and CTs have been evaluated through the CFD method. Moreover, the rotors with different chord lengths of inner and outer airfoil are also investigated.

In Chapter 7, a novel optimal design process is developed and established to improve the CP of the Darrieus rotor based on the CFD discussion in Chapter 4. This novel optimal design process includes an automatic CFD simulation process and the design of experiment optimal design. This novel optimal design method is adopted for the NACA modified airfoils to find the right airfoil for the Darrieus rotor.

Chapter 8 summarizes the main conclusions and achievements of this thesis and gives

some recommendations and suggestions for the future work.

In appendix A, a real 1.5kW Darrieus rotor is designed and developed based on the simulation works conducted in Chapter 5 and Chapter 7 for future testing. An opening is made at the blade tip and the optimal airfoil is used for this real Darrieus rotor. A novel magnetic bearing is also introduced to this 1.5kW wind turbine system. An axial flux permanent-magnet synchronous generator (AFPMSG) is adopted to reduce the starting torque of the VAWTs system.

In Appendix B, the principle and simulated experience of the lift-type and drag-type vertical axis wind turbines are used in an inline vertical axis water turbine for generating small hydropower for the data monitoring systems along the water pipelines. This is the application of the vertical axis wind turbines in the confined condition of water pipelines.



## **CHAPTER 2 LITERATURE REVIEW OF THE VAWTs**

### **2.1 Review of the drag type VAWTs -Savonius rotor**

A detailed literature review of the VAWTs' research and development is conducted. This literature review includes the research focus related to VAWTs, research methodology of VAWTs and research insufficiency of VAWTs. The aim of this review is to depict a general outline of the development of VAWTs, types of VAWTs, effect of geometry parameters and research methodologies for VAWTs. This review can provide a valuable guide to find some methods which can improve the CTs and CP of Darrieus rotors.

#### **2.1.1 Review of the research focus related to drag type VAWTs**

The Savonius rotor, which consists of two or more semicircular buckets (blades) with a small overlap between them, was conceived by a Finnish engineer, Sigurd Savonius in 1925. It is a drag type vertical axis wind turbine. From the point of aerodynamic efficiency, this type of VAWTs does not compare with lift type VAWTs, but it has a simple design and good starting characteristics. The system can also withstand "strong" winds when most fast running wind turbines must be stopped.

However, this kind of VAWTs has some serious disadvantages, such as working at a lower tip speed ratio; the large Savonius rotor can only be installed close to the

ground; more material is used than the other type of wind turbines when the rated power is the same; and it had a low power coefficient. Therefore, a lot of researches has been performed the studies of Savonius rotor to improve the performance of the Savonius rotor and to understand the mechanism of the force production using experimental and simulation methods.

The basic structure of the traditional Savonius rotor formed by an advanced and a return blade is presented on the left side of Figure 2.1. The right side of Figure 2.1 is a two-stage Savonius rotor built through the superposition of two traditional Savonius rotors.

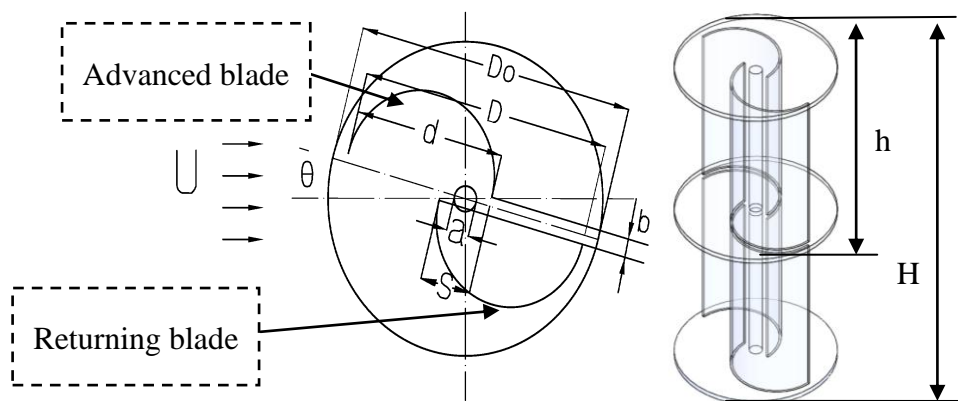


Figure 2.1 A traditional Savonius rotor

Previous researches of the Savonius rotor mainly focused on four areas listed in Table 2.1. These four areas are geometrical design, external or augmentation devices, interaction between the rotors and flow field in and out of the Savonius rotor. The geometric design of the Savonius rotor is to improve the whole performance of the rotors including the starting ability and power coefficient.

Table 2.1 The research focus of the Savonius rotors

<i>Research focus</i>	<i>Name of investigation</i>	<i>Nomenclature</i>
<i>Geometry design</i>	Diameter of blade	d
	Height of the rotor	H
	Number of blades	N
	Diameter of Central column	a
	Separation gap ratio	b
	Blade thickness	BT
	Diameter of endplate	D0
	Gap rate	$\beta = (S-a)/D$
	Rotor aspect ratio	RAR=H/D
	Stage aspect ratio	SAR=h/D
	Number of Stage	NS
Phase shift angle	PSA	
<i>External or augmentation devices</i>	Blade profile	
	Guide vanes	
	Diffuser	
	Obstacle	
<i>Interaction between the rotors</i>	Ancillary surfaces	
	Distance between two rotors	
<i>Flow fields</i>	Distribution of the rotors	
	The mechanism of the force produces	
	Flow around Savonius rotor	

Although the structure of the Savonius rotor is very simple, many design parameters are involved. Parts of the design parameters of conventional semicircular Savonius rotors are listed in Table 2.1. The design parameters' nomenclatures can be found in

Figure 2.1. Different blade profiles have different design parameters and geometry nomenclatures.

External or augmentation devices are adapted to increase the velocity of the wind and generate more power. However, those external or augmentation devices will invalidate the ability of taking the wind from all the direction.

The research on the interaction between the rotors can provide valuable guidance about the construction of small vertical axis wind farms. And the flow patterns in and out of a Savonius rotor are used not only to understand the lift and drag characteristics but also to give valuable indication of the design of its geometry. The following discussion will give a detailed review of the four parts mentioned above.

#### **2.1.1.1 Geometry design parameters and the optimum design**

In order to better understand the influence of the geometry parameters on the performance of the Savonius rotor, classification of the Savonius rotors is very important. However, it is difficult to classify Savonius rotors because many researchers have proposed many kinds of creative Savonius rotors for the past several decades. And different of kinds Savonius rotors have their own design parameters. For example, the geometry design parameters of the one-stage traditional semicircular-blade Savonius rotor is its diameter of blade, height of the rotor, number of blade diameter of the central column, separation gap ratio, blade thickness, diameter of endplate, swept area, gap rate and rotor aspect ratio.

The stage aspect ratio, phase shift angle and number of stages are the design

parameters of the traditional semicircular-blade multi-stage Savonius rotor. If the blade sectional geometry of the traditional Savonius rotor is modified, most the design parameters related to the blade profile will be changed. In order to well classify the Savonius rotor, a classification standard should be established. Based on a literature review, it is found that the blade sectional geometric design is the most important issue in terms of geometric design. The blade sectional geometry design will not only influence the performance significantly, but determine the design parameters. Thus, the blade sectional geometry was used as a standard to classify the Savonius rotors.

#### ***2.1.1.1.1 Evolution of the blade sectional geometry of the Savonius rotor***

The blade sectional geometry design consists mainly of two parts, the number of blades and the blade profile. Generally, the static torque coefficient will increase and power output will decrease if the blade number is increased. The blade number is mainly from two to six. In terms of blade profile, it can be semicircular buckets (Savonius 1931), Bach type, 4-fold multiplication of the NACA 0024 airfoil section cut in half (Khan 1978), swinging-blade (Aldos 1984), canfield slatted, twisted (Saha and Rajkumar 2006), helical blades (Kamoji et al. 2009) and the blades optimized through genetic algorithms.

##### ***2.1.1.1.1.1 Traditional semicircular blade***

The original blade profile is a semicircular section proposed by Sigurd Savonius in 1925. Two semicircular blades were used to build the traditional Savonius rotor. The

idea of this design came from the principle of Fletterners rotor ship. The Fletterners cylinder was cut from top to bottom and two semicircular blades move sideways along the cutting plane. The main design parameters of traditional Savonius rotor are gap rate, blade number and aspect ratio. In order to find the highest performance of this type of VAWT, more than 30 different models were tested in a wind tunnel by Sigurd Savonius. The best power coefficient stated by Savonius was 31 percent. However, Simonds and Bodek (1964) undertook a full scale measurement of the traditional Savonius rotor in a natural wind at the Brace Research Institute. The maximum power coefficient was only 15 percent at 0.7 tip speed ratio.

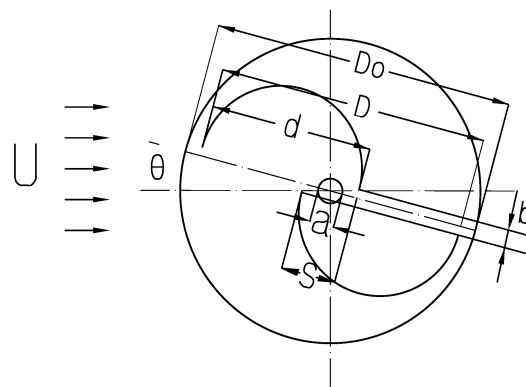


Figure 2.2 A semicircular blade

In 1974, Newman (1974) made some wind tunnel measurements on the Savonius rotor for a range of gap sizes. Five Savonius rotors with different gap sizes and one Bach rotor were tested at nominal wind speed of 30 mph and less in the McGill 3ft x 2ft wind tunnel. The test results showed that the Bach rotor had the best performance for large and small values of the tip speed ratio, although not for intermediate values. The best rotor is No.2 for which the ratio between the gap size

and the diameter of the bucket is  $1/6$ . The uncorrected highest power coefficient is about 0.29 when the tip speed ratio is about 0.9.

#### 2.1.1.1.2 Bach type profile

The second profile proposed by Bach (1931) is called the Bach profile, who stated that the power coefficient can be improved by replacing blades with semicircular arc sections with blades with sections composed of an arc and a straight line.

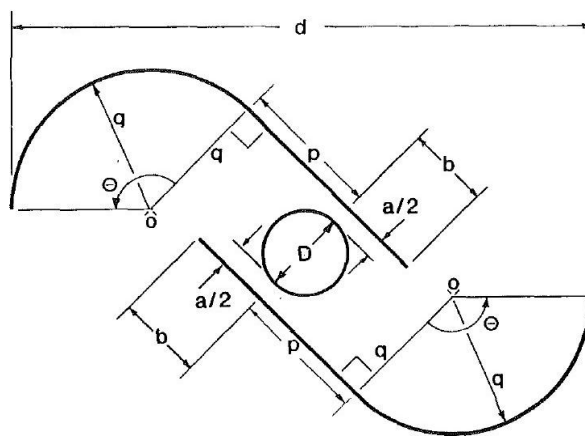


Figure 2.3 The Bach's blade profile

A comparison between Bach and Savonius' blade profiles was made by Ushiyama et al. (1986). They claimed that the maximum power coefficient of the Bach rotor is about 0.23 when the gap rate ranges from 0 to 0.3. However, the maximum power coefficient of the semi-circular type is only 0.21. A detailed parameter investigation of the Bach type was conducted by Modi and Fernando (1989). The rotor geometry tested by them is presented in Figure 2.3. The test results showed that the maximum power decreased as the gap separation increased. The peak power coefficient is achieved when  $a$  is zero. The optimum  $b$  (blade overlap) is about 10 percent of the

rotor diameter. The optimum  $h/d$  (aspect ratio) is 0.77. The influence of the blade shape factors,  $q/p$  and  $\theta$ , was also investigated. The peak power coefficient is gained when  $q/p$  is 0.2 and the optimum  $\theta$  is  $135^\circ$  at fixed  $q/p$  of 0.2.

#### ***2.1.1.1.3 The Sivasegaram profile***

A new type of blade profile was tested by Sivasegaram (1978). This blade is made by a small and a big curvature arc presented in Figure 2.4. The test results of this profile showed that the two-blade rotor with blades of a circular arc section and a blade angle of  $120^\circ$ - $150^\circ$  has a better power coefficient than that of the blade with a semicircular section. The test results also indicate that the two-blade rotor achieves the highest power coefficient when  $n=2$ ,  $\theta=127^\circ$ ,  $s/R=3.11$  and  $ns/D=2.8$ . This maximum power coefficient is about 0.2 under the test condition. In 1978, Sivasegaram extended the above investigation to testing the effect of blade numbers. Rotors with four blades were studied experimentally.

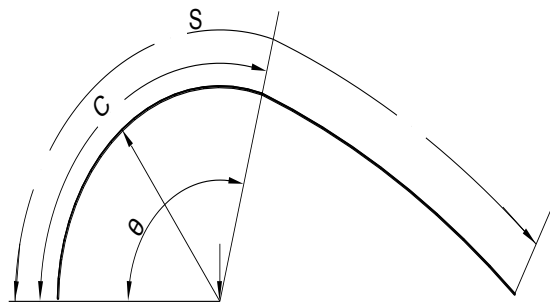


Figure 2.4 The blade profile proposed by Sivasegaram

#### ***2.1.1.1.4 NACA airfoil and double rotor profile***

Five different blade profiles presented in Figure 2.5 were studied by Khan (1978)

through a wind tunnel test. These profiles include a traditional semi-circular section, a NACA 0024 airfoil section, an S-section, an inverted S-section and a double rotor section. The use of the NACA 0024 airfoil section was to get the minimum drag force. The S-section composed by two circular arc profiles is different from the Bach type section.

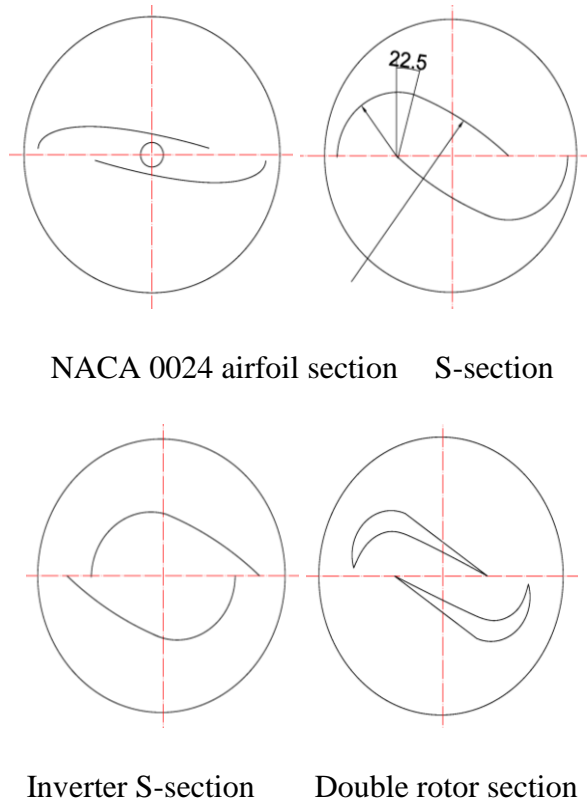


Figure 2.5 Different profiles tested by Khan

The test results showed that the optimum gap rate of the rotor varied with the rotor's profile. The optimum gap rate for an original Savonius rotor and the rotor with S-section is 16 and 30 percent, respectively. The power coefficient of the rotor with S-section is the highest among five different blade profiles. They stated that the use of airfoil did not work out probably because the NACA airfoil section gives minimum

drag at low angle of attack only. The performance of the rotor with the inverter S-section and double section was much inferior to the rotor with S-section. The author emphasized that the most encouraging characteristic of this rotor is that the prototype can generate power even when wind speed is 4 miles per hour. The maximum power coefficient and optimum gap rate of the semicircular section, NACA section, S-section, inverted s-section and double rotor section are (0.325 0.16), (0.32, 17.6), (0.375, 0.3), (0.175, 0.35) and (0.3, 0.26), respectively.

#### ***2.1.1.1.1.5 Sail profile***

A new version of the Savonius rotor with a sail was proposed by Fleming and Probert (1982) to reduce the ratio between the weight and projected area and improve the rotor's power coefficient. They claimed that the rotor will not only become much lighter than a rigid blade rotor with flexible soles, but may improve the power coefficient by properly distributing the rollers whose location determines the blade profile. Five different blade profiles shown in Figure 2.6 were tested by Fleming and Probert. The results showed that the power curves of the profiles 1, 2 and 3 are similar, except the profile 3, which gives the highest maximum power. The rotor with profile 5, which has the deepest curve, generated only 80% power of the profile 3. A comparison was made between a two-blade rotor with profiles 3 and 5 and a three-blade rotor with profiles 3 and 5. The test results showed that the power coefficient of the three-blade rotor with flexible sails is about one third higher than that of the two-blade rotor. This is contrary to the findings of the rotor with rigid blades.

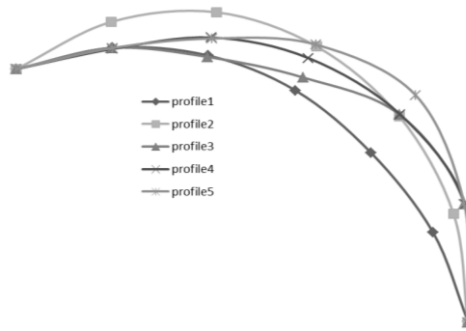


Figure 2.6 Five different profiles tested by Fleming

### 2.1.1.1.6 *Swinging profile*

The idea of swinging blades is to reduce the drag force generated by the returning blades. Aldoss (1984) conducted an experimental test of the swinging blades. The basic structure of this rotor is shown in Figure 2.7.

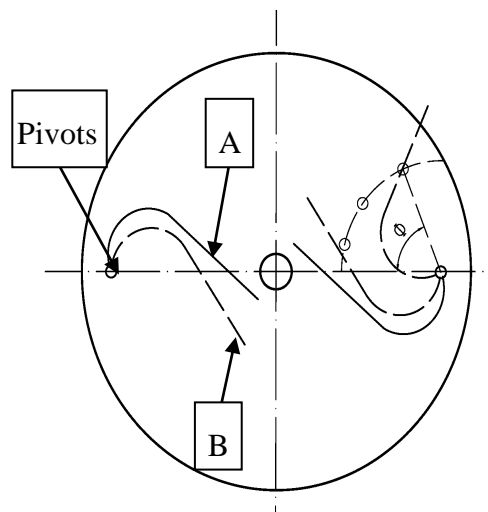


Figure 2.7 The swinging blades

The blades were rolled using the galvanized sheet and allowed to rotate around the pivots. The upwind blade will be pushed to contact with the shaft, and this will

increase the thrust force. When wind acts on the returning blade, a gap between the returning blade and shaft will be created to reduce the drag force.

Two different configurations A and B were tested at five swinging angles  $\phi$ . The results indicated that the torque and power output curves are shifted up with the increasing swinging angle. And the profile B generates less power than that of the profile A. The maximum power coefficient of all the rotors is about 0.11 which is much less than that of the traditional Savonius rotor.

#### ***2.1.1.1.1.7 Slated profile***

Following the idea of reducing the drag force of the returning blades, a modified swinging rotor called slatted-blade Savonius was studied by Reupke and Probert (1991). This slatted-blade Savonius rotor is presented in Figure 2.8. The basic configuration is fairly like the traditional semicircular Savonius rotor, except that the blade profile is cut into several slats. These slats were fixed by some rollers slats and would open when a blade returned and closed when a blade was advancing.

An unmodified traditional Savonius rotor, slatted rotor with 8 wide flaps and slatted rotor with 16 narrow flaps were tested to compare the performance. The experimental results showed that the slatted rotors could not improve the power coefficient because these slats were always locked at high rotational speed, although the slatted rotor developed higher static torque than the traditional Savonius rotor because the slats on the returning blade would open.

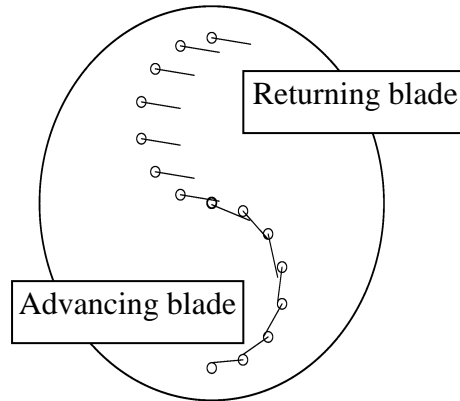


Figure 2.8 The cranfield slatted rotor

#### 2.1.1.1.1.8 *Twisted blade*

All the blade profile designs above focus on two dimensional (2D) profiles. These blades are formed by extending the 2D profile along the  $z$  direction. A 3D twisted blade was constructed and tested by Grinspan et al. (2001). The profiles of the rotor blade at the top and bottom are different. The angle between blade edge and rotor shaft is defined as  $\theta$ . The detailed geometry of this rotor with twisted blades is shown in Figure 2.9. Rotors with three curved, straight, airfoil, and twisted blades were tested and compared. And the twist parameters were also studied. Based on the power curves presented by the Grinspan, the twisted blades could not improve the rotor's power coefficient. However, a negative range of  $CT$  can be reduced by using the twisted blades. The maximum power coefficient of the rotors tested by Grinspan is about 0.6. Several similar rotors with twisted blades were tested by Saha and Rajumar (2006). The results show that the performance of the three-blade rotor could be improved when the twisted angle of the blade increased. The optimum twisted

angle is  $15^\circ$ , but the maximum power coefficient is only 0.14.

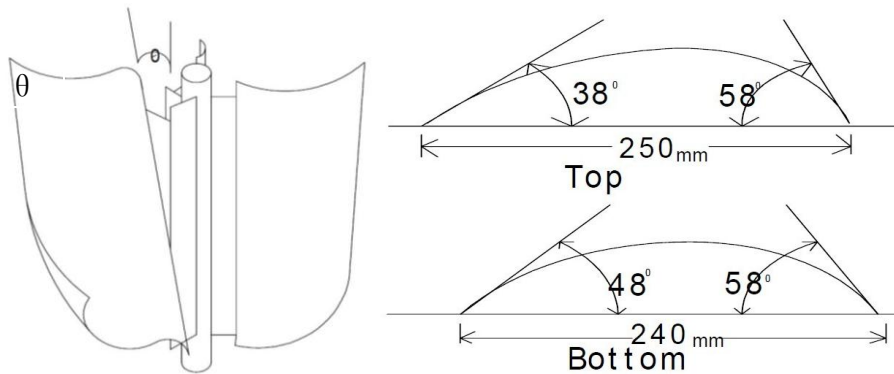


Figure 2.9 The twisted rotor and blade (Saha and Rajumar, 2006)

### 2.1.1.1.9 Helical blade

Another three dimensional blade was tested by Nemoto et al. (2003). This 3D blade (Figure 2.10) is different from the Grinspan's twisted blade. The blade profiles at the top and bottom is the same. This type of blade is called helix blade now.

Type	(a)	(b)	(c)	(d)	(e)
Cross section					
Shape					
Curvature	None	None	Small	Small	Large
Twist	None	Twisted	None	Twisted	Twisted

Figure 2.10 The Savonius rotor tested by Nemoto

The maximum power coefficient of rotors without endplates is about 0.05, 0.051, 0.1,

0.95 and 0.125 for type (a) to type (e), respectively. The maximum power coefficient of the type (e) with endplates is about 0.175. Thus, they claimed that the power coefficient and the range of the tip speed ratio of the Twisted-Sweeney rotor could be increased by raising the curvature of the blade. The rotor with both twist and curvature could give the maximum power output.

Another helical Savonius (Figure 2.11) rotor was tested by the Kamoji et al. (2009) to eliminate the negative value of CTs. A helix is a three dimensional space curve. Coil springs are the typical examples of the helix. The inner edge of the helical Savonius rotor remains vertical and the out edge twisted by  $90^\circ$ .

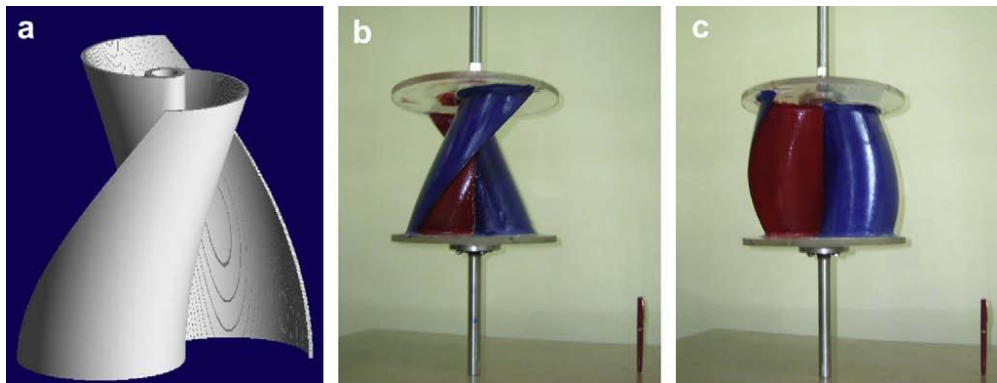


Figure 2.11 A helical Savonius rotor tested by Kamoji

The tested results showed that the static torque coefficients of the helical Savonius at all azimuth angles were positive for all the helical rotors. And the power coefficient of the helical rotor without shaft and with zero gap rate was nearly as good as that of a conventional Savonius rotor. The maximum power coefficient of the helical rotor without shaft and with zero gap rate was about 0.174 when the Reynolds number was 150,000. However, the helical rotor with shaft presented the lowest power

coefficient, which is only 0.9, when the tip speed ratio is 0.9. In fact, the power coefficient of the semi-circular rotor without shaft is the lowest among the conventional Savonius rotors

#### ***2.1.1.1.10 Profile designed by genetic algorithm***

Based on the above review, the design methodology of the blade profile design had been improved from 2 dimensions to 3 dimensions. However, all the designs mentioned above are more likely a random design based on experimental tests. In fact, there are countless curves which can be used for the rotor blade profile. Thus, how to find an optimum profile is the final aim of the Savonius rotor's design. With the development of computational fluid dynamics (CFD), modern design has been evolved from random surmise experimental testing to the combination of virtual CFD simulation and experimental testing. 2D virtual CFD design has been conducted by Moharmed et al. (2011). The design of the blade profile was not based on a surmise or guess. An evolutionary algorithm (EA), a search heuristic aims to minimize the search process within an appointed solution domain, was adopted to find the optimum blade profile of the Savonius rotor.

The blade profiles (Figure 2.12) from Moharmed consist of five points. Two points are fixed points which decide the chord length of the curves. Three points are variable points whose coordinates are needed to be found based on the maximum power coefficient while considering the obstacle to shield the returning blade. It is found that the power output can be increased for about 38.9% when the tip speed ratio is 0.7. It is too bad that the rotor without obstacle has not been optimized by

this method.

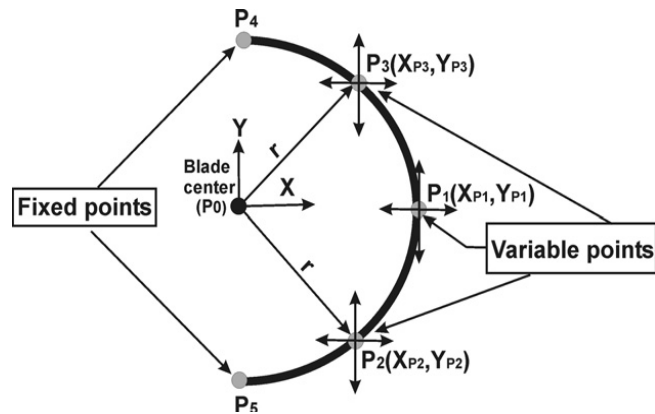


Figure 2.12 The evolutionary algorithm optimization of the blade (Moharmed et al)

A general review of the blade profile designs is presented in the above section. In the following parts, I will give a brief review about the influence of the blade numbering on the performance of the Savonius rotor.

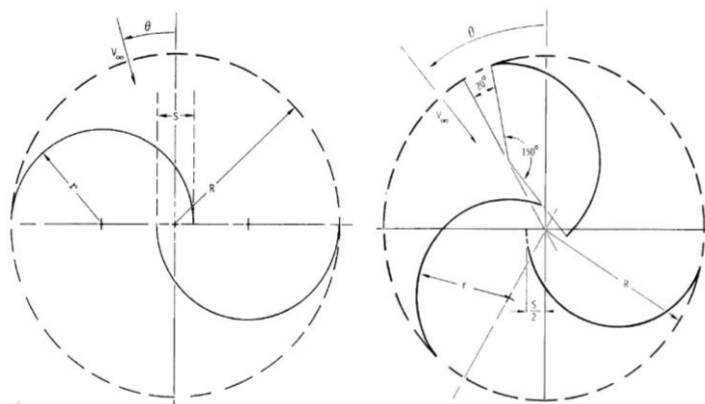


Figure 2.13 The two- and three-blade rotors tested by Blackwell

Blackwell et al. (1977) conducted a wind tunnel investigation on the performance of the two-blade and three-blade traditional Savonius rotors. The two-blade rotor is a traditional semicircular blade. The three-blade rotors were built with an  $150^\circ$  arc to

eliminate the mechanical interference between Savonius and Darrieus rotors. 15 configurations of the Savonius rotor were tested. The power coefficient of the two-blade rotor is better than that of the three-blade rotor. However, the three-blade rotors have better static torque coefficient than that of the two-blade rotor.

The comparison between the two- and three-bucket semicircular rotors were also made by Ushiyama et al. (1986). The results showed that the static torque curve of the three-bucket rotor was smoother than that of the two-bucket rotor. However, the dynamic torque and the power coefficient of the three-bucket rotor are much lower than those of the two-bucket rotor. In terms of starting characteristics, more time is needed to reach the maximum rotational speed for the three-bucket rotor.

A brief summary was conducted by Sivasegaram (1981) about the effect of the blade profile and numbers on the performance of the Savonius rotor. The conclusion is that the power coefficient of the rotor which has several blades is not highly sensitive to the blade profile. The power coefficient of the rotor with two blades is sensitive to the blade profile. Thus, it is very important to design the blade profile properly.

At this point, a review about the blade geometry design is finished. However, the performance of the Savonius rotor is influenced not only by the blade geometry design, but also by the secondary design parameters. Thus, the effect of the secondary design parameters on the rotor's performance will be reviewed below.

#### ***2.1.1.1.2 Secondary design parameters of the Savonius rotor***

The secondary design parameters of the Savonius rotor are the size of endplate, with and without endplate, the shape of the endplate, aspect ratio, number of stage and

phase shift angle. The effects of the secondary design parameters can be classified into three effects, the effect of the endplate, the effect of the aspect ratio and the effect of the multi-stage, but all these secondary design parameters, in fact, interact with each other.

#### ***2.1.1.1.2.1 The effect of the endplate***

The effect of the endplate includes the effect with and without endplate, the size of the endplate and the shape of the endplate. Uhiyama et al. (1986) conducted a comparison between the rotor with and without endplates. The endplates are two circular plates. It is found that the torque coefficient of the rotor without the endplates decreases rapidly when the tip speed ratio is larger than 0.5. The power coefficient is reduced remarkably and operation range is narrowed. Ogawa and Yoshida (1986) investigated five different shape endplates. Rotor No.1 has two brass-disk endplates which has the same size as the rotor diameter. Rotor No.2 designed for no endplate case has two very small disks to fix the rotor blades. Two semicircular disks which have the same shape of the bucket were used for the rotor No.3. The endplates of the rotors No.4 and No.5 are two cut planes which have inclination angle of  $45^\circ$  and  $60^\circ$  related to a horizontal plane. The results are presented in Figure 2.14.

It is also found that the difference of static torque is very small among the five rotors, but the difference of the power coefficient is significantly large. It is clear that the rotor No.1 gained the highest power coefficient. Based on the two experiments mentioned above, it is very clear that the endplate is absolutely necessary for a

semicircular Savonius rotor and the best shape of the endplates for the Saonius rotor is a circular plate. The size of the endplates was tested by Sivasegaram (1978) for three kinds of aspect ratios. The results show that the power coefficient increases when the ratio between the diameter of the endplate to the diameter of the rotor is 1.1. After this ratio, the power coefficient will be reduced.

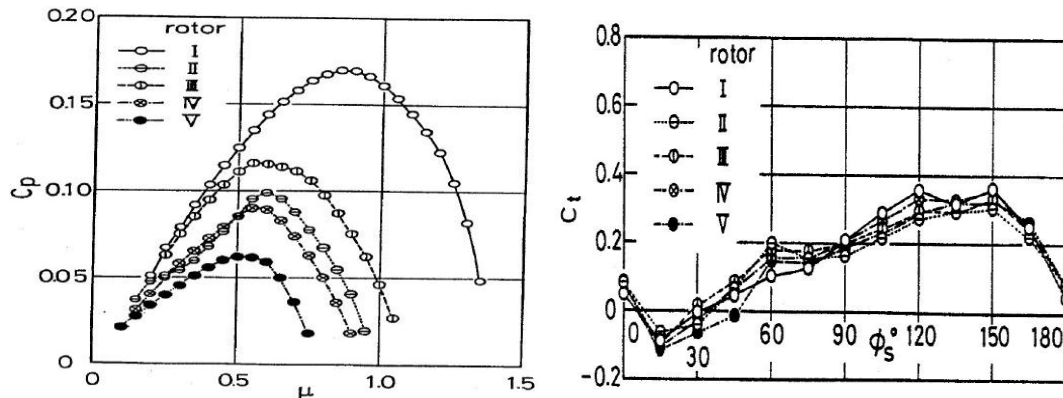


Figure 2.14 The effect of the endplate shapes (Sivasegaram, 1978)

#### 2.1.1.1.2.2 Effect of aspect ratio

There are two different aspect ratios, i.e. the rotor aspect ratio and stage aspect ratio. The rotor aspect ratio means the rotor diameter is divided by the rotor's height. The stage aspect ratio is only suitable for multi-stage rotors. Rotor aspect ratio is discussed here. The stage aspect ratio will be discussed in the effect of the rotor stage section. In this paragraph, the impact of the aspect ratio on the performance on a single stage rotor is discussed. Vance (1973) gave a summary of the impact of the aspect (Figure 2.15) on the rotor acceleration. He defined the ratio of the torque on the rotor to its polar inertia as the rotor's acceleration ability. It is found that the acceleration ability is proportional to the square root of the aspect ratio. But, there

must be some limitation of the aspect ratio due to the consideration of the structure. The test results conducted by Sivasegaram also show that the maximum power coefficient is increased due to the increasing aspect ratio. The static torque coefficient and power coefficient of the rotor with different aspect ratios were tested by Ushiyama et al. (1986). And it is found that the smaller the aspect ratio, the larger the distribution of the static torque. The power output increase is proportional to the increasing aspect ratio.

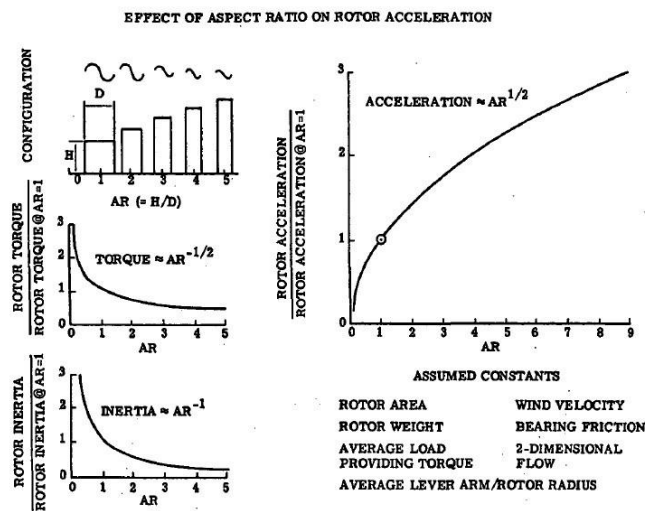


Figure 2.15 The impact of aspect ratio on acceleration ability (Ushiyama et al.,1986)

### 2.1.1.1.2.3 Effect of rotor stage

The stage aspect ratio, numbers of stage and phase shift angle are the design parameters of the multistage rotor without considering the design of the blade profile. The effect of the numbers of stage was investigated by Ushiyama et al. (1986). This was a comparison of the semicircular two-blade single-stage rotor and the semicircular two-blade double-stage rotor with the upper rotor shift of 90 degrees

when two kinds of rotors have the same sweep area. Thus, the rotor aspect ratio of the two-stage rotor is the same as that of the single-stage rotor. And the stage aspect ratio of the two-stage rotor is half of the single-stage rotor. The results show that a smooth static torque can be gained by using the double-stage rotor, although the value of the static torque of the two-stage rotor is smaller than that of the single-stage rotor. And the two-stage rotor is slightly slower in starting but a bit higher in the maximum rotational speed and power coefficient than those of the one-stage rotor. A three-stage rotor with three blades was compared with a single-stage rotor with three blades by Hayashi et al. (2005). The rotor aspect ratio of the three-stage rotor is the same as that of the single-stage rotor. The stage aspect ratio of the three-stage rotor is one third of the single-stage rotor's rotor aspect ratio. The improvement of the static torque by using the multi-stage rotor is clear. However, the power coefficient seems to decrease by using the three-stage. This is opposite to the conclusion made by Ushiyama.

Table 2.2 The multi-stage rotors tested by Kamoji

<i>Case No</i>	<i>Stage</i>	<i>Diameter of rotor (D)</i>	<i>Height of rotor (H)</i>	<i>Height of stage (h)</i>	<i>Stage aspect ratio (h/D)</i>	<i>Rotor aspect ratio (H/D)</i>
1	Single	208	208	208	1	1
2	Two	226	226	113	0.5	1
3		131	262	131	1.0	2
4	Three	225	225	75	0.33	1
5		96.6	289.9	96.6	1.0	3

Five kinds of rotors (Table 2.2) with different stage aspect ratios and rotor aspect ratios were tested by Kamoji et al. (2008). Cases 1, 3 and 5 were compared to study the effect of the rotor aspect ratio on the performance when the stage aspect ratio is fixed. And the results show that case 1 has the best performance among the three cases and the power coefficient of case 3 is almost the same as that of case 5. The cases 1, 2 and 4 were compared to investigate the influence of the stage aspect ratios on the performance. It is found that the power coefficient will decrease by reducing of the stage aspect ratio when the rotor aspect ratio is fixed. And the static torque curve will become smooth with the decrease of the stage aspect ratio.

Table 2.3 The double-stage rotors tested by Nakajima

<i>Case No</i>	<i>Stage</i>	<i>Diameter of rotor (D)</i>	<i>Height of rotor (H)</i>	<i>Height of stage (h)</i>	<i>Stage aspect ratio (h/D)</i>	<i>Rotor aspect ratio (H/D)</i>	<i>Phase shaft</i>
A	Single	142	210	210	1	1	0
B	Two	142	210	103	0.5	1	0
C		142	210	103	0.5	1	90

Three different rotors, presented in Table 2.3, were tested by Nakajima et al. (2008) to develop a nano-hydraulic turbine. The power coefficient of the rotor C is the highest among three rotors. It means that a phase shift will increase the power performance of the rotor. The comparison between rotor A and rotor B shows that decreasing the stage aspect ratio will reduce the power coefficient.

### 2.1.1.2 Augmentation devices

The power coefficient of the Savonius rotor has been improved a lot by the optimization of the rotor design. However, the diffuse nature of wind limited the utilization of the Savonius rotor, especially considering the cost effectiveness in low wind environment. Thus, a number of improvements have been done to improve the power output by using augmentation systems.

Sabzevari (1977) tested a duct augmentation system (Figure 2.16) which is composed of concentrator and diffuser. He claimed that the power augmentation factor could be improved by using the augmentation system at certain wind speed.

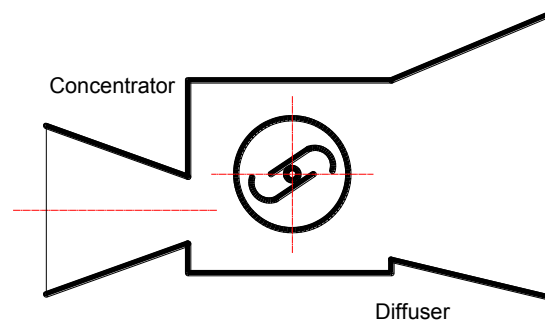


Figure 2.16 A ducted augmentation system (Sabzevari, 1977)

Following Sabzevari, a more detailed study of the duct type augmentation system is conducted by Sivasegaram (1979). He claimed that the possible power augmentation factor is only 1.5 which is much less than that of the Sabzevari's case. He also mentioned that the duct power augmentation will deprive Savonius rotor's performance, one of the biggest advantages of direction-independent operation. Thus, Sivapalan and Sivasegaram (1980) proposed a direction-independent concentration

augmentation system by using several straight vanes presented on the right side of Figure 2.17. A six-blade rotor is adopted. It was found that the use of the straight vanes of a moderate size can improve the power output. And the concentrators with a smaller number of blades cause a fall in power output at certain wind directions.

Sivasegarm and Sivapalan (1983) also tested an augmentation system built by two flat rectangular vanes of moderate size on the left side of Figure 2.17. The rotor used is a two-blade Bach type Savonius rotor. This augmentation system can improve the power output of about 80%. Type a is better than type b in terms of power output. And he claimed that the geometric parameters of this augmentation system would not affect the power output significantly. Therefore, a considerable tolerance of design and construction is allowable. Following the idea from Sivasegarm, an augmentation system with one deflecting plate was tested by Ogawa and Yoshida (1986) for a two-blade Savonius rotor. Three kinds of deflecting plates were used and compared. And the most effective deflecting plate is a simple flat plate which can improve the power output for about 24 %.

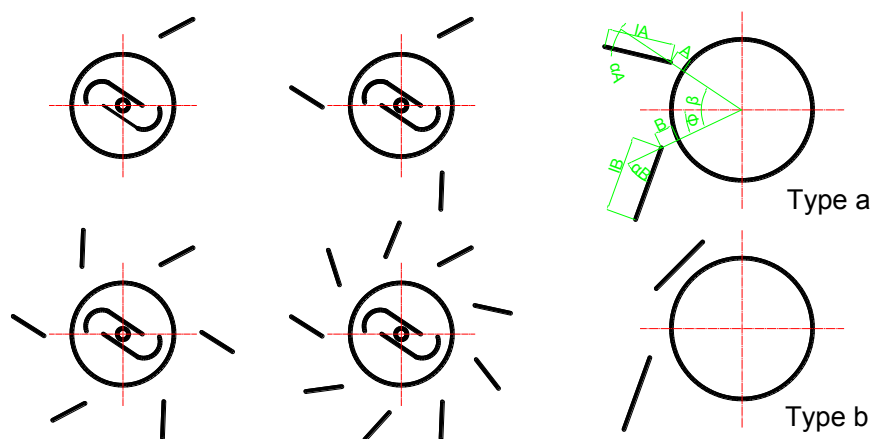


Figure 2.17 The straight-vane augmentation systems (Ogawa and Yoshida, 1986)

In 2005, several augmentation systems with vanes ranging from 3 to 12 were tested by Hayashi et al. (2005) for one stage three-blade rotor and three stage three-blade rotor. The test results show that the power output will decrease with the increasing number of the vanes for one-stage rotor and three-stage rotor. The decrease of power may due to the length of the vane is too small to augment the wind.

Table 2.4 Three two-straight vanes tested by Altan

<i>Type of curtain arrangement</i>	<i>Distance <math>l_1</math> (cm)</i>	<i>Distance <math>l_2</math> (cm)</i>
Curtain 1	45	52
Curtain 2	34	39
Curtain 3	22	26

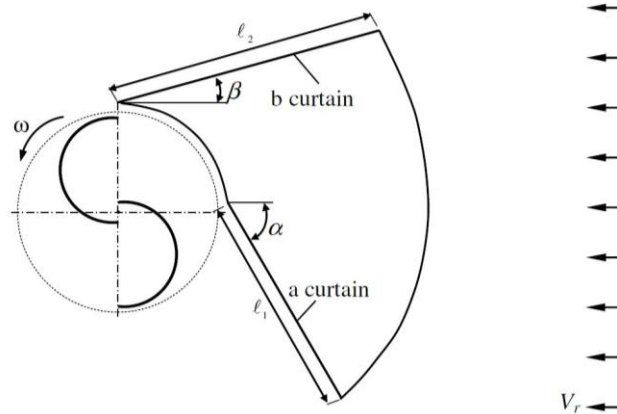


Figure 2.18 Two straight vanes tested (Altan et al, 2005)

In 2008, an augmentation system with two-flat rectangular (Figure 2.18) vanes were tested again by Altan et al. (2008) for a two-blade semi-circular rotor. The

augmentation system of Altan's rotor is similar to one of Sivasegarm's rotors as type a. Three different curtains presented in Table 2.4 were compared. The optimum curtain is the curtain 1. Then, the curtain 1 was used to find the optimum curtain angle. The optimum  $\alpha$  is  $45^\circ$  and the optimum  $\beta$  is  $15^\circ$  for the curtain 1.

An augmentation system shown in Figure 2.19 with one straight vane was optimized by Mohamed et al. (2011) through coupling the CFD and EA for the two- and three-blade Savonius rotors.  $X_1$ ,  $Y_1$  and  $X_2$  are three free parameters which were optimized simultaneously by the CFD evaluations. The objective function is the maximum power coefficient. The optimal  $X_1/R$ ,  $Y_1/R$  and  $X_2/R$  are -1.23830, -0.45390 and -1.09993 and -1.05632, -0.36912 and -1.38162 for two- and three-blade rotor, respectively. The maximum power coefficient of the optimal two- and three-blade rotor is 0.25 and 0.21, respectively.

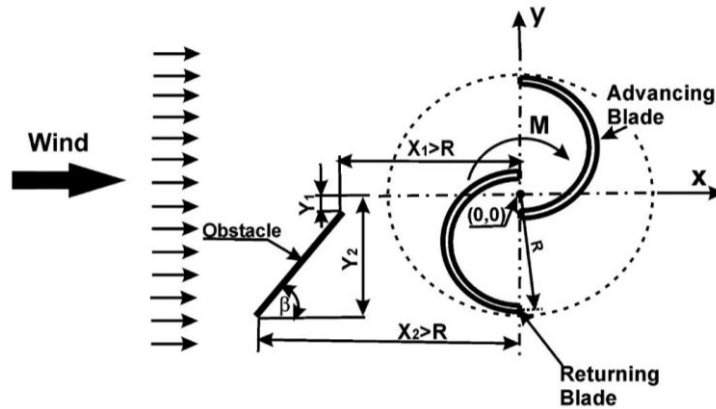


Figure 2.19 An augmentation system with one straight vane (Mohamed et al, 2011)

Two-blade and three-blade rotors with a guide-box tunnel (GBT) shown in Figure 2.20 were tested by Irabu and Roy (2007). The ratio between the length of the guide box and rotor diameter is defined as the GBT width ratio named as  $\delta$ . The area ratio

between the inlet and outlet is defined as  $AR_g$ . The test results show that the optimum  $\delta$  and  $AR_g$  are 1.4 and 0.43, respectively. By using such optimum guide box tunnel, 1.23 and 1.4 times of the power output can be gained in the two and three-blade rotors compared with the related rotors without the guide box tunnel. The two-blade rotor with GBT is 1.08 times as much as that of the three-blade rotor with GBT.

Based on the review of the augmentation system, it can be summarized that the widely used augmentation systems are ducted type, straight vane type and a guide box. All these augmentation systems do improve the power output of the Savonius rotor. The increasing fact of  $CP$  is range from 1.2 to 2. However, all these augmentation systems suffer the same problem, i.e. the use of augmentation system will week the wind direction independence ability of VAWTs, except the straight vane system with multiple vanes. And the omnidirectional ability is one of the most important features which makes VAWT a completer of the HAWT.

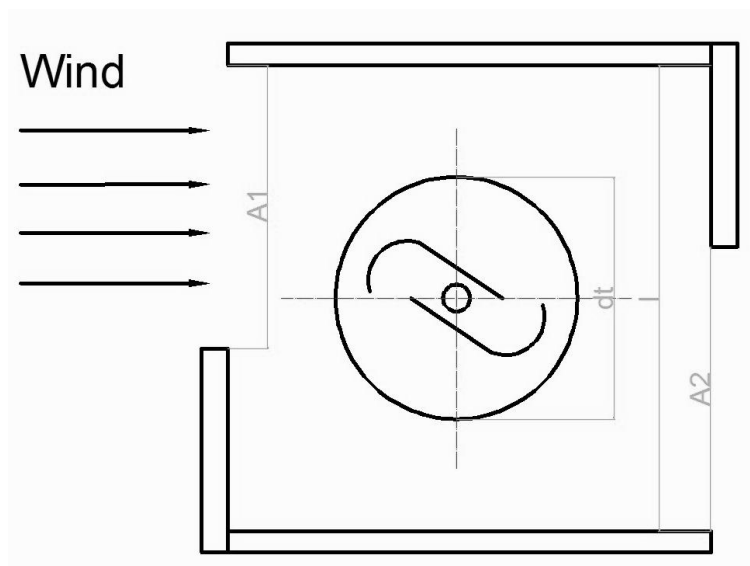


Figure 2.20 A guide-box tunnel augmentation system

### 2.1.1.3 Interaction between the rotors

Based on the literature review, the intention of the investigation about the interaction between the rotors is to utilize pulsed turbulence. The experimental test about the coupled rotors was conducted by Bowden and McAleese (1984). The settlement of the two Savonius rotors is shown in Figure 2.21. It was found that a natural phase locking happened when two rotors run side by side in the wind tunnel. And the sum of the power output generated by the coupled rotors is lower than that of two rotors run independently when the distance of the blade tip between two rotors is 12mm.

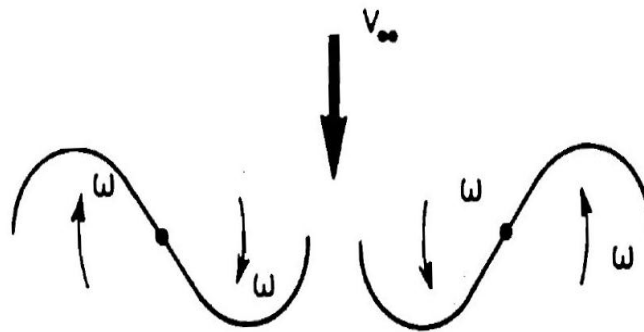
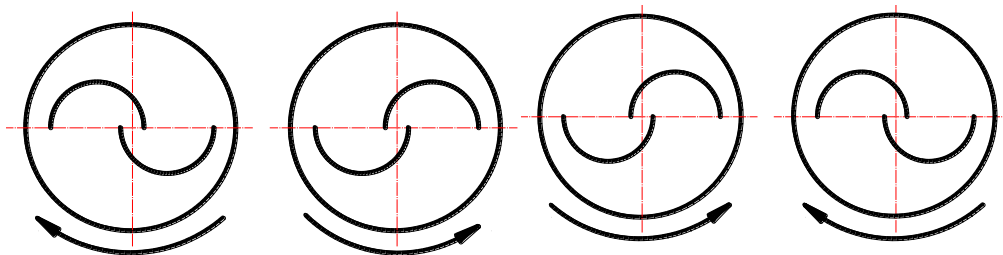


Figure 2.21 The coupled rotors tested by Bowden and McAleese (1984)



Configuration No.1

Configuration No.2

Figure 2.22 The coupled rotors tested by Aldoss and Najjar (1987)

Two kinds of coupled rotors were tested by Aldoss and Najjar (1987). One kind is two-counter rotors placed side by side with the advancing blade turning out off the center of the two rotors. Another one is two counter rotors placed side by side with the advancing blade turning into the center of the two rotors. They are presented in Figure 2.22. The test result indicates that the power coefficient of the coupled rotors increases with the increase of the separation distance between the two counter-rotating rotors when the  $S/D$  is less than 1.7.  $S$  is the separation distance and  $D$  is the diameter of the rotor. In addition, Configuration No.1 can get higher power output than that of Configuration 2.

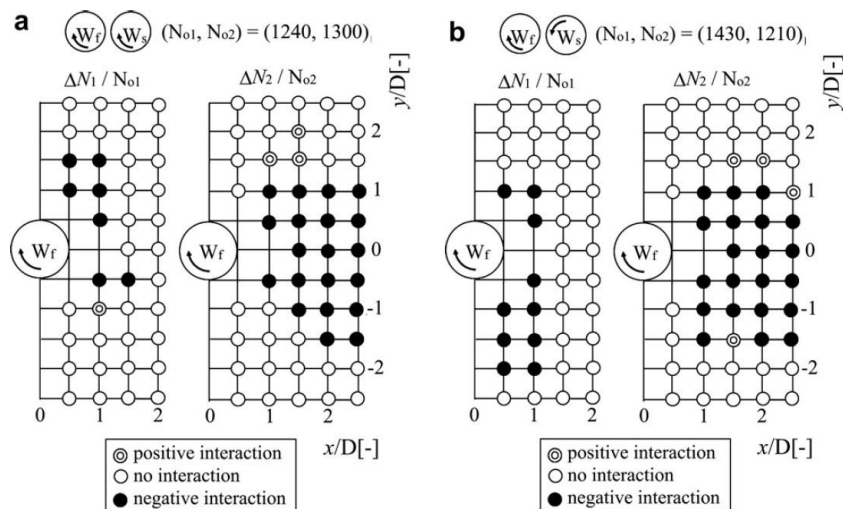


Figure 2.23 The coupled rotors tested by Shigetomi et al. (2011)

A detailed investigation of the horizontal interaction between two Savonius rotors was conducted by Shigetomi et al. (2011) to offer some indication for the installations of a small Savonius wind farm. The interaction pattern was classified into four categories. Four locations offer the positive effect on the power coefficient. The effect of the coupling on the rotor's rotational speed and tested position were

presented in Figure 2.23. The flow pattern of interaction was classified into four categories based on the unsteady flow and effective distance in one direction.

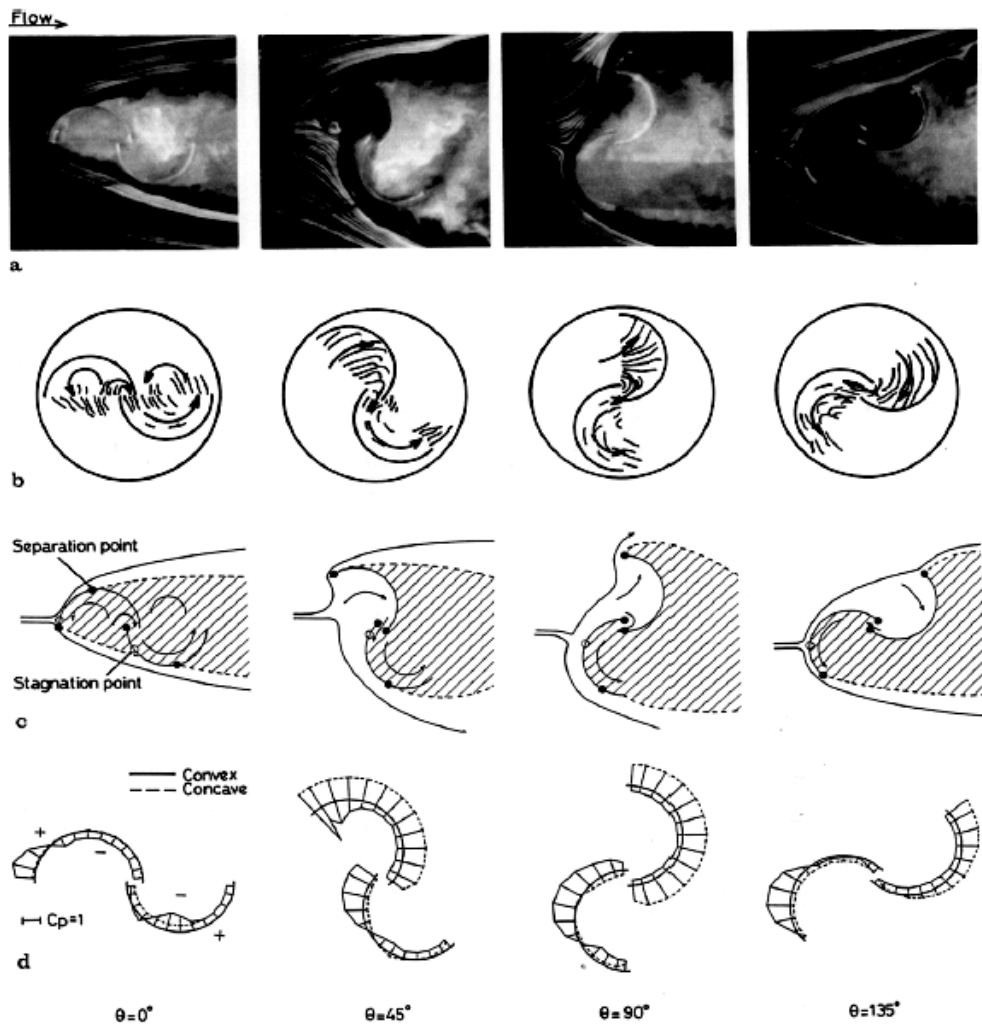
#### **2.1.1.4 Force mechanism of the Savonius rotor**

In order to understand the force mechanism of the Savonius rotor, many subtle experimental tests about the flow field and pressure distribution of the Savonius rotor were conducted by many researchers. These studies are visualization of the flow field, pressure measure and analysis of the lift and drag characteristics. Bergeles and Athanassiadis (1982) presented a flow field visualization around a two-blade semi-circular rotor. They found the following phenomenon. A large recirculation region presents just downstream of the rotor. There is a large velocity deficit behind the rotor and the velocity can recover within 3 times of the rotor diameter.

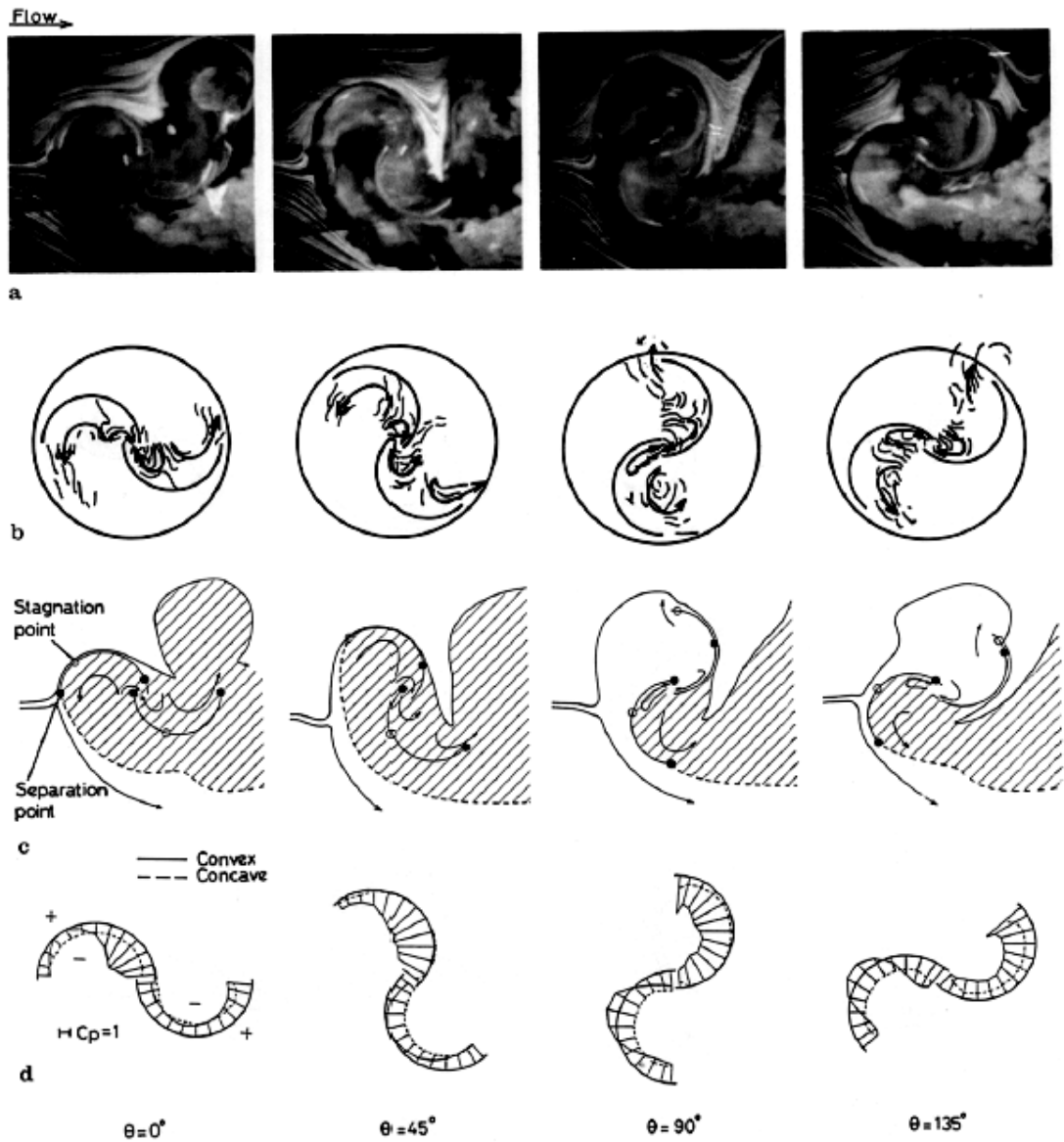
Swada and Nakamura (1986) conducted force measurements and flow visualization on a two semi-circular rotor. The flow visualization is conducted for the static and rotating rotor. They found that the static torque coefficient is positive for all attitude angles when the gap rate is 0.21. This result is different from most the tested results conducted by other authors. They also mentioned that the lift force contributed a lot to the torque when the altitude angle ranges from 240 to 330 degrees.

Fujisawa and Shirai (1987) conducted an experimental investigation of the steady and unsteady flow around the Savonius rotor. The flow visualization of the still rotor shows that the driving force is generated by the drag force when the altitude angle is less than 90 degrees. And the static torque became smaller for large attitude angle

due to the movement of the stagnation point. A coanda-like flow pattern was found on the convex side of the advancing part to form a low pressure area which produces the lift force when the altitude angle is less than 90 degrees. More detailed flow field studies around the Savonius rotor, such as the visualized flow field, flow inside the rotor, flow model and surface pressure distribution of the still and rotational Savonius rotor, were presented in Figure 2.24 by Fujisawa and Gotoh (1992).



(still rotor)



(rotational rotor at TSR=0.9)

Figure 2.24 Flow in and around a Savonius rotor (Fujisawa and Gotoh, 1992)

The vortex formation of a Savonius rotor was visualized by Benghrib et al. (1998) in a water tunnel using the dye emitted from the center of the rotor. It is found that the wake shedding behind the rotor is composed of three vortex shedding systems. Two propulsive vortices, one is located at the right side of the wake and another one is to

the left, are generated from the advancing blades. The returning blades produced two counter-rotating vortices. One is captured by the propulsive vortices and another one leaves the rotor.



Figure 2.25 The vortices generated by the Savonius rotor (Benghrib et al, 1998)

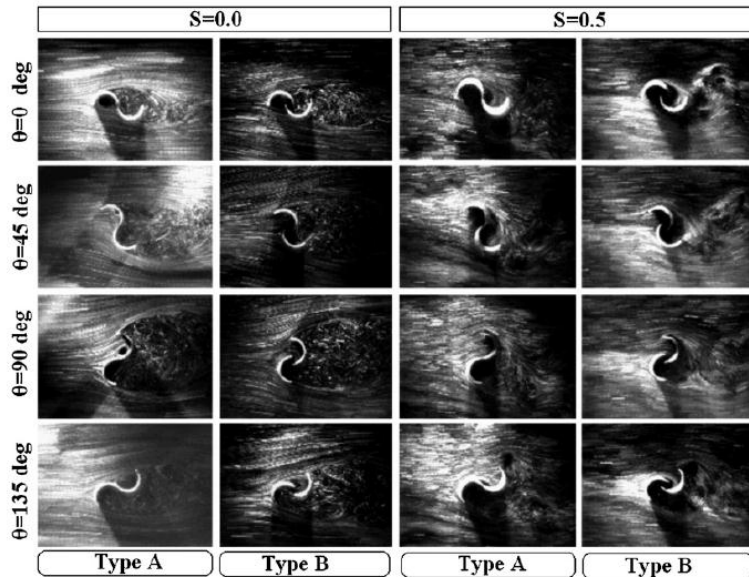


Figure 2.26 The flow field visualized through PIV (Murai et al. 2007)

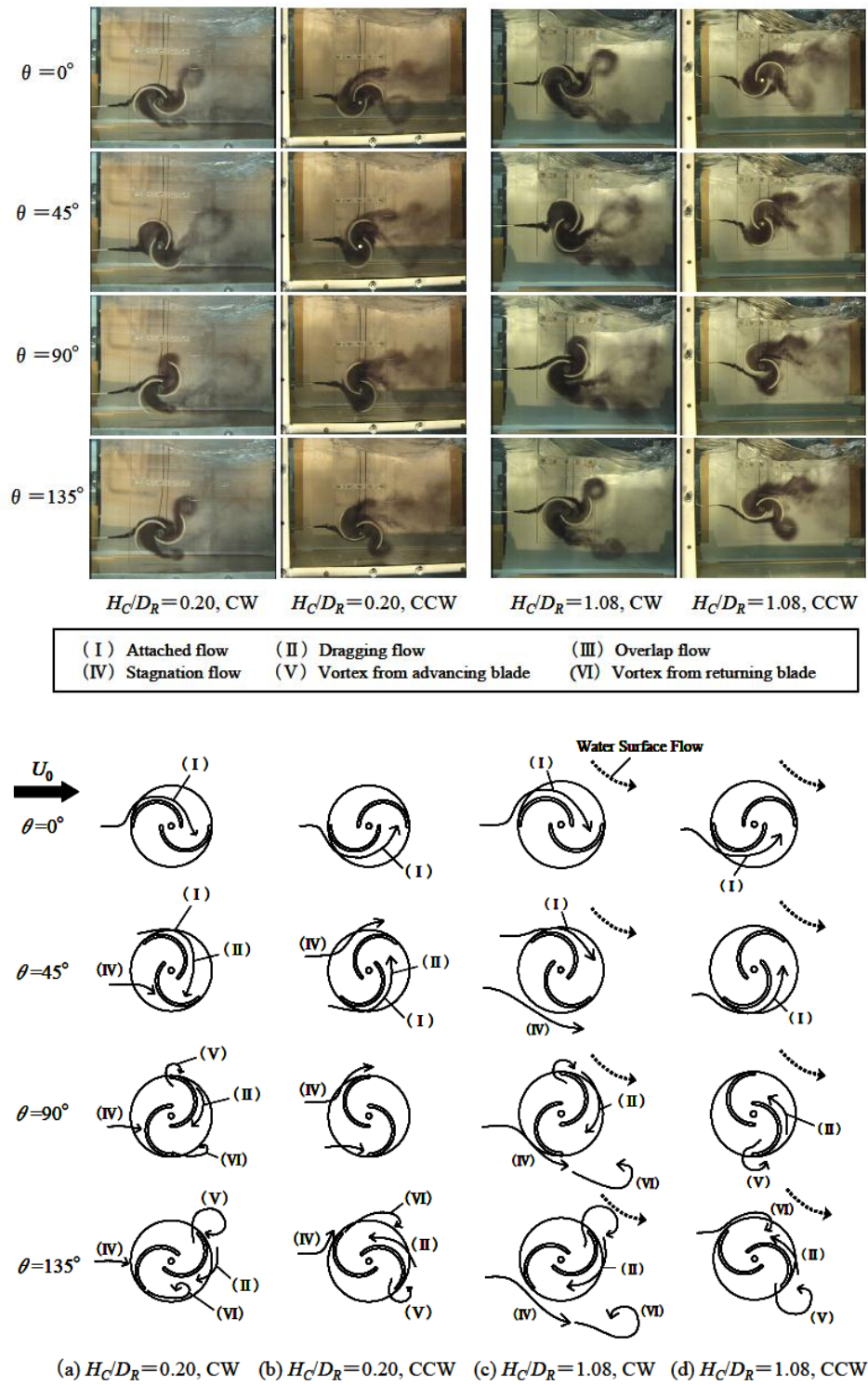


Figure 2.27 The flow patterns summarized by Nakajima et al (2008)

The flow pattern, presented in Figure 2.26, of two types of Savonius rotors was

visualized through the partial tracking velocimetry (PIV) by Murai et al. (2007). It is found that the wake structure of the rotor with a gap rate is quite different from that of the rotor without a gap rate. The stagnation region size of the static rotor is larger than that of the rotational rotor. The drag force of the turbine is reduced due to the through-flow which reduces the stagnated region.

Different flow patterns were summarized by Nakajima et al. (2008). They are (I) attached flow on the convex side of the advancing blade; (II) dragging flow from the convex surface of the advancing blade to the concave surface of the returning blade; (III) through-flow within the overlap region; (IV) flow which comes from the upstream act on the convex side of the returning blade, (V) vortex shed from the tip of the advancing blade and (VI) vortex shed from the tip of the returning blade. And they claimed that the lift force is produced by the flow (I). And flow (II) and flow (III) resume the pressure on the concave side of the returning blade. Flow (V) is the reason for the fall of the power output.

The lift coefficient and drag coefficient of the Savonius rotor were tested by Chauvin and Beghrib (1989) for two different wind speeds. The result shows that the drag coefficient of Savonius rotor is always negative. In other words, the direction of the drag force is opposite to the flow direction. In terms of the lift coefficient, it is negative at low tip speed ratio. It becomes positive for  $Re$  is  $6.9 \times 10^4$  and  $8.7 \times 10^4$  when tip speed ratio is larger than 0.25 and 0.55, respectively. Following Chauvin and Beghrib, Gavalda et al. (1991) conducted a more detailed testing about the lift and drag character of the static and rotational Savonius rotor. The lift and drag coefficient of the Savonius rotor were compared with those of the rotating cylinder.

It is found that the maximum and minimum drag coefficients of the static rotor are 1.6 and 0.65, respectively, when its altitude angle is  $0^\circ$  and range from  $75^\circ$  to  $90^\circ$ , respectively. The testing results indicate that the drag and lift coefficient depends on the Reynolds number slightly. At the fixed Reynolds number, the drag and lift coefficient is almost constant when the tip speed ratio is less than 1.25.

### **2.1.2 Review of the research methodology related to drag type VAWTs**

The research about the drag type VAWTs is just a branch of the fluid machinery. Thus the research methodology of the drag type VAWTs is the same as that of the fluid machinery. The research methods for fluid machinery are experiment, theory and numerical simulation. Although the structure of the Savonius rotor seems very simple, the fluid mechanism behind the drag-type Savonius rotor is quite complicated. Thus, it is very difficult to find a theoretical approach which can predict the complicated unsteady flow in and around the Savonius rotor appropriately. Until now, most the research work was conducted through wind tunnel testing. Only a few studies were conducted through numerical simulations. A brief review below was presented to summarize the research methodology about the drag type VAWTs.

#### **2.1.2.1 Experiments**

In terms of the testing contents, the testing of the Savonius rotor can be classified into two categories according to the types of testing contents. One is the performance

testing, such as the testing of the starting ability, measurement of the static torque, counting the rotational speed and measurement of the dynamic torque which evaluate the power coefficient of the Savonius rotor. Another one is the testing to understand the rotor force mechanism which includes visualization of the flow field and pressure measurement on the blade.

Based on the wind tunnel types, the experiment can be conducted inside or outside a wind tunnel. In terms of the setup orientation of the testing rig, the setup of the performance testing can be placed horizontally or vertically. Those two kinds of test rigs are presented in Figure 2.28 and Figure 2.29. However, some attention must be paid when the horizontal testing rig is used. Firstly, the horizontal testing rig will cause some errors when the static torque is measured due to the effect of the gravity. In other words, the rotor can only balance when the altitude angle is zero.

Another problem is that it is more suitable to place the horizontal testing rig out of the wind tunnel due to the consideration of the blockage ratio and the alignment, especially when the small wind tunnel is available. The alignment of the horizontal testing rig's all components is much more difficult than that of the vertical testing rig when the testing rig is placed inside the small wind tunnel. Of course, this will not be a problem for the large wind tunnel.

The third one is the unbalanced nature of this setting. The shaft will become a beam fixed at both ends. And the rotor acts as a load in the middle of the shaft. Thus the shaft must be strong enough to sustain unbalance of the gravity force and the rotating rotors. A small unbalance mass of the rotating system will generate tremendously excessive stresses, vibration and noise when the rotating system works at very high

rotational speed.



Figure 2.28 A vertical testing rig

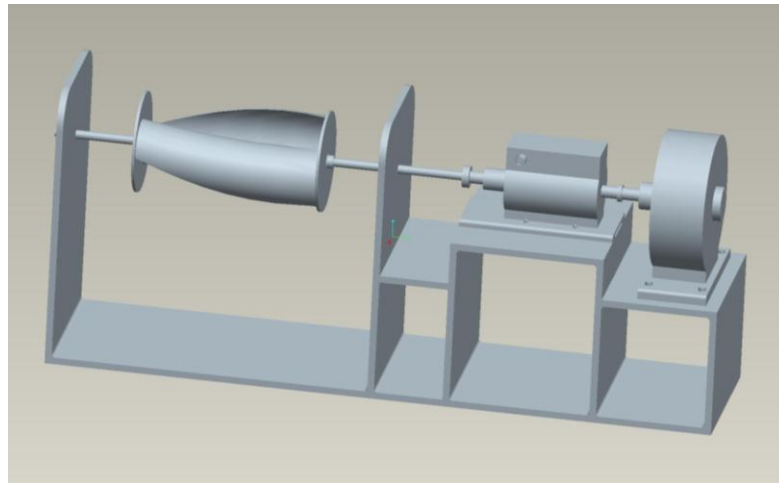


Figure 2.29 A horizontal testing rig

Another important issue of the experimental testing is the blockage ratio and data correction based on the blockage ratio. The wind tunnel blockage correction about the vertical axis wind turbine is summarized by Ross (2010). There are mainly two types of the data correction. One was proposed by Pope and Harper (1966). Another one was proposed by Maskwell (1965), and it was extended by Alexander (1978) to determine the data correction of the Savonius rotor later. The correct equation of the Pope and Harper is summarized below.

$$\text{Correction of the velocity: } V = V_u(1 + \varepsilon_i) \quad \text{Equation 2.1}$$

$$\text{Correction of the dynamic pressure: } q = q_u(1 + 2\varepsilon_i) \quad \text{Equation 2.2}$$

$$\text{Correction of the Reynolds number: } Re = Re_u(1 + 2\varepsilon_i) \quad \text{Equation 2.3}$$

Correction of the drag coefficient:

$$CD0 = CD_u(1 - 3\varepsilon_{sb} - 2\varepsilon_{wb}) \quad \text{Equation 2.4}$$

$$\varepsilon_i = \text{Solid Blockage} + \text{Wake Blockage} = \varepsilon_{sb} + \varepsilon_{wb} \quad \text{Equation 2.5}$$

$$\varepsilon_i = \frac{\text{Model frontal area}}{4 \text{ Test section area}} \quad \text{Equation 2.6}$$

where  $V$  is the corrected wind velocity;  $V_u$  is the undisturbed wind velocity. These equations were suggested to use when the ratio of the model frontal-area to wind tunnel test-section area is less than 7.5% (Barlow et al. 1999).

The correction of Maskell was the first approach to concern the non-streamline flow bodies in closed wind tunnel sections. A semi-empirical term  $m$  was introduced in

the correction of the blockage based on the experimental data gained from the testing of the four flat plates up to 4.5% blockage. The term  $m$  was calculated based on the coefficient of drag and pressure.

$$m = \frac{C_D(S/A) - C_{ps} - \sqrt{(C_D(S/A) - C_{ps})^2 - 4C_D(1 - C_{ps})(S/A)}}{2(1 - C_{ps})(S/A)}$$

Equation 2.7

$$\varphi = \frac{C_D}{C_{D\infty}} = \frac{1}{1 - m(S/A)}$$

Equation 2.8

where  $S$  is the maximum frontal area of the testing model,  $A$  is the testing section area of the wind tunnel. The above correction is extended by Alexander to correct the Savonius rotor.

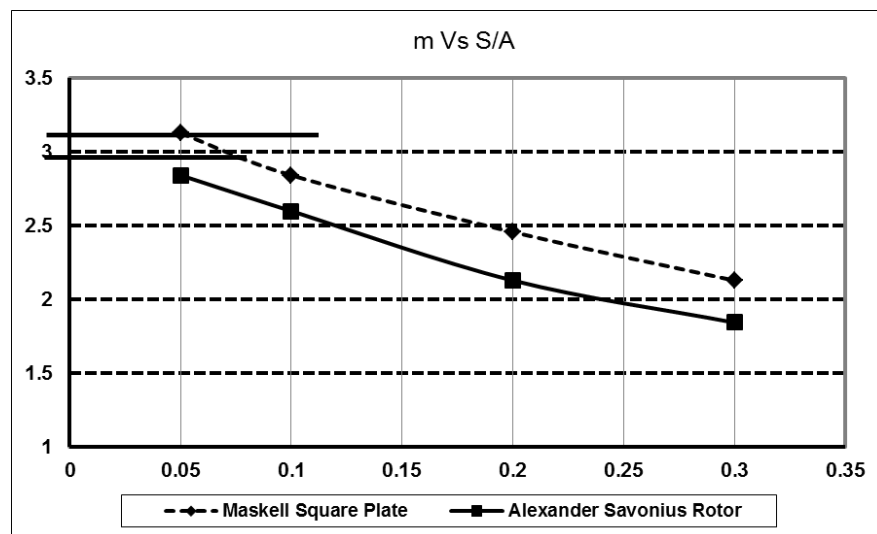


Figure 2.30 The  $m$  values of the square plate and Savonius rotor (Alexander, 1978)

The semi-empirical term  $m$  is determined through the drag force measuring in the closed wind tunnel. The curves of the  $m$  vs  $S/A$  of Maskell and Alexander were

reproduced in Figure 2.30. When the blockage ratio was less than 0.045, Maskell applied the constant value 3.15 for  $m$ . The most striking characteristic of the correction of Maskell and Alexander is that it can get quite accurate correction results even when the S/A value reaches up to the 0.334. This is very useful because most the Savonius testing was conducted in wind tunnels which only have related small size of the test-section due to the rarity of large wind tunnel resources.

### **2.1.2.2 Numerical simulations**

A general method to predict the power output of VAWTs is momentum theory. However, it cannot distinguish the difference between different rotors. The combination of the momentum theory and blade element theory (Strickland 1975) and the combination of the vortex theories and blade element theory (Strickland et al. 1979, Brownlee 1988) are widely used for the analysis of the propeller-type turbines. But, those combination methods cannot be directly applied to predict the performance of the Savonius rotor.

Thus, utilization of a more complicated numerical simulation seems to be the best way to optimize the design of the Savonius rotor. The vortex sheet method proposed by Wilson et al. (1976) and by Van Dusen and Kirchhoff (1978) presents only an approximate behavior of the Savonius rotor due to the lack of consideration of the flow separation. However, the flow around and in the Saovonius rotor is very complex and the separation flow occurs at all bucket angular positions. Thus, Ogawa (1984) conducted a simulation on the Savonius rotor by combining the singularity method and discrete vortex method when the rotor is working in the stationary and

rotating condition. He claimed that the separated viscous flow can be analyzed as a potential flow through the discrete vortices.

Although the simulated power coefficient does not agree with that of the testing results, this method does offer a valuable approach to present the flow pattern qualitatively. Following Ogawa, Aldoss and Kotb (1988) conducted a similar simulation about the flow field around a Savonius rotor. And the comparison between the flow field simulated by Aldoss and the flow field visualized by Fujisawa and Shirai (1987) indicates that the discrete vortex approach, in general, can well depict the flow field around the Savonius rotor.

Fujisawa (1996) conducted a velocity measurement and a discrete vortex simulation on the flow field of the Savonius rotor. It is found that the general features of the flow field can be predicted by the discrete vortex method, but the discrete vortex method cannot predict very well the flow inside and downstream of the stationary rotor due to the assumption of tip-blade separation. The prediction for the rotating rotor is much better than that of the static rotor.

Afungchui et al. (2010) conducted a detailed investigation of the application of the discrete vortex method on the Savonius rotor. The influence of the number of the segments and time step was demonstrated. And the results showed that the validated tip speed ratio range of the simulation is from 0 to 0.6 due to the effects of viscosity. Thus the discrete vortex method can be used to predict the performance of the rotor qualitatively.

A reliable method needs to be found to predict the rotor's performance quantitatively. The development of the CFD offers a new approach to better understand and predict

the performance of the Savonius rotor.

Table 2.5 A brief review of the CFD works conducted by different authors

<i>Author</i>	<i>Altan, B. D., et al (2008)</i>	<i>D'Alessandro, V., et al (2010)</i>	<i>Mohamed, MH (2011)</i>	<i>Akwa, J. V., et al (2012)</i>
<b>Blade number</b>	2	2	2	2
<b>Diameter</b>	0.32m	0.4m	*	1m
<b>Height of the rotor</b>	0.32m	1m	*	*
<b>Mesh type</b>	Tetrahedron	Tetrahedron	Tetrahedron	Hybrid
<b>Dimension</b>	3D	2D	2D	2D
<b>RN or velocity</b>	7m/s	6m/s to 12m/s	10m/s	7m/s
<b>Domain size</b>	*	*	10D*10D	12D*26D
<b>Time step</b>	*	Variable	Constant	Constant
<b>Turbulence model</b>	Standard $k - \varepsilon$	$\overline{V^2} - f$	Realizable $k - \varepsilon$	$k - \omega$ SST
<b><math>Y_+</math> on blade</b>	*	0.1 to 4	60	$Y_+ < 3$
<b>Wall function</b>	*	*	Standard	Hybrid treatment
<b>Interpolating scheme</b>	Second	Second	Second upwind	Second upwind
<b>Inlet</b>	Velocity inlet	Velocity inlet	*	Velocity inlet
<b>Outlet</b>	Outflow	Outflow	*	Pressure outlet

A brief review of the CFD simulation on the Savonius rotor is presented in Table 2.5.

From this table, it is found that different authors used a variety of simulation strategies. And their simulation strategy was not given in detail, especially the time step, the influence of the turbulence model, the wall function and the mesh aspect ratio of the blades. Although the simulation strategies are different, their simulated results were validated through experimental results. This will cause the confusion for those who want to use the CFD method to investigate the performance of the Savonius rotor.

### **2.1.3 Current shortcoming of drag-type VAWTs**

A brief review was conducted in the above paragraphs. Based on this review work, some of the shortcomings of the research work of the drag-type VAWTs can be concluded according to the different research focus.

#### **2.1.3.1 Optimum geometric design of drag-type VAWTs**

The method combined with the CFD and GA selection needs to be adopted for the one-stage rotor analysis without block which will eliminate the omnidirectional ability.

The method of the combination of the CFD and GA selection is used only for the 2D geometry design of one-stage rotor currently, especially for the design of the blade profile. It also can be extended to the 3D geometry design which will consider the influence from the z direction. This will take account into the effect of the aspect ratio and the effect of the helix and twist. After the simulation through the CFD and

GA selection, the related experiment should be conducted to validate the simulated results.

The research of the effect of the rotor stage seems not sufficient. Most researches were conducted keeping the same sweep area for testing rotors. By keeping the same sweep area, the stage aspect will be different. Thus, the comparison between the rotors with the same stage aspect ratio should be investigated. In addition, the influence of a combination of the blade number and rotor stage ratio seems less reported in the literature. It is very difficult to conduct research about the effect of the rotor stage using the CFD and GA selection due to the complexity of the multi-stage rotor. Thus, the best way to investigate the effect of the rotor stage and blade number, until now, is using experiment test.

### **2.1.3.2 Augmentation devices**

The research about the one straight plate is conducted using the CFD and GA selection. This method also can be extended to the research about the two straight, ducted and guided box augmentation systems. Those augmentation systems can be used for the wind condition which has a constant wind direction for the most the time.

The systems with multiple vanes also can be optimized using the CFD and GA selection. As discussed before, the multiple vanes will not eliminate the omnidirectional ability of VAWTs. This system is more suitable for the urban wind conditions.

The researches about the augmentation system mainly focus on the combination of the augmentation system with the conventional Savonius rotor. The augmentation effect will be different when the augmentation systems work with the other type of Savonius rotor, such as the Bach type, sail type, twisted type and helical types.

### **2.1.3.3 Interaction between rotors**

The interaction between the rotors is very difficult to understand. Several researches about the interaction between two rotors have been done. However, those researchers mainly investigated the interaction when the wind comes from one direction. Those researchers do offer valuable guidance for the wind direction is constant most the time. Thus, more experimental research needs to be conducted considering the variation of the wind condition.

In urban conditions, the interaction is not only the interaction between rotors, but also the interaction among building shapes and rotors.

### **2.1.3.4 Force mechanism of the Savonius rotor**

Most researches about the force mechanism of the Savonius rotor are mainly focused on the traditional Savonius rotors. In fact, the force mechanism of the different types of Savonius rotors will be different. More research needs to be done to understand the force mechanism of the different types of rotors.

The surface roughness of the rotor blade will also influence the force mechanism of the Savonius rotor. However, no such researches has been done in this area.

### **2.1.3.5 Research methodology**

The research methods for the Savonius rotor currently used are mainly experimental methods. More effect needs to be taken to improve and standardize the simulation work.

The Savonius rotor's dynamic torque of some testing was measured with a spring balance. The results of this testing are arguably due to the varying nature of the dynamic torque. It is difficult to read the torque value from a spring balance.

## **2.2 Review of the fixed pitch lift-type VAWTs -Darrieus rotor**

The most common lift-type VAWTs is a Darrieus rotor which is patent in 1931 by a French engineer named George Jean Mary Darrieus. According to the pitch control, the Darrieus can be classified into fixed and variable pitch Darrieus rotor. Based on the blade appearance, The Darrieus can be the eggbeater Darrieus, canted Darrieus, arrowhead Darrieus, H-Darrieus and helical Darrieus. The investigated rotor is fixed pitch H-Darrieus due to the consideration of the simple structure and relatively minor maintenance.

The working principle of the Darrieus is different from the Savonius rotor. An airfoil is used as the cross section profile of the Darrieus blade. The lift force generated by the airfoil drives the Darrieus turbine. The force and velocity vectors acting on the blade section of the fixed pitch Darrieus are shown in Figure 2.31. In this Figure,  $V_\infty$  is the undisturbed velocity.  $V_a$  is the induced velocity.  $R$  is the radius of the rotor.  $\omega$

is the rotor's rotational speed.  $W$  is the relative wind speed which is the sum of the induced velocity vector and the rotor's velocity vector. The angle of attack ( $\alpha$ ) is the angle between the relative velocity vector and the rotor's velocity vector. The lift force ( $L$ ) is always perpendicular to the relative velocity vector ( $W$ ). The drag force ( $D$ ) is parallel to relative velocity vector ( $W$ ).

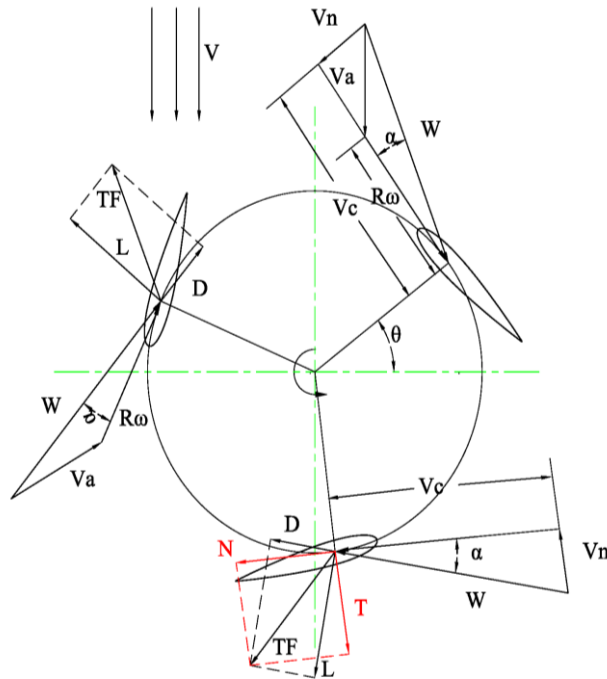


Figure 2.31 The working principle of the VAWTs

The relative velocity vector ( $W$ ) can be resolved into orthogonal components. One is  $V_c$  which is perpendicular to the rotor's velocity vector. Another one is  $V_n$  which is parallel to the rotor's velocity vector. The total force (TF) can be resolved into two orthogonal components which have the same direction as the two components of the relative velocity vectors. These two forces are tangential force (T) and the normal force (N). The relationship between the different velocity vectors is expressed in the following expressions (Islam et al. 2008):

$$W = \sqrt{V_c^2 + V_n^2} \quad \text{Equation 2.9}$$

$$V_c = R\omega + V_a \cos \theta \quad \text{Equation 2.10}$$

$$V_n = V_a \sin \theta \quad \text{Equation 2.11}$$

The relationship between different forces which act on the airfoil is expressed in the following expressions:

$$\alpha = \tan^{-1}\left(\frac{V_n}{V_c}\right) \quad \text{Equation 2.12}$$

$$T = L \sin \alpha - D \cos \alpha \quad \text{Equation 2.13}$$

$$N = L \cos \alpha + D \sin \alpha \quad \text{Equation 2.14}$$

If the L, D, T and N are replaced by the related force coefficient, the above expressions can be written as:

$$C_T = C_L \sin \alpha - C_D \cos \alpha \quad \text{Equation 2.15}$$

$$C_N = C_L \cos \alpha + C_D \sin \alpha \quad \text{Equation 2.16}$$

$$L = C_L * \frac{1}{2} \rho c h W^2 \quad \text{Equation 2.17}$$

$$D = C_D * \frac{1}{2} \rho c h W^2 \quad \text{Equation 2.18}$$

$$T = C_T * \frac{1}{2} \rho c h W^2 \quad \text{Equation 2.19}$$

$$N = C_n * \frac{1}{2} \rho c h W^2 \quad \text{Equation 2.20}$$

Above equations only calculate the forces for one of the azimuth position. Thus, the total force ( $F_{ta}$ ), the average force ( $F_{av}$ ) and the total torque ( $Q$ ) can be obtained as:

$$F_{ta} = \int_0^{2\pi} F_t(\theta)d\theta \quad \text{Equation 2.21}$$

$$F_{av} = \frac{1}{2\pi} \int_0^{2\pi} F_t(\theta)d\theta \quad \text{Equation 2.22}$$

$$Q = NF_{av}R \quad \text{Equation 2.23}$$

The power output is the product of the torque and angular velocity.

$$P = Q\omega \quad \text{Equation 2.24}$$

The above equations are only suitable for the fixed pitch H-Darrieus rotors. For other type Darrieus rotors, minor modification needs to be conducted in the related equations. For Egger, canted and arrowhead type Darrieus rotors, the local blade slope ( $\delta$ ) need to be added into the related equations. For the variable pitch rotors, the pitch angle ( $\gamma$ ) needs to be added into the equation of angle of attack.

As mentioned above, there are two types of the Darrieus rotor based on the pitch control. The fixed pitch Darrieus and variable pitch Darrieus. However, in this part, the review will mainly focus on the fixed pitch Darrieus. Many researches were conducted in order to improve the performance of the Darrieus rotors including the power coefficient and starting ability. The starting ability of the rotors is very important for a standing alone system. And the power coefficient ensures the enough power output to match the energy demand. Those researches focus on the following areas:

- a) Geometry design
- b) Aerodynamic investigation of the rotor
- c) Improvement of the research methodology

Thus, the following part will give a general review of the fixed pitch Darrieus based on above three areas.

## **2.2.1 Review of the research focus related to lift type VAWTs**

### **2.2.1.1 Geometric design**

The geometric design part includes an evolution review of the rotor's appearance and the most important design parameters of the Darrieus rotor. The aim of the evolution review of the rotor's appearance is to give a general review of different types of Darrieus rotors and to some indication for a further design improvement.

#### ***2.2.1.1.1 Evolution of the Darrieus rotor appearance***

##### ***2.2.1.1.1.1 Egger Darrieus***

The idea of using the Egger (curved blade) is to minimize the blades' bending stress. The curved blade can be catenary, parabolic, torposkien and Sandia blade. A survey about the blade shape design was conducted by Ashwill et al. (1986). The first known test about the curved blade Darrieus wind turbine was conducted by R.S. Rangi and P. South (1972) of the National Research Council of Canada. Then, a lot

of research work was carried out by the Sandia National Laboratories (SNL) to develop the curved blade Darrieus rotor including the experimental testing (Worstell 1978), performance prediction models (Strickland 1975) and real field testing (Ashwill 1992). A detailed survey about the development of the curved blade Darrieus was presented by Paraschivoiu (2002). And he also mentioned that a first large-scale Darrieus turbine manufactured by the Canadians was destroyed due to an unexpected self-start.

In fact, the patent submitted in 1931 by George Jean Marie Darrieus included the eggbeater (curved blade) and straight-blade VAWTs which is also called H Darrieus. A H Darrieus has some advantages over eggbeater type blade rotors. For the same rated power output, the size of H Darrieus is smaller than the curved blade rotor. A H Darrieus is the simplest configuration among all types of Darrieus rotor.

The early studies of the H Darrieus were conducted by Moran (1977). The test three-blade rotor had a diameter of 2.13 m and a height of 1.52m. The chord length of the airfoil was 210mm. Thus, the corresponding rotor's solidity was 0.3. The test maximum power coefficient was about 0.55 which is very close to the value of Betz limitation. A three-blade H Darrieus was tested by Kiho et al. (1996) for the tidal power generation. The height and diameter were 4.2m and 1.6m, respectively.

The airfoil section used was NACA6330018 and the chord length is 0.3m. The solidity is 0.42. The maximum coefficient was about 0.56 when the tip speed ratio is 2.1. Bravo et al. (2007) tested an H-Darrieus rotor with a chord of 0.4m and a diameter 2.5m. Thus, the solidity of the rotor was 0.96. The maximum power coefficient is about 0.3. A two-blade and a three-blade H-Darrieus rotors were tested

by Howell et al. (2010) to investigate the influence of the airfoil roughness on the rotor performance. The related solidity of the two- and three-blade rotor is 0.67 and 1, respectively. The maximum power of the two-blade rotor is about 0.25. Several three-blade H Darrieus with a solidity of 0.96 were tested by Fiedler and Tullis (2009) to study the effect of the blade offset and pitch on the rotor performance. The maximum power output of the rotor with zero-pitch is about 0.35. Several rotor with solidity 0.9 and 0.848 were tested by McLaren (2011). The maximum power coefficient was about 0.32. Based on the above experiment conducted recently, it should be mentioned that the experimental power coefficient of a small H-Darrieus is range from 0.25 to 0.35. And the H-Darrieus also has a poor self-starting ability.

#### **2.2.1.1.1.2 V-VAWT**

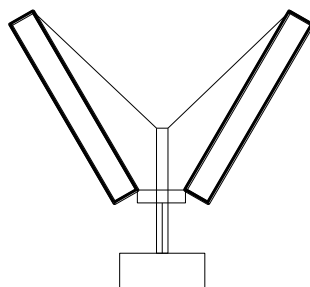


Figure 2.32 The V-VAWT

Due to the poor self-starting ability of the curved Darrieus and H-Darrieus rotor, Baker (1983) indicated that the use of the inclined blades may improve the starting ability of the Darrieus rotor. Those rotors with inclined blades were called coning or Vee Darrieus rotor presented in Figure 2.32. Sharp and Taylor (1985) claimed that the starting torque of the V-VAWT is unexpectedly high. But, they addressed later

that this was only a theoretical prediction. In terms of the structure, this arrangement will increase the bending force to the supporting struts or cables. In fact, this arrangement is similar to the curved blade Darrieus whose blades are partly inclined. But, the curved blade Darrieus cannot start by itself.

### 2.2.1.1.3 The VAWT with several sets of blades

The idea of using several sets of blades was firstly proposed and patented by Ljungstrom (1982) for the Egger and straight type Darrieus rotor. Two and three sets of blades were mentioned in the patent. They are presented in Figure 2.33. The purpose of this design is to absorb the load and increase the efficiency at high wind speed. Unfortunately, there no enough evidence to prove that this kind of design can improve the performance of the Darrieus rotor due to the absence of the simulation and experimental testing.

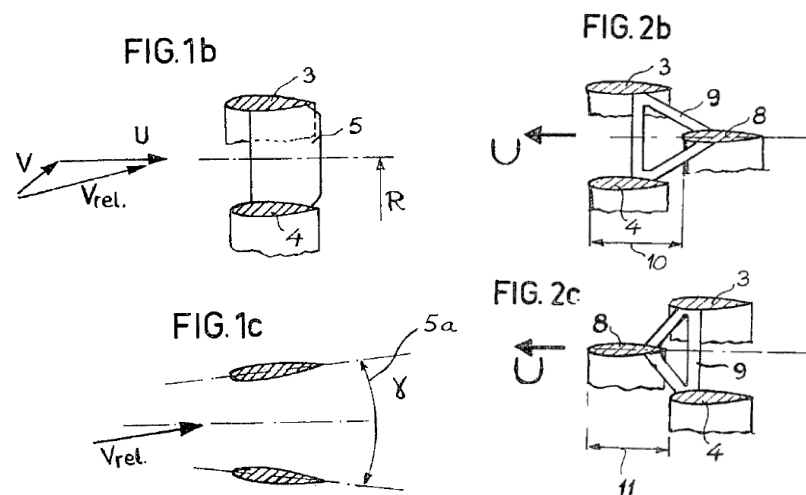


Figure 2.33 The rotor with double blades (Ljungstrom 1982)

A similar rotor with two sets of blades presented in Figure 2.34 was studied by Li et

al. (1983) to improve the self-starting ability of the Darrieus rotor. Li et al. (1983) stated that the power output of the rotor with two sets of blades is 20-25 percent higher than that of a rotor with one set of blade. In fact, the cost of construction of this rotor will be increased. And the increased cost must be balanced by the power output. Thus, a further investigation about this rotor should be conducted to evaluate the feasibility of this design.

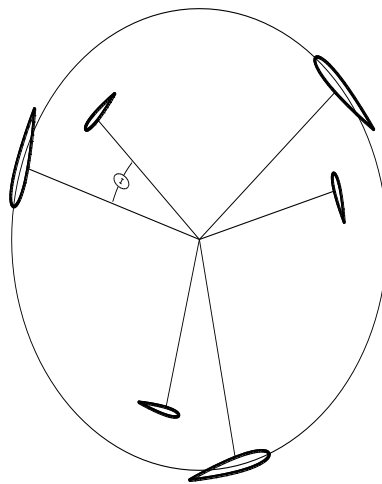


Figure 2.34 The Darrieus rotor with double blades

#### **2.2.1.1.1.4 Arrowhead Darrieus**

The arrowhead Darrieus, in fact, is a declining straight-blade rotor and is similar to the V-VAWT. The detailed arrowhead Darrieus tested by Morcos and Abdel-Hafez (1996) was presented in Figure 2.35. Two types of blade sections were tested. The results showed that the power coefficient of the rectangular section was higher than that of the airfoil section. The power coefficient increases with the increasing of the angle of attack ( $\phi$ ) and the decreasing of the blade angle ( $\theta$ ). The testing results

should be considered with suspicion because the turbine's torque was measured by a spring scale. In fact, this arrowhead Darrieus rotor is more like a curved blade Darrieus rotor with straight blade. Thus, it can be estimated that the self-starting ability will not be improved.

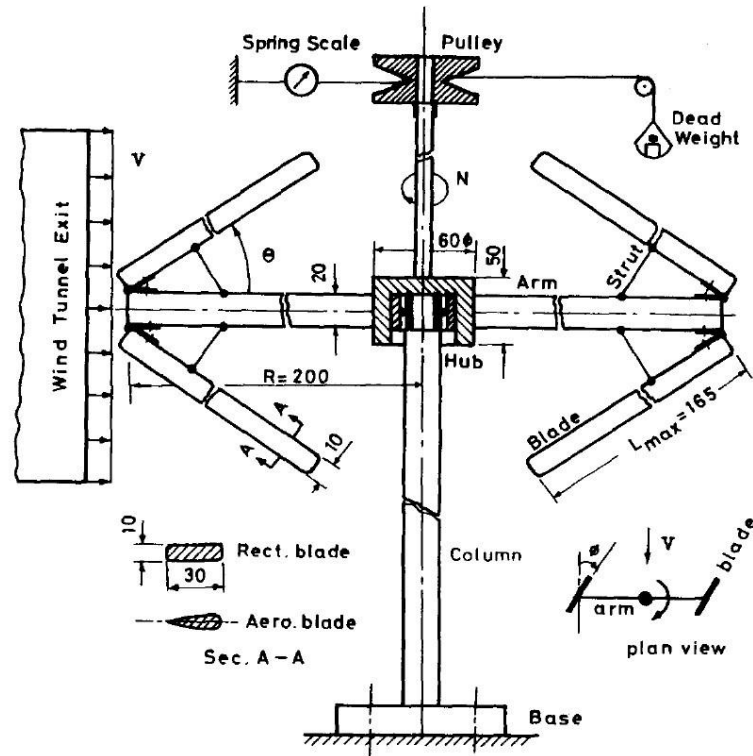


Figure 2.35 The arrowhead Darrieus (Morcos and Abdel-Hafez 1996)

#### 2.2.1.1.1.5 Helix Darrieus

The helical Darrieus turbine was designed firstly by Gorlov (1998) to harness the hydraulic power from low head applications. The idea of the using of the helical Darrieus is to lower the vibration and improve the self-starting ability of the curved or straight blade Darrieus turbine.

The airfoil adopted by Gorlov is NACA-0020 with 7 inch chord length. And he

claimed that the helical turbine demonstrates substantially better performance and stability than the straight-blade Darrieus. However, it should be noted that the power performance comparison between the straight rotor and helical rotor was conducted as a function of water head. And in terms of the vibration, no related measurement was undertaken quantitatively.



Figure 2.36 Helix or helical Darrieus tested by the Gorlov (2001)

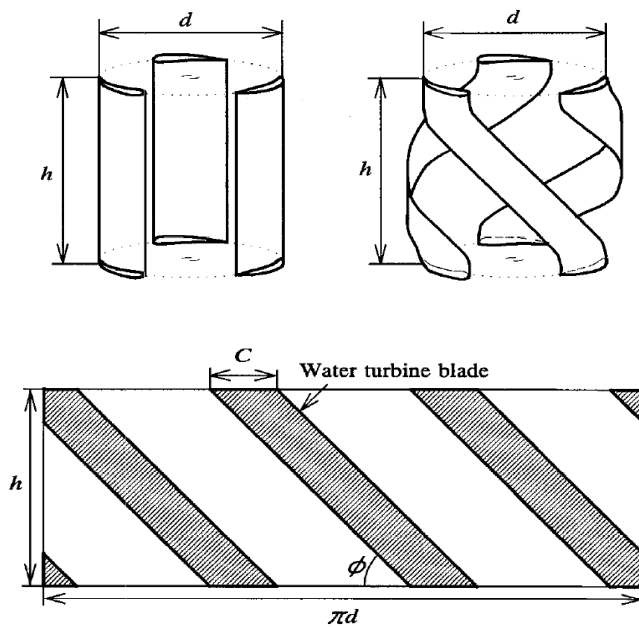


Figure 2.37 The helical rotor and the inclined angle  $\phi$  from Shiono (2002)

Following this study, Shiono et al. (2002) undertook a detailed study about the influence of the rotor solidity and blade inclined angle on the performance of the helical rotors presented in Figure 2.37. The result indicated that the starting ability can be improved by using the helical blade. However, the power coefficient will increase as the increasing of the blade inclination angle. In other words, the straight blade rotor has the best power coefficient among all tested rotors.

Scheurich et al. (2010) also conducted a simulation about the performance of the curve-blade, straight-blade and helix-blade Darrieus rotor through the Vorticity Transport Model. It is found that variations of the blade load of the helical rotor are much smoother than that of the curve-blade and straight-blade rotors. However, the comparison of the power coefficient was not presented.



Figure 2.38 The straight and helical Darrieus rotors tested by the Kirke (2011)

A real field testing about the straight-blade and helical blade Darrieus was carried out by Kirke (2011). Those Darrieus rotors shown in Figure 2.38 were used for the

generation of hydropower in Australia and Canada. He claimed that “ despite helical turbines readily self-start, this was not the case with the helical turbines tested, despite the fact that they were of high solidity, which can be expected to improve starting torque”. Moreover, the efficiency of the helical rotor is slightly less than that of the straight blade fixed pitch rotor. The fixed pitch Darrieus rotors including the straight-blade and helical blade rotors had small starting torque and cannot self-start at high current velocity. Cambered airfoils do improve the starting torque, but results in high peak efficiency. In terms of the smooth operation, the helical rotors work smoothly, but the straight blade rotors shake violently.

The phase shift angle between the bottom and top of the blade sections were investigated by Castelli and Benini (2012) through CFD simulation. The simulation results show that the performance will decrease with the increasing of the phase shift angle.

In the end, it should be mentioned that the length of the helical blade is much longer than the straight. In the case of the Gorlov’s helical Darrieus rotor, the rotor has three blades twisted on a  $60^\circ$ . The diameter and height of the rotor is 8.5 in and 9 in, respectively. The length of the twisted blade can be calculated by the equation below:

$$L = \sqrt{(\beta r)^2 + h^2} \quad \text{Equation 2.25}$$

where  $\beta$  is the twisted angle,  $r$  is the radius of the rotor and  $h$  is the height of the rotor. Based on the geometry size given by the Gordo’s report, the length of the twisted blade is about 12.66 in. Thus, the length of the twisted blade is 40.6% longer than the straight blade for one blade. In terms of three-blade rotor, the total length

the twisted blade is about 121.8% longer than that of the straight blade. Thus, more material will be used for the helical rotor. And more cost is needed for the helical rotor.

#### ***2.2.1.1.1.6 Achard turbine***

The Achard type turbine is firstly patented by J.L Achard in 2004 of the hydropower generation. This turbine is shown in Figure 2.39. J.L Achard replaced the straight blade with backswept blade. The backswept blade is quite similar to the backswept wing keeping the same blade cross section along the direction of the wing span. 2D simulation was carried by Bernad et al. (2008). However, 2D simulation can't reflect this special configuration design. Most 2D simulations were conducted for the straight blade Darrieus rotor by assuming the infinite length of the blade. Thus, Zanette et al. (2010) conducted a 3D investigation about the straight blade, Achard blade and proposed a new type of trapezoidal Achard blade which has a variable blade cross section along the wingspan direction. Those blades are presented in Figure 2.40.

He claimed that the important advantage, compared with the Gorlov turbine, is to equilibrate axial loading on the blade. The numerical results show that the trapezoidal-blade can reduce the mean value of the stress and improve the durability the turbine. However, the comparison about the power coefficient of three different types of Darrieus wasn't conducted. And the self-starting ability of this Achard type Darrieus rotor was also not investigated.

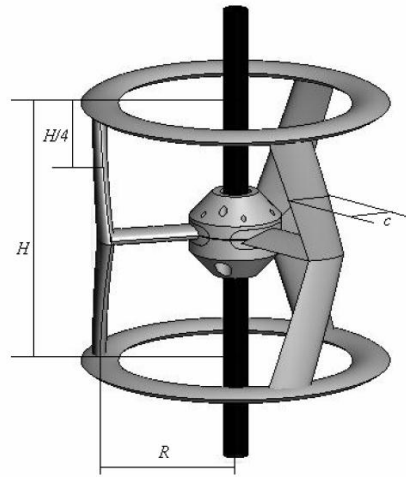


Figure 2.39 The Achard turbine (by courtesy of LEGI)

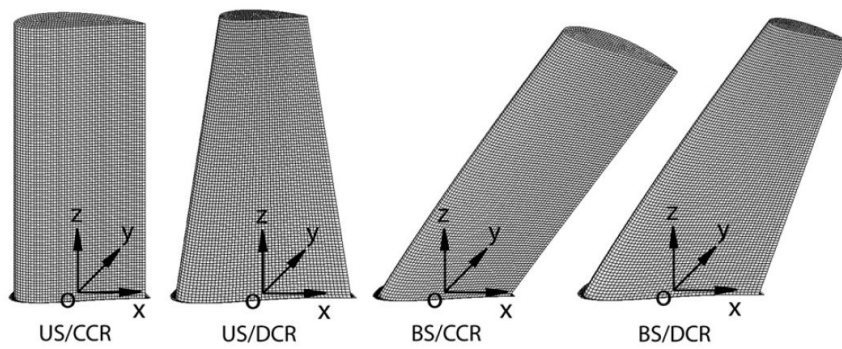


Figure 2.40 The blade type simulated by the Zanette et al. (2010)

#### 2.2.1.1.1.7 Canted Darrieus

The canted blade shown in Figure 2.41 was proposed by Armstrong and Tullis (2011) to produce the blade easily. A canted blade shown in Figure 2.41 is more like the blade of the horizontal axis turbines.

A straight vertical blade was inclined to certain angle firstly, then the blade section was twisted to certain angle which can maintain a local pitch angle of the chord to

the shaft constantly. It is found that the performance of the canted blade rotor is slightly higher than that of the straight blade rotor. But the comparison between the vibration response and self-starting ability was not conducted. In addition, the canted blades is much more difficult to build than the straight blades.

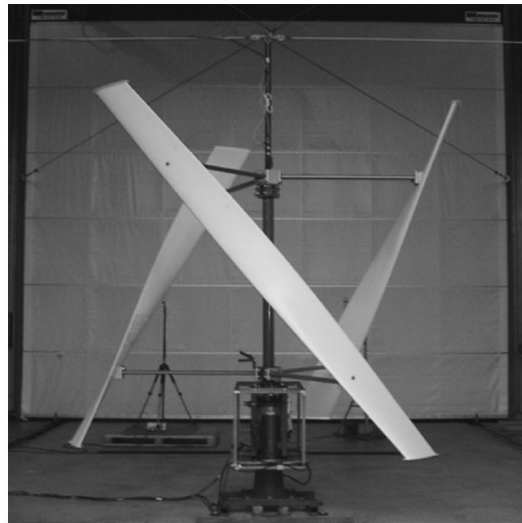


Figure 2.41 The canted blade (Armstrong and Tullis 2011)

#### ***2.2.1.1.2 Design parameters of the Darrieus***

##### ***2.2.1.1.2.1 Blade number***

The selection of the blade number will be influenced by many considerations. They are wind resource, cost, starting ability, performance, structure stability and noise. Wind resource is the most important issue needed to be considered firstly. At the low wind conditions, design of rotor with multi-blades is needed to generate higher starting torque although the power coefficient decreases with the increase of the

blade number. In the case of higher wind conditions, the rotor with less blades can be used to generate higher power. In terms of commercialization, the cost is the very important issue. The cost includes the fabrication cost, transportation cost, assembly cost and maintenance cost. It is clear that more blades need more fabrication, transportation and assembly cost. However, the maintenance cost is decided by the stability of the system. As mentioned by Paraschivoiu (2002), two-bladed rotors will experience “butterfly” excitation and will be easily damaged by the fatigue stresses. But the three-bladed rotors are more stable than the two-blade rotors due to the structural non-directional. In terms of stand alone systems, the starting ability is very important. The more blades the rotor has the easier the rotor can self-start. More blades will also sharpen the rotor’s power curves. Finally, the noise of the rotor with fewer blades is lower than that of the rotor with many blades because the rotational speed of the rotor with less number of blades is low. Thus, the selection of the blade number must take into the above considerations.

#### **2.2.1.1.2.2 Solidity**

The solidity of the rotor is defined as the ratio of the blade surface area to the rotor’s frontal swept area. The equations for the rotor with curved blade and rotor with straight blade are different. The effect of blade solidity on the performance was predicted using the single stream tube model by Templin (1974). The rotor is a curved blade with a height-diameter ratio of 1 and blade zero-lift drag coefficient of 0.01. The effect of the solidity on the performance is presented in Figure 2.42.

It is found that the maximum power coefficient changes a little when the solidity

ranges from 0.2 to 0.5. The maximum power coefficient will decrease rapidly when the solidity is larger than 0.2. And the optimum tip speed ratio will increase with the decrease of the solidity. This means that the operating range of the rotor with the lower solidity is wider than that of the rotor with higher solidity.

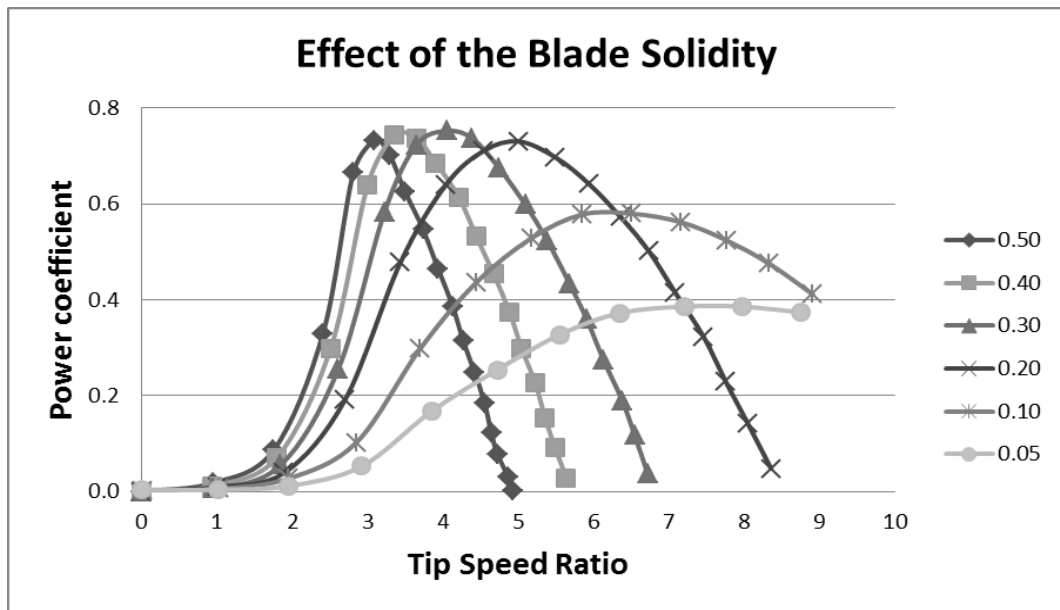


Figure 2.42 The effect of the blade solidity (Templin 1974)

Thus, it seems that the solidity should be larger than 0.2 to ensure the power coefficient of the rotor. And the rotor with higher solidity has a better self-starting ability. Moreover, the noise of the rotor and centrifugal force on the blade will decrease at relative higher solidity. In the other hand, the rotor with higher solidity will narrow the operating range and increase the cost of the manufacture. Strickland (1975) also conducted a similar study of the effect of the solidity on the performance. The results gained by Strickland are similar to the results of Templin. The work of the Strickland also considered the interactive effect of solidity and Reynolds number

(RN). His work is presented in Figure 2.43 and Figure 2.44.

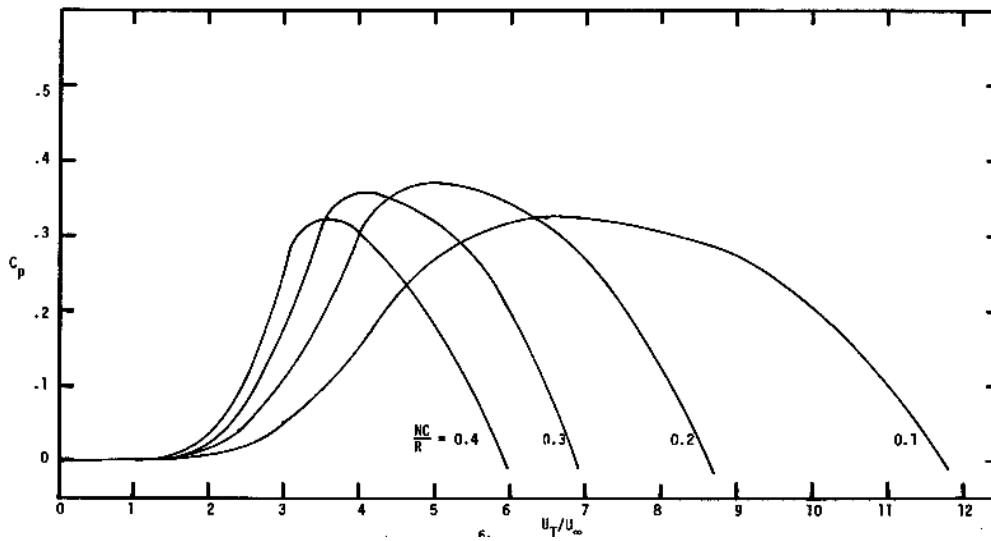


Figure 2.43 Effects of the solidity (Strickland 1975)  $Re = 0.3 \times 10^6$

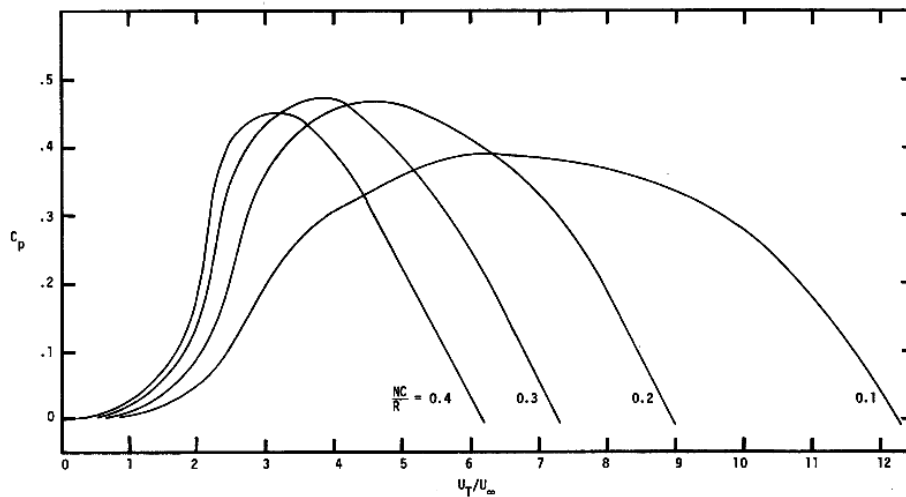


Figure 2.44 Effects of the solidity (Strickland 1975)  $Re = 3 \times 10^6$

### 2.2.1.1.2.3 Aspect ratio (AR)

The AR is defined as the ratio of height to diameter of the turbine. The rotor with high aspect ratio has a better power coefficient from the aerodynamic point of view.

Based on the Prantl's lifting-line theory, the relationship between the induced drag coefficient ( $C_{D,i}$ ) and the AR of a finite blade can be expressed:

$$C_{D,i} = \frac{C_L}{\pi AR} \quad \text{Equation 2.26}$$

It is clear that  $C_{D,i}$  is inversely proportional to the AR. Thus, a blade with high aspect ratio is needed to reduce the induced drag. According to the research of Kirke (1998), the blade AR of the H-Darrieus should be higher than 7.5 to achieve an acceptable peak power coefficient. Moreover, increasing of the AR is the easiest way to increase the swept area when the rotor diameter is fixed.

#### ***2.2.1.1.2.4 Airfoil selection***

The selection of the airfoil is the core issues in terms of the design of the Darrieus rotor. It will not only affect the rotor's power coefficient but also the rotor's self-starting ability. However, the selection of the right airfoil is very difficult because there are so many different airfoil families which may suit for the Darrieus. In the case of US National Advisory Committee on Aeronautics (NACA) airfoil families, it can be the four-digit series, five-digit series, 1-series, 6-series, 7-series and 8-series.

The most popular airfoils used as the blade section of the Darrieus rotor are the symmetric four-digit original NACA airfoils. They are NACA 0012, 0015, 0018 and 0021. This four digit NACA airfoil section is originally designed for aircraft wings. The reason why many researchers adopted the NACA airfoils is that the four-digit NACA airfoils are the most well documented airfoils for their lift, drag, pitching moment characteristics. And those characteristics can be used for the theoretical

prediction of the Darrieus rotor. Thickness is the only design parameter for the four digit NACA airfoils. Based on the theoretical work conducted by Healy, thicker airfoils, at least up to 18%, offer better performance at RN from  $0.2 - 0.3 \times 10^6$ .

The six-digit NACA airfoils tend to maximize laminar flow. Six-digit and four-digit NACA airfoils were compared by Migliore (1983). The rotor has a height of 17m and diameter of 16.8m. The predicted results show that by using the six-digit NACA airfoils, the annual energy output was improved by 17% and 20% for the rotor with solidity 7% and 14%. However, this finding has little guidance for the small Darrieus rotors.

The Gottingen series airfoils were investigated by Healy (1978) to evaluate the effect of the camber on the performance of the Darrieus. The reason why Healy used the Gottingen series is that they are the only cambered airfoils that have a reasonable amount of data in that era. And the results show that the airfoil which is close to being symmetric generates higher power. Baker (1983) investigated the rotors with NACA 0012, Go 420 and Wortmann FX63-137. He found that the rotor with Go 420 achieves the highest power coefficient among three rotors. Kirke also conducted some of the investigation on the effect of the camber on the performance of the Darrieus rotor. He claimed that the symmetrical airfoils used for the small VAWTs perform poorly in the RN range from 80,000 to 150,000, but cambered airfoils perform better when the airfoils.

Claessens (2006) conducted a comparative investigation using the four digit NACA airfoils, six-digit NACA airfoils and NLF profiles to find a suitable airfoil for a small vertical axis wind turbine. And he found that NLF series is the most promising series

for the basis of the new VAWT profile which has low drag at small angles of attack and a wide drag bucket.

Islam et al. (2007) summarized the airfoils used before and analyzed desirable airfoil features for smaller capacity H-Darrieus rotor. Desirable aerodynamic and geometric features were suggested based on the previous researchers. His suggestions were listed below:

- 1) Aerodynamic features
- 2) Large stall angle at small Reynolds number
- 3) Wide drag bucket
- 4) Small zero-lift-drag coefficient
- 5) Large  $C_l / C_d$  ratio
- 6) Large maximum lift-coefficient
- 7) Delayed deep-stall property
- 8) Small roughness sensitivity
- 9) Small trailing edge noise generation
- 10) Large negative pitching moment
- 11) Desirable geometric features
- 12) Camber airfoil
- 13) Greater thickness

14) Large leading edge radius

15) Sharp trailing edge

#### 2.2.1.1.2.5 *Supporting strut type and central column*

Supporting strut is a major difference between the curved blade Darrieus and H Darrieus. Different types of supporting system will not only influence the power coefficient, but also the stabilization of the system. In the current state, there are mainly three kinds of horizontal supporting system which are shown in Figure 2.45.

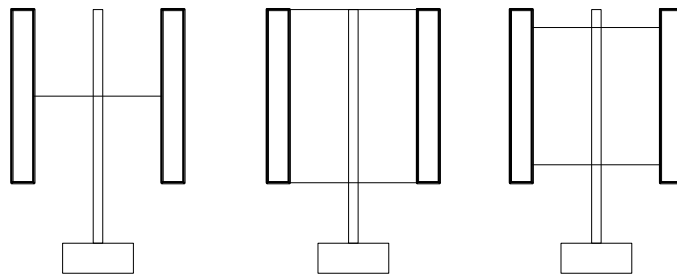


Figure 2.45 Three types of horizontal supporting systems

From the left to right, they are cantilever type support with one arm per blade, simple type support and overhang type support with two arms per blade. Due to the consideration of the cost and parasitic drag, cantilever type support seems the best way to support the blades. However, this support system cannot withstand the load and stiffness, unless it is strong enough. Thus, the support system with two arms per blade seems preferable. And considering the distribution of the bending moment, overhang type support is superior to the simple type support.

The drag coefficient of various supporting struts' shape is significantly different.

Thus, the right choice of the shape of the supporting struts is also very important. Figure 2.46 shows the drag coefficients of various typical bodies. The drag coefficient of the cylinders ranges from 0.6 to 1.2. However, the drag coefficient of the streamline body is only 0.12 at Re number of  $1 \times 10^5$ . Thus, supporting struts with low value of drag coefficient is preferable in terms of the performance.

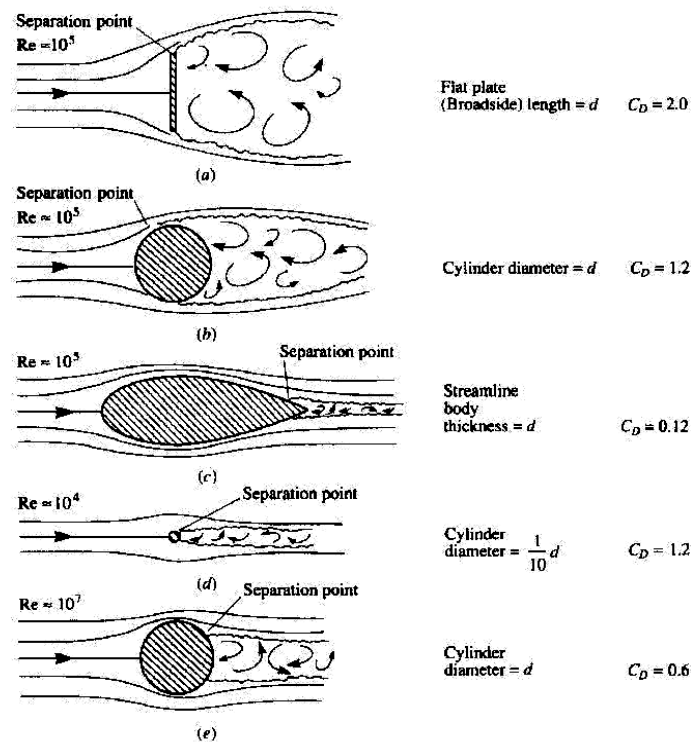


Figure 2.46 The drag coefficient of various typical bodies (Talay 1975)

Islam et al. (2008) proposed a new type of the airfoil named “MI-SRUT1” for the supporting struts of a small VAWT. It has been found that the power coefficient of the rotor with the MI-SRUT1 is significantly higher than that of the rotor with blunt training edge and much higher than that of the E862 airfoil when the Re number is 100,000. Li and Calisal (2010) conducted a comparison testing for two different

supporting struts presented in Figure 2.47. It is found that the power coefficient of type A is greatly higher than that of type B.

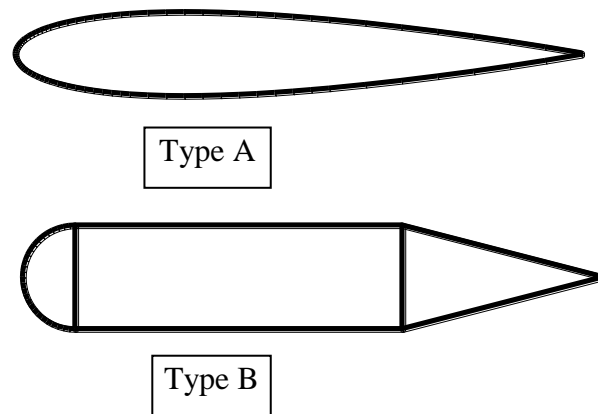


Figure 2.47 The supporting struts (Li and Calisal 2010)

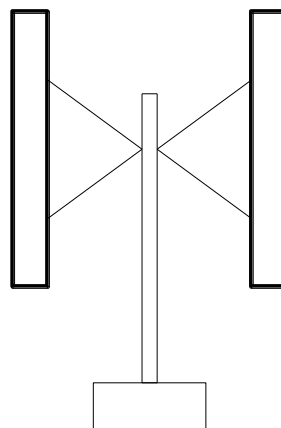


Figure 2.48 The supporting system with inclined supporting struts

In fact, there is another type of supporting system called inclined supporting system which has been less studied. This system is shown in Figure 2.48. By using this system, the center column can be shortened to reduce the weight and cost. In addition, the struts can not only be used for supporting frame, but can also generate

power if those inclined struts are well designed. The reason why those struts can generate the power is that the arrangement of those struts is just like the V-VAWTs.

#### **2.2.1.1.2.6 Mounting location and blade pitch angle**

In fact, the performance of the fixed pitch Darrieus will be affected by the pitch angle and mounting location of the blades. The mounting location ratio is defined as the ratio of the distance between the airfoil leading edge and the center of the struts to the chord length. And the pitch angle is defined as the angle between the tangential velocity at the equator and the chord line of the airfoil.

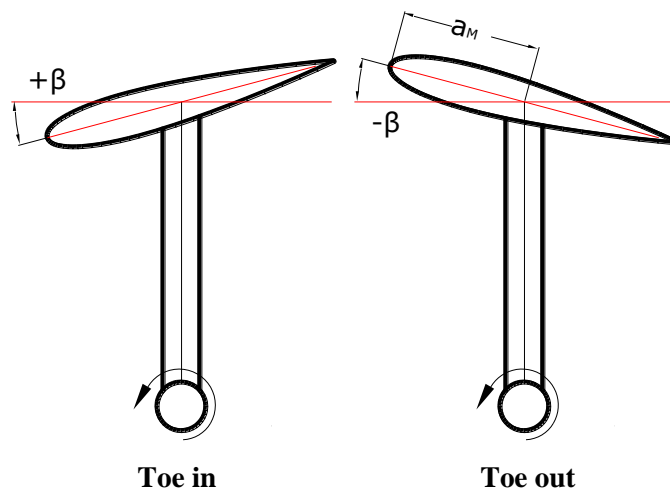


Figure 2.49 The mounting location and pitch angle

There are two types of pitch methods, toe-in and toe-out. The mounting location and blade pitch methods were presented in Figure 2.49. The pitch angle of the toe-in method is positive. In the case of the cambered airfoils, the mounting parameters include the cambered outward and inward. South and Rangi (1972) conducted a wind tunnel testing of a Darrieus with two blades and a diameter of 4.27. The

solidity is 0.07. Their blades were pitched out  $-4^\circ$  by an intentionally manufactured error. When they pitched the blades from  $-4^\circ$  to  $0^\circ$ , they found that the power coefficient was increased about 11%.

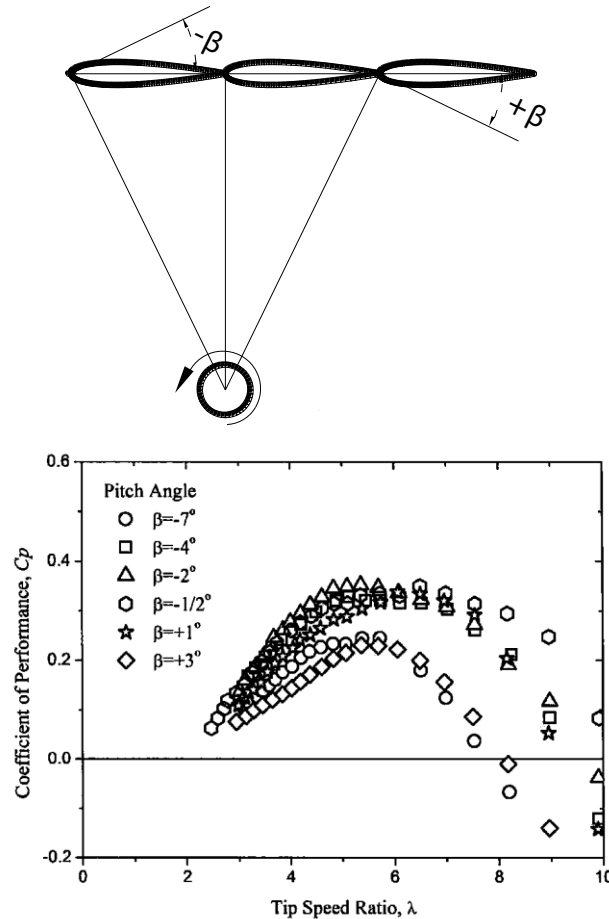


Figure 2.50 The pitch angle definition (Klimas and Worstell 1981)

A detailed investigation of the blade pitch's effects was conducted by Klimas and Worstell (1981). The test rotor is a 5-m curved Darrieus rotor. Their definition of the pitch angle is presented in Figure 2.50. In fact, the positive pitch angle is the toe-in method presented in Figure 2.49. And the negative pitch angle is toe-out method. The results show that the maximum power coefficient and the range of the tip speed

ratio vary with the pitch angle. The maximum power is about 0.35 when the pitch angle is  $-4^\circ$ . For the pitch angle  $-1/2^\circ$ , the widest range of the tip speed ratio is gained.

The mounting location and pitch effects were studied by Fiedler (2009). The results suggested that 29% of power coefficient was increased using the toe-out configuration. The optimum pitch angle is  $-7.8^\circ$  for two different values of  $a_M$ , which are 145mm and 150mm. The power coefficient of the case with  $a_M$  is 145mm, lower than that of the case with  $a_M$  is 150mm.

#### ***2.2.1.1.2.7 Blade tip design***

The design of the blade tip is an important issue to improve the aerodynamic performances of the Darrieus, especially for the large size Darrieus. Modern aviation offers a lot of guidance for the design of the Darrieus rotor blade tip due to the similarity of the theory. The reason why aerodynamicists use the wingtips is that the tip vortex generated at the tip of the wings can influence the aircraft's stability and efficiency significantly. The drag induced from these vortices can account for up to half of all drag (Bargsten and Gibson 2011). Thus, it is very important to design the wing tip well to reduce the drag force induced by the tip vortices.

The wingtips include the wing end-plates, the winglet, the traditional winglet, the blended winglet, the wingtip fence and the ranked wingtips. The most popular blade tip designs are winglets and endplates. The winglets are near-vertical surfaces which mounted at the wing tips and located at the low pressure side of the wing. The using of the winglets not only recovers part of the wasted energy in the tip vortices, but

also reduces the strength of the tip vortices. The endplates are a very simple structure in terms of applications. By using the endplates, the air cannot circulate from the high pressure side to the low pressure side at wing tips. Thus, the wingtip drag can be reduced. An investigation on the effect of the endplates on the performance of the rotor was tested by Li and Calisal (2010). It was found that the maximum power coefficient is gained for the rotor with NACA 0012 endplates. The power coefficient of the rotor without endplates is the highest when the tip speed is less than about 2.2. However, the situation is reversed when the TSP is larger than 2.2. The effect of the endplate seems not very significant for small turbines.

### **2.2.1.2 Force mechanism of the Darrieus rotor**

The above section is mainly focused on the parameter design of the Darrieus rotors. The aerodynamic story behind the Darrieus is very complicated although its appearance seems very simple.

#### ***2.2.1.2.1 Static and dynamic stall***

The static stall happens when the angle of attack of the airfoil exceeds a certain angle. This angle called stall angle. A typical variation of the lift coefficient as a function of the angle of attack is presented in Figure 2.51. It is found that the lift coefficient varies linearly with AOA, when the angle of attack is lower than the stall angle. In this region, the air flow moves smoothly over the airfoil. With the increase of the AOA, the flow tends to separate from the top surface of the airfoil. And the lift coefficient of the airfoil decreases dramatically. This is a common aerodynamics for

all of the airfoils.

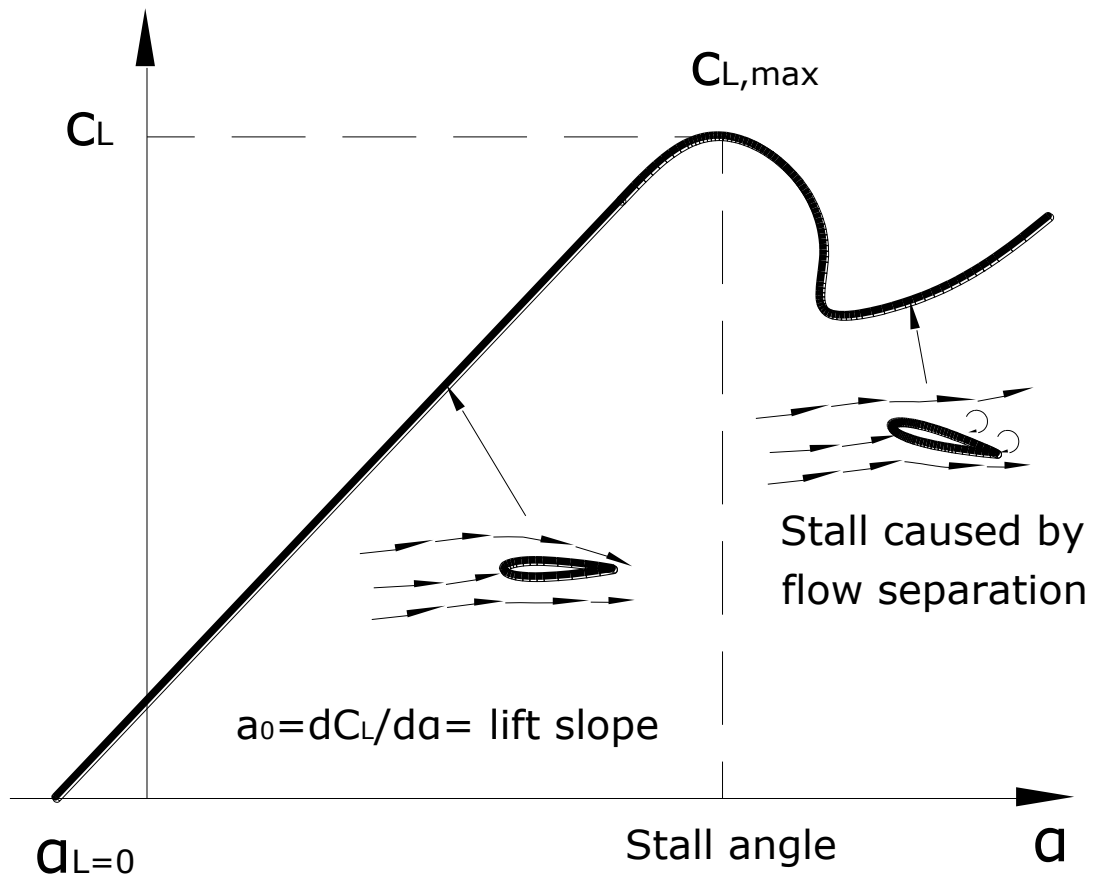


Figure 2.51 Lift coefficient vs. angle of attack

Following the discussion of the stall angle, the definition of the AOA and azimuth angle and the variation of the AOA as a function of the azimuth angle ( $\theta$ ) were shown at left and right of Figure 2.52. Two double dash lines represent the maximum and minimum stall angles. From this figure, it is found that the AOA of three blades, at most of the azimuth angle, is larger than the stall angle. In other words, the static torque of the Darrieus generally comes from the drag force instead of the lift force. This is may be the reason to explain why low-solidity Darrieus cannot self-start.

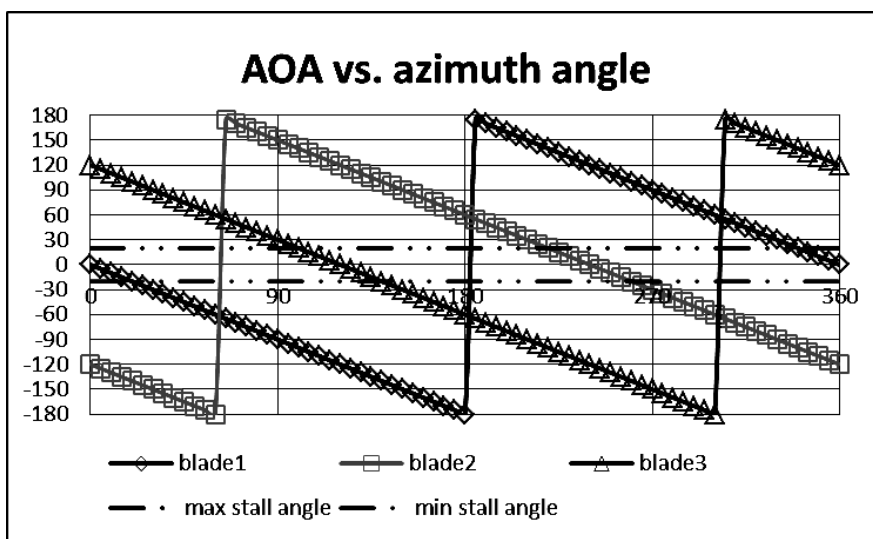
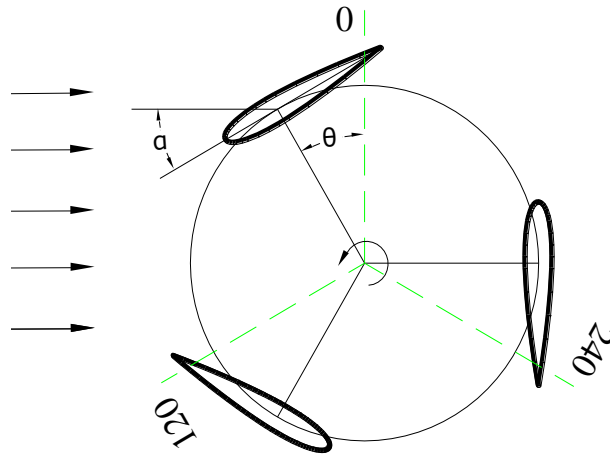


Figure 2.52 AoA ( $\alpha$ ) vs. azimuth angle ( $\theta$ ) for dynamic stall

Due to the periodical rotation of the airfoils, the local aerodynamic AOA is a function of the azimuth angle and the tip speed ratio. The variation magnitude of the AOA is highly dependent on the TSR as shown in Figure 2.53. It is found the variation of the AOA ranges from  $-57^\circ$  to  $+57^\circ$  when the TSR is 1.2. The maximum AOA of this situation is far larger than that of the static stall angle of the normal airfoils. With the increase of the TSR, the variation magnitude of the AOA is decreased. In the situation of the TSR is 6, the maximum AOA is less than  $9^\circ$  for the

entire range of azimuth angle. It means that the AOA of the airfoils will always be less than that of the stall angle of the static condition. But, the Darrieus rotors always have the opportunity to work on the situation of small TSR. When the Darrieus rotors work at the small TSR, dynamic stall happens.

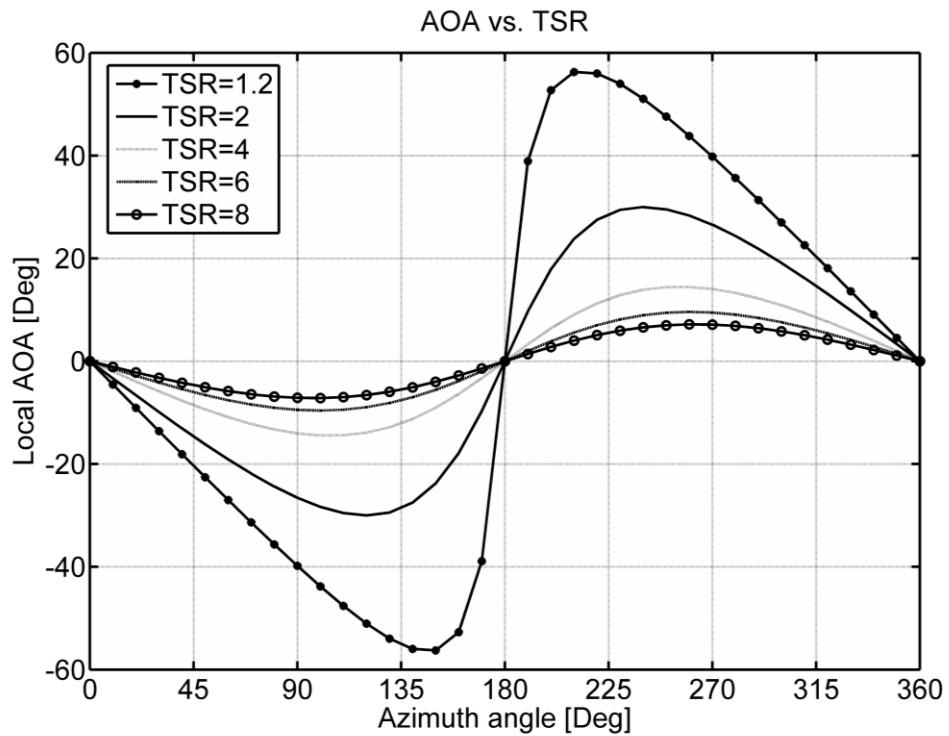


Figure 2.53 AOA vs. TSR

The dynamic stall is different from the static stall, which is a phenomenon when the AOA is larger than a stall angle. The dynamic stall is more like a cycle of several different flow states, such as attached states, transition states, and fully separated states. This cycle presented in Figure 2.54 is depicted by Carr (1985). And this dynamic stall sequence is strongly affected by the motion of the airfoil, the geometry of the airfoil and the Reynolds and Mach number which the airfoil is exposed.

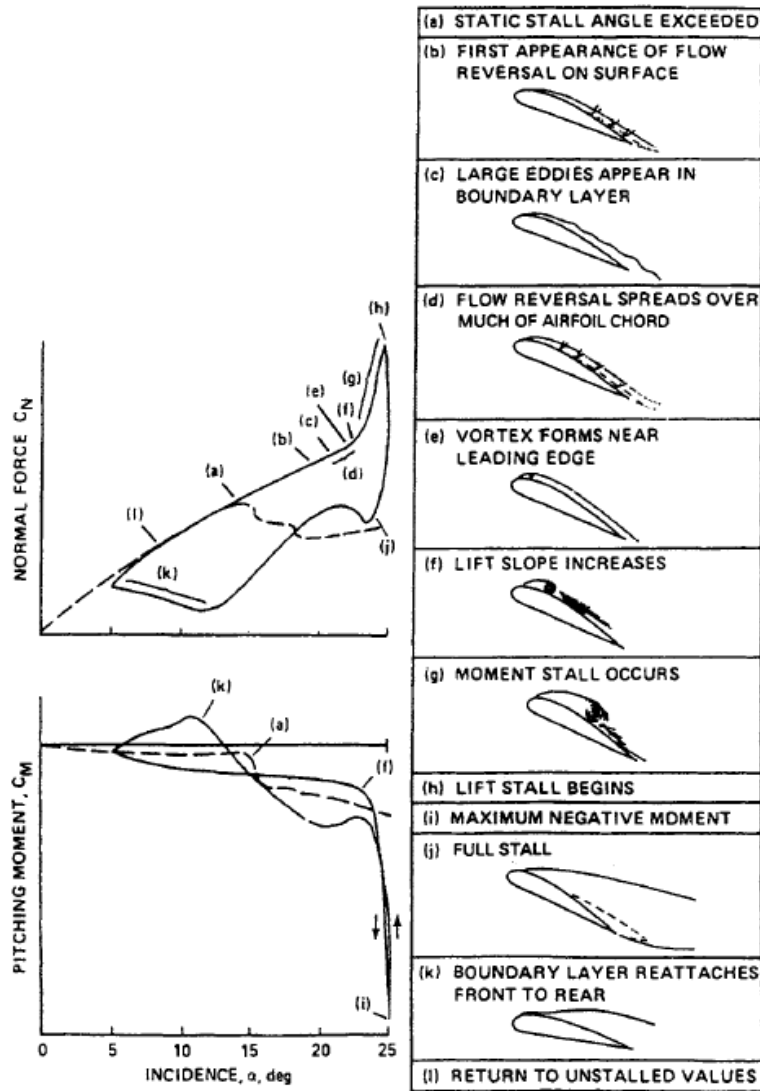


Figure 2.54 The dynamic stall on a NACA 0012 airfoil at low free-stream Mach number (Carr 1985)

The most distinctive feature of the dynamic stall is the vortex-shedding process Paraschivoiu (2002). It is a combination phenomenon between the rapid changes of airfoil's AOA and the separation of the boundary layer. The detailed review of the dynamic stall of the Darreius rotors was conducted by Paraschivoiu (2002) and McLaren (2011).

### 2.2.1.2.2 Tip vortex

As mentioned in the section of the blade tip design, the tip vortex is another aerodynamic issue of the straight-blade Darrieus. And different types of the tip design result in different flow patterns. The flow patterns of a small Darrieus rotor without any tip design was visualized by Ferreira et al. (2006) at eight different locations presented in Figure 2.55. It is clear that tip vortices were shaded from the tip of the blade at most of the azimuth angle. The upstream tip vortices moved downstream and may interact with the tip vortices generated by the blades at the downstream and the vortices generated at the trailing edge of the blade airfoils. Thus, the design of the blade tip is quite important to avoid those interactions which will degrade the performance of the rotors.

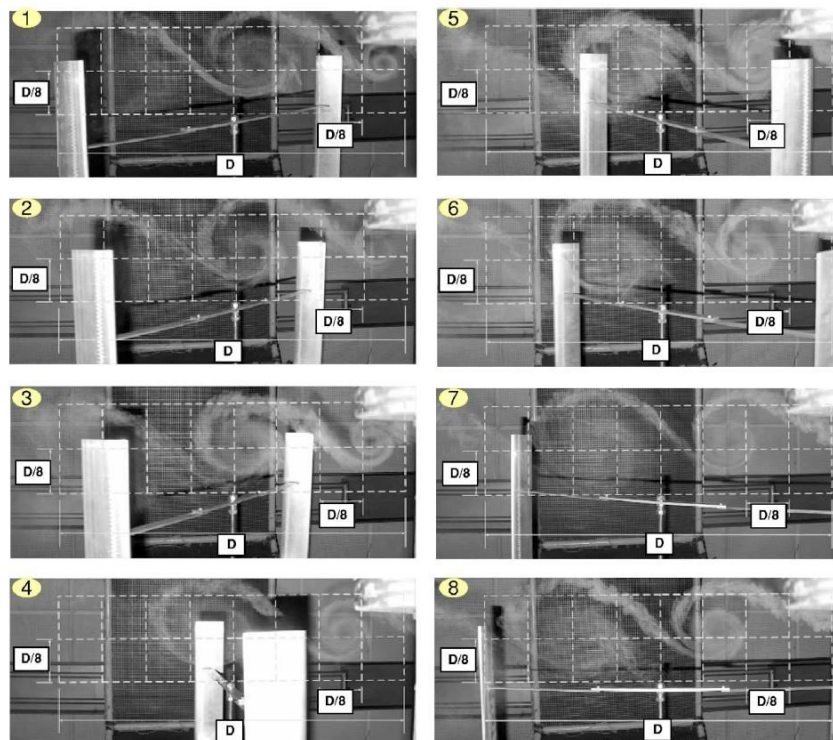


Figure 2.55 The blade tip vortex (Ferreira et al. 2006)

## **2.2.2 Review of the research methodology**

### **2.2.2.1 Experiment test**

The test of the Darrieus rotors is rather similar to the test of the Savonius rotors. The test also includes the testing performance and flow field. The testing can be conducted inside and outside a wind tunnel. And the test results should be corrected considering the blockage of the rotor.

### **2.2.2.2 Simulation method**

#### ***2.2.2.2.1 Method based on the Momentum, Vortex and Cascade theory***

The prediction models of the Darrieus rotors are more mature than that of the Savonius rotors. Islam et al. (2008) summarized three kinds of aerodynamics models for the Darrieus rotor. They are models based on the Momentum, Vortex and Cascade theory. These three models have an advantage of relative less computational effort. The general computational process of the above three models was described by Islam et al. (2008):

**STEP 1** Construction of the pre-stall airfoil characteristics gained from experiments and prediction models at different Reynolds number azimuth angle;

**STEP 2** Construction of the post-stall airfoil characteristics gained from post-stall models at different Reynolds number and azimuth angle;

**STEP 3** Correction of airfoil characteristics considering the finite aspect ratio;

**STEP 4** Estimation of the local angle of attacks and local relative velocities at a whole range of tip speed ratios and azimuth locations;

**STEP 5** Calculation of the ratio of the induced velocity and free stream velocity;

**STEP 6** Calculation of the local normal and tangential forces based on different theories (Momentum, Vortex and Cascade theory);

**STEP 7** Dynamic stall consideration

**STEP 8** Flow Curvature model consideration

**STEP 9** Consideration of the influence of the struts and towers

**STEP 10** Wind shear consideration

The three models mentioned above have several disadvantages. Momentum and vortex models have a convergence problem in some cases. All three models need airfoil characteristics of entire AOA ranging from  $0^\circ$  to  $360^\circ$  at different Reynolds numbers. However, most airfoil characteristics are limited at a narrow range of AOA and at high Reynolds number. All this restricts the application of the above three models. Thus, two new methods have been used recently. They are the panel method based on the potential theory and the CFD method based on the Euler equations. The two methods mentioned above have been widely used to analyze and design the aviation airfoils.

#### **2.2.2.2.2 Panel method**

In fact, it is not a new idea to predict the power coefficient and depict the flow field

in and around the vertical axis wind turbine using the panel method. Oler et al. (Oler et al. 1983) used a doublet panel method with an integral boundary layer scheme and discrete vortices to predict the lift, drag, pressure distribution of the airfoils to understand the mechanism of the dynamic stall. As reviewed in the previous section, panel method also can be used to predict the performance of the Savonius rotors. In 2006, Wang et al. (2007) conducted a 2D panel simulation based on singularity elements of a vertical axis tidal turbine. And some researchers (Dixon 2008, Sim ã Ferreira 2009) also applied 3D panel method to predict the performance of VAWTs recently. The general computational process of the panel method can be listed below:

**STEP 1** Definition of the coordinate frame

**STEP 2** Selection of appropriate singularity element distribution on the surface

**STEP 3** Selection of the boundary conditions

**STEP 4** Selection of the wake models

**STEP 5** Discretization of surface and singularity distributions

**STEP 6** Discretization of governing equations (fulfillment of the zero normal flow condition on surface, Kutta condition and Kelvin condition)

**STEP 7** Calculation of pressure, load and velocity

The above process is only suitable for the potential flow which is the flow without the consideration of viscosity. In the real flow, the effect of the viscosity should be not ignored. The coupling of outer potential flow and inner viscous flow was proposed to introduce the effect of the viscosity into the panel method. However,

this coupling method only can handle cases of ‘mild’ separation. Due to the nature of the large separated vortex structure, especially the flow of the dynamic stall, more sophisticated method should be adopted.

#### ***2.2.2.2.3 CFD method solves the incompressible Navier-Stokes equations***

CFD investigation of VAWTs has become more and more popular recently since the development of the computer and appealing ability of the CFD compared to the momentum and potential theory. A lot of researchers conducted the CFD simulation on VAWTs. Table 2.6 presents a brief summary of the CFD simulation of VAWTs. Based on this brief review, most researchers reached a consensus on several CFD modeling settings, such as the inlet boundary condition, outlet boundary condition, and domain size. The inlet and outlet boundary conditions are velocity inlet and outflow. The size of the domain is about 10 times of the turbine diameter. However, some of the controversial issues, such as node number on the airfoil surface, turbulence models and time step need to be investigated in details to offer a valuable guidance for the CFD simulation of VAWTs.

Table 2.6 A brief review of the CFD simulation of VAWTs

<i>Author</i>	Ferreira et al. (2007)	Amet et al. (2009)	Howell et al. (2010)	Lain and Osorio (2010)	Gupta et al. (2010)	Hamada et al. (2008)	McLaren (2011)
<i>Dimension</i>	2D	2D	2D,3D	2D	2D	2D,3D	2D
<i>Blade profile</i>	NACA 0015	NACA 0018	NACA 0022	NACA 0025	NACA 0012	NACA0022	Tailed NACA0021&0015
<i>Diameter(D)</i>	0.4m	0.12m	0.3mm	0.9m	*	2.5m	2.5m
<i>Chord length(c)</i>	50mm	20mm	100mm	132.75mm	50mm	200mm	400mm&420mm
<i>Mesh number(N)</i>	2D 1.6 million	2D 160,000	2D 3D 1.3 million	2D 157,130	2D 112,465	3D 2million	2D 7.2*10e4~5.67*10e5
<i>Nodes on blades(N0)</i>	*	188	*	*	*	*	989
<i>Height of the blade first layer</i>	0.02%c	25um	*	*	*	*	*
<i>Mesh type</i>	Quadrilateral	Structured	Tetrahedron	Triangles	Triangles	Tetrahedron	Unstructured
<i>RN or velocity</i>		1.0×10e4	3.9×10e4	2.5m/s-20m/s	5.31×10e4	1.15×10e6	2.7×10e5

Table 2.6 A brief review of the CFD simulation of VAWTs (continued)

<i>Author</i>	Ferreira et al. (2007)	Amet et al. (2009)	Howell et al. (2010)	Lain and Osorio (2010)	Gupta et al. (2010)	Hamada et al. (2008)	McLaren (2011)
<i>Domain size</i>	10D*14D	30c	16D	8D*5D	6c	50c*30c	3.2D*5.6D~9.6D*16.8D
<i>Degree at each step</i>	1/16 °; 1/8 ° 1/4 °; 1/2 °	0.25 °					0.5~10
<i>Turbulence model</i>	Spalart-Allmaras Standard $\kappa - \varepsilon$ LES and DES	$\kappa - \omega$	RNG $\kappa - \varepsilon$	SST $\kappa - \omega$	Standard $\kappa - \varepsilon$	RNG $\kappa - \varepsilon$	SST $\kappa - \omega$
<i>Y+ and Wall treatment</i>	Y+ close to 1	Y+ close to 1	Y+<10, Standard	*	Y+<15, enhanced	Standard	Average 1.3
<i>Algorithm</i>		*	*	SIMPLE	SIMPLE	*	*
<i>Interpolating scheme</i>		Third-order upwind	Second-order	Second-order upwind	Second-order upwind	Second-order upwind	*
<i>Inlet</i>	Velocity inlet	Velocity inlet	Velocity inlet	Velocity inlet	Velocity inlet	Velocity inlet	Velocity inlet
<i>Outlet</i>		Pressure outlet	Outflow	Pressure outlet	Outflow	Outflow	Outflow

### **2.2.3 Current insufficiency of the fixed pitch lift-type VAWTs**

A brief review was conducted in the above paragraphs. Based on this review work, some of the shortcomings of the research work of the fixed pitch lift-type VAWTs can be concluded below.

Although there are many types of fixed pitch Darrieus rotors proposed by previous researchers, it seems that the self-starting ability of the fixed pitch Darrieus is still very poor. Thus, more effort needs to be done to improve the self-starting ability of the fixed pitch Darrieus rotors through the shape design and modification of the design parameters.

In terms of the power coefficient, most the Darrieus rotors have adopted the four-digit NACA airfoils. Although some of the researchers have studied the cambered airfoils, low Reynold number airfoil and high-lift airfoils, there is not an efficient way and theories to choose the right airfoils for the Darrieus rotors.

Moreover, some of the controversial issues about the CFD settings need to be standardized in order to predict the performance of the Darrieus rotors.

## **2.3 Review of hybrid VAWTs-Savonius-Darrieus rotor**

Due to the fact that the Darrieus rotor has poor self-starting ability and the Savonius has a poor power coefficient, some researchers proposed hybrid rotors which is a combination of a Savonius and a Darrieus rotor. Two types hybrid VAWT (Shankar 1975) rated 1 kW presented in Figure 2.56 (a) was fabricated by the National

Aerospace Laboratories (NAL) of India. The testing results show that the self-starting of the hybrid rotor with the Savonius rotor inside of the Darrieus occurred when the wind is larger than 10km/hr. The Savonius rotor of the second type of hybrid rotor is placed out of the Darrieus rotor. And the Darrieus rotor has three blades. They claimed that the second type of hybrid rotor is superior to the first type of rotor in terms of starting ability.

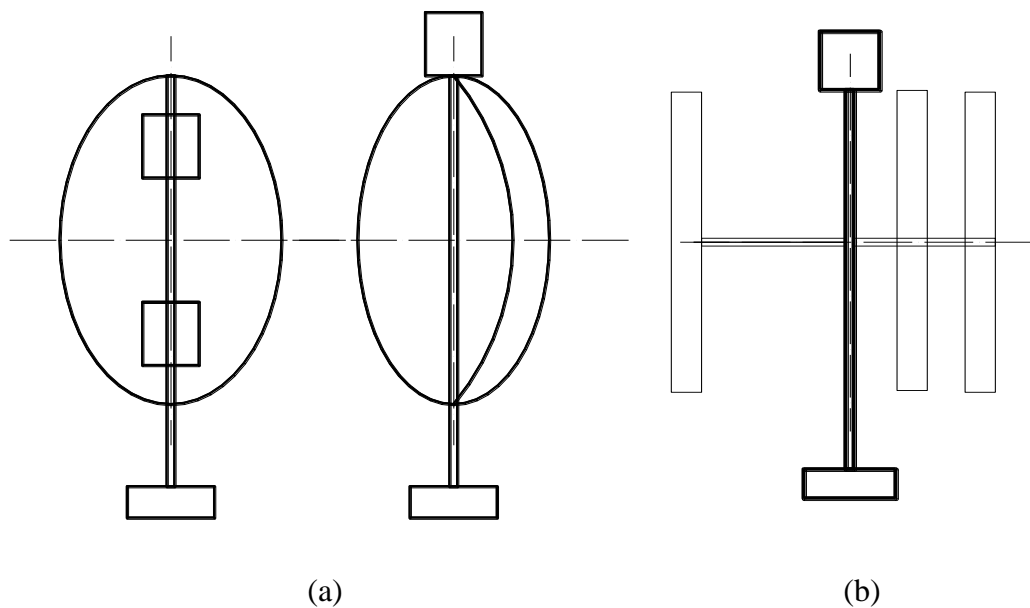


Figure 2.56 Two types of hybrid rotors tested by NAL and a Waded turbine tested by NAL (a) A hybrid rotor called Waded turbine tested by NAL (Shankar 1979) (b).

This rotor presented in Figure 2.56 (b) is a combination of the Savonius rotor and a straight blade Darrieus rotor. The frontal area of the Savonius rotor and Darrieus rotor is  $2 m^2$  and  $17 m^2$ , respectively. Based on this arrangement, the total frontal area is  $19 m^2$ . The power output of this rotor is 1kW at wind speed 25km/hr. Consequently, the power coefficient is about 0.25.

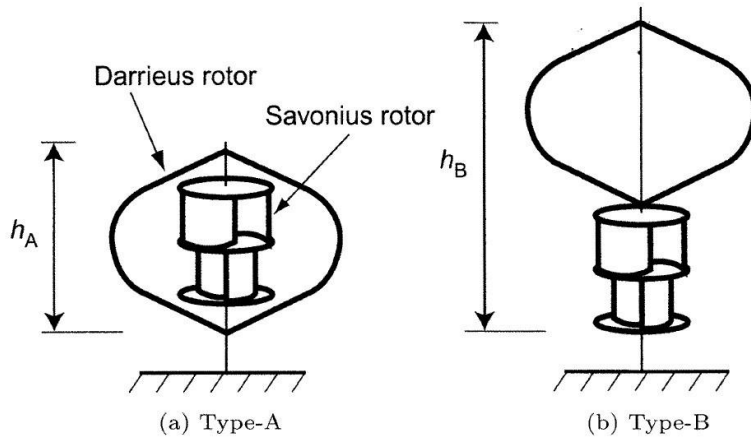


Figure 2.57 Two types of hybrid rotors (Wakui et al. 2005)

Following the above researches, Wakui et al. (2005) conducted a detailed comparison between two different hybrid configurations presented in Figure 2.57.

The maximum powers of type A and B are about 0.204 and 0.231. Thus, Type B is more efficient than Type A. However, the startup time and stabilization of type B is longer than that of type A. Then they claimed that Type A is more useful due to the compaction of its structure.

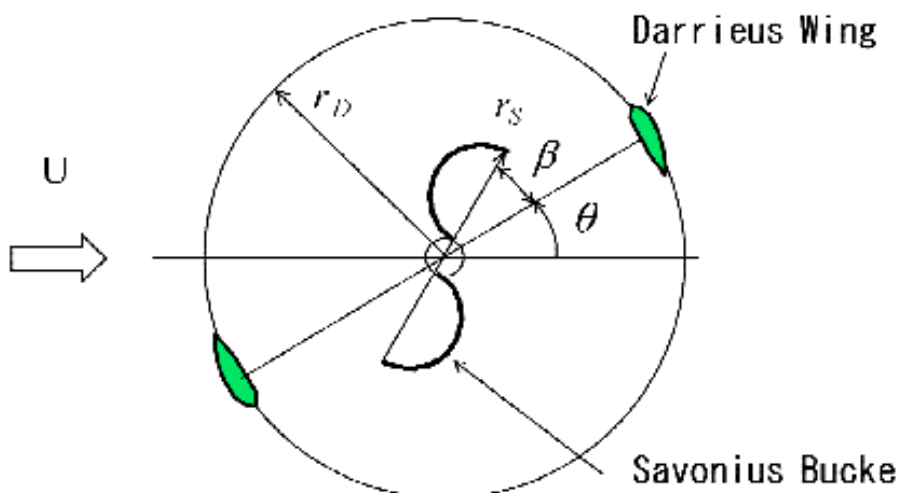


Figure 2.58 The definition of attached angle (Kyojuka 2008)

The effect of attaching angle between the Darrieus and Savoniu rotor was investigated by Kyozuka (2008). This angle is defined as  $\beta$  and shown in Figure 2.58. And the testing results were presented in Figure 2.59. It is clear that the maximum power is achieved for the rotor without the Savonius rotor. And the 30% power coefficient is reduced when the Darrieus rotor is attached the Savonius rotor.

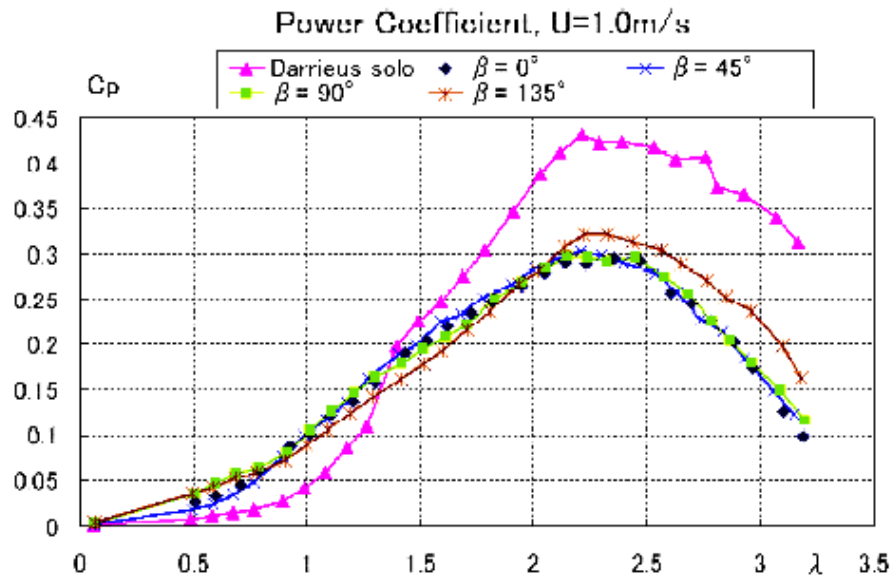


Figure 2.59 Comparison of the power coefficient (Kyozuka 2008).

## 2.4 Summary

This chapter presented a comprehensive literature review covering the vertical axis wind turbine. It can be found that the Savonius rotors have relatively lower power coefficient and better starting ability. The Darrieus rotors have a relatively high power coefficient and generate very little starting torque, and they may fail to accelerate beyond a “dead band” even when they do begin to move.

Due to the low power coefficient of the Savonius rotor, the main objective of this thesis is to improve the starting ability and the power coefficient of the Darrieus rotor. Hence, there are two objectives of this thesis.

The first objective of this thesis is to improve the starting ability of the Darrieus rotor. Based on the literature review, two possible methods can improve the starting ability of the Darrieus rotor. Those two methods are the usage of the two-stage rotor with the Darrieus rotor and the usage of two sets of blades. As stated in the previous paragraphs, these two methods have not been investigated sufficiently or carefully, especially the usage of two sets of blades.

In addition, the author has proposed a new method to improve the starting ability of the Darrieus rotor. This new method is the Darrieus rotor with an opening at the blade tip. Thus, in Chapter 3, a detailed wind tunnel study was conducted with respect to the two-stage Savonius rotor. In the Chapter 5 and Chapter 6, the CFD simulation research about the rotor with an opening at the blade tip and two sets of blades will be presented.

The second objective of this thesis is to improve the CP of the Darrieus rotor. A novel airfoil optimal design process will be built in the Chapter 7 due to the fact that the research method for the airfoil design of the Darrieus rotor is not efficient and only suitable for several kinds of airfoil.

To sum it up, three methods which may improve the starting ability of the Darrieus rotor and one airfoil optimal design process which improve the CP of the Darrieus rotor are presented and studied in this thesis.

## **CHAPTER 3      SIMULATION AND WIND TUNNEL TEST OF THE TWO-STAGE SAVONIUS ROTOR**

### **3.1 Introduction**

In this chapter, the work mainly focuses on the first method, the two-stage Savonius rotor, which is regarded as a traditional self-starting assistance for the Darrieus rotor due to the fairly large torque variation and the negative CTs of one-stage Savonius rotor at some angular positions. Understanding the starting ability of the two-stage Savonius rotor is very important to integrate the Savonius rotor with the Darrieus rotor. The two-stage Savonius rotor is studied independently without the Darrieus rotor in this thesis. The two-stage rotor can be the two-blade rotor or three-blade rotor. And the comparison between the one-stage Savonius and two-stage Savonius rotor is also made in this chapter.

### **3.2 Research methodology of the two-stage Savonius rotor**

The research methods of two-stage Savonius rotor include CFD analysis and experimental tests. The best way to study the two-stage Savonius rotor is the CFD simulation which will save a lot of cost and time of the real testing.

However, the reliable and feasible of the CFD method must be evaluated firstly. Thus, in the beginning, 2D and 3D CFD simulations of the one-stage Savonius rotors were conducted to check whether the CFD method is reliable and feasible to conduct

the visual experimental testing of the Savonius rotor.

### 3.3 2D and 3D simulations of the Savonius rotor

#### 3.3.1 Simulation models and simulation setup

The simulation models are the same size as the two-blade one-stage Savonius rotor tested by Hayashi et al. (2005). The diameter of the rotor is 0.33m and its height is 0.23m. The computational domain is divided into inner and outer zones. The inner zone is a circle which contains two blades and shaft. The outer domain is a rectangular area which is 20 times of the rotor diameter.

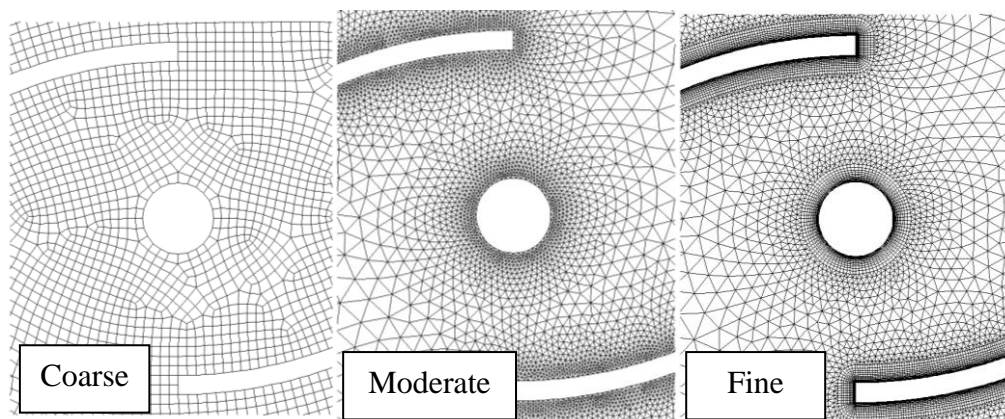


Figure 3.1 Three meshing methods

For the 2D simulation, three types of meshing methods were adopted to study the mesh type influence on the power coefficient. There are no local refinement and boundary layers on the blades in the case with coarse mesh. Thus, the total mesh number of this case is only 252846. For the case with moderate mesh, the meshes on

and around the blades were refined using the size function. The total mesh number of the case with moderate mesh is 434047. In the case with fine mesh, the boundary layer was attracted to the blade surface. The height of the first layer is about 0.1mm to ensure the  $Y^+$  value on the blades close to 1. And the total mesh number is 644518. The effect of the three types of turbulence models was also investigated. Figure 3.1 presents the three difference types of mesh methods adopted. The inlet of the computational domain is velocity inlet. The outlet is set as pressure outlet. Two side surface is set as walls.

For the 3D simulation, two cases with different mesh nodes and two cases with different turbulence models were conducted. The mesh numbers of case 1 and case 2 are about 2 million and 4 million. The boundary condition of the 3D simulation is similar to the 2D simulation.

### 3.3.2 2D simulation and results

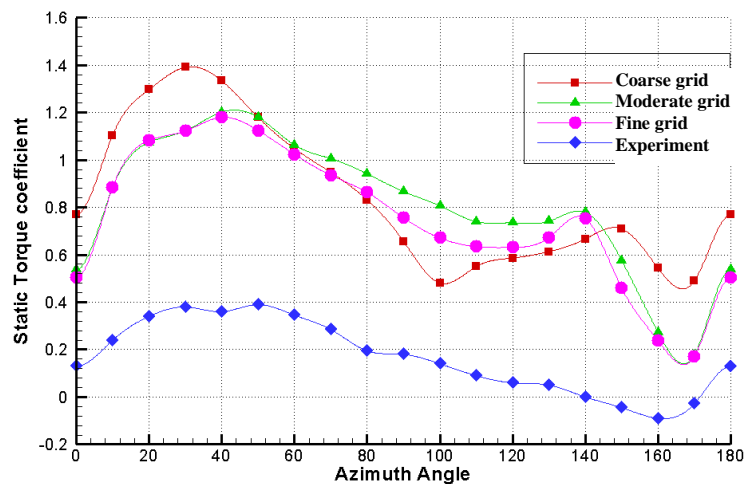


Figure 3.2 The 2D simulation results of three different mesh methods

Figure 3.2 presents the comparison of the simulation results and experimental results from Hayashi et al. (2005). From the comparisons, the simulation results for the case with coarse grid seem a less reasonable than that of the case with moderate grid and the case with fine grid, especially at low and high azimuth angle. The deviation between the results of the case with moderate grid and the case with fine grid is not significant. However, it is found that the differences between the results of the simulation and experiment are quite large. And the simulation result is about three times larger than that of the experimental results. Many factors may contribute to this large deviation between the results of the simulation and experiment. They may be affected by the turbulence models, node number on the blades and relaxation factor.

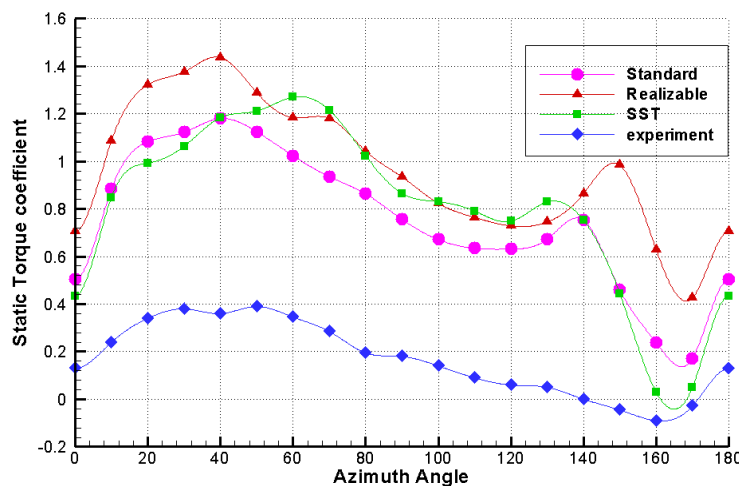


Figure 3.3 The effect of the turbulence models

Thus, the Standard  $\kappa-\varepsilon$ , Realizable  $\kappa-\varepsilon$  and SST  $\kappa-\varepsilon$  models are chosen for the 2D simulation to validate the adaptation of the turbulence model. The case with moderate grid is chosen as the baseline for obtaining more accurate simulation results for this comparison. The simulation results are plotted in Figure 3.3. It is

found that these simulation results of the three turbulent models show a general similar trend on the static torque distribution varying with different azimuth angles, although all the simulation results of the three turbulent models depict large discrepancies from that of the experimental results. It is known that both the Realizable  $\kappa-\varepsilon$  and SST  $\kappa-\varepsilon$  models predict the flow field more accurately than the Standard  $\kappa-\varepsilon$  model when the flow features include strong curvature, vortices and rotation. However, it is not easy to say which one is better than others, because the quantity of the simulation results is larger than that of the experimental results, as shown in Figure 3.3. It seems that the 2D simulation cannot give an accurate result, so that the 3D simulation is carried out in the following section.

### **3.3.3 3D simulation and results**

The grid numbers of the 3D Case 1 and Case 2 are about 2 million and 4 million, respectively. All the setup is similar to the 2D model. The validation work starts from the effect of the grid number.

The effect of the grid number is presented in Figure 3.4. The results of the cases with different grid numbers are quite close to each other in terms of trend and magnitude. Thus, the effect of the turbulence models is applied to Case 1 because less computational time is used for Case 2 and the different turbulence models can be evaluated economically.

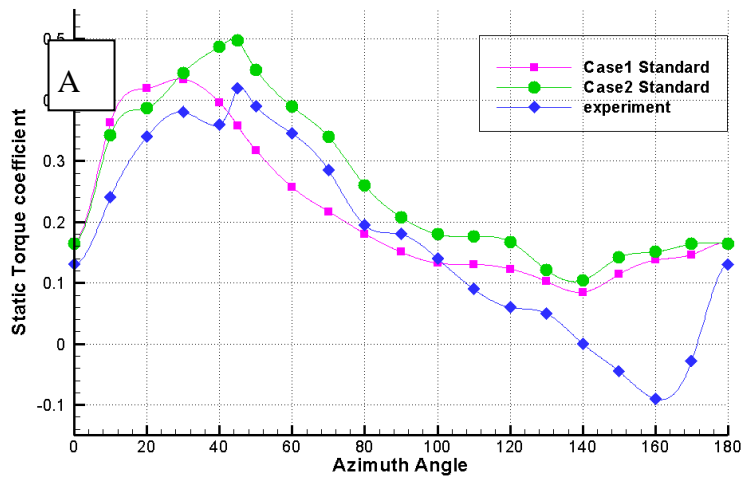


Figure 3.4 The 3D simulation results of the Savonius rotor

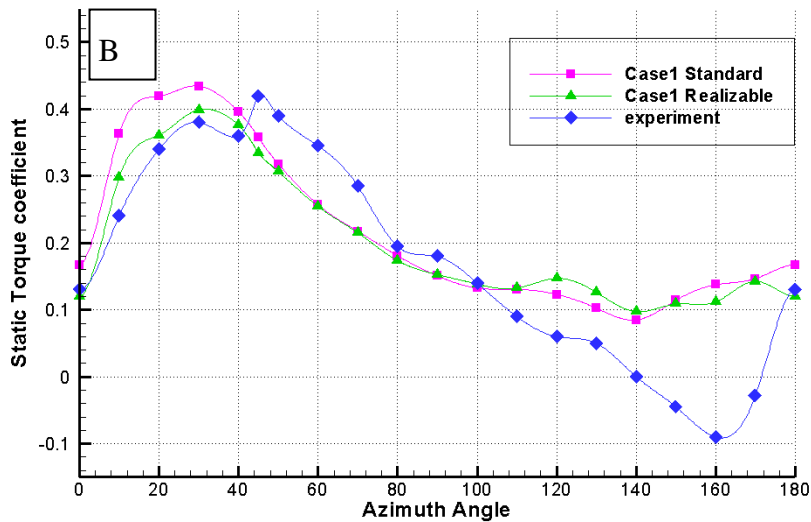


Figure 3.5 The 3D simulation results of the Savonius rotor

The results shown in Figure 3.5 present the effect of the turbulence models. There is no significant difference in the solution when the Standard  $\kappa-\varepsilon$  and Realizable  $\kappa-\varepsilon$  turbulence models were used. However, the simulation datum of the Realizable  $\kappa-\varepsilon$  turbulence model for the azimuth angles from  $0^\circ$  to  $40^\circ$  is more

accurate than that of the Standard  $\kappa-\varepsilon$  turbulence model. The changing trend and magnitude of the simulation results are comparable well with the experimental data for the azimuth angle range from  $0^\circ$  to  $130^\circ$ . The maximum static torque of the simulation occurs at the azimuth angle of  $30^\circ$ , while the maximum static torque of the experiment is at the azimuth angle of  $45^\circ$ . The difference between the simulation and experiment is larger for the azimuth angles from  $130^\circ$  to  $170^\circ$ .

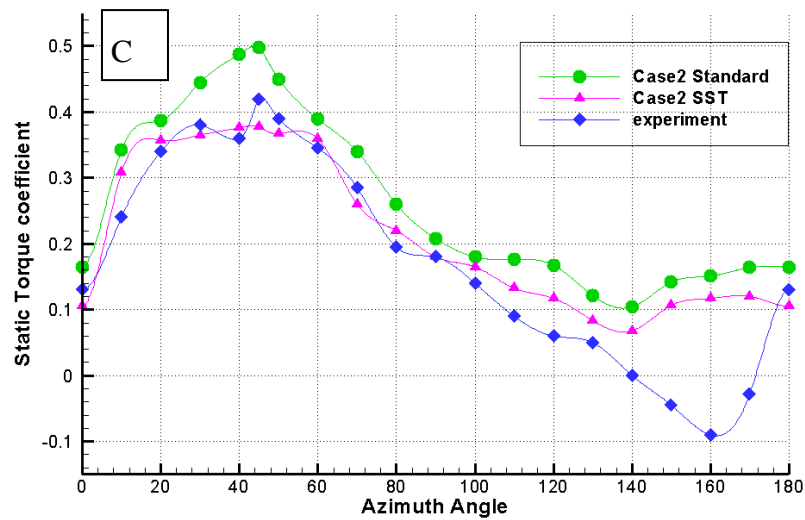


Figure 3.6 The 3D simulation results of the Savonius rotor

In order to find the reason for this discrimination, a further investigation was conducted using the fine mesh. The results are depicted in Figure 3.6. The results gained from the SST turbulence model are closer to the experiment results than the Standard  $\kappa-\varepsilon$  turbulence model due to the additional features added into the SST  $\kappa-\omega$  model (FLUENT 2009). But, The discrimination between the simulation and experiment still is larger for the azimuth angles from  $130^\circ$  to  $170^\circ$ . The CTs of the real Savonius rotor is negative for the azimuth angles from  $130^\circ$  to  $170^\circ$ . However,

the simulation results is positive. It indicates that the steady CFD simulation can not grasp the unsteady nature of the separation flow around the Savonius rotor, especially for the azimuth angles from  $130^\circ$  to  $170^\circ$ .

### 3.3.4 Discussions on the simulation of the Savonius rotor

Based on the simulation work conducted in the previous section, several indications can be concluded, i.e. the grid number of the 2D and 3D seems fine enough because the differences between the cases with different grid numbers is fairly small. Secondly, it seems that the 3D simulation is much more accurate than the 2D simulation because the 3D effects can be well presented by the 3D simulation. Those effects can be located inside the rotor and outside the rotor which are visualized in Figure 3.7.

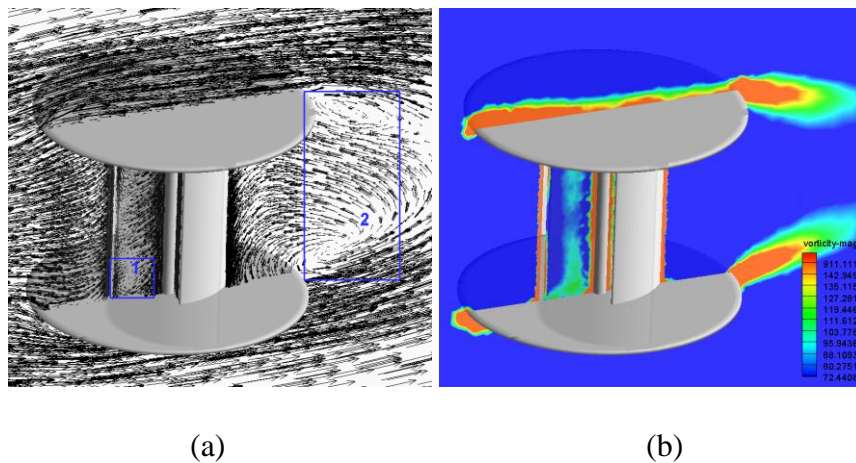


Figure 3.7 The velocity field and vorticity magnitude distribution in and around the Savonius rotor: (a) velocity field distribution; (b) vorticity magnitude distribution

The flow patterns of the rotor from the 2D and 3D simulations at the center section

of the rotor are also fairly different, which is depicted in Figure 3.8 and Figure 3.9. Last, the simulation conducted by the author is not sufficient because only a few different CFD settings have been investigated. There are still many CFD settings to be further studied, such as the mesh independence, node number, domain size, time steps and so on.

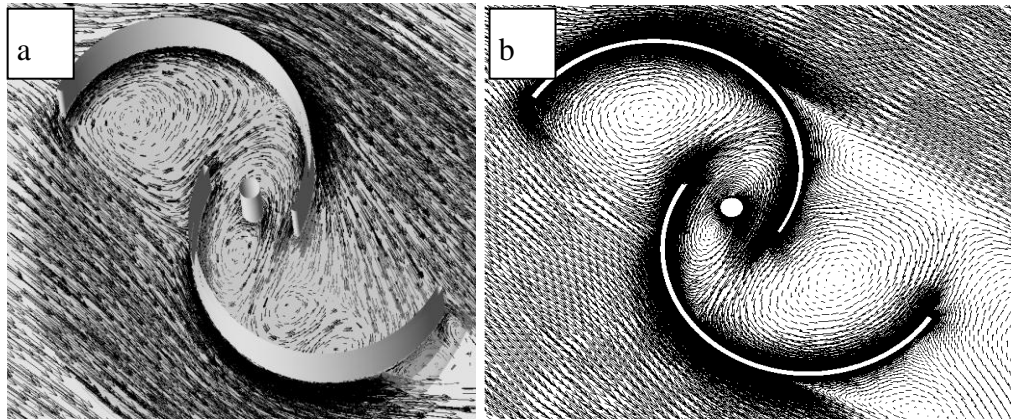


Figure 3.8 The velocity distributions in and around the stationary Savonius rotor ( $\theta=0^\circ$ ): (a) 3D simulation; (b) 2D simulation

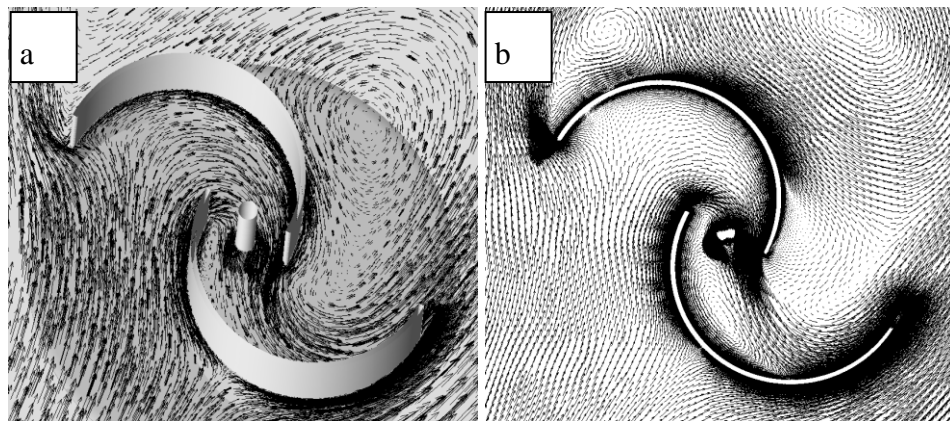


Figure 3.9 The velocity distributions in and around the stationary Savonius rotor ( $\theta=90^\circ$ ): (a) 3D simulation; (b) 2D simulation

In general, the 2D simulated results do not match well with experimental results and the 3D complicated configurations of two-stage need great computational efforts. Thus, the experimental testing is selected for the research method for the two-stage Savonius rotors.

### 3.4 Wind tunnel testing of one-stage and two-stage Savonius rotors

#### 3.4.1 Introduction of an environmental wind tunnel (EWT)

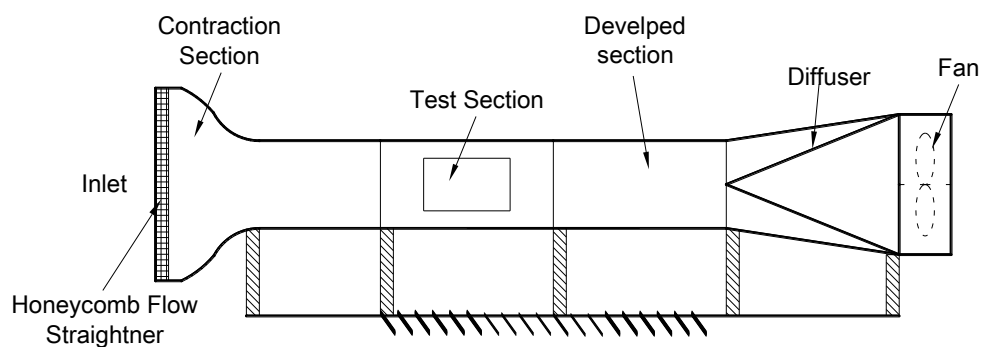


Figure 3.10 The environmental wind tunnel

The experiment was carried out in an open-circuit Environmental Wind Tunnel (EWT) shown in Figure 3.10. The EWT comprises of a contraction section, a test section, developed and diffuser sections. Air is sucked into the wind tunnel through an axial fan installed at the end of the wind tunnel. Turbulence is removed through the honeycombs located at the inlet of the wind tunnel. And the contraction section is used to increase the velocity of the wind and to stabilize the wind speed. Following the contraction section, the test section is several meters away downstream, which has a square cross-section of  $1050\text{mm} \times 1050\text{ mm}$ . The tested wind turbine is positioned almost at the center of the wind tunnel's test section. A variable frequency controller drives the fan to run at different rotational speeds to regulate the wind velocity in the range of 0 to 30 m/s.

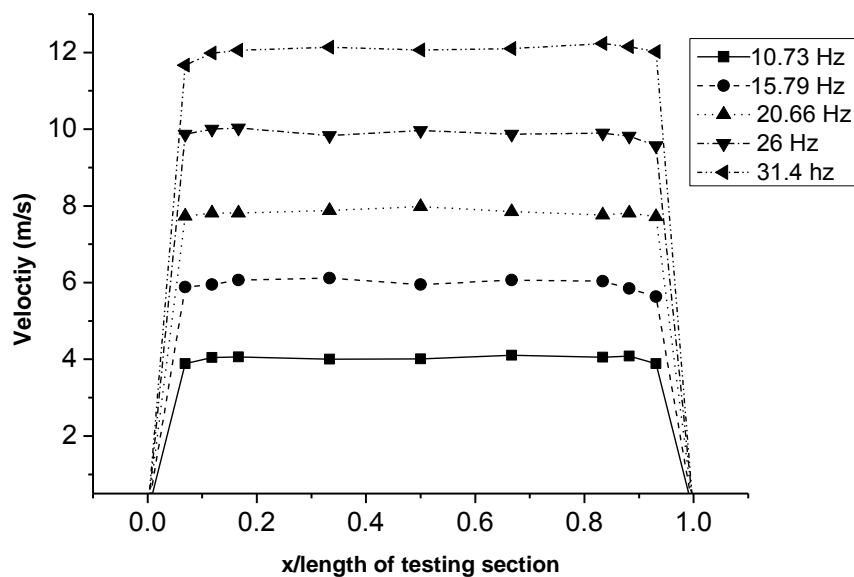


Figure 3.11 The wind speed distribution of the wind tunnel

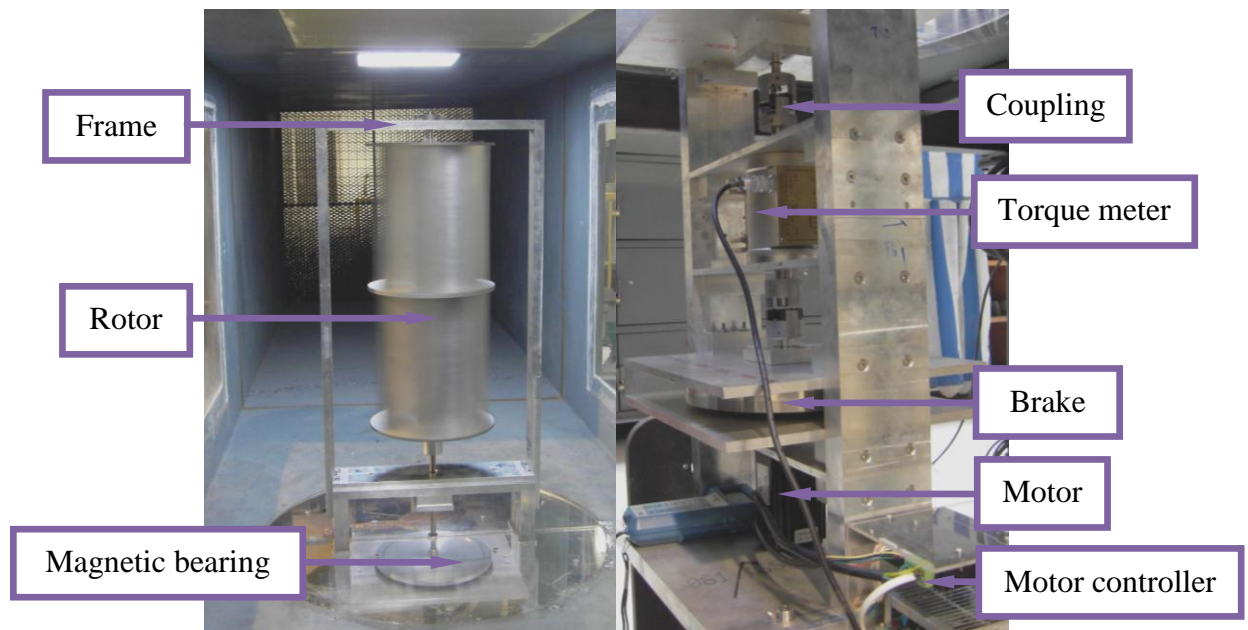
The wind speed distribution along the horizontal center line of the testing section was measured to investigate the turbulence intensity and the wind velocity

distribution of the wind tunnel. It is very important to know the wind tunnel's turbulence intensity which presents the quality of the wind tunnel. The lower is the turbulence intensity; the higher is the quality of the wind tunnel. The velocity distribution of the main flow in the horizontal center line of the test section without rotor, at five different frequencies, was measured through a hot wire anemometer. The test results are shown in Figure 3.11. It is found that the flow is fairly uniform in the region from 0.12 to 0.88 for different frequencies, although the density of the testing points is not relatively high. Moreover, the calculated turbulence intensity of the wind tunnel ranges from only 0.32% to 0.47% at different frequencies. This turbulence intensity is low enough to conduct the wind turbine test.

### **3.4.2 Introduction of the testing rig**

The test rig of VAWTs is presented in Figure 3.12. There are mainly four parts of the test rig. They are the rotor, torque meter, motor and frame. The key issue for the precision measurement of the torque and rotational speed of the sample wind turbines is to keep all the components in line. A small offset of any components would result in instability of the whole system and the instability of the system would increase with the rising of the rotational speed. For the above reason, the testing rig was manufactured by a CNC machine and built to a tolerance of 0.01 millimeters for each component of the frame to make sure the alignment of all the devices. According to the relative position between the test rig and the wind tunnel, the test rig was separated into higher and lower parts. The higher part of the testing rig held the Savonius rotor and was placed inside the wind tunnel as indicated in

Figure 3.12(a).



(a) The VAWT

(b) The whole test rig

Figure 3.12 The test rig in the wind tunnel

At the same time, the lower part (Figure 3.12 (b)) of the testing rig accommodated the couplings, torque meter, brake and motor in line was placed out of the wind tunnel. In addition, a magnetic bearing replaced the traditional mechanical bearing for the purpose of friction reduction. A DC motor regulated by the motor controller drives the rotor at fixed rotational speed. The torque meter connected to the computer through an RS-232 port, recorded the torque and rotational speed data. At the same time, a hot-wire anemometer was installed on the side wall of the wind tunnel and placed 1.4 m upstream of the wind rotor to measure the undisturbed wind velocity. In the testing, the static torque was measured at a fixed azimuth angle  $\theta$  for 30 seconds and was averaged to obtain curves of static torque coefficient versus

azimuth angle. The interval of the azimuth angle  $\theta$  is 5 degrees for the static torque. The dynamic torque was tested at different rotational speeds or TSR for 30 seconds and averaged at fixed wind speed to obtain curves of torque coefficient versus TSR.

### 3.4.3 Wind tunnel correction

Correction for the experimental results was reviewed in the previous chapter. Two of the most popular ways to correct wind tunnel data were developed by Alan Pope [12] and Maskell [13] when the tested object is placed inside the wind tunnel. Alexander [14] [15] has extended the Maskell's method by applying it to correcting Savonius rotors, which can provide quite accurate correction results even when the  $A/C$  value reaches 0.334.

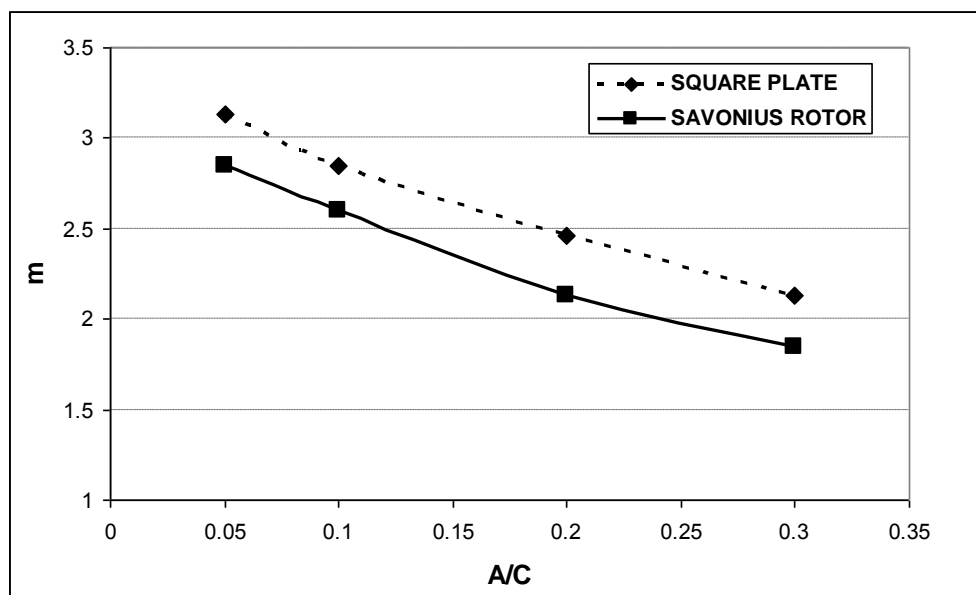


Figure 3.13 The relationship of  $m$  vs.  $A/C$  for a square plate and Savonius rotor [14]

The blockage values of the single-stage and two-stage rotors are 0.068 and 0.136,

respectively. Those blockage values are much less than the maximum blockage value of Alexander. The form of the Alexander's blockage correction is represented as:

$$\varphi = \frac{C_{Du}}{C_{D\infty}} = \frac{q_c}{q_u} = \frac{V_c^2}{V_u^2} = \frac{1}{1 - m(A/C)} \quad \text{Equation 2.7}$$

where  $m$  is a factor determined by the wind tunnel test;  $V_c$  is the corrected wind velocity;  $V_u$  is the undisturbed wind velocity;  $A$  is the maximum frontal area of the Savonius rotor;  $C$  is the testing section area of the wind tunnel and  $m$  can be interpolated through the datum presented in Figure 3.13.

#### 3.4.4 Measurement uncertainty

The percentage of the measurement uncertainty is defined as the ratio of the average value of the measurement variable to the standard deviation of this measurement variable. If the measurement variable is  $x$ , the average of  $x$  and standard deviation of  $x$  is calculated in the following equations:

$$x_{ave} = \frac{x_1 + x_2 + \dots + x_n}{n} \quad \text{Equation 3.1}$$

$$x_{SD} = \sqrt{\frac{(x_1 - x_{ave})^2 + (x_2 - x_{ave})^2 + \dots + (x_n - x_{ave})^2}{n - 1}} \quad \text{Equation 3.2}$$

$$\text{Percentage of uncertainty} = \frac{x_{ave}}{x_{SD}} 100 \quad \text{Equation 3.3}$$

This method is used to find the uncertainty of the air velocity of the wind tunnel, power coefficient, torque and the RPM of the turbine. The percentage of the

measurement uncertainty is presented in Table 3.1.

Table 3.1 Percentage of the measurement uncertainty

Parameter	Uncertainty(%)
Air velocity of wind tunnel	+/- <b>1.8</b>
Power coefficient	+/- <b>8.24</b>
Torque of the rotor	+/- <b>3.4</b>
RPM of the rotor	+/- <b>3.2</b>

During the test, some measurements produced unforeseen results (the power curve has two or three peak) were repeated several times over a couple of days to minimize the error of measure.

### 3.4.5 Dimensions and abbreviations of the tested Savonius rotors

The main parameters and configuration of the tested Savonius rotor are depicted in Figure 3.14. The shaft diameter is  $a=12\text{mm}$ , the height of the one-stage rotor is  $H=270\text{mm}$  and the diameter of the end plate is  $D_0=250\text{mm}$ ; the rotor aspect ratio (AR) of the single-stage rotor and two-stage rotors are 1.088 and 2.176, respectively. The stage AR of the two-stage rotors is 1.088. According to previous researches, the best gap rate for the Savonius rotor is  $1/6$  [9] without the shaft or between 0.15-0.2 [2, 10, 11]. Three types of one-stage rotors with gap rates of  $\beta=0, 0.167$  and  $0.333$  were tested while the swept area of the rotors was kept constantly at  $A=0.06664\text{m}^2$ .

Nine types of two-stage rotors were tested at 4m/s, 6m/s, 8m/s and 10m/s by considering three different phase-shift angles from 0°, 45° to 90° and three different gap rates, i.e.  $\beta$  values which are the same as those used in the one-stage rotors. The name of each model is defined as S1 $\beta$ 0 for one-stage models and S2 $\beta$ 0PS0 for two-stage models, where ‘S’ means the stage of rotor, ‘ $\beta$ ’ denotes the gap rate of the rotor and ‘PS’ denotes the phase-shift. If a rotor is a three-blade rotor, then ‘BN3’ will be added at the end of the abbreviation.

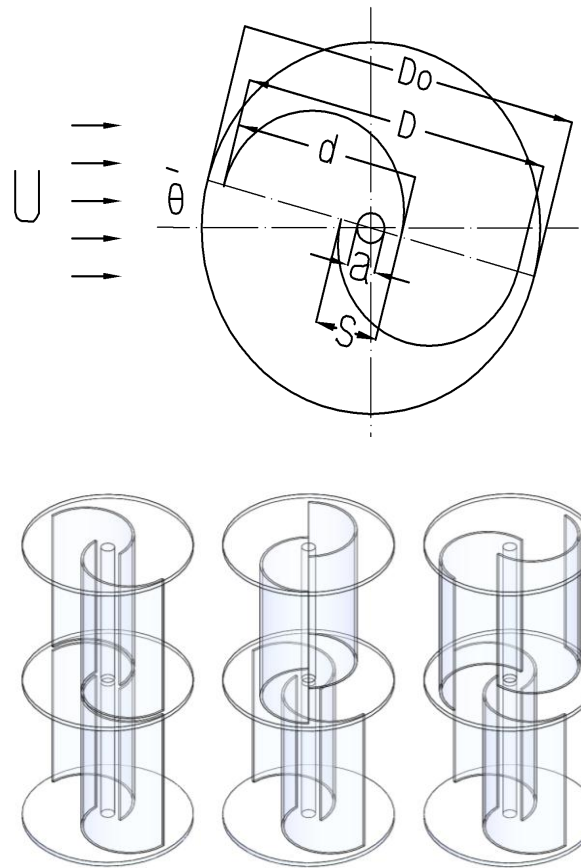


Figure 3.14 The parameters and configuration of the tested two-blade Savonius rotor

The detailed dimensions of different kinds of wind turbines are summarized in Table 3.2. And the abbreviation of the rotor with two blades and three blades is shown in

Table 3.3 and Table 3.4, respectively.

All the parameters of the three-blade rotor are the same as the two-blade rotor, except the numbers of the blade and phase shift angle. For the rotor with three-blade, five kinds of phase-shift angles were tested, they are  $PSA=0^\circ$ ,  $PSA=15^\circ$ ,  $PSA=30^\circ$ ,  $PSA=45^\circ$ , and  $PSA=60^\circ$ .

Real rotors with two and three blades are presented in Figure 3.15. Several 3mm aluminum plates were stacked together and cut by the wire cut machine to fabricate the endplates. There are two or three slots which are 1.2mm in width to fit and fix the blades with 1.1mm thickness. The dimension of the tested rotors with two blades is summarized in Table 3.2.



Figure 3.15 The real rotors with two and three blades

The dimensions of the tested rotors with three blades are almost the same as the rotors with two blades. The difference between rotors with two and three blades is the blade number and the phase shaft angle. According to the definition of the abbreviation, all the abbreviations of the tested rotors are listed in Table 3.3 and

Table 3.4 for two-blade rotor and three-blade rotor.

Table 3.2 Detailed dimensions of the tested rotors with two blades

	<i>Two-blade design 1</i>	<i>Two-blade design 2</i>	<i>Two-blade design 3</i>
<i>Rotor diameter D (m)</i>	0.25	0.25	0.25
<i>Rotor height of one-stage rotor H(m)</i>	0.27	0.27	0.27
<i>Rotor height of two-stage rotor H(m)</i>	0.54	0.54	0.54
<i>Stage height of two-stage rotor H(m)</i>	0.27	0.27	0.27
<i>Gap rate <math>\beta</math></i>	0	0.166	0.333
<i>Overlap of rotor S (m)</i>	0.012	0.034	0.06
<i>Blade diameter d (m)</i>	121	132	145
<i>Phase shift angle PSA (degree)</i>	0,45,90	0,45,90	0,45,90
<i>Swept area of one-stage rotor (m)</i>	0.0675	0.0675	0.0675
<i>Swept area of one-stage rotor (m)</i>	0.135	0.135	0.135
<i>Blockage value of the one-stage rotor</i>	0.0675	0.0675	0.0675
<i>Blockage value of the two-stage rotor</i>	0.135	0.135	0.135
<i>Rotor aspect ratio of the one-stage rotor</i>	2.16	2.16	2.16
<i>Rotor aspect of the two-stage rotor</i>	1.08	1.08	1.08
<i>Stage aspect of the two-stage rotor</i>	1.08	1.08	1.08

Table 3.3 Abbreviations of the rotor with two-blade

	<i>Gap rate <math>\beta=0</math></i>	<i>Gap rate <math>\beta=0.166</math></i>	<i>Gap rate <math>\beta=0.333</math></i>
<i>One-stage rotor</i>	S1 $\beta$ 0	S1 $\beta$ 0.166	S1 $\beta$ 0.333
<i>Two-stage rotor with PSA = 0°</i>	S2 $\beta$ 0 PS0	S2 $\beta$ 0.166 PS0	S2 $\beta$ 0.333 PS0
<i>Two-stage rotor with PSA = 45°</i>	S2 $\beta$ 0 PS45	S2 $\beta$ 0.166 PS45	S2 $\beta$ 0.333 PS45
<i>Two-stage rotor with PSA = 90°</i>	S2 $\beta$ 0 PS90	S2 $\beta$ 0.166 PS90	S2 $\beta$ 0.333 PS90

Table 3.4 Abbreviations of the rotor with three-blade

	<i>Gap rate <math>\beta=0</math></i>	<i>Gap rate <math>\beta=0.166</math></i>	<i>Gap rate <math>\beta=0.333</math></i>
<i>One-stage rotor</i>	S1 $\beta$ 0 BN3	S1 $\beta$ 0.166 BN3	S1 $\beta$ 0.333 BN3
<i>Two-stage rotor with PSA = 0°</i>	S2 $\beta$ 0 PS0 BN3	S2 $\beta$ 0.166 PS0 BN3	S2 $\beta$ 0.333 PS0 BN3
<i>Two-stage rotor with PSA = 15°</i>	S2 $\beta$ 0 PS15 BN3	S2 $\beta$ 0.166 PS15 BN3	S2 $\beta$ 0.333 PS15 BN3
<i>Two-stage rotor with PSA = 30°</i>	S2 $\beta$ 0 PS30 BN3	S2 $\beta$ 0.166 PS30 BN3	S2 $\beta$ 0.333 PS30 BN3
<i>Two-stage rotor with PSA = 45°</i>	S2 $\beta$ 0 PS45 BN3	S2 $\beta$ 0.166 PS45 BN3	S2 $\beta$ 0.333 PS45 BN3
<i>Two-stage rotor with PSA = 60°</i>	S2 $\beta$ 0 PS60 BN3	S2 $\beta$ 0.166 PS60 BN3	S2 $\beta$ 0.333 PS60 BN3

### 3.4.6 Experimental results of the two-blade Savonius rotors

#### 3.4.6.1 Gap rate influence on the CTs and CP of the one-stage two-blade rotor

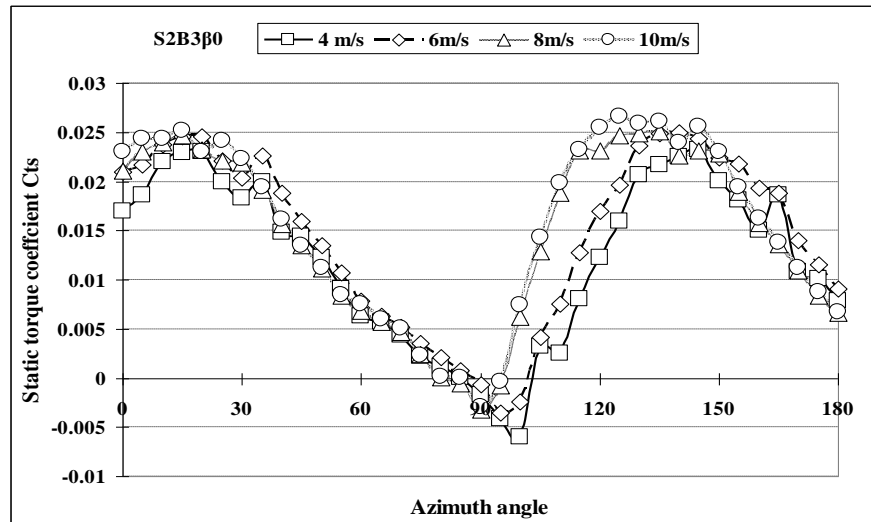


Figure 3.16 The  $C_{ts}$  of the two-stage rotor

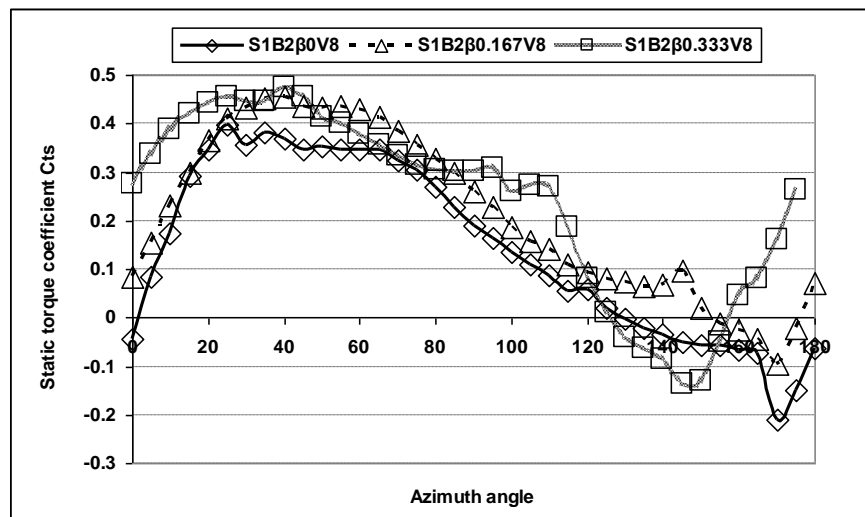


Figure 3.17 The  $C_{ts}$  of one-stage rotor at wind velocity 8m/s

According to previous studies and our experiments, the  $C_{ts}$  should be independent

of the wind speed. Figure 3.16 presents the CTs of  $S2B3\beta0$  at different wind velocities. Through this figure, it is found that CTs curves maintain the similarity tendency at four different wind speeds. The only difference present is in between 90 and 120 degrees of azimuth angle for wind velocities less than 8m/s. When the wind velocity is larger than 8m/s, the difference between CTs curves is not visible. Therefore, the influence of  $\beta$  on the static torque coefficient is investigated at wind velocity of 8m/s.

Figure 3.17 demonstrates that with the increase of  $\beta$ , the value of CTs can be significantly improved in the range of  $0^\circ$  to  $45^\circ$ . The value of CTs increased from -0.05 in the case  $S1\beta0$  to 0.3 in case  $S1\beta0.333$ . The minimum CTs also increased from -0.2 to -0.1. The negative torque coefficient of  $S1\beta0$  ranged from  $125^\circ$  to  $180^\circ$ . The negative CTs of  $S1\beta0.166$  and  $S1\beta0.333$  ranged from  $155^\circ$  to  $175^\circ$  and  $125^\circ$  to  $160^\circ$ , respectively.

The results demonstrate that at least 36% of the range of the negative torque CTs can be reduced by adding overlap between the two blades. The negative CTs region will move to lower azimuth angles by the increasing of  $\beta$ .

It is suggested that  $\beta$  can not only increase the magnitude of the torque coefficient but can also reduce the range of negative torque; This can be explained by the fact that with the increase of  $\beta$ , the amount of the wind flow which passes through the gap is increased. Since wind flow can pass through the gap, it will have the opportunity to act on the concave side of the returning blades and produce effective thrust force.

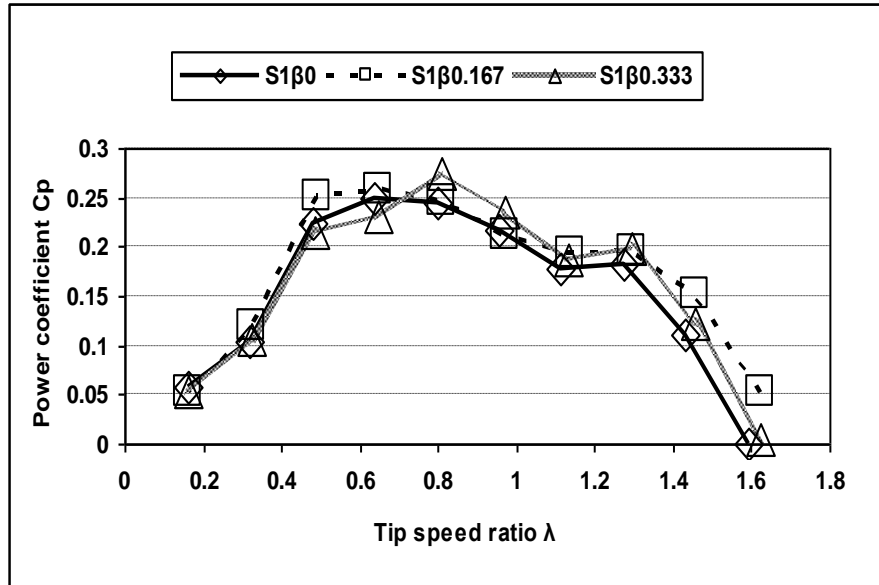


Figure 3.18 The  $C_p$  of the one-stage Savonius rotor at wind velocity 8m/s

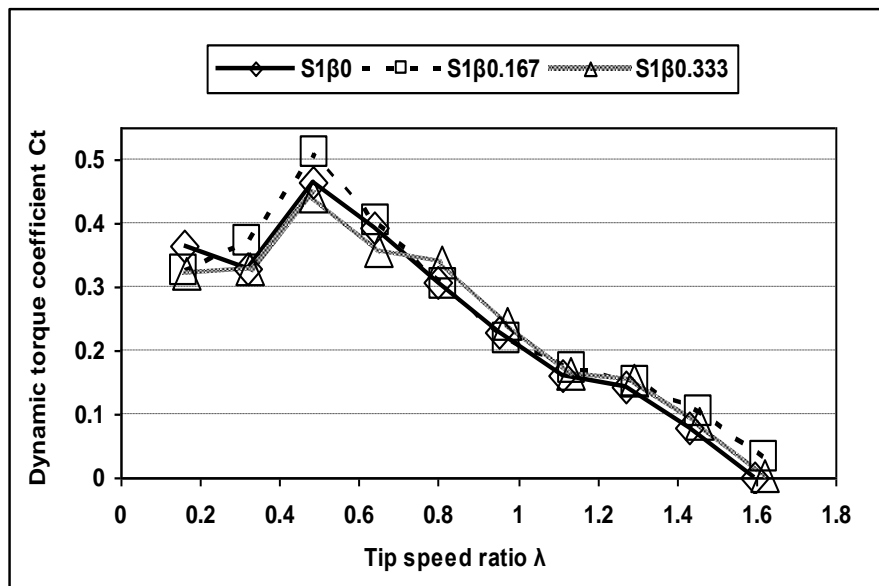


Figure 3.19 The  $C_t$  of the one-stage Savonius rotor at wind velocity 8m/s

The influence of  $\beta$  on the power coefficient of the one-stage rotors working at 8m/s is demonstrated in Figure 3.18. The  $C_p$  of  $S1\beta_{0.166}$  is about 6 percent higher for

most of the  $\lambda$  range as compared with other rotors. The CP of  $S1\beta0$  and  $S1\beta0.333$  gets close in the range of lower  $\lambda$ , while in the higher  $\lambda$  range the CP of  $S1\beta0.333$  is about 7% higher than that of  $S1\beta0$ . In Figure 3.19,  $C_t$  is large in the lower  $\lambda$  range and decreases with the increase of  $\lambda$  at any  $\beta$ . It indicates that  $S1\beta0.166$  can generate more power than other cases since 0.166 is close to the optimum  $\beta$ .

### 3.4.6.2 Gap rate influence on the CTs and CP of the two-stage two-blade rotors

By doubling the stages using the same two single-stage rotors one could expect to keep CTs unchanged. However, the test results illustrated in Figure 3.20 and Figure 3.21 indicate that the CTs value of the one-stage rotor is 25% higher than that of the two-stage rotor in the azimuth angle range of  $0^\circ$  to  $80^\circ$ . But, this static torque difference between one-stage and two-stage rotors will diminish when the azimuth angles are larger than  $80^\circ$  for the cases with  $\beta = 0$  and  $\beta = 0.166$ .

For the case with  $\beta = 0.333$ , the static torque of the one-stage rotor is higher than the two-stage rotor in the azimuth angle range of  $0^\circ$  to  $120^\circ$ . However, the trend is reversed when  $\theta > 120^\circ$ . The difference between the two-stage and single-stage rotor may result from the influence of the central endplate and the higher rotor AR value. The results indicate that the static torque coefficient of the one-stage rotor is higher than the two-stage rotor for most of the azimuth angle range when PSA is zero. Although the CTs value is different between the single-stage and two-stage rotors, the variation of CTs of the two-stage rotors keeps a similar tendency with that of the one-stage rotor. The influence of  $\beta$  on the two-stage rotor with two blades and zero

PSA in Figure 3.23 shows the same effect on the two-stage rotor as for the one-stage rotor.

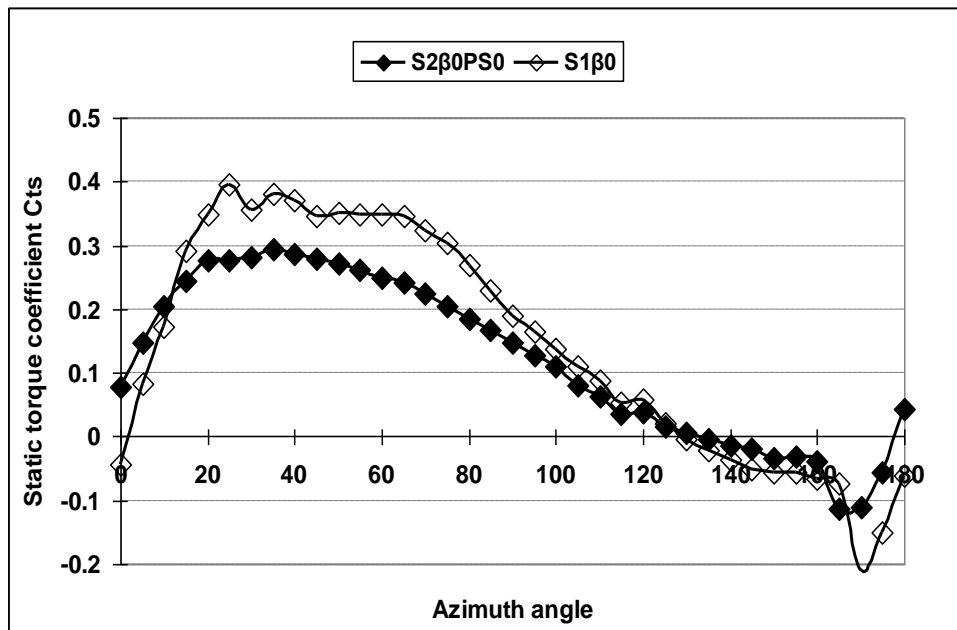


Figure 3.20 The  $C_{ts}$  of the one-stage and two-stage Savonius rotors at 8m/s

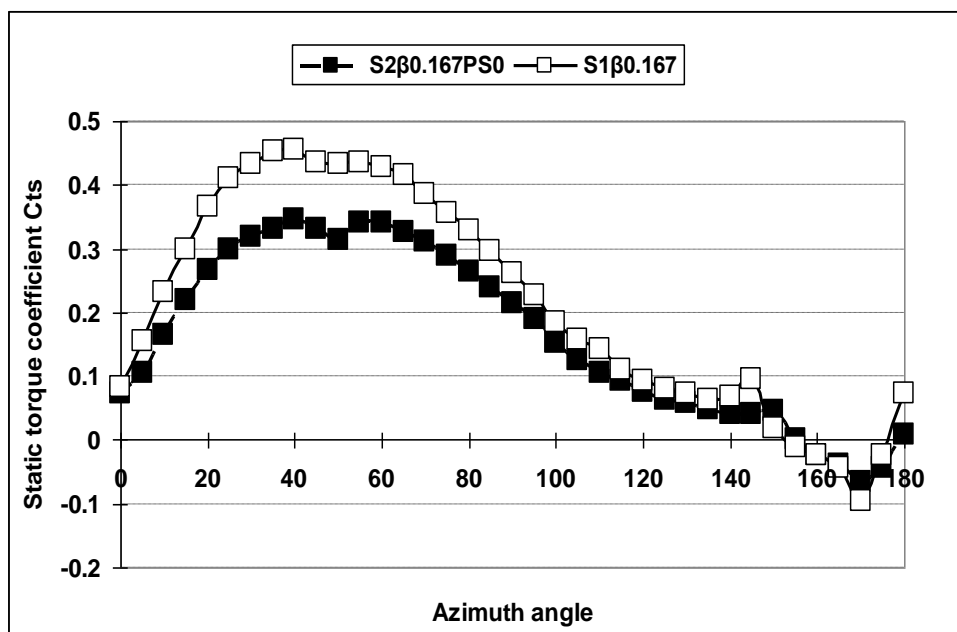


Figure 3.21 The  $C_{ts}$  of the one-stage and two-stage Savonius rotors at 8m/s

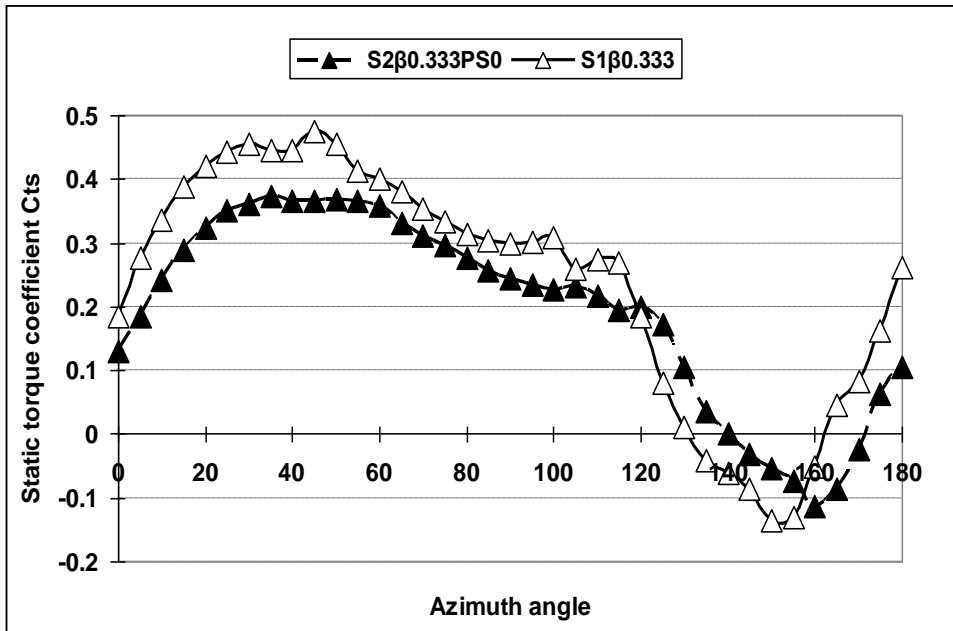


Figure 3.22 The  $C_{ts}$  of the one-stage and two-stage Savonius rotors at 8m/s

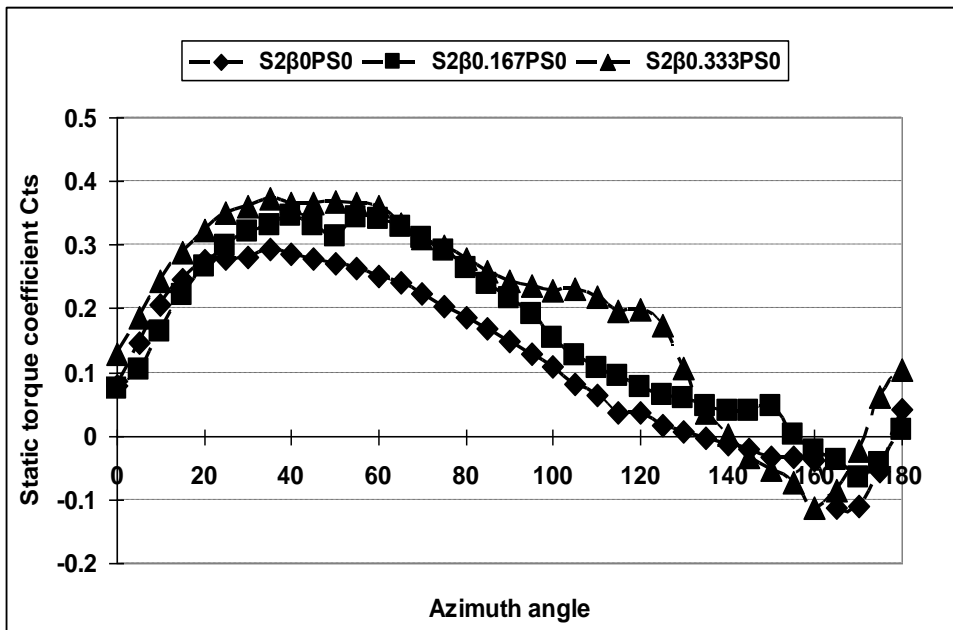


Figure 3.23 The  $C_{ts}$  of the one-stage and two-stage Savonius rotors at 8m/s

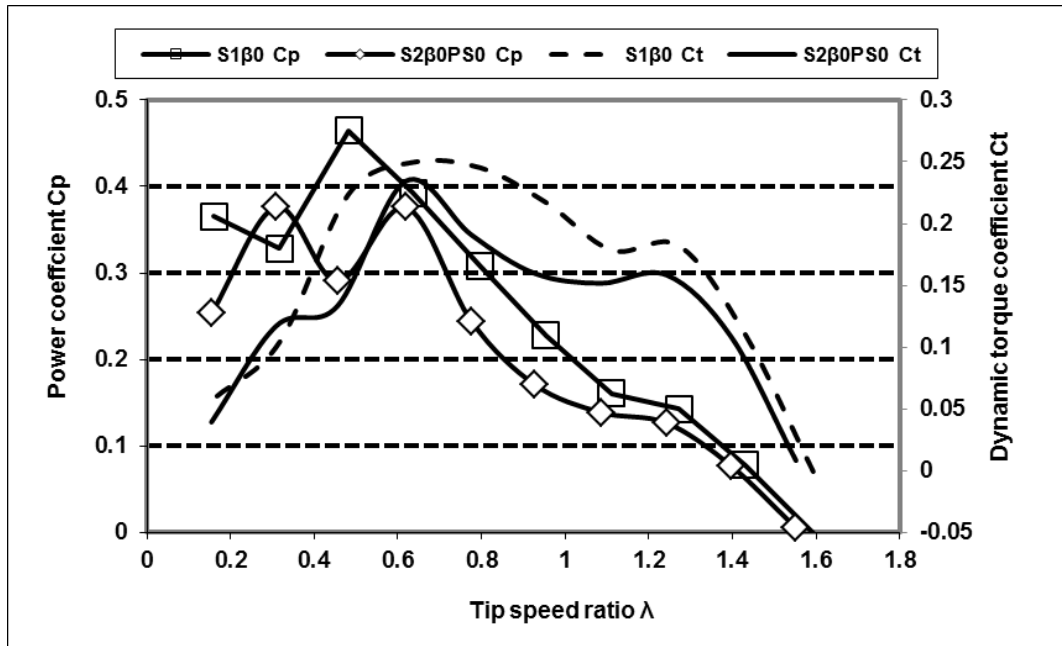


Figure 3.24 The comparisons between one-stage and two-stage rotors for gap rates 0

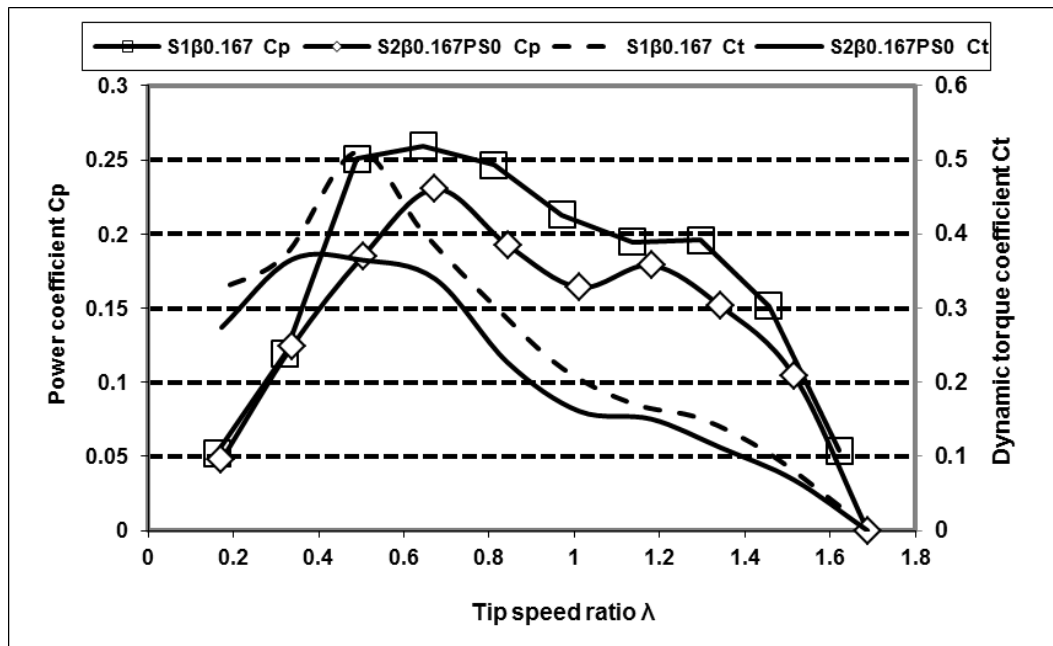


Figure 3.25 The comparisons between one-stage and two-stage rotors for gap rates

0.167

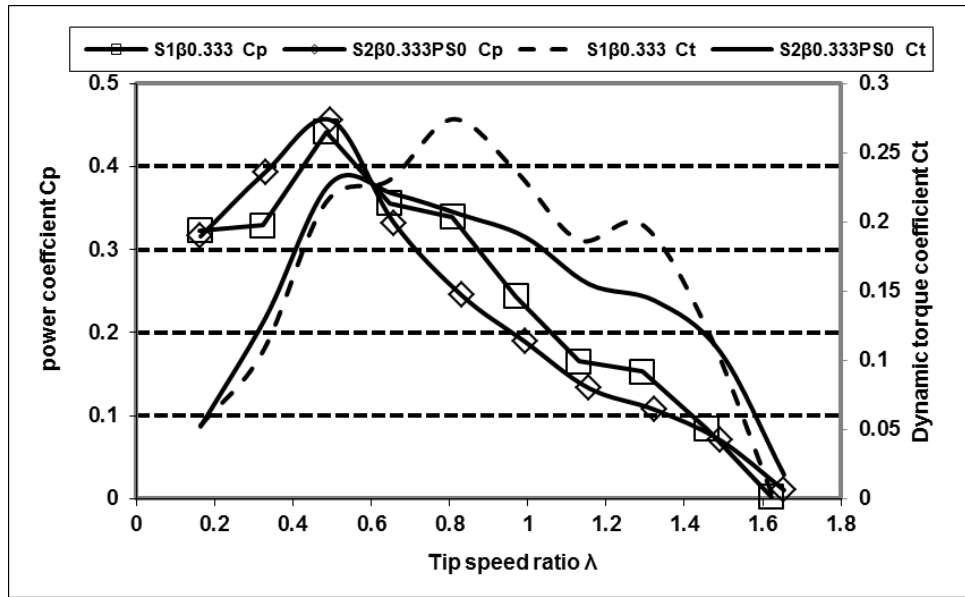


Figure 3.26 The comparisons between one-stage and two-stage rotors for gap rate 0.333

The effect of adding one more stage on the performance is shown in Figure 3.24, Figure 3.25 and Figure 3.26. The CP of the one stage-rotor was about 20% higher than that of the two-stage rotor for all the three different cap rates, especially in the  $\lambda$  range from 0.5 to 1.4. The difference in  $C_t$  between the one-stage and two-stage rotors decreased with the increase of  $\beta$ . So the conclusion of previous research that adding stages degrades the performance is confirmed. One possible explanation for the reduction of the power coefficient is that the flow pattern of the two-stage rotor is different from the single-stage rotor especially at the center of the rotor due to the presence of the center endplate. Another reason is that the rotor aspect ratio of the two-stage rotor is higher than that of the single-stage rotor. It may indicate that CP of the rotor of which are separated into several layers by the semi-circular plates is

likely to decrease.

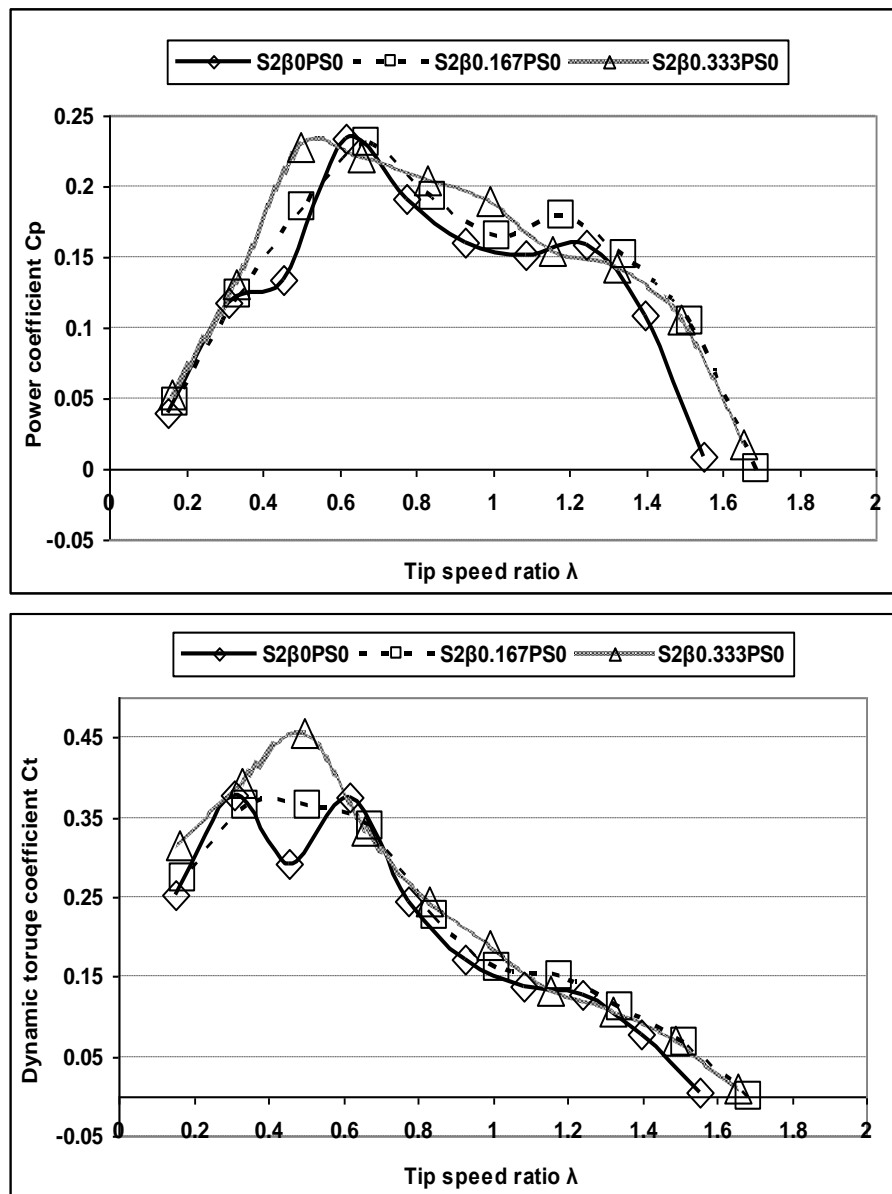


Figure 3.27 The  $C_p$  and  $C_t$  of the two-stage Savonius rotor with  $PSA=0^\circ$

Figure 3.27 shows  $\beta$  influence on the  $C_p$  and  $C_t$  of the two-stage Savonius rotor when  $PSA=0^\circ$  at wind velocity 8m/s. The  $C_p$  curve of  $S2\beta0PS0$  is the lowest compared with that of other cases for most of the  $\lambda$  range. In the range of  $\lambda$  from

0.4 to 1.2, the CP curve of  $S2\beta 0.333PS0$  is the highest among the three cases. The CP curves of  $S2\beta 0.167PS0$  and  $S2\beta 0.333PS0$  are getting close when  $\lambda < 0.4$  and  $\lambda > 1.5$ . This indicates that the maximum power output of the two-stage rotor at  $PSA=0^\circ$  is  $S2\beta 0.333PS0$  when  $\beta$  is 0.333, which is different from corresponding  $\beta$  value for the one-stage rotor.

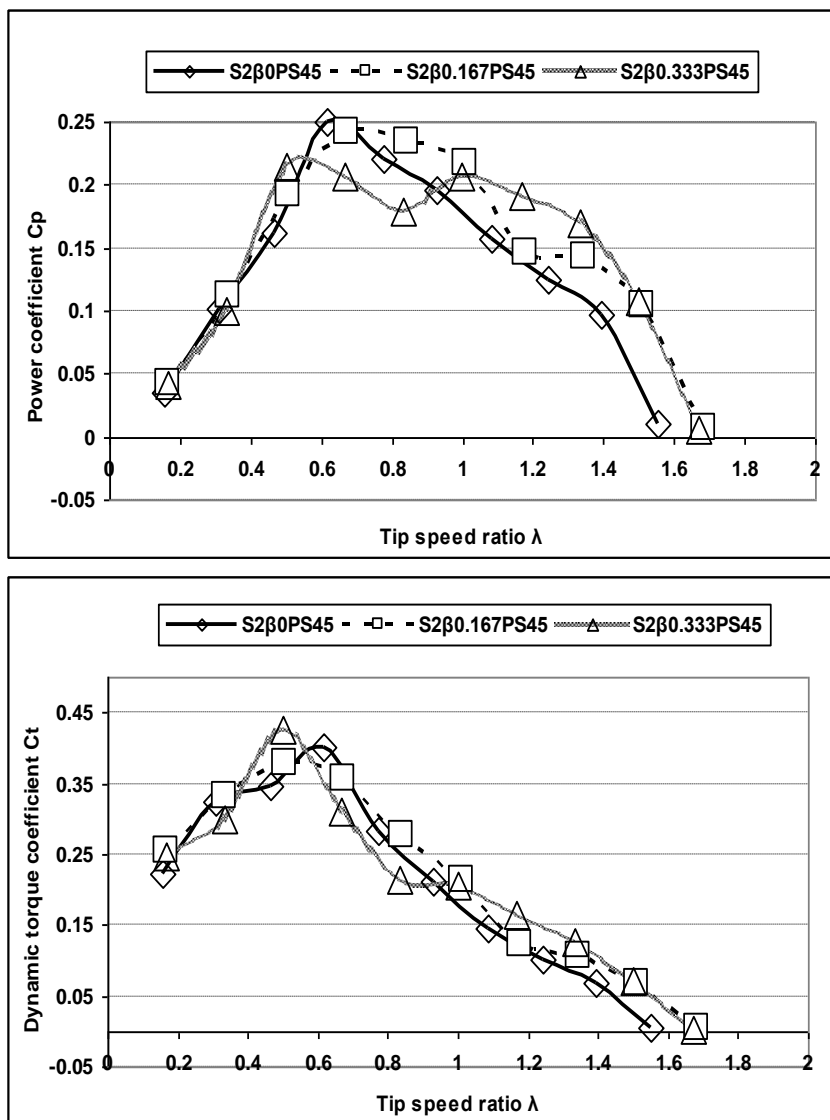


Figure 3.28 The  $C_p$  and  $C_t$  of the two-stage Savonius rotor at  $PSA=45^\circ$

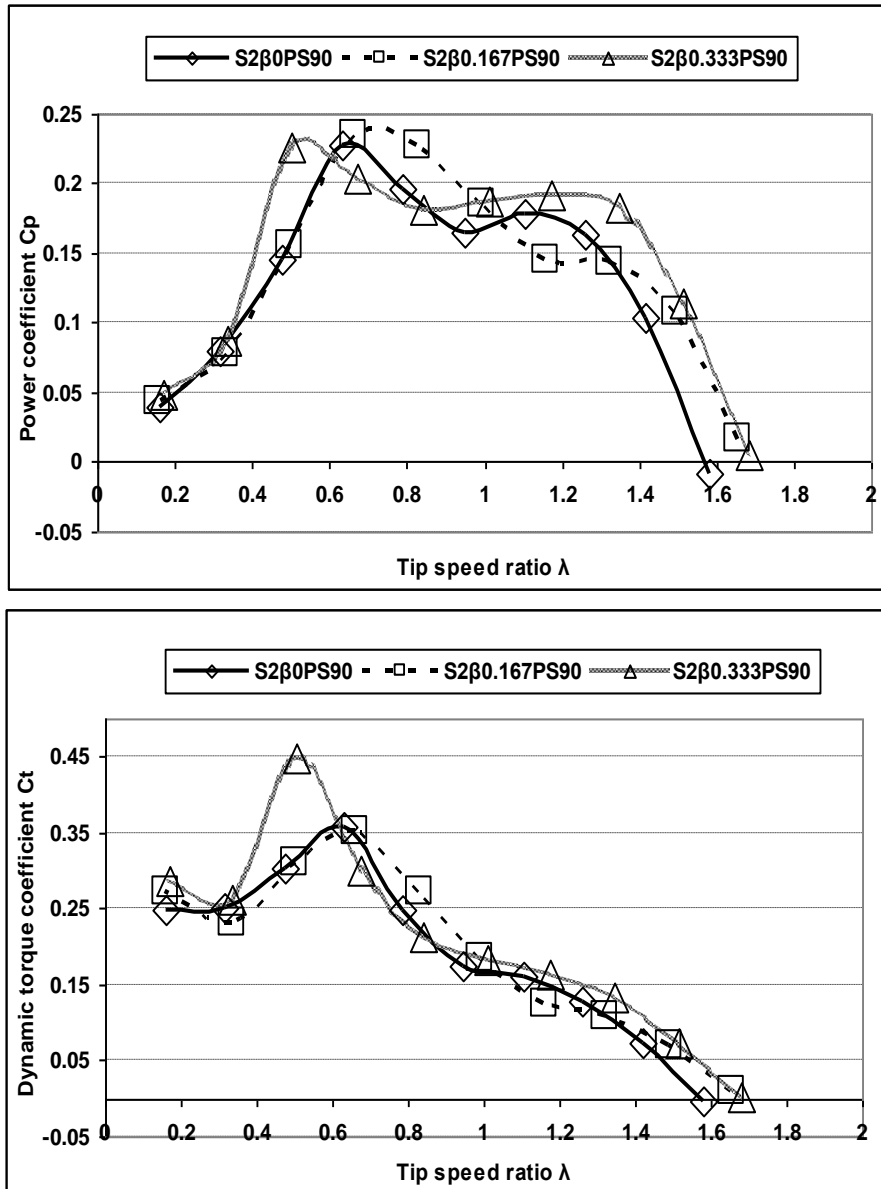


Figure 3.29 The  $C_p$  and  $C_t$  of the two-stage Savonius rotor at  $PSA=90^\circ$

Figure 3.28 demonstrates the gap rate influence on the  $C_p$  and  $C_t$  of the two-stage Savonius rotors whose  $PSA$  is  $45^\circ$  at wind velocity  $8\text{m/s}$ . The  $C_p$  of  $S2\beta0.333PS45$  is higher than that of other configurations for most of the  $\lambda$  range. The  $C_p$  curves of  $S2\beta0.167PS45$  and  $S2\beta0PS45$  give smaller differences when  $\lambda < 0.4$ ; however,

there is a 40% difference between the two configurations when  $\lambda > 0.4$ .

On the contrary, the CP curve of  $S2\beta 0.167PS45$  is better than that of  $S2\beta 0.333PS45$  when  $\lambda < 1.2$ . The  $C_i$  curve of  $S2\beta 0.333PS45$  is slightly better than the  $C_i$  curve of  $S2\beta 0.167PS45$  when  $\lambda > 1.2$ . Figure 3.29 shows similar trend in Figure 3.28. The results suggest that the influence of  $\beta$  on the two-stage rotors at  $PSA=45^\circ$  and  $PSA=90^\circ$  is the same as the influence of  $\beta$  on one-stage rotors.

### **3.4.6.3 Phase-shift influence on the CTs of the two-stage two-blade rotors**

With the increase of PSA, the curves of CTs will become smoother. Figure 3.30 indicates that most of the rotors with PSA can eliminate the range of negative CTs values (except for case  $S2\beta 0PS45$ ) and smooth the curves of CTs of the rotors.

Thus, the rotor with PSA can self-start regardless of wind directions. By increasing  $\beta$ , the azimuth angle range, within which the CTs of the rotor with  $PSA=45^\circ$  is higher than that of the rotor with  $PSA=90^\circ$ , expands from  $90^\circ$  to  $110^\circ$ .

Next in Figure 3.31, the effect of an increased  $\beta$  is shown. The CTs increases with  $\beta$  for fixed PSA. This may be attributed to the fact that the airflow can pass through the gap between the blades and act on the concave side of the returning blades. As a result, the static torque difference between the rotors with  $\beta = 0$  and  $\beta = 0.333$  is significantly larger.

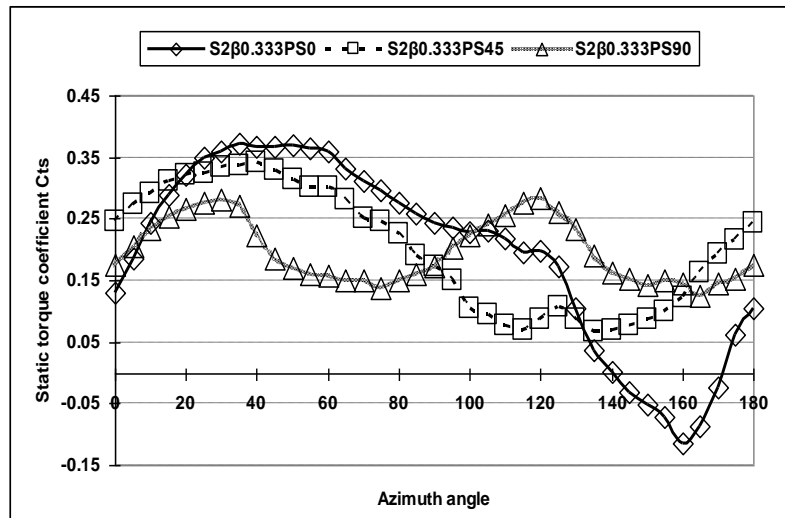
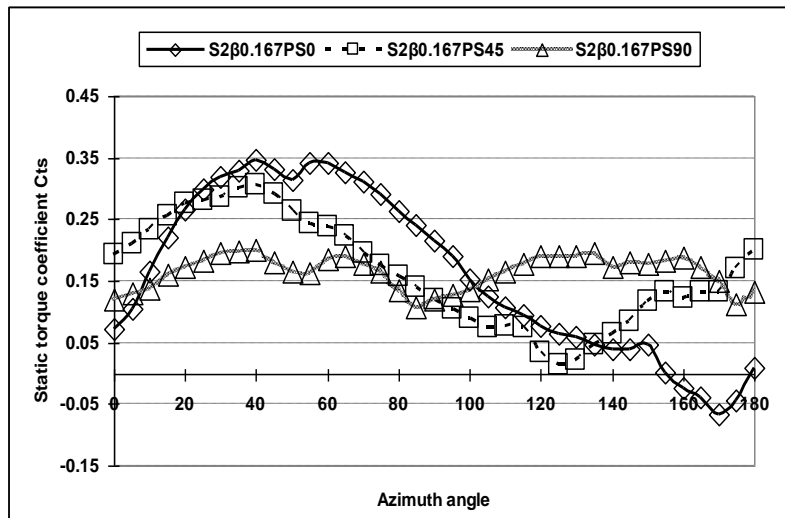
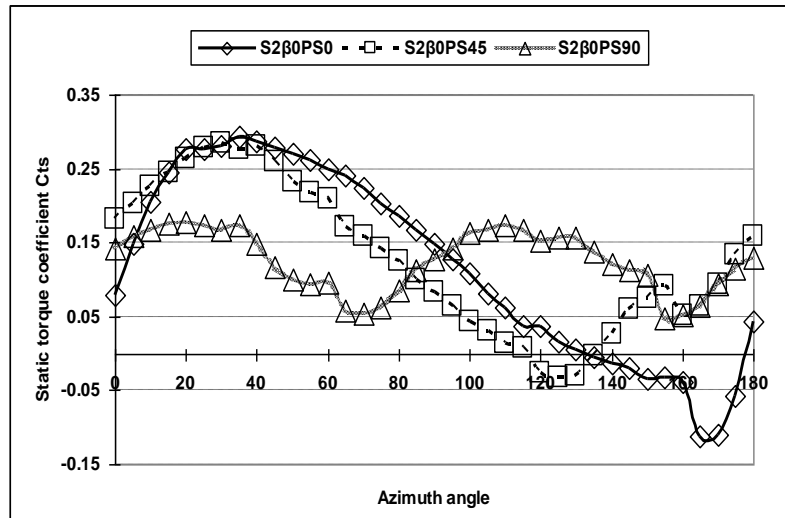


Figure 3.30 The CTs of the two-stage Savonius rotor at wind velocity 8m/s

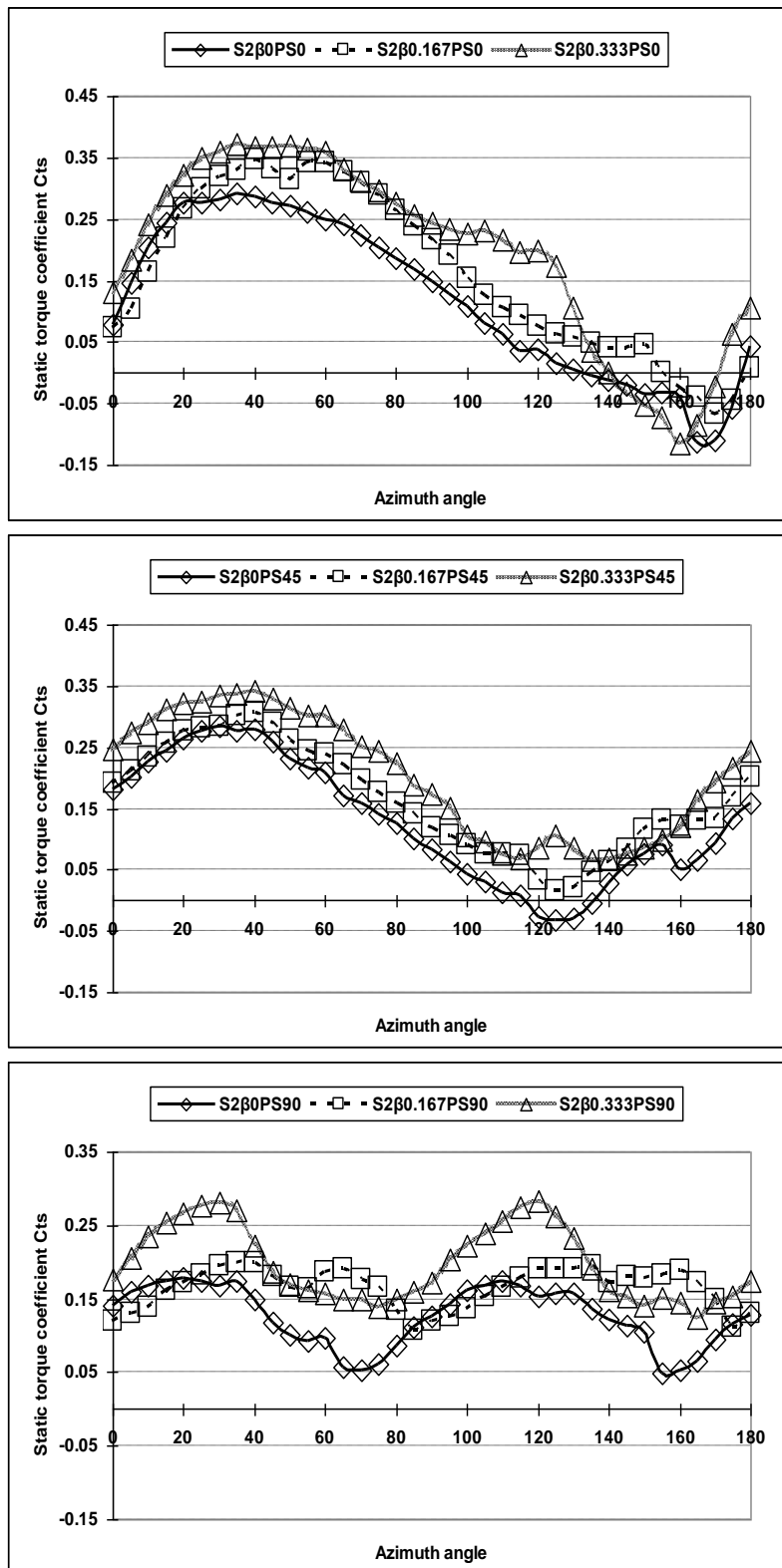


Figure 3.31 The CTs of the two-stage Savonius rotor at wind velocity 8m/s

#### 3.4.6.4 Phase-shift influence on the CP of the two-stage two-blade rotors

In this part, the phase-shift influence on the rotor performance is discussed when the two-stage rotors are tested at wind speed of 8m/s. In Figure 3.32, Figure 3.33 and Figure 3.34, the CP and  $C_t$  for three different phase-shift angles and three the gap rates are compared. In general, the CP curves of the rotors are quite close in  $\lambda$  range from 0.2 to 0.6 and from 1.4 to 1.8. The highest CP difference occurred in  $\lambda$  range from 0.6 to 1.4. Over the range  $0.2 < \lambda < 0.6$ , there are significant differences in  $C_t$  that increased as PSA decreased. Although the difference of the  $C_t$  values was quite big in this region, the difference of the CP values was small due to the lower angular speeds.

Table 3.5 lists the average CTs and CP values of the various two stage rotors in comparison to those of the one-stage rotor. It follows that the average CTs and CP values of the one-stage rotors are greater than those of two-stage rotors. Meanwhile, the maximum CTs and CP difference between the one-stage and two-stage rotors occurs when the  $\beta$  is 0.167. Based on the comparison among the two-stage rotors, the rotor with PSA of  $45^\circ$  can gain the best CTs and CP when the  $\beta = 0$  and  $\beta = 0.167$ . The CP of the rotor decreases as PSA increases for  $\beta = 0.333$ . The best CTs and CP were gained for the rotor with PSA =  $0^\circ$ , which suggests that  $\beta$  influences the best PSA and higher angle of PSA will decrease the values of CTs and CP.

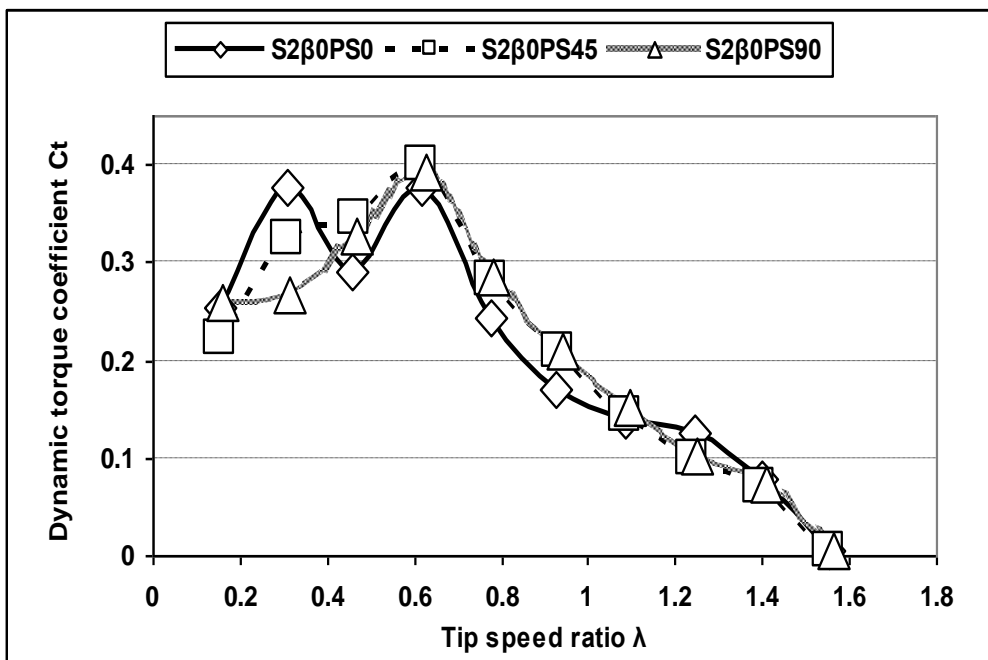
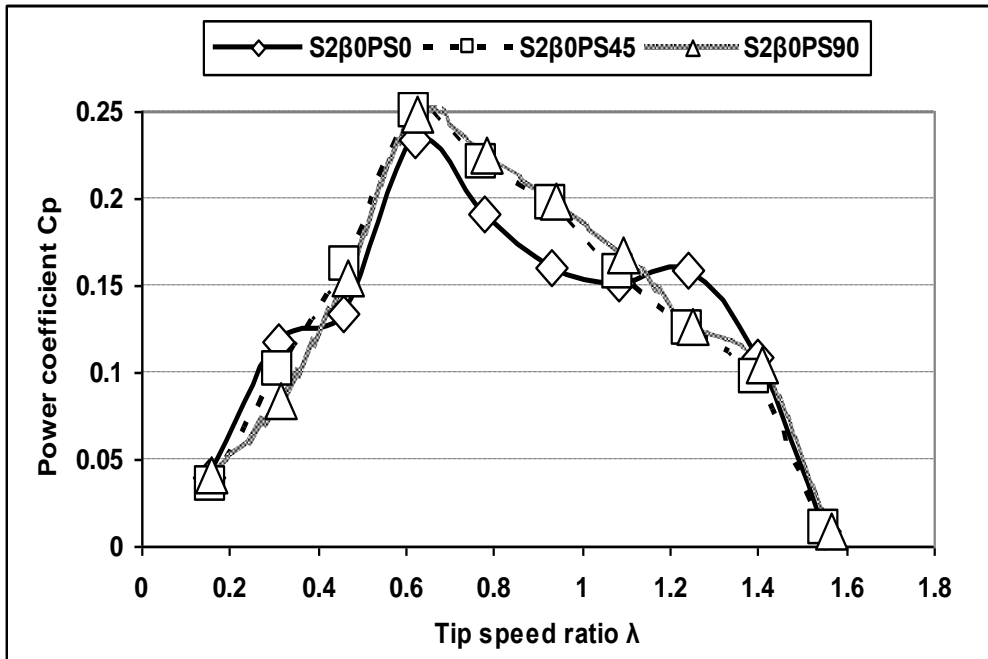


Figure 3.32 The  $C_p$  and  $C_t$  of the two-stage Savonius rotor with  $\beta = 0$

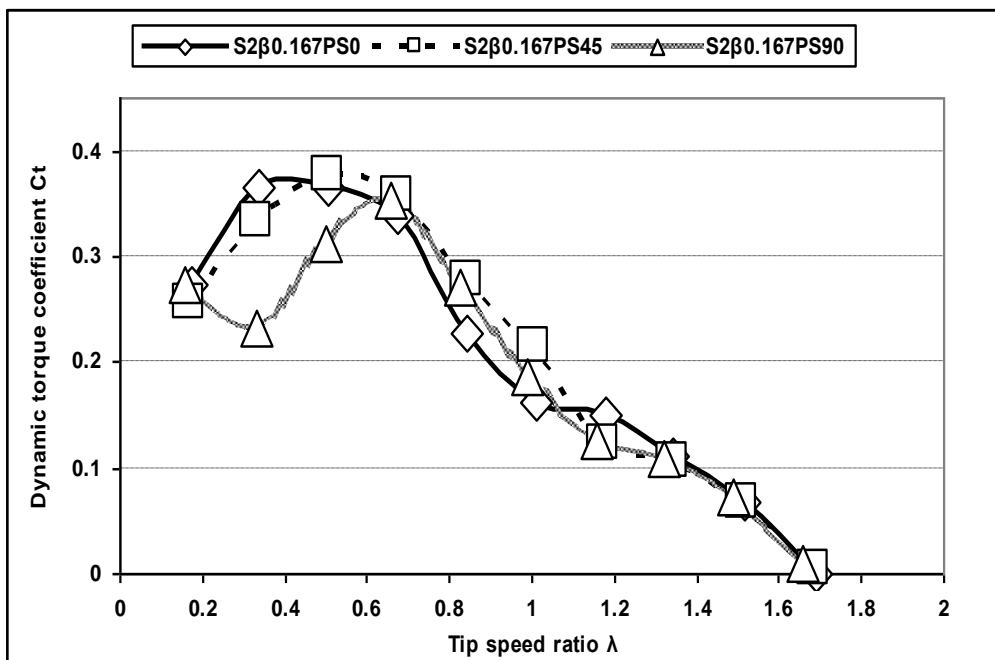
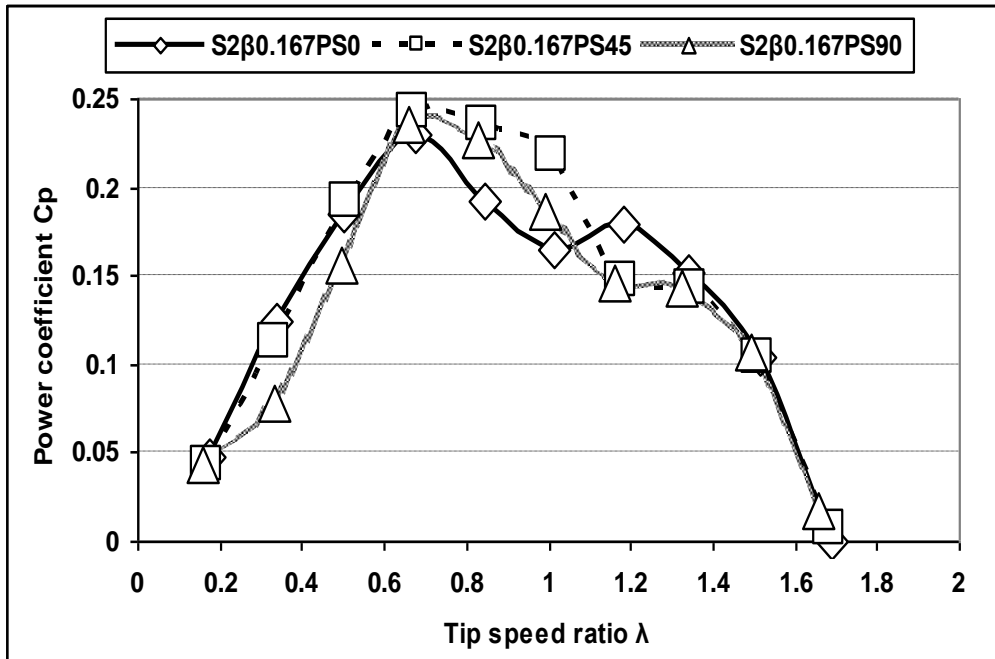


Figure 3.33 The  $C_p$  and  $C_t$  of the two-stage Savonius rotor with  $\beta = 0.167$

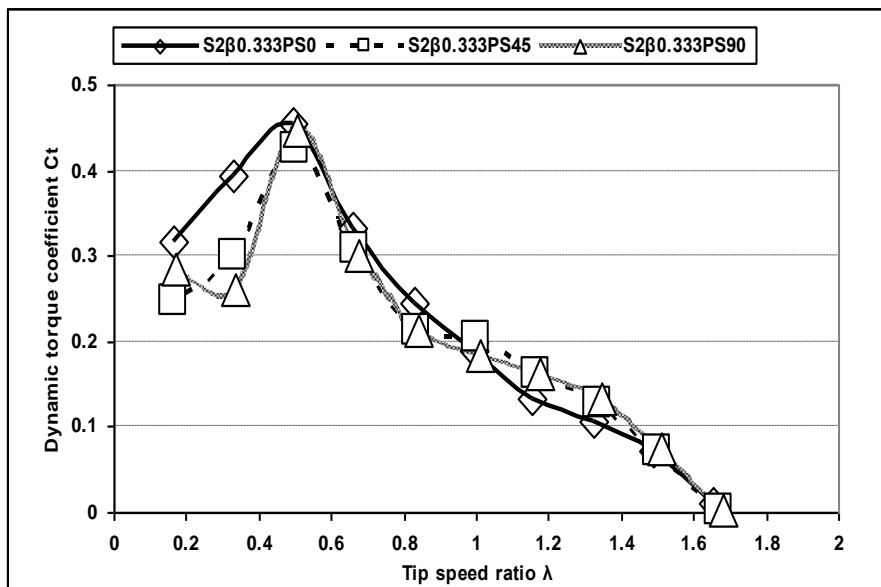
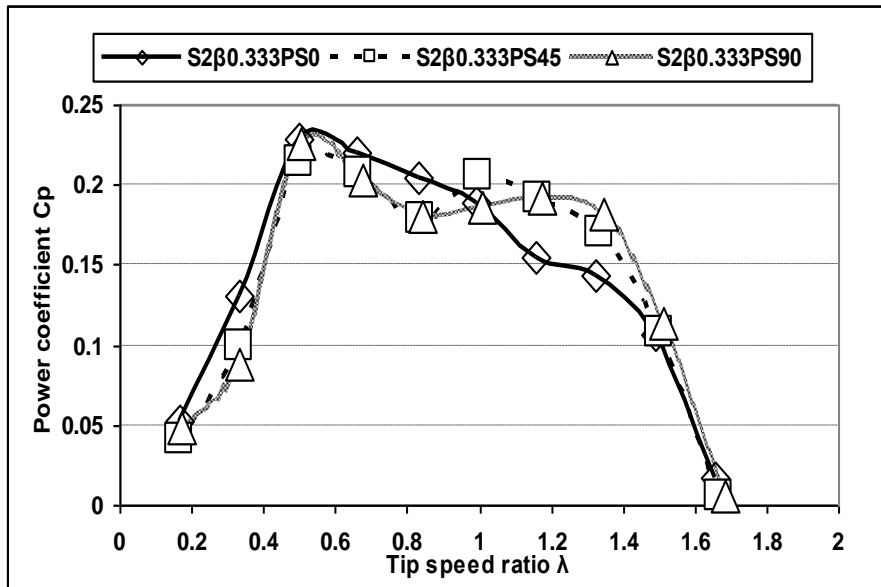


Figure 3.34 The  $C_p$  and  $C_t$  of the two-stage Savonius rotor with  $\beta = 0.333$

Based on the above analysis, in order to gain higher power output, the best single-stage and two-stage rotors were found to be  $S1\beta0.167PS0$  and  $S2\beta0.333PS0$  respectively. However, the static torque of the single-stage rotor is negative at certain azimuth angles presented in Figure 3.17. Smooth variation and high starting torque

are needed when used as an auxiliary starting device or for pumping water device. Thus,  $S2\beta0.333PS90$  seems to be the best option. Although the differences in CP of two-stage rotors are small, the averaged CP does vary with respect to  $\beta$  and PSA. Targeting higher power output and accepted starting capability,  $S2\beta0.167PS45$  appears to be the suitable rotor for standing alone system.

Table 3.5 The average  $C_{ts}$  and  $C_p$  of the two-stage Savonius rotor

	$\beta = 0$		$\beta = 0.167$		$\beta = 0.333$	
	Av. $C_{ts}$	Av. $C_p$	Av. $C_{ts}$	Av. $C_p$	Av. $C_{ts}$	Av. $C_p$
<b>SI</b>	0.243924	0.16263	0.259206	0.173742	0.246683	0.156925
<b>S2 PSA 0</b>	0.20586	0.130165	0.206253	0.137851	0.225355	0.144827
<b>S2 PSA 45</b>	0.207023	0.131907	0.212035	0.144528	0.206575	0.142472
<b>S2 PSA 90</b>	0.193656	0.129185	0.194496	0.134074	0.206419	0.142693

### 3.4.7 Experimental results of the three-blade Savonius rotors

#### 3.4.7.1 Gap rate influence on the performance of one-stage three-blade rotors

The effect of the gap rate on the CTs is presented in Figure 3.35. For the rotor with zero gap rate, there is a very narrow range of azimuth angle where the static torque coefficient is negative. This range is highlighted by the blue ellipse. And there are two ridges of the CTs. The maximum and minimum CTs are about 0.085 and 0.012, respectively. When the gap rate is nonzero, the negative CTs vanishes. Moreover, the

maximum and minimum CTs were raised dramatically. The maximum and minimum CTs are about 0.15 and 0.04, respectively. It should be pointed that there are three ridges on CTs curves. And one of the ridges is significantly higher than the others. This ridge is caused by the nonzero gap rate. The reason for this ridge is the same as that of the one-stage two-blade rotors. Generally speaking, the CTs increases as the gap rate increases. And the CTs curves of the one-stage three-blade rotors are generally higher than the CTs curves of the one-stage two-blade rotors. Thus, starting ability of the one-stage three-blade rotors surpasses that of the one-stage two-blade rotors.

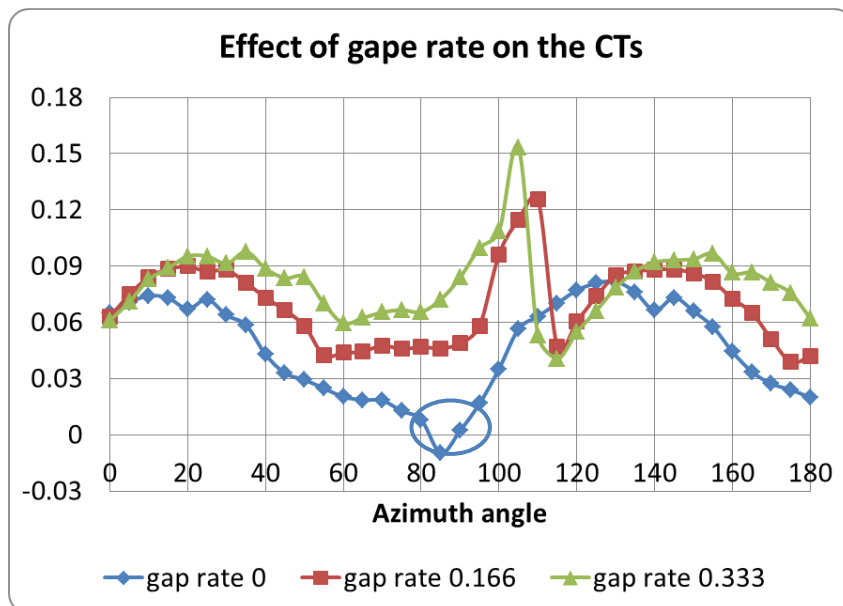


Figure 3.35 The static torque coefficient of one-stage three-blade rotors

The power coefficient of the one-stage three-blade rotors is compared to three different gap rates at three different velocities of the wind in Figure 3.36. As a whole, the power curves of rotor with 0.1667 gap rate surpassed all the tested one-stage

three-blade rotors, especially at wind velocities of 6m/s and 10m/s. The power curve of the rotor with a zero gap rate is similar to that of the rotor with a 0.333 gap rate mostly. The discrepancy is mainly located in the TSR range from 0.5 to 0.7. Thus, the effect of the gap rate on the CTs of the one-stage three-blade rotor is similar to that of the gap rate on CTs of the one-stage two-blade rotor.

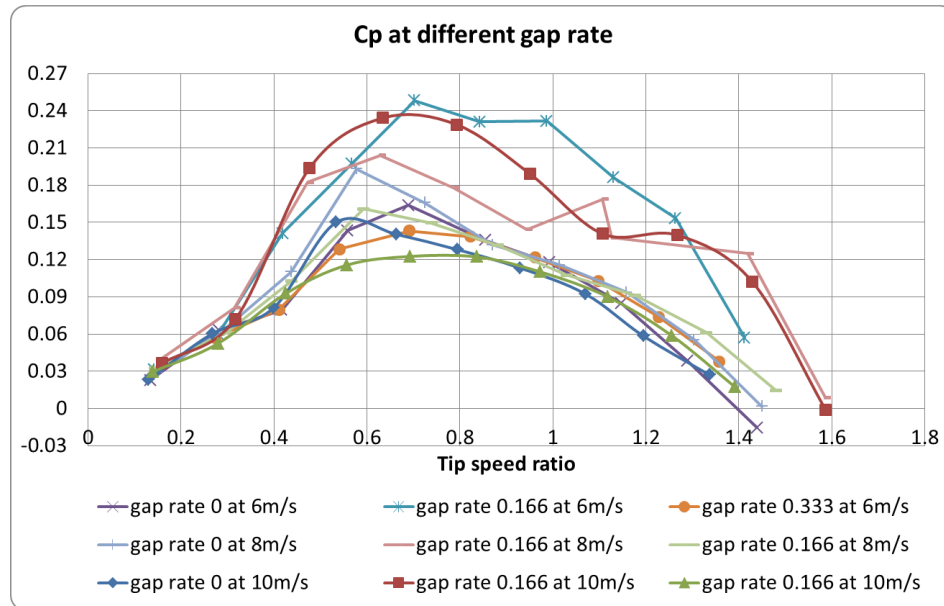


Figure 3.36 The power coefficient of one-stage three-blade rotors

### 3.4.7.2 Influence of gap rate on performance of the two-stage three-blade rotors

The influence of the gap rate on the power coefficient is presented in Figure 3.37, Figure 3.38, Figure 3.39, Figure 3.40 and Figure 3.41 based on different values of PSA. It is found that the power coefficient of the rotor with 0.16 gap rate is, in general, higher than that of the rotors with 0 gap rate and 0.333 gap rate for any PSA. And this difference is significant at 6m/s. With the increase of the wind speed, the difference will be reduced slightly. The reason for this may be that the flow passing

through the gap between two blades will be reduced due to the higher rotational speed at higher wind speed. And the impact of the gap rate will become smaller. In addition, the performance of the rotor with the 0 gap rate is lowest. This has been proved by most researchers. However, the power coefficient of the two-stage three-blade rotor with 0.333 gap rate is higher than that of the two-stage three-blade rotor with 0 gap rate. This is not the same as the conclusion gained in the one-stage three-blade rotor. The power coefficient of the two-stage three-blade rotor is higher than that of the one-stage two-blade rotor. Another influence of the gap rate is the range of the tip speed ratio. This impact is not very clear at the 6m/s wind speed. However, it is fairly obvious that the rotors with higher power coefficient have a wider range of tip speed ratio. With the PSA increase, the effect of the gap rate is not changed for the three-blade rotors.

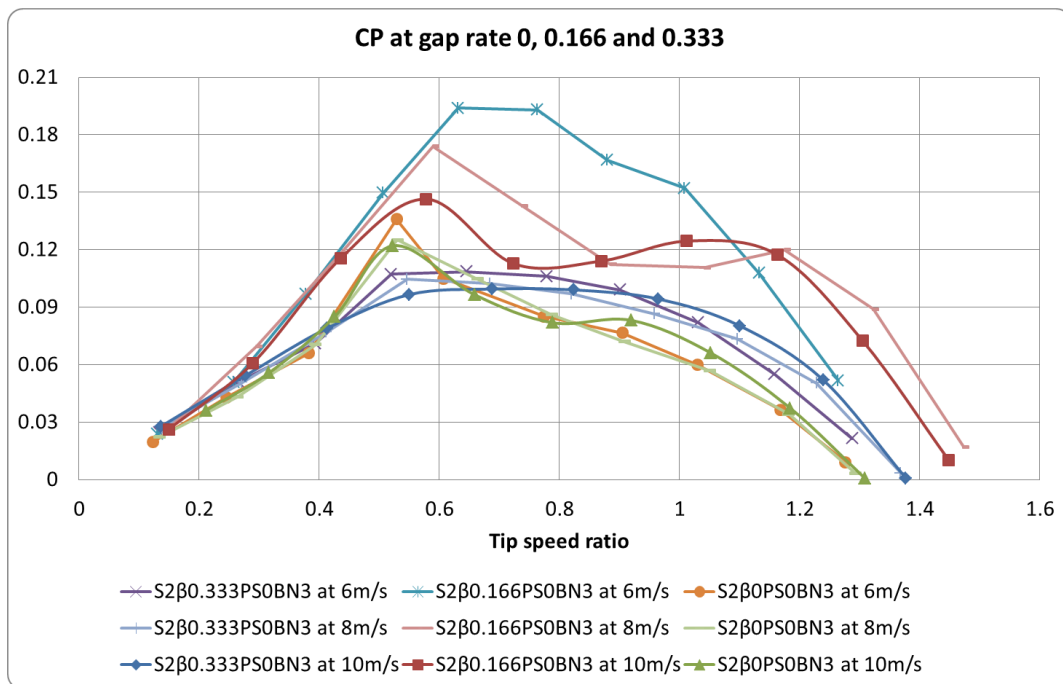


Figure 3.37 The effect of gap rate on CP at PSA=0

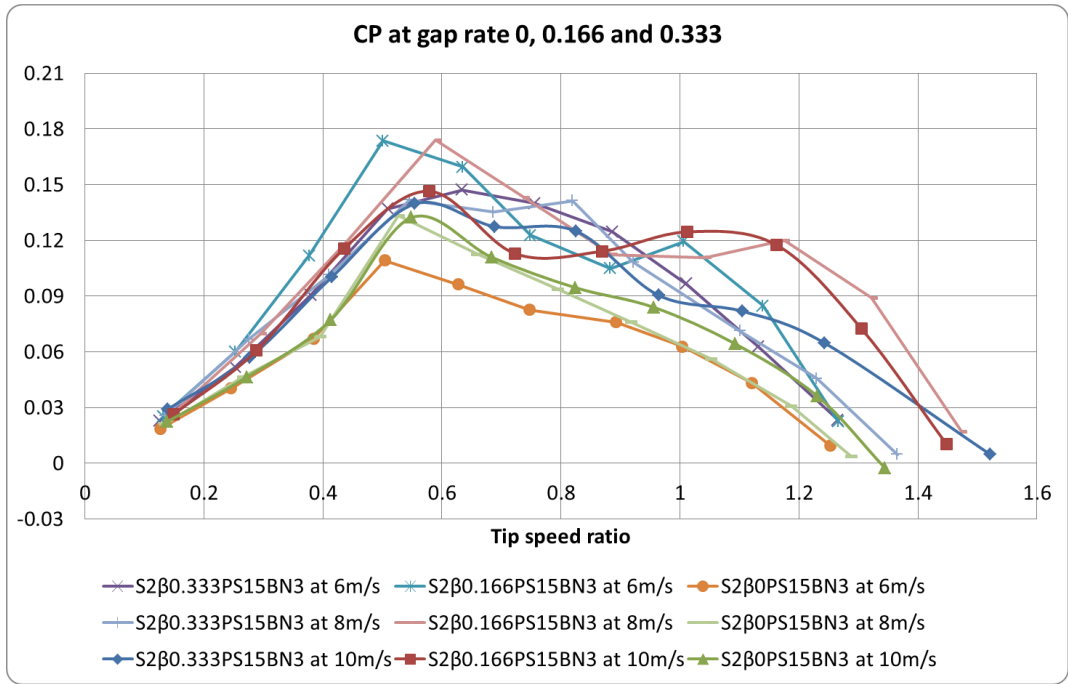


Figure 3.38 The effect of gap rate on CP at PSA=15

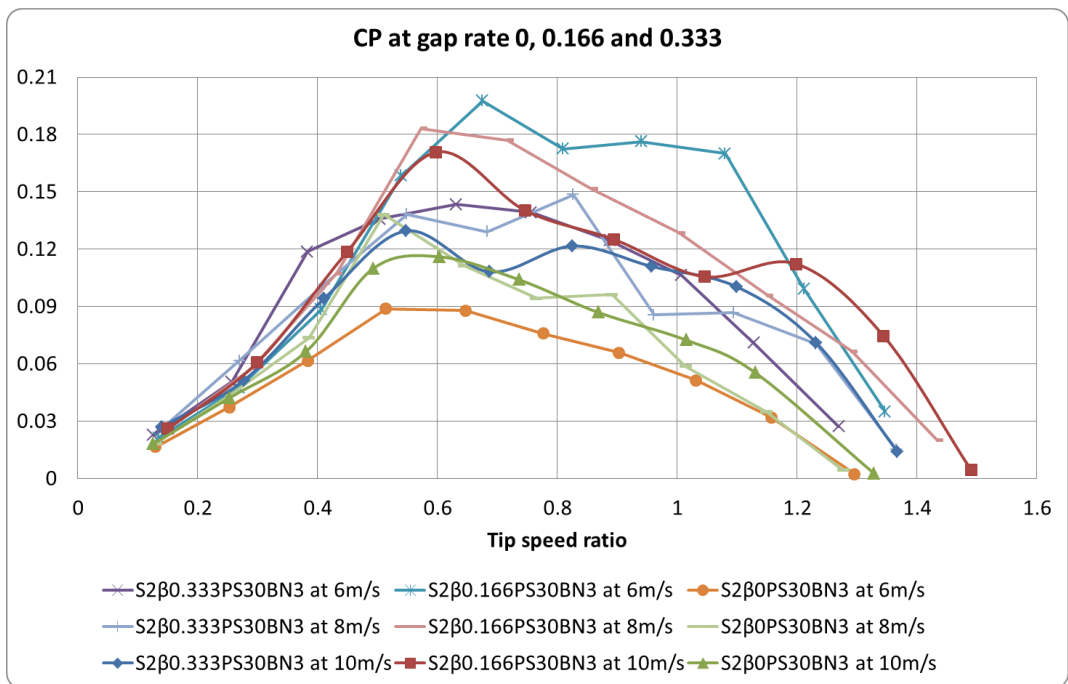


Figure 3.39 The effect of gap rate on CP at PSA=30

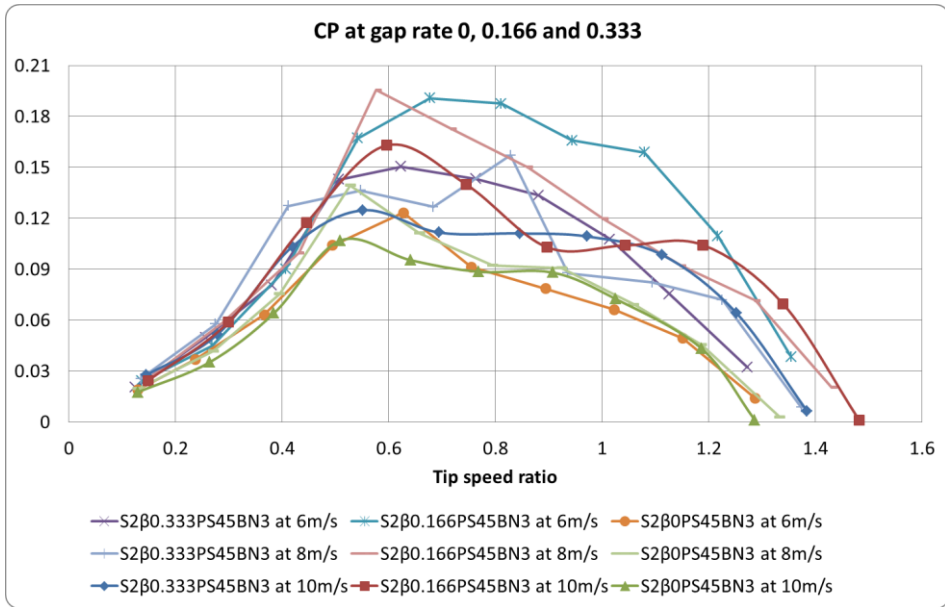


Figure 3.40 The effect of gap rate on CP at PSA=45

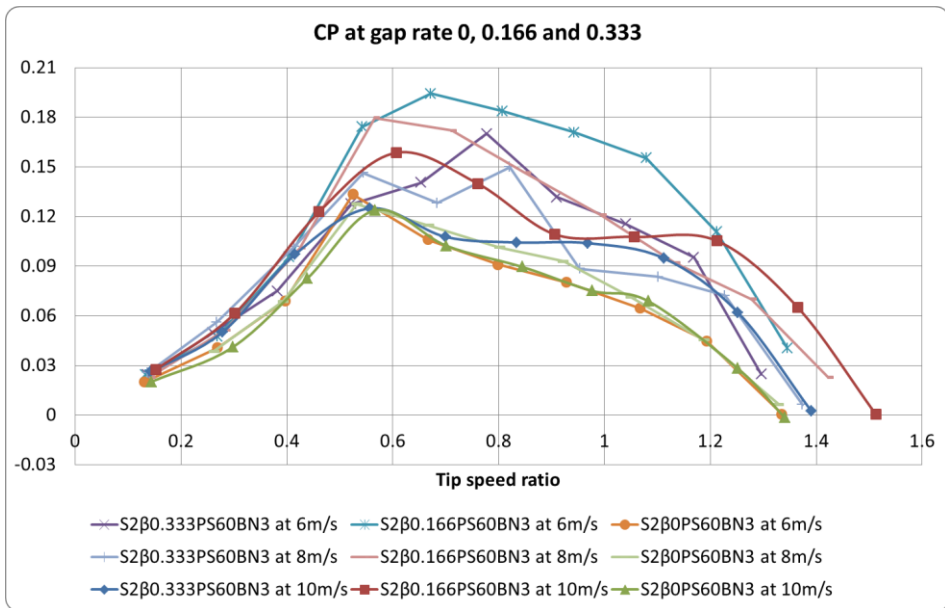


Figure 3.41 The effect of gap rate on CP at PSA=60

### 3.4.7.3 Influence of gap rate on the CTs of the two-stage three-blade rotors

As discussed in the previous section, the CTs of the one-stage three-blade rotor are increased with the increase of the gap rate. Therefore, the CTs of the one-stage three-blade rotor are smoothed as the increase of the PSA shown in Figure 3.42, Figure 3.43 and Figure 3.44. The varied range of the CTs of the rotor is 0.3, 0.27 and 0.21 for the gap rate is 0, 0.1667 and 0.333, respectively. The varied range of the CTs is also narrowed as the increase of the PSA due to the superimposed effect. Thus, two-stage three-blade rotors with nonzero gap rate and 60 degrees of PSA have a best good starting ability.

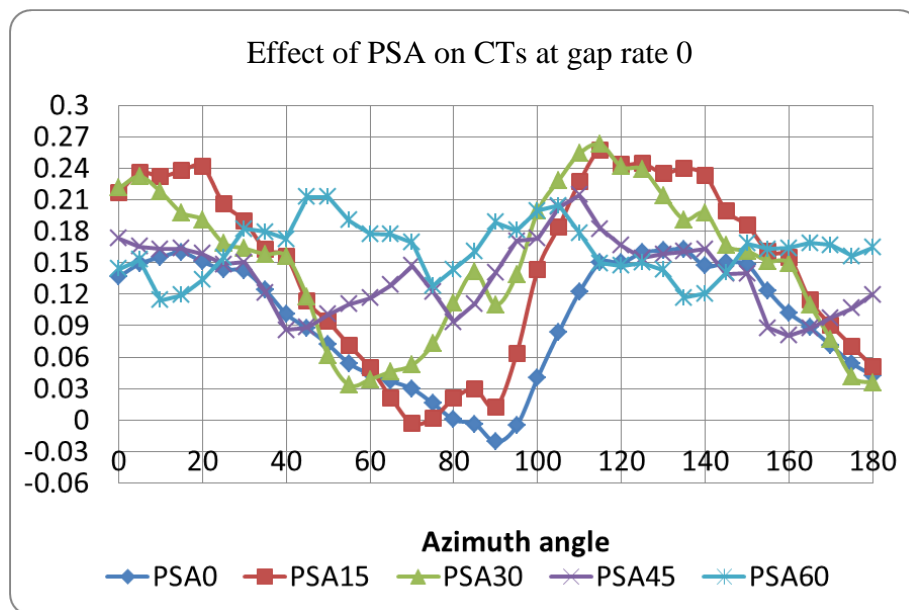


Figure 3.42 The effect of gap rate and PSA on CTs at 8m/s

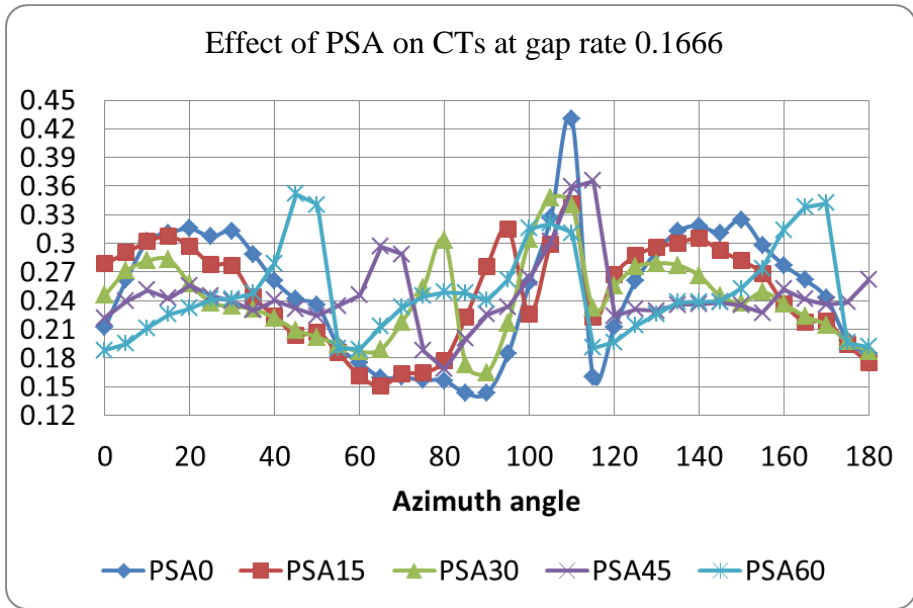


Figure 3.43 The effect of gap rate and PSA on CTs at 8m/s

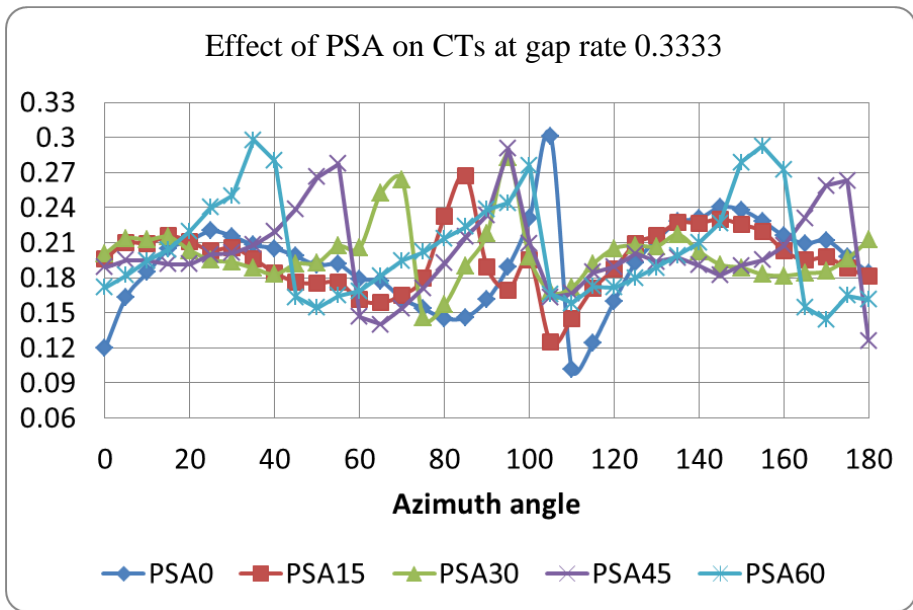


Figure 3.44 The effect of gap rate and PSA on CTs at 8m/s

#### **3.4.7.4 Phase-shift influence on CP of the two-stage three-blade rotors**

The effect of the PSA on the CP is presented in Figure 3.45, Figure 3.46 and Figure 3.47, for different gap rates. The maximum and minimum power curves are different for different gap rate. At a wind velocity 6m/s, the lowest power curve is a rotor with PSA=30 degree for gap rate 0. The highest power curve is a rotor with PSA 45 degree for 0 gap rate. The lowest power curve is a rotor with PSA 15 degree for a 0.166 gap rate. The highest power curve is a rotor with PSA 30 degree for a 0.166 gap rate. The lowest power curve is a rotor with PSA=0 degree a 0.333 gap rate. The highest power curve is a rotor with PSA 60 degree for 0.333 cap rate.

At wind velocity 8m/s, the lowest power curve is a rotor with PSA=0 degree with a 0 gap rate. The highest power curve is a rotor with PSA=60 degree with a 0 gap rate. The lowest power curve is a rotor with PSA=0 degree with a 0.166 gap rate. The highest power curve is a rotor with PSA=30 degree with a 0.166 gap rate. The lowest power curve is a rotor with PSA=0 degree and 0.333 gap rate. The highest power curve is a rotor with PSA=60 degree with a 0.333 gap rate.

At the wind velocity of 10m/s, the lowest power curve is a rotor with PSA=45 degree with a 0 gap rate. The lowest power curve is a rotor with PSA=0 degree with a 0.166 gap rate. The lowest power curve is a rotor with PSA=0 degree with a 0.333 gap rate. The highest power curve is not very clear for three kinds of gap rates. From the statement above, it is found that the power coefficient will generally increase with the effect of PSA although the increase value is not very large.

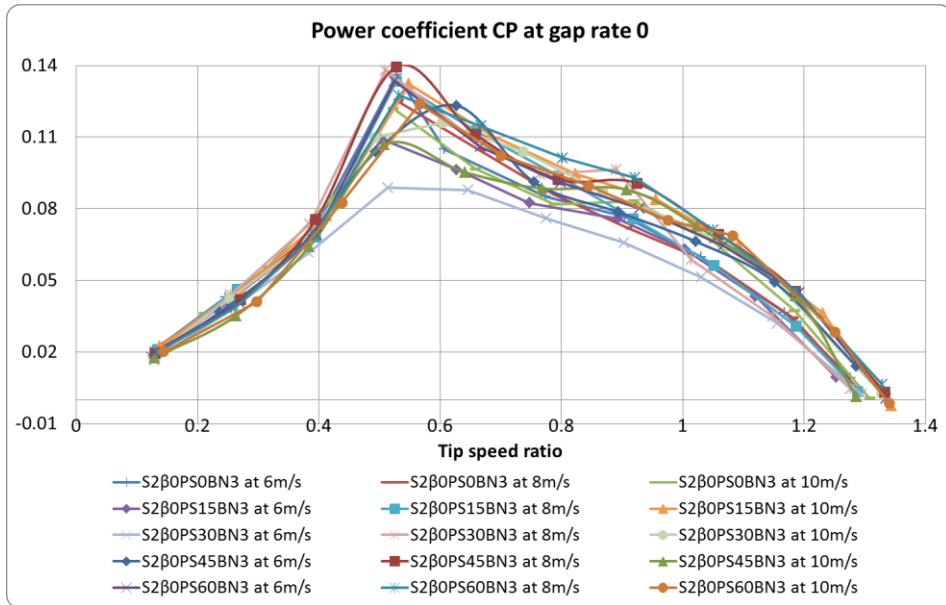


Figure 3.45 The effect of phase-shift angle at gap rate is 0

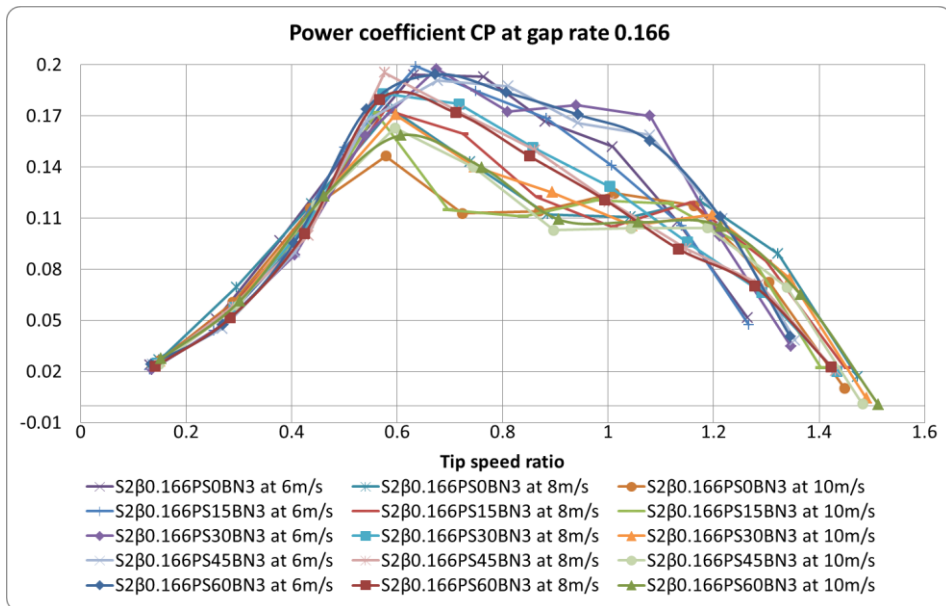


Figure 3.46 The effect of phase-shift angle at gap rate is 0.166

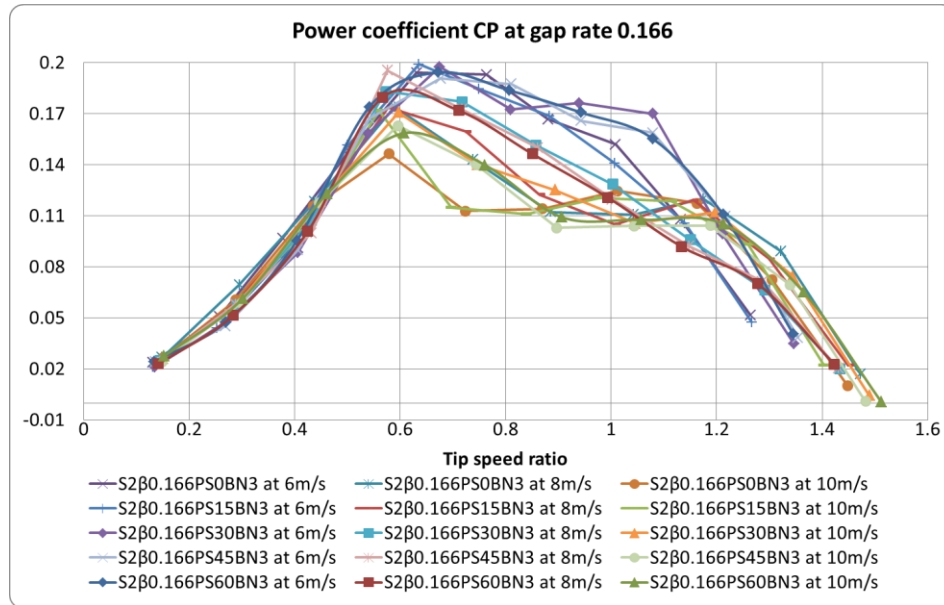


Figure 3.47 The effect of phase-shift angle at gap rate is 0.333

### 3.5 Summary

In this chapter, two-stage rotors with two-blade and three-blades are investigated through the wind tunnel test. The effects of the three design parameters on the CTs and CP are also studied. And the one-stage Savonius rotors are compared with two-stage rotors. The main conclusions are summarized below:

- a) For the two-stage Savonius rotors with two-blade, the highest and smoothest CTs curve is the rotor with 0.333 gap rate and 90 degree of PSA. Thus, this Savonius rotor is the best device for the starting assistants of the Darrieus rotor among two-stage rotors with two-blade. However, the CP of this Savonius rotor is not the highest among the two-stage rotor with two-blade. It is also found that the CTs curve of the two-stage Savonius rotor with two-

blade will become smoother with the increase of the PSA. The small variation of the CTs curve will make the Darrieus rotor start easily.

- b) For the two-stage Savonius rotors with three-blade, the highest and smoothest CTs curve is the Savonius rotor with 0.333 gap rate and 60 degree of PSA. The CTs of this two-stage Savonius rotor with three-blade is even higher than that of the best two-stage Savonius rotor with two-blade. From the improvement of the starting ability of the Darrieus rotor, this two-stage Savonius rotor with three-blade is recommended as the starting assistant of the Darrieus rotor. The effect of the PSA on the CTs variation of the two-stage Savonius rotor with three-blades is the same as that of the two-stage Savonius rotor with two-blades
- c) The wind tunnel tests also showed that the CP of two-stage Savonius rotor is generally lower than that of the one-stage Savonius rotor whatever the blade number of the Savonius rotor is two or three.
- d) A remarkable finding is that the CTs value of one-stage Savonius rotor with three blades in the entire azimuth angle is positive. That means one-stage Savonius rotor with three-blade can also be used as the starting assistance of the Darrieus rotor.

# **CHAPTER 4 THE CFD SIMULATION PROCESSES AND STRATEGIES OF DARRIEUS ROTOR**

## **4.1 Introduction**

The traditional method (two-stage Savonius rotor) to improve the starting ability of lift-type VAWTs has been studied in Chapter 3.

In Chapter 5 and Chapter 6, another two methods which improve the starting ability of the Darrieus rotor are investigated through CFD simulation. The CFD simulation will also be used to improve the CP of the Darrieus rotor will be discussed in Chapter 7.

Hence, it is very important to address the processes, strategies and reliability of the CFD simulation for the design of the Darrieus rotor. In this chapter, CFD simulation processes and strategies are discussed to find the right CFD simulation process and strategies for different research topics of the Darrieus rotor.

## **4.2 CFD simulation processes for the Darrieus rotor**

In the literature review, the methods to predict the performance of the lift-type Darrieus rotor are summarized. And the CFD method based on the incompressible Navier-Stokes equations was adopted to investigate the performance of the lift-type Darrieus. The reasons for the adoption of this CFD method are stated as follows:

The methods based on the Momentum theory such as the Multiple or Double-Multiple streamtube model not only suffer convergence problems but also are invalid for a rotor with high solid or working low high tip speed ratios. And these methods cannot present the dynamic effects and flow field of the Darrieus rotors.

The panel and vortex methods are mainly based on the potential flow theory. Although the effect of viscosity and boundary separation models can be introduced into the panel and vortex methods, these models are mainly empirical models.

Thus, more and more researchers have applied the CFD method to predict the performance of the Darrieus rotor, especially with the rapid development of computer. The common CFD process includes three parts. They are pre-procedure, simulation procedure and post-procedure as presented in Figure 4.1.

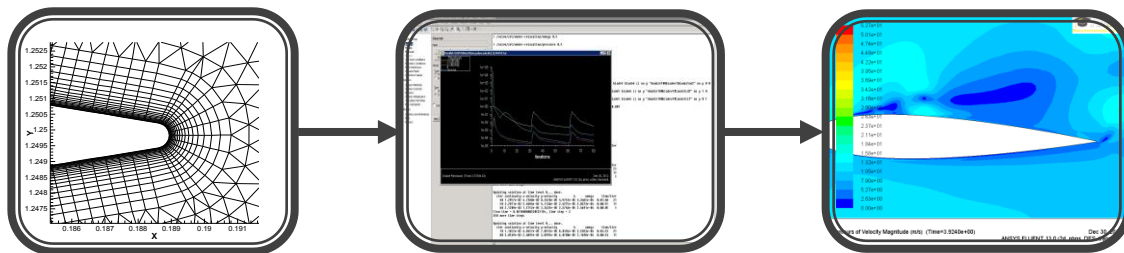


Figure 4.1 The three steps of common CFD simulation process of VAWTs

The pre-procedure is to create the flow domain and generate the mesh for the flow domain. The simulation procedure includes the input of the boundary conditions, selection of the simulation strategy and output of the simulation results. The post-procedure is to analyze the output of the flow properties or flow field. And the common CFD design process of VAWTs is to repeat these three procedures

according to the analysis results.

The greatest disadvantage of the common CFD process is that users need to modify the geometry, generate the mesh, select the setting of simulation and analyze the results manually when the design parameters are changed. For this reason, an automatic CFD analysis process is developed based on the system command function of the MATLAB program. This automatic CFD analysis process is presented in Figure 4.2.

The MATLAB program arranges sequence of the automatic CFD analysis process. A lot of functions (Banks et al. 2007) and mathematical tools (Sobieczky 1998, Kulfan 2008) have been established to describe the geometry of the airfoils with the development of the aviation and the turbo machinery industry.

By using these functions and tools, the section of the airfoils can be generated through the code of the MATLAB program to create several .dat files of the airfoil. These .dat files are imported into the meshing program to prepare the geometry of the models. At the same time, a journal file which controls the meshing strategy will be created to execute the meshing procedure in batch. Thus, there are two files needed to be prepared when the meshing procedure is conducted.

The execution of the meshing procedure will produce a file whose postfix is mesh. This file will import into the simulation program. MATLAB program will create the journal file of the simulation procedure. The file generated by the meshing procedure and the journal file of the simulation were imported into the simulation program to execute the simulation procedure in batch.

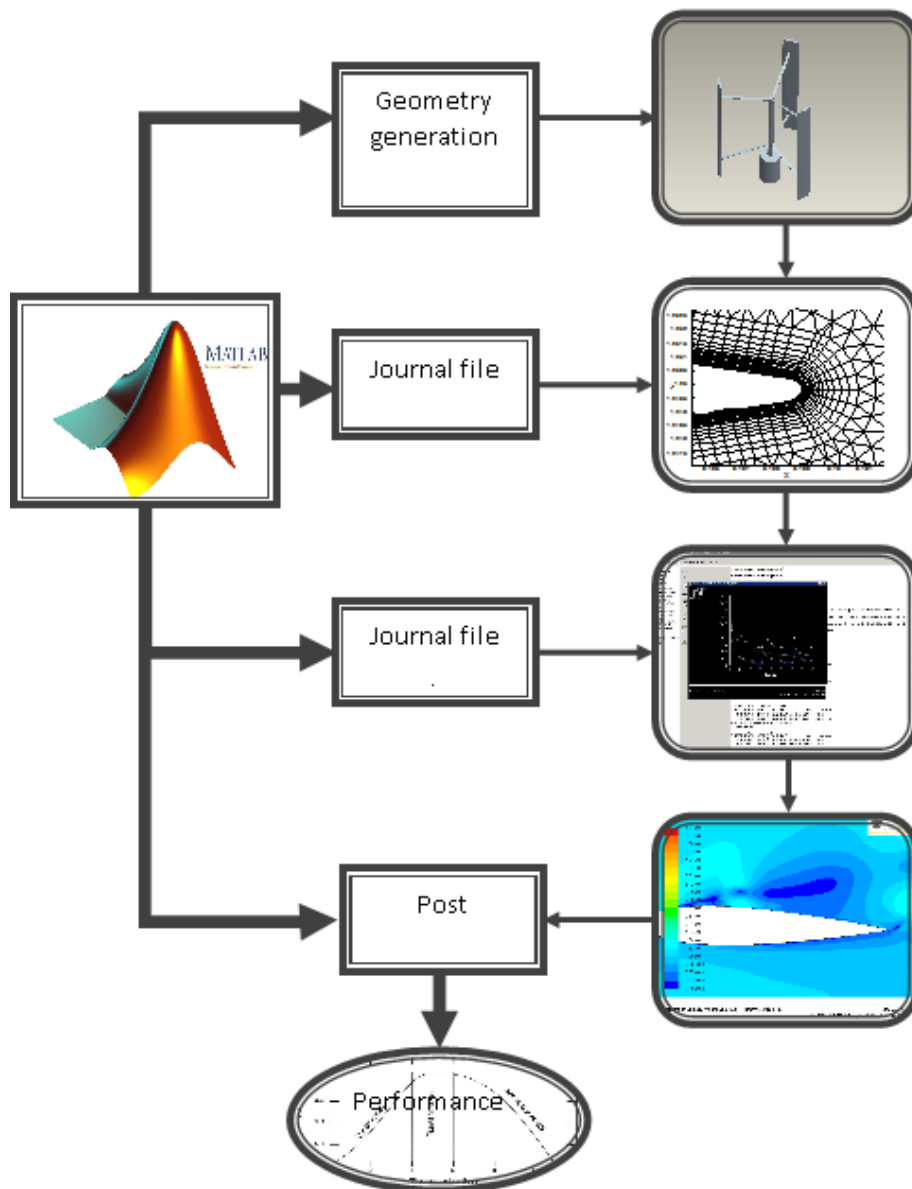


Figure 4.2 An automatic CFD analysis process

After the simulation, a monitoring file will be created to report the flow properties. This monitoring file will be read into the MATLAB program to get the performance of the design models. At this point, a complete automatic CFD analysis process is finished. If the design parameters of the airfoils are changed, the users only need to input the parameters of the airfoils to the MATLAB program. Then, the MATLAB

program will repeat the above procedures automatically. This automatic CFD analysis process not only replaces the manual operation, but also lays the foundation of the parameter optimization process.

This parametric optimization process is presented in Figure 4.3 and includes five parts. They are the initial case, the automatic CFD analysis, the optimization algorithm, the new case and final case. In the initial case, the parameter of the models is set randomly. Then, the automatic CFD analysis module will conduct the simulation of the initial models. After that, the optimization algorithm will generate new case based on some of approach of selection. And the new case will be simulated repeatedly till the final case meets the design aims. The core parts of this parametric optimization process are the automatic CFD analysis and the optimization algorithm. The optimization algorithm can be the one dimensional liner algorithms, orthogonal algorithms, evolutionary algorithms and so on. The aim of all optimization algorithms is to find the best element in the entire defined domain.

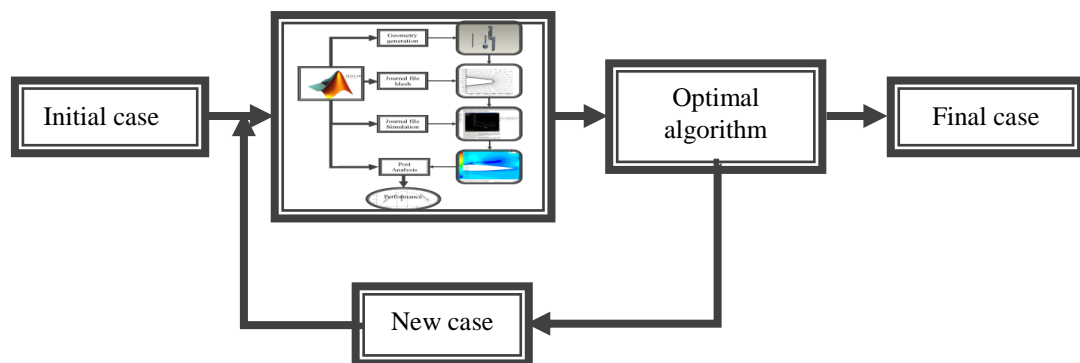


Figure 4.3 The parametric optimization CFD process

In this thesis, the common CFD analysis method is used for the rotors with an

opening (Chapter 5) and two sets of blades (Chapter 6) due to the fact that those rotors have relatively complicated geometry to parameterize the design elements. And the automatic CFD analysis process will be used for the one dimensional liner and orthogonal analysis to establish a novel airfoil optimal design process in Chapter 7. And the parametric optimization process will be conducted in the future works.

### 4.3 Computational domain

A two-dimensional computational domain is built to evaluate the effect of different CFD strategies and to validate the simulation results finally. This 2D computational domain is presented in including a clear mesh view around the airfoil surface.

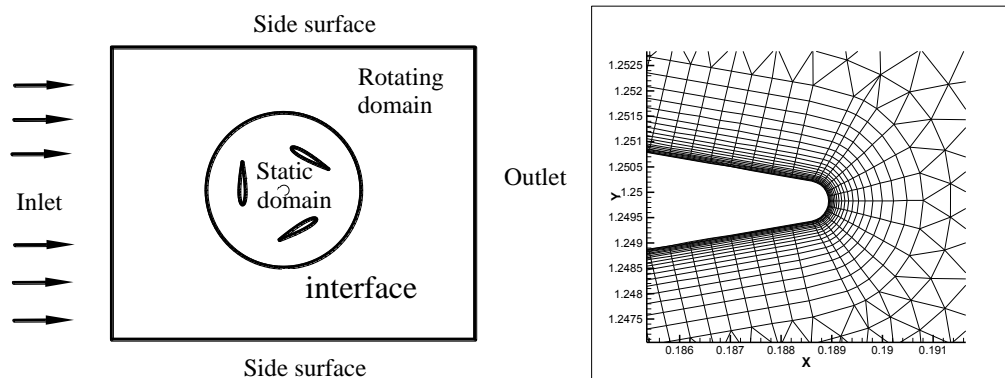


Figure 4.4 The computational domain

The computational domain includes static domain and rotating domain. The circle between the static domain and rotating domain is defined as an interface that allows the usage of the sliding mesh technology. The inlet is the velocity inlet which was fixed at 10m/s normal to the inlet. The outlet of the domain is defined as the pressure outlet. The side surfaces are defined as the wall boundary. The size of the domain,

mesh number, turbulence models will be evaluated in the following sections.

## **4.4 CFD Strategies and validation**

Before conducting the CFD analysis of VAWTs, the validation of the CFD method is very important. The validation does not mean getting a simulation result exactly the same as the experimental result.

It is unreliable and unnecessary to predict the performance of VAWTs very precisely using the CFD methods. Meanwhile, an uncorrected time-saving prediction is useless to offer the valuable guidance for the design of VAWTs.

Thus, there is one principle for the CFD optimum design when conducting the selection of the CFD strategies. This principle is that the simulation results must be relatively accurate under the circumstance of relatively lower computational effort.

It should be stated that the main work of a validation is about the proper selection of the CFD strategies under the principles mentioned above. These strategies can be the size of the computational domain, number of the grid, the  $Y^+$  close to the wall, the turbulence models, the size of each time step and so on.

### **4.4.1 Domain size**

The size of the domain will not only affect the pressure distribution on the blade but also determine the computation time will be. Generally, the larger the domain is, the larger the computational time. Based on the literature review, there are two

dimensionless values to determine the domain size. One is the length to chord ratio which is the ratio between the length of the domain and the length of the airfoil chord, such as  $30c$ ,  $50c \times 30c$  shown in Table 2.6. Another is the length to diameter ratio that is the ratio between the length of the domain and the length of rotor diameter.

In terms of the shape of the domain, it could be the rectangular or square. Some researches related to the domain size have been done in the past. Mohamed et al. (2011) conducted the square domain investigation about the influence of the length to diameter ratio on torque coefficient of the drag type VAWTs. The results show that the square computational domain should extend at least 10 times the rotor radius in each direction.

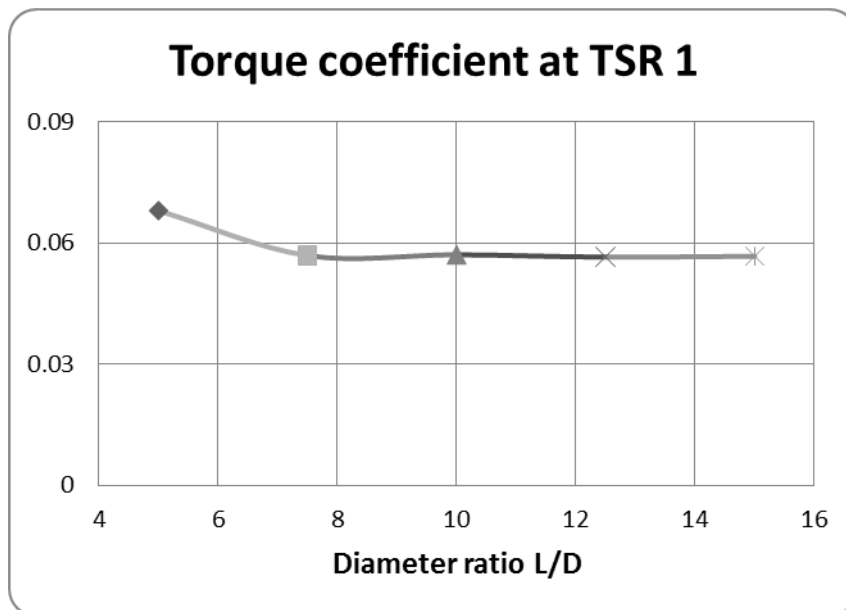


Figure 4.5 The effect of the diameter ratio on the torque coefficient

McLaren (2011) also conducted the investigation of the effect of length to diameter

ratio on the thrust coefficient. However, rectangle domain was used. The simulation results show that the difference between the domain with a length to diameter ratio 14 and a width to diameter ratio 8 and the domain with a length to diameter ratio 42 and a width to diameter ratio 24 is less than 2%.

In this thesis, the domain shape is square and the length-to-diameter ratios investigated include 5, 7.5, 10, 12.5 and 15. The results are shown in Figure 4.5. It seems that the torque coefficient fluctuates very little when the diameter ratio is larger than 7.5. This ratio is quite close to that of the Mohamed and McLaren's case. Thus, the length to diameter ratio of the following cases is 10.

#### **4.4.2 Mesh number**

After determining the domain size, the effect of the mesh number on the accuracy of the simulated results is investigated. Theoretically, the finer the mesh is, the more precise the result is. However, fine mesh needs a lot of computational resources. Thus, a balance between the accuracy and computational time needs to be found.

McLaren (2011) used five different mesh nodes which are 72,000, 111,000, 135,000, 242,000, 485,000 and 567,000 nodes to investigate the mesh number independence. The results showed that the power coefficient varies by just 5% for the four finest meshes. The presented works, three different mesh nodes were used. The simulated results are presented in Figure 4.6. It is found that the torque coefficient fluctuates very little for three different mesh numbers. This compares well to the work of the McLaren. Thus, the 0.2 million mesh number was applied to all the following cases.

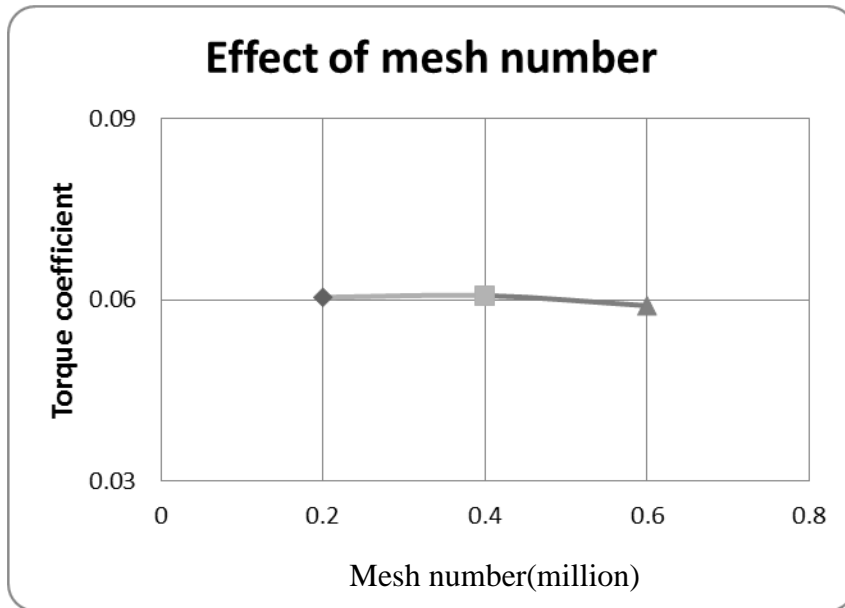


Figure 4.6 The effect of the mesh number on the torque coefficient

#### 4.4.3 Number of mesh node on the blade surface

Some papers mentioned the mesh node number on the blade surface. In fact, this number will also affect the precise prediction of the torque coefficient. The main effect of the number of mesh node on the blade surface is the aspect ratio of the mesh. The aspect ratio for the quadrilateral is defined as:

$$Q_{AR} = \frac{\max[e_1, e_2, \dots, e_n]}{\min[e_1, e_2, \dots, e_n]}$$

where  $e_i$  is the average length of the edges in a coordinate direction ( $i$ ) local to element (see Figure 4.7) and  $n$  is the total number of coordinate directions associated with the element (FLUENT 2009)

The aspect ratio of the flow volume and in the boundary layer should be less than 5

and 100, respectively. Based on the definition of the aspect ratio, the first height of the boundary layer must be given to calculate the aspect ratio of the mesh. However, the first height of the boundary layer is decided by Y plus close to the surface. The Y plus value is different for the different wall treatment methods. The lower limit of Y plus of the standard wall functions is at the order of 15. The Y plus of the enhanced wall treatment should be close to 1 to resolve the viscous sub layer (FLUENT 2009). The estimation of the Y plus can be obtained from the NASA website (Jones 1997).

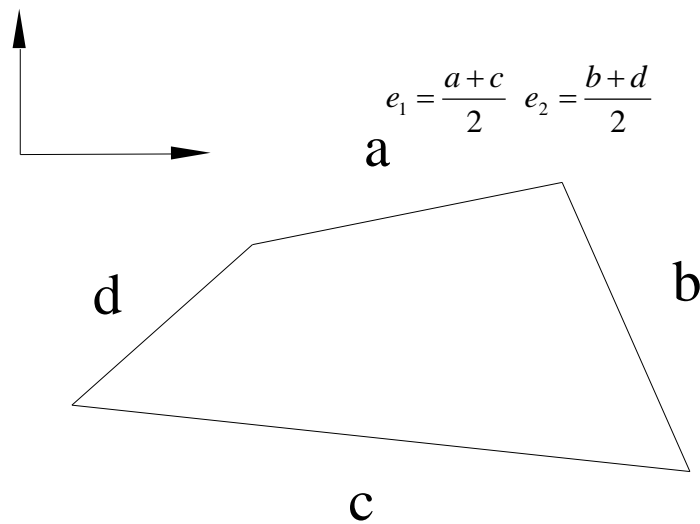


Figure 4.7 The aspect ratio of a quadrilateral element

Based on the estimation, the first height of the boundary layer is about 0.01mm. The half circumference of the airfoil is about 257mm. Three cases with 600, 1200, and 2400 nodes on the upper surface of airfoil were investigated. Thus, the aspect ratios of the cases with different nodes can be calculated and were listed in Table 4.1. The case with 2400 nodes is very close to 100. The simulation results were presented in Figure 4.8. The simulation results of the three cases are fairly close to each other. It

is found the simulation results will not significantly be affected by the aspect ratio when the aspect ratio is less than the 42.9. But, more nodes are associated with more number of meshes. Thus, the aspect ratio 42.9 was applied to all following cases.

Table 4.1 The aspect ratio of the first boundary layer attached to the airfoil surface

	<i>600 Node</i>	<i>1200 Node</i>	<i>2400 Node</i>
<i>Interval between two nodes</i>	0.428mm	0.214mm	0.107mm
<i>Height of the first layer</i>	0.01mm	0.01mm	0.01mm
<i>Aspect ratio</i>	42.9	21.4	10.7

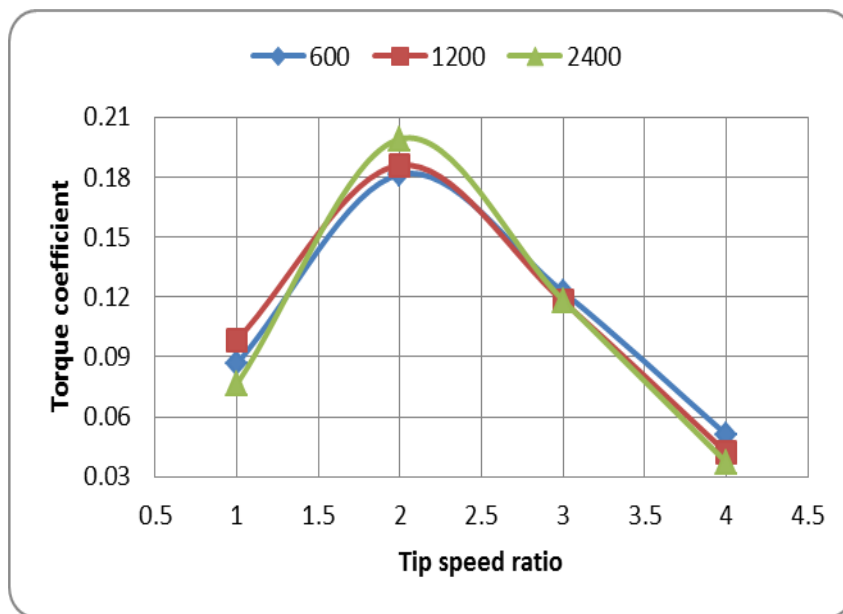


Figure 4.8 The effect of the mesh node number on the airfoil surface

#### 4.4.4 Turbulence models

It is unfortunate that no single turbulence model is universally accepted for all classes of problems (FLUENT 2009). Thus, the choice of the turbulence model will

influence the simulation results significantly. Six kinds of turbulence models are used to simulate the torque coefficient of the VAWT. The simulation results are presented in Figure 4.9. It is found that there is a wide gap between the results simulated by the  $\kappa-\varepsilon$  models and RSM models and the results simulated by other turbulence models. The reason is that all  $\kappa-\varepsilon$  models are insensitive to adverse pressure gradients and boundary layers separation which are common event when a VAWT is under periodicity rotation. Therefore, the  $\kappa-\varepsilon$  model is not widely used in external aerodynamics (FLUENT 2009).

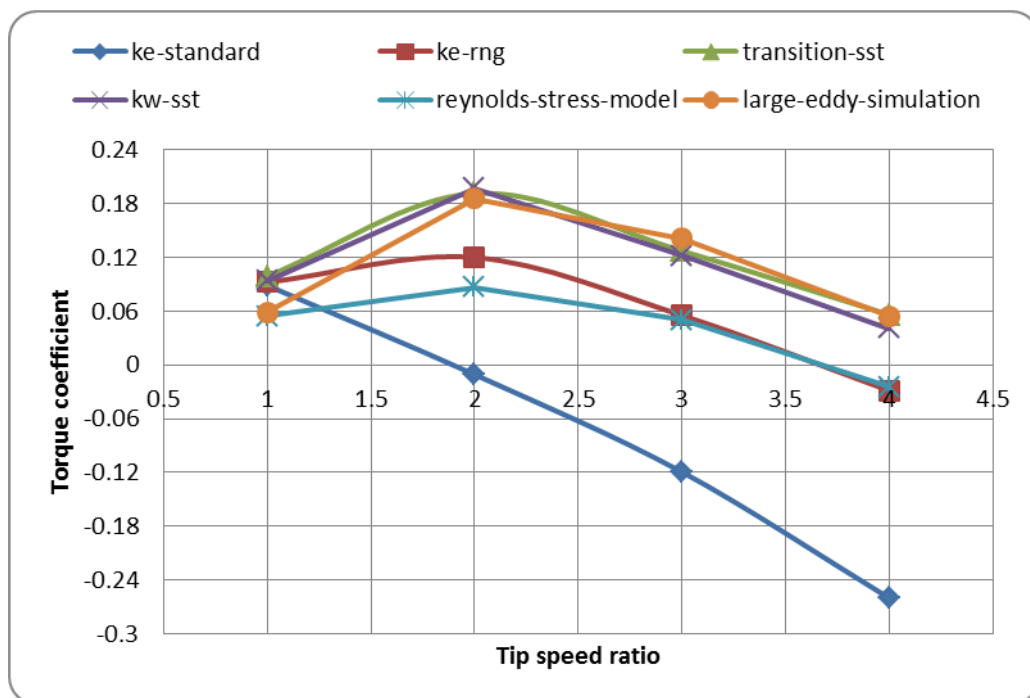


Figure 4.9 Comparison between six turbulence models

The torque coefficient curves of the  $\kappa-\omega$  model, laminar-turbulent transition models and LES model are fairly close because those models are typically better in predicting adverse pressure gradient boundary layer flows and separation. Thus, the

SST  $\kappa-\omega$  model which has been calibrated to accurately compute flow separation from smooth surfaces is chosen for all the cases.

#### 4.4.5 Influence of time step size and number of turns

Table 4.2 Detailed time step for different tip speed ratio at 10m/s

<i>Tip Speed Ratio</i>	<i>0.5</i>	<i>1</i>	<i>1.5</i>	<i>2</i>	<i>2.5</i>	<i>3</i>	<i>4</i>
<i>Rotational speed(rad/s)</i>	4	8	12	16	20	24	32
<i>Time step for 1 degree</i>	0.00436	0.002182	0.001454	0.001091	0.000873	0.00073	0.00054
<i>Time step for 2.5 degree</i>	0.01091	0.005454	0.003636	0.002727	0.002182	0.00182	0.00136
<i>Time step for 5degree</i>	0.02182	0.010908	0.007272	0.005454	0.004363	0.00367	0.00273
<i>Recommended time step</i>	0.00683	0.003417	0.002278	0.001708	0.0013667	0.00114	0.00085

Table 4.3 The percentage of chord length moved per time step

<i>Degree of moving/time step</i>	<i>% Chord length/time step</i>
1	8.72
2.5	21.8
5	43.6

In general, taking larger time steps leads to faster convergence, so it is advantageous

to set the size of time step as large as possible. Based the guidance of the ANSYS training files, the time step size should be no larger than the time taken for a moving cell to advance past a stationary point. Thus, the time step can be calculated as:

$$\Delta t = \frac{\Delta s}{\omega R} \quad \text{Equation 4.1}$$

where  $\Delta s$  is the mesh spacing at sliding interface.  $R$  is the radius of the interface and  $\omega$  is the rotational speed.

Hence the recommendatory maximum time step size is about  $8.54 \times 10^{-4}$  at the highest rotational speed. The time step size for all the cases is presented in

Table 4.2.

The time step size for the case where the degree of moving is 1 degree each size of the time step is less than the recommended time step size. The percentage of chord length traversed is presented in Table 4.3.

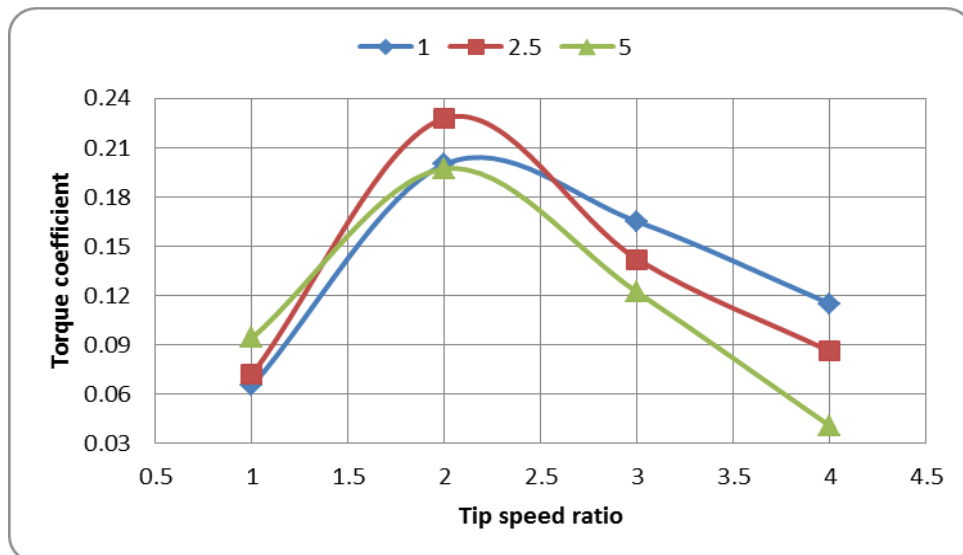


Figure 4.10 The effect of the time step size

The effect of the time step size is depicted in Figure 4.10. In general, power curves of three cases show the same tendency, although there are some difference between the simulation results at higher tip speed ratio. The maximum power coefficient happens when the tip speed ratio is about 2.2. The power coefficient of the smallest time step is the smallest when the tip speed ratio is less than 2.2. The power coefficient became the highest at higher tip speed ratio. Theoretically, the smaller the time step size, the higher the prediction accuracy is. The total computational time of one case with 5 degree is about 1 a day. It means that 5 days were needed to calculate one complete power curve which has 7 points. Currently, this computational time is not acceptable. Thus, 5 degrees movement per time step is used considering the computational effort.

The number of turns is another important issue which affects the accuracy and computational cost. Generally speaking, the larger number of turns, the more stable and accurate the results are. However, a large number of turns means great computational effort. Thus, the selection of the number of turns must consider the balance between the accuracy and computational cost. The CP varying with the number of turns is presented in Figure 4.11, and it is found that the CP varies quite little when the number of turns is larger than 4.

The effect of the number of turns is analyzed in Table 4.4. The first row in Table 4.4 is the range of the number of turns. The second column calculates the average, standard deviation (STDEV) and error from the third turn to tenth turn. The rest of the columns calculate the average, standard deviation (STDEV) and error for different range of number of turns. The average CP for different ranges of number of

turns varies very little. The lowest average CP happens when the range of number of turns is from 4-10. The STDEV and error of the column number 5 is the lowest among the five columns. Thus, six turns are selected for the number of turns considering the accuracy and accepted computational cost.

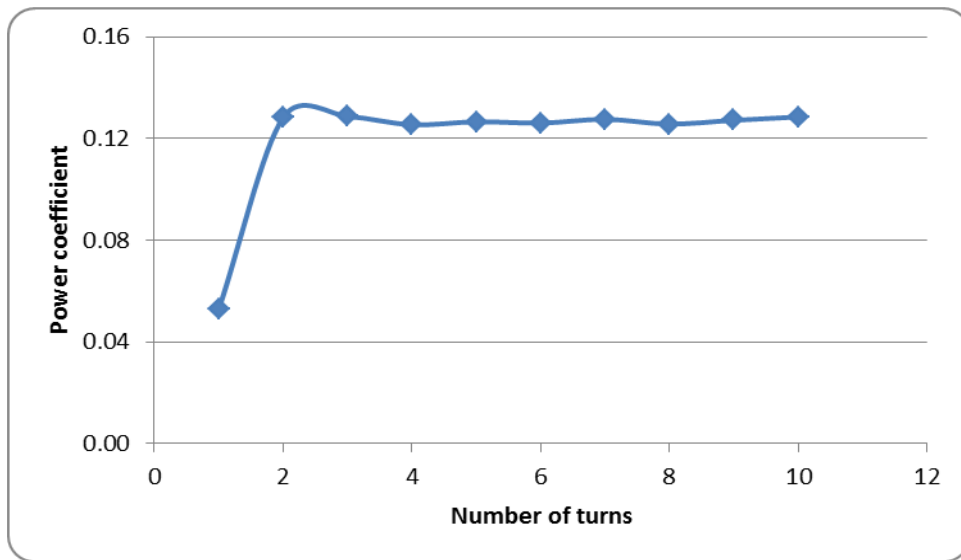


Figure 4.11 CP varies with number of turns

Table 4.4 The Effect of the number of turns

<i>Number of turns</i>	3-10	4-10	5-10	6-10	7-10
<i>Analysis results</i>					
<i>Average</i>	0.1269	0.1267	0.1269	0.1269	0.1270
<i>STDEV</i>	0.0012	0.0011	0.0012	0.0010	0.0011
<i>Error</i>	0.0097	0.0087	0.0097	0.0081	0.0089

#### 4.4.6 Validation

Based on the selection of the CFD strategies, a new model is created according to the experiment conducted by Fiedler and Tullis (2009). The domain size of the outer space is 10. The mesh numbers of this case are about 0.2 million. The number of mesh nodes on the blade surface is 600. And the SST k-w turbulence model is selected. The time step size selected is to turn the blade five degrees at each time step. And the number of turns is six turns. The comparison between the simulated results and experimental results is shown in Figure 4.12.

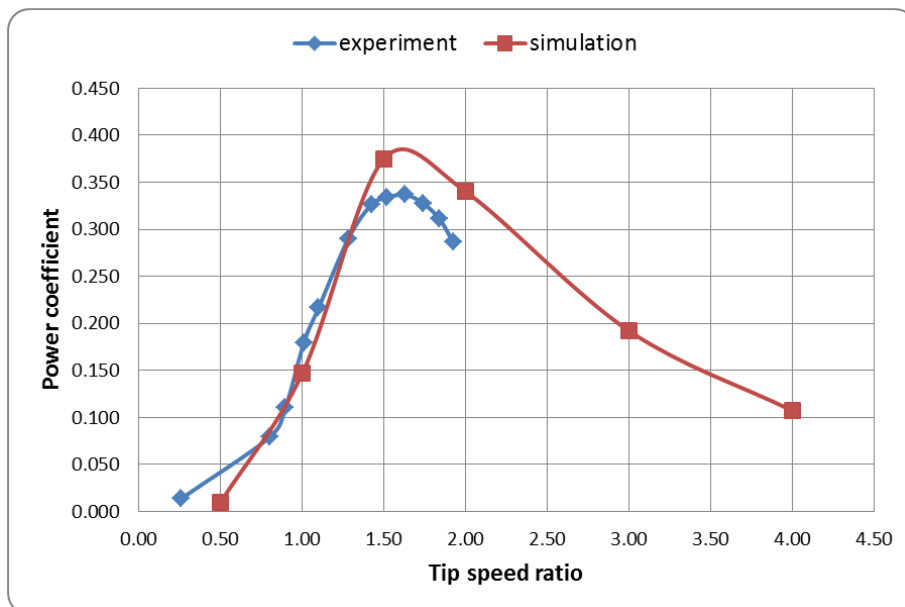


Figure 4.12 The validation of simulation

The simulation curve is gained using 2D geometry without consideration of the struts and central shaft. Thus, the simulated curve should be larger than the experimental curve. However, it is found that the power curves of the simulation and experiment are fairly close to each other at low tip speed ratio. The reason for this close fit may

be due to the large time step size. As discussed in the section of time step size effect, the smaller time step size is, the higher the power coefficient is at a low tip speed ratio. At a higher tip speed ratio, a divergence is founded. But, this divergence will become larger if the smaller time step size is used.

However, the simulated CP curve shows the same tendency as the experimental CP curve qualitatively. The simulated CP curve not only fit well with the experiment CP curve at low tip speed ratio, but also show the same tip speed ratio of maximum CP as the experimental CP curve. Thus, the CFD strategies used in this validation case will be used in Chapter 5, Chapter 6 and Chapter 7 to conduct the CFD simulation of the two starting ability improvement methods and airfoil optimal design.

## **4.5 Summary**

In this chapter, CFD simulation processes and strategies are discussed to find the right CFD simulation process and strategies for different research topics of the Darrieus rotor. The works of this chapter will be concluded as below:

- a) The common CFD analysis process is discussed and will be used to simulate the Darrieus rotor with an opening at the blade tip (Chapter 5) and the Darrieus rotor with two sets of blades (Chapter 6) due to the fact that those two Darrieus rotors have relatively complicated geometry to parameterize the design parameters.
- b) An automatic CFD analysis process is proposed and established to eliminate the manual operation of the common CFD analysis process. This automatic

CFD analysis process will work with the one dimensional liner and orthogonal analysis algorithm in Chapter 7 to establish a novel airfoil optimal design process.

- c) This automatic CFD analysis process also lays the foundation of parameter optimization CFD analysis process which is proposed for the future research studies of the Darrieus rotor.
- d) A careful and wide investigation of the effects of the different CFD strategies is conducted in this chapter to find the right strategies for the simulation of the second and third starting ability improvement methods and the establishment the novel airfoil optimal design process.
- e) In the end, the simulation result is validated through the comparison with the experimental result. The simulated CP curve not only fit well with the experiment CP curve at low tip speed ratio, but also show the same tip speed ratio of maximum CP as the experimental CP curve. It is suggested that the CFD strategies selected in this chapter are suitable for the simulation of the Darrieus rotor.

# CHAPTER 5 THE DARRIEUS ROTOR WITH AN OPENING AT THE BLADE TIP

## 5.1 Introduction

By using the CFD simulation process and strategies selected in chapter 4, the second method to improve the starting ability will be investigated in this chapter. This second method is the Darrieus rotor with an opening at the blade tip.

In Chapter 3, the two-stage Savonius rotors have been used as an assistance of the Darrieus rotor. However, the CP of this hybrid Savonius-Darrieus rotor is about 30% less than that of the Darrieus rotor without Savonius rotor. And the hybrid Savonius-Darrieus rotor increases the cost and complexity of structure.

Thus, the Darrieus rotor with an opening at the blade tip is proposed not only to improve the starting ability, but also to reduce the loss of CP. The Darrieus turbine with an opening is a rotor with a combination of a normal airfoil and an airfoil with an opening which is located at the training edge of the airfoil. The airfoil with an opening will act as a drag type turbine at the low wind speed or low tip speed ratio.

This Darrieus turbine with an opening is designed to fill in the gap between the hybrid Savonius-Darrieus and Darrieus turbine. Structural simplicity is the greatest advantage of this novel Darrieus rotor with an opening. Figure 5.1 presents the four types of VAWTs. From left to right, they are traditional drag-type Savonius turbine, hybrid type Savonius-Darrieus turbine, new proposed Darrieus turbine with an

opening and the traditional Darrieus turbine. The blue ellipse in Figure 5.1 highlights the difference between the new proposed Darrieus turbine with an opening and the traditional Darrieus turbine. And the performance of this new type Darrieus rotor will be estimated in the following section.

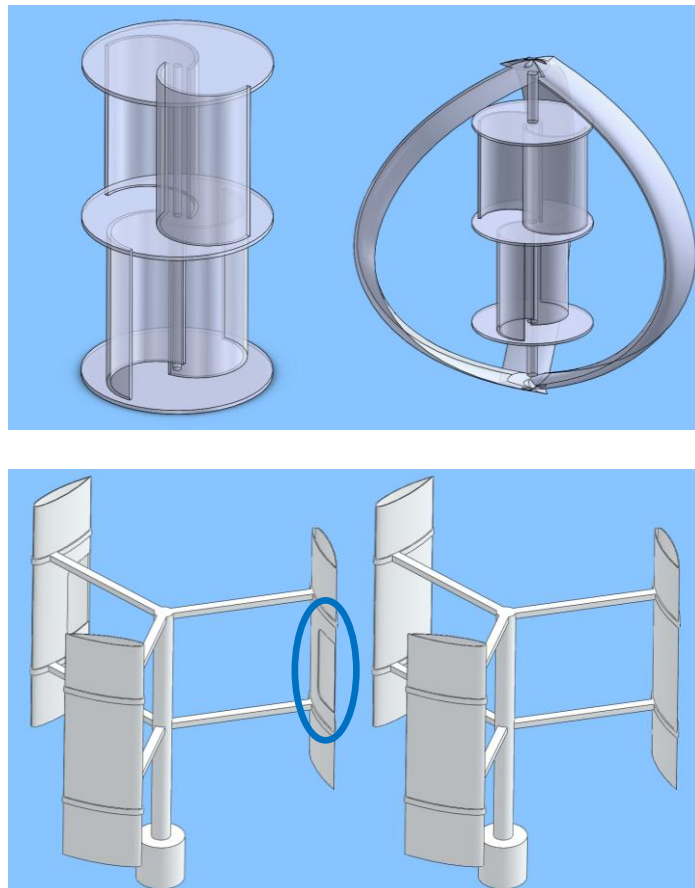


Figure 5.1 Four kinds of VAWTs

## 5.2 Geometry of the investigated rotors

The VAWTs used in the urban environment are usually micro type of wind turbines whose capacities are always range from 0.4 to 2.5kW (Peacock et al. 2008). A 1.5kW Darrieus rotor using the NACA 0015 and 4415 airfoils is presented in Figure

## 5.2.

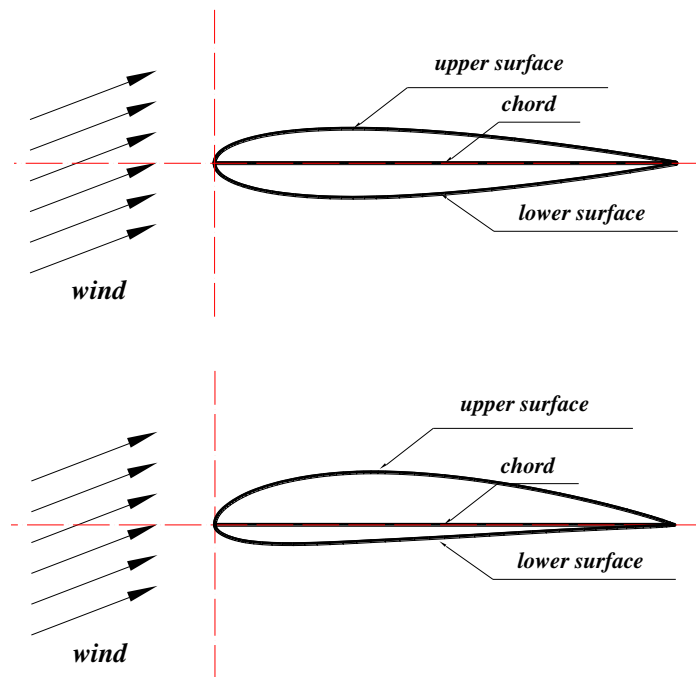


Figure 5.2 The airfoils used for the Darrieus rotor with an opening

Two types of NACA airfoils are selected for this Darrieus rotor with an opening. They are the NACA 0015 and NACA4415 airfoil. NACA 0015 airfoil is a symmetrical section and a common section used for the traditional Darrieus turbine. And the cambered NACA4415 airfoil is regarded as a promising one which can improve the self-starting ability of the Darrieus turbine (Kirke 1998, Islam et al. 2007). In order to improve the starting ability, a rotor with relatively high solidity which is 0.3 was used. The chord length of the airfoil is 250mm. The radius of the turbine and the height blades are 1.25m and 2.5m, respectively.

The design parameters of this Darrieus rotor with an opening can be the mounting point, opening ratio, opening location and the shaft influence. Different mounting

methods will influence the power output significantly. The aerodynamic center of the airfoil is chosen for the mounting location for most Darrieus rotors. And the aerodynamic center of the NACA families locates at one quarter of the chord length. Three mounting locations were investigated. The mounting ratio is defined the distance from leading point to the mounting point and the chord. Three mounting ratios are  $1/8$ ,  $1/4$ , and  $3/8$ . Those mounting ratios are shown at the left of the Figure 5.3.

The opening ratio is defined as the ratio between the size of the opening and the chord length of the airfoil. Three opening ratios, 0.12, 0.24 and 0.36, were investigated for the NACA 4415 airfoil. And eight opening ratios were investigated for the NACA 0015 airfoil. The effect of the opening location was also considered. Inside opening means the opening is located at the airfoil surface close to the rotating shaft. The opening ratio and opening location are described in the right of Figure 5.3. The first step of the optimization process is to select the mounting point location. Then, the opening location and opening ratio were investigated together. In the end, the influence of the shaft on the power coefficient was investigated.

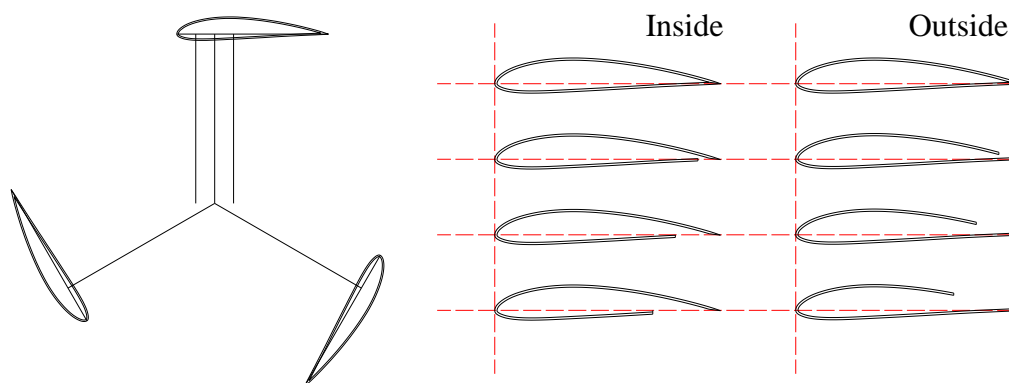


Figure 5.3 Design parameters of the H-Darrieus turbines

### 5.3 The effect of the mounting ratio

Different mounting locations will affect the power output significantly. Largely, the aerodynamic center of the airfoil is chosen as the mounting point for most Darrieus turbines. And the aerodynamic center of the most NACA families locates generally at one quarter of the chord length.

The simulation results of the effect of the mounting ratio on the performance are presented in Figure 5.4. It is clear that torque coefficient of the rotor with 1/4 mounting ratio is maximum when the  $c/r=0.2$ . Five kinds of mounting ratio were studied by Fiedler (2009) for the NACA 0015 airfoil with 400mm chord length and 1475mm radius. These five mounting ratios are 0.1325, 0.31625, 0.5, 0.68375 and 0.8675. The experimental results showed that the optimal mounting ratio is located in the range of 0.1325 to 0.31625. And the best mounting ratio of this paper just fell into this range.

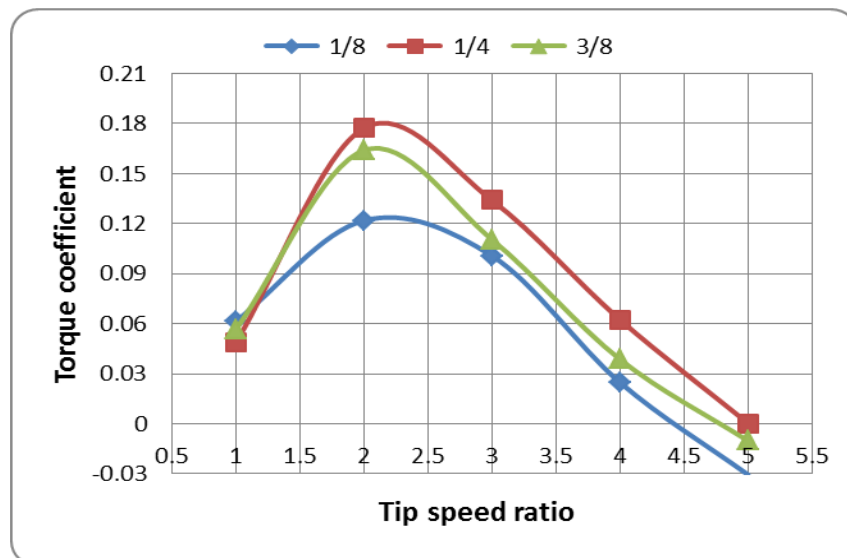


Figure 5.4 The effect of the mounting ratio

## 5.4 The effect of the center shaft

The diameter of center shaft investigated is 250mm. The ratio between the diameter of the shaft and the diameter of the rotor is 0.1. The simulation results are presented in Figure 5.5. From this figure, it is found that the effect of the shaft can be ignored when the tip speed ratio is less than 2. And the effect of the shaft increases as the tip speed increases from 2 to 4. Generally, dynamic stall happens when the tip speed ratio is less than 4. And dynamic stall becomes even worse with the decrease of the tip speed ratio.

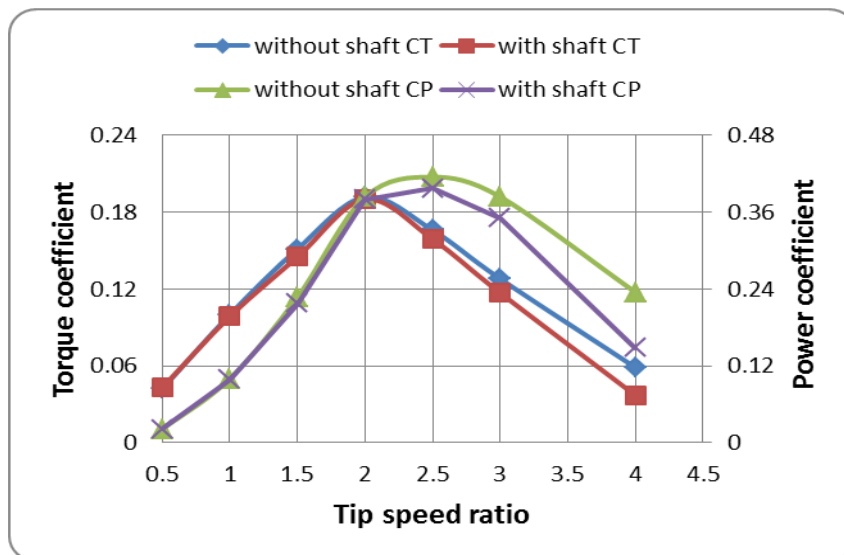


Figure 5.5 The effect of the shaft on the torque and power coefficient of the rotor

The possible reason for the small effect of the shaft at low tip speed ratio is that the effect of the dynamic stall is larger than the effect of wake behind the shaft on the pressure distribution of the airfoil. However, the effect of the dynamic stall will be reduced at higher tip speed ratio. The difference of one blade between the case with

shaft and without shaft for the entire azimuth angle is presented in Figure 5.6. A very small difference exists in the range of azimuth angle from 100 to 120 and from 265 to 290. The locations where the difference happens were also shown in Figure 5.6.

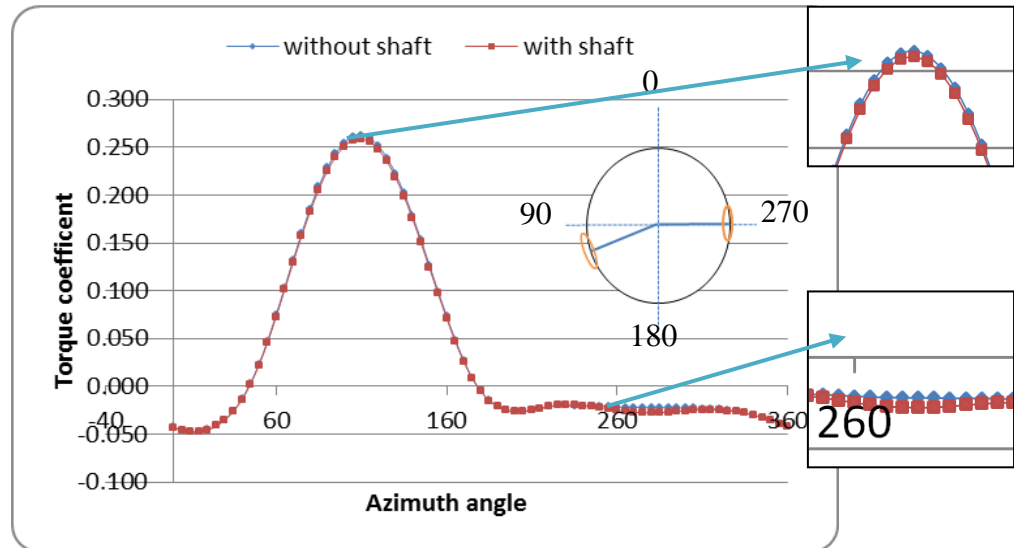


Figure 5.6 The difference between the rotors with and without shaft at TSR=3

## 5.5 Comparison between the NACA 0015 and NACA 4415 airfoil

Several researchers suggested that the camber airfoil will improve the self-starting ability of the rotor. Here, the comparison between the NACA 0015 airfoil and NACA 4415 airfoil was made for the CP and CTs. The simulated CTs of the NACA 0015 and NACA 4415 airfoil is 0.0207 and 0.0133, respectively. It seems that a cambered airfoil doesn't improve the starting torque of the Darrieus rotor at low wind speed. The CTs of the rotor with NACA 0015 airfoil is almost two times higher than that of the rotor with NACA 4415 airfoil. And the CP of two rotors is compared in Figure 5.7. It is obvious that the total torque of the rotor with NACA 0015 airfoil

is much higher than that of the rotor with NACA 4415 at the tip speed range from 1 to 4. The maximum CP is 0.42 and 0.37 for the rotor with NACA 0015 and NACA 0015 airfoil, respectively.

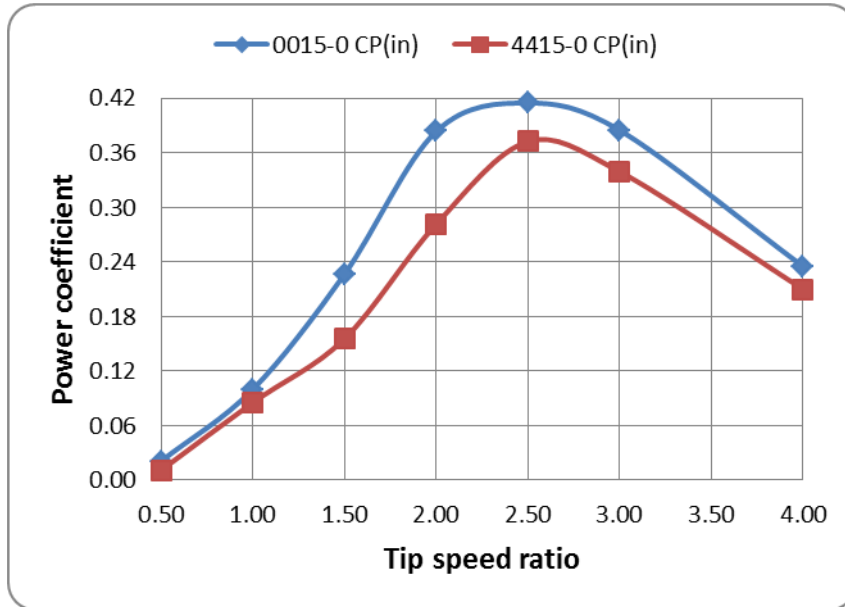


Figure 5.7 Comparison between NACA 0015 airfoil and NACA 4415 airfoil

Similar performance comparison was made by Islam et al. (2008) through the Cascade model for a rotor with solidity of 0.2 at different wind speed. He stated that, generally, the CP of the rotor with NACA 0015 is higher than that of the rotor with NACA 4415.

The possible reason can be explained in Figure 5.8. The comparison is made in the optimal tip speed ratio. For the comparison of one blade, the torque coefficient of rotor with NACA 0015 is higher than that of the rotor with NACA 4415 in the upstream half of the rotor, especially in the azimuth angle range from  $65^\circ$  to  $150^\circ$ . In the downstream half of the rotor, the torque coefficient of the rotor with NACA 4415

is a slightly higher than the rotor with NACA 0015. For the comparison of total torque coefficient, the rotor with NACA 0015 is generally slightly higher than the rotor with NACA 4415.

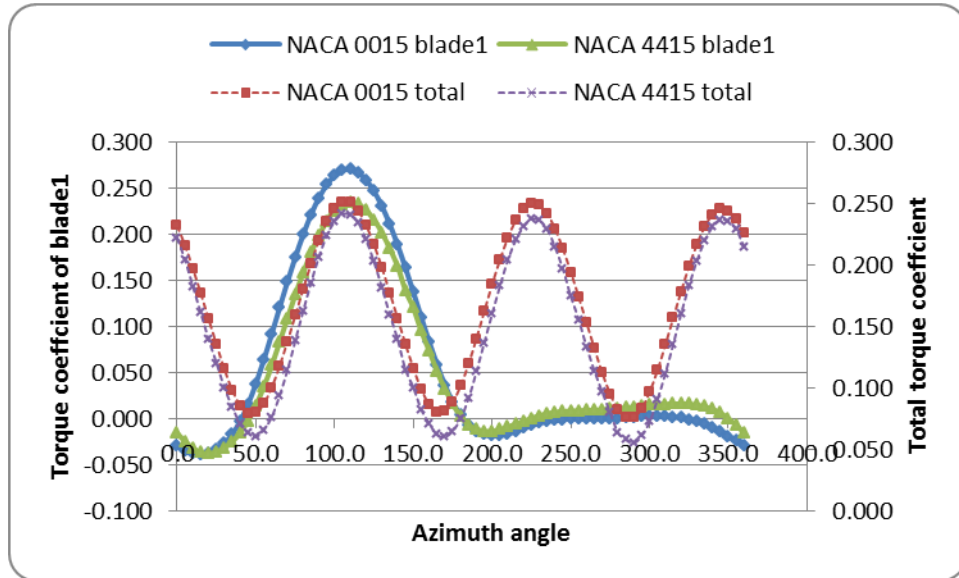


Figure 5.8 Comparison for the entire azimuth angle

## 5.6 The effect of the opening for the NACA 4415 airfoil

In this part, the effect of the opening location and the opening ratio on the performance of the rotor with NACA 4415 was investigated at two different opening locations and four different opening ratios without considering the effect of the shaft. The mounting ratio is 1/4. The opening ratio effect when the opening location is inside is presented in Figure 5.9. It is found that the power coefficient decreases slightly when the opening ratio increases from 0 to 0.36. The opening ratio effect when the opening location is outside is presented in Figure 5.10.

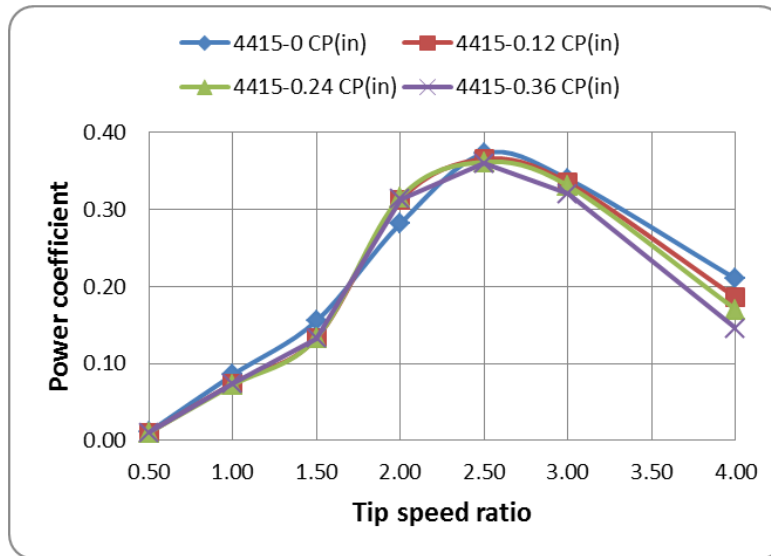


Figure 5.9 The NACA 4415 airfoil with inside opening

Different from the inside opening, the power coefficient of the four different opening ratios is fairly close when the tip speed ratio is less than 2. When the TSR increases from 2 to 4, the power coefficient discrepancy of the four different opening ratios was enlarged. The possible reason for why the discrepancy is large when the opening location is outside is that the flow separation always occurs at the outside surface in the upstream half of the rotor. If the opening is located on the outer surface, it may cause stronger flow separation at the outside surface. However, this phenomenon probably is not significant in the case of inside opening.

The standard deviation, maximum power coefficient and optimal TSR for the eight cases are listed in Table 5.1. The standard deviation represents the shape of the power curves. Higher standard deviation means a sharper the CP curve. The sharper the curve is, the narrower the working range of the rotor is. The H-Darrieus turbine cannot always work at optimal TSR. Thus, the rotor with smooth power curve has a

stable power output. For the case of inside opening, the changes of the maximum power coefficient and standard deviation are very small. However, this change is large in the case of outside opening.

Table 5.1 The maximum power coefficient for NACA 4415 airfoil

	<i>4415-0 CP (in)</i>	<i>4415-0.12 CP (in)</i>	<i>4415-0.24 CP (in)</i>	<i>4415-0.36 CP (in)</i>
<i>STDEV</i>	0.133	0.138	0.138	0.137
<i>MAX</i>	0.373	0.366	0.362	0.360
<i>TSR</i>	2.5	2.5	2.5	2.5
	<i>4415-0 CP (out)</i>	<i>4415-0.12 CP (out)</i>	<i>4415-0.24 CP (out)</i>	<i>4415-0.36 CP (out)</i>
<i>STDEV</i>	0.133	0.167	0.142	0.151
<i>MAX</i>	0.373	0.331	0.325	0.309
<i>TSR</i>	2.5	2.5	2.5	2.5

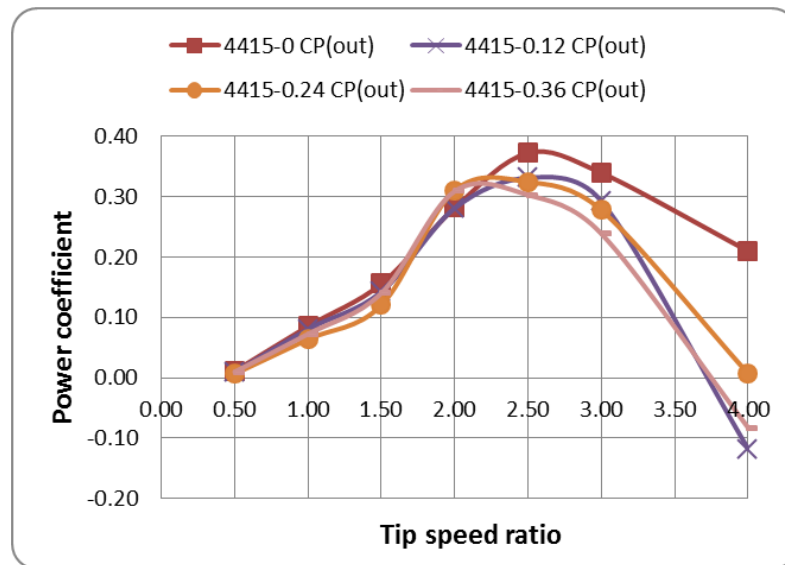


Figure 5.10 The NACA 4415 airfoil with outside opening

The CTs of the eight cases were depicted in Figure 5.11. Generally, the rotors with an opening at the blade tip have the better starting ability. And the starting ability of the rotor with inside opening is much better than the rotor with the outside opening when the opening ratio is less than 0.25. When the opening ratio is larger than 0.25, the static torque coefficient of the rotor with outside opening rises dramatically. It should be pointed out that the power coefficient of the rotor without an opening is higher than that of the rotor with an opening and the static torque coefficient of the rotor without an opening is lower than that of the rotor with an opening.

Thus, a balance needs to be found between the static torque coefficient and power coefficient. In order to find this balance, the increased percentage of the static torque and decreased percentage of the power coefficient are presented in Figure 5.12.

For the cases with inside opening, the curve of increased torque coefficient percentage surpasses the curve of the decreased of the power coefficient percentage for the opening ratio range from 0 to 0.36. The percentage of power coefficient decrease of the case with 0.12 opening ratio is about 2. And the percentage of static torque coefficient increase of the case with 0.12 opening ratio is about 6. Thus, it indicates that the rotor with 0.12 opening ratio is optimal among the rotors with inside opening.

For the cases with outside opening, the curve of decreased of the power coefficient percentage, however, surpasses the curve of increased torque coefficient percentage for the opening ratio range from 0 to 0.34. The maximum percentage of power coefficient decrease of the rotors with outside opening is about 17. And the maximum percentage of static torque coefficient increase for the rotor with outside

opening is about 19. Therefore, the Darrieus rotor with an opening is superior to the Savonius-Darrieus hybrid rotor which has a power decrease of 30% than the Darrieus rotor.

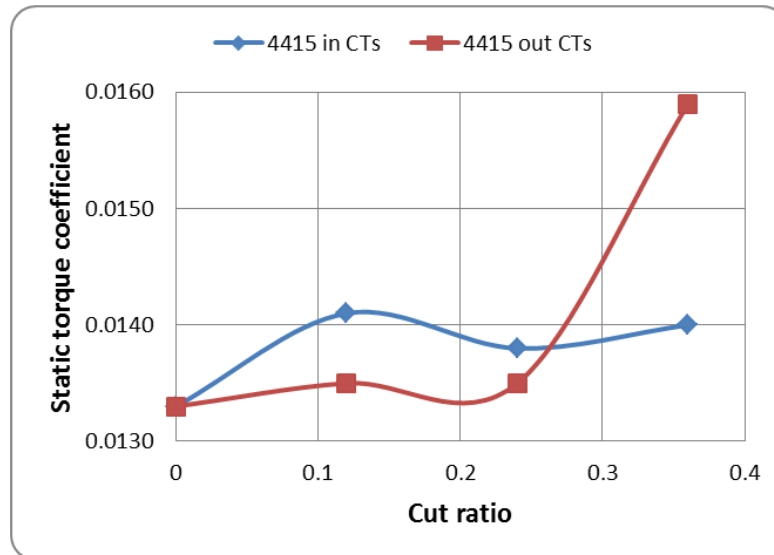


Figure 5.11 The effect of the opening ratio and opening location on the CTs

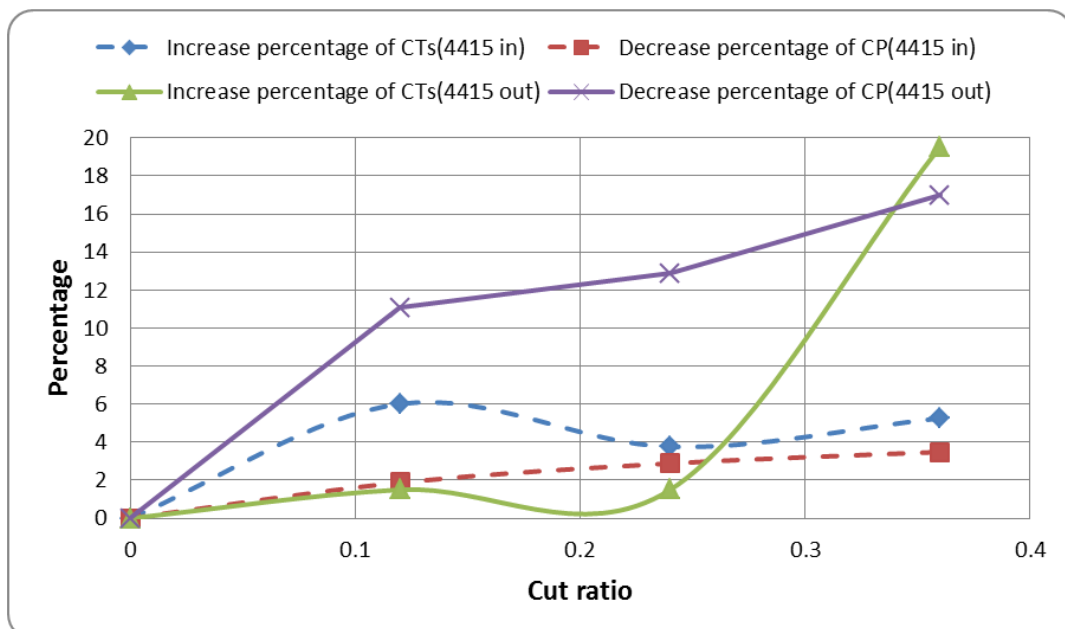


Figure 5.12 The increase percentage of CTs and decrease percentage of CP

## 5.7 The effect of the opening for the NACA 0015 airfoil

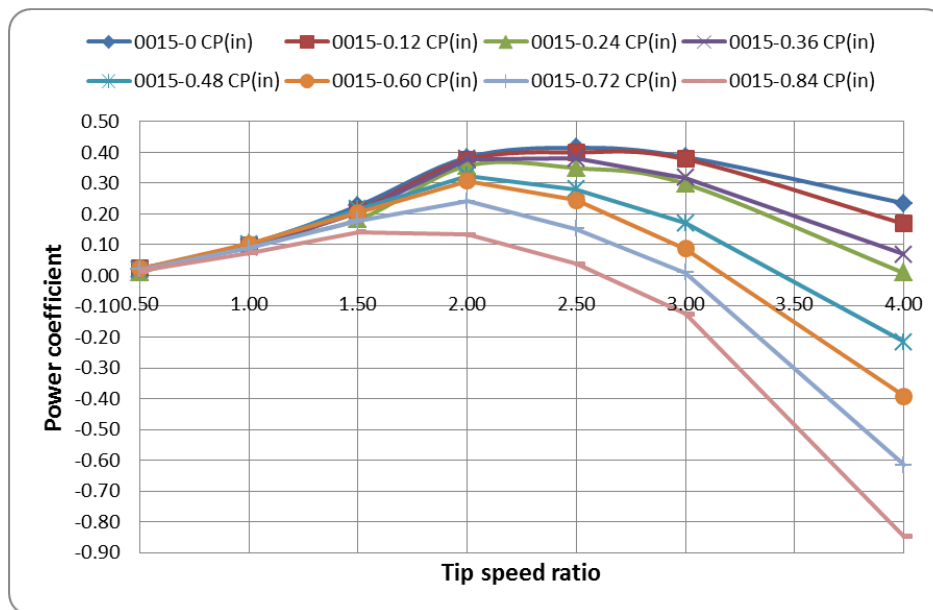


Figure 5.13 Effect of the opening ratio on the airfoil (inside opening)

In the above section, it is found that the Darrieus rotor with an opening and with NACA 4415 has great potential to improve the starting ability with a small percentage of power declination. Thus, the rotors with NACA 0015 airfoil were studied for a wide opening ratio from 0 to 0.84 because the rotor with NACA 0015 has a better power coefficient and static torque coefficient. The effect of the opening ratio on the power coefficient for the rotors with inside opening is presented in Figure 5.13.

Generally speaking, the power coefficient is declining with the increase of the opening ratio. The power curve of the rotor with 0 opening ratio is close to the power curve of the rotor with 0.12 opening ratio when the tip speed ratio is less than 3. The

power curve of the rotor with 0.24 opening ratio is close to the power curve of the rotor with 0.36 opening ratio when the tip speed ratio is less than 3. The declination rose dramatically when the opening ratio is larger than 0.48. The maximum power coefficient is only 0.14 for the rotor with opening ratio 0.84. One possible reason for this decline is that the separation area in the lower surface of the airfoil enlarged with the growth of the opening ratio.

The effect of the opening ratio on the power coefficient for the rotors with outside opening is presented in Figure 5.14. The declination of the power coefficient is also increasing with the increasing of the opening ratio. But the declination of the power coefficient is fairly large when the opening ratio has a small value. It indicates that the opening in the upper surface has greater effect than the opening in the lower surface when the opening ratio is small. The tip speed ratio of the rotors maximum CP with outside opening changes very small with the increase of the opening ratio.

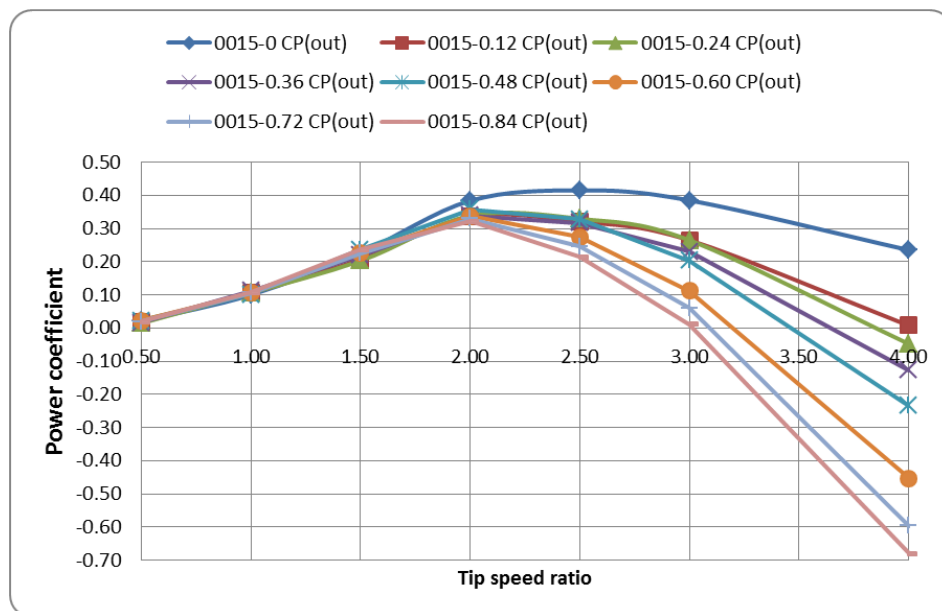


Figure 5.14 Effect of the opening ratio on the airfoil (outside opening)

Table 5.2 The maximum CP for NACA 0015 airfoil (inside opening)

	<i>0015-0 CP(in)</i>	<i>0015-0.12 CP(in)</i>	<i>0015-0.24 CP(in)</i>	<i>0015-0.36 CP(in)</i>
<b>STDEV</b>	0.152	0.151	0.1512	0.152
<b>MAX</b>	0.415	0.40	0.3566	0.38
<b>TSR</b>	2.5	2.5	2.5	2.5
	<i>0015-0.48 CP(in)</i>	<i>0015-0.60 CP(in)</i>	<i>0015-0.72 CP(in)</i>	<i>0015-0.84 CP(in)</i>
<b>STDEV</b>	0.1837	0.231	0.289	0.349
<b>MAX</b>	0.3236	0.307	0.241	0.141
<b>TSR</b>	2	2	2	1.5

Table 5.3 The maximum CP for NACA 0015 airfoil (outside opening)

	<i>0015-0 CP(out)</i>	<i>0015-0.12 CP(out)</i>	<i>0015-0.24 CP(out)</i>	<i>0015-0.36 CP(out)</i>
<b>STDEV</b>	0.152	0.137	0.152	0.168
<b>MAX</b>	0.415	0.335	0.338	0.338
<b>TSR</b>	2.5	2.5	2.5	2.5
	<i>0015-0.48 CP(out)</i>	<i>0015-0.60 CP(out)</i>	<i>0015-0.72 CP(out)</i>	<i>0015-0.84 CP(out)</i>
<b>STDEV</b>	0.205	0.263	0.308	0.335
<b>MAX</b>	0.358	0.337	0.329	0.321
<b>TSR</b>	2.5	2	2	2

The maximum power, standard deviation of the power curve and TSR related to the maximum CP are listed in Table 5.2 and Table 5.3. The maximum CP is decreased as the increase of the opening ratio whether the blades are opened inside or outside.

The change of optimal TSR has the same tendency as the change of maximum power. The shape of the power curves became sharper with the increase of the opening ratio. The effect of the opening ratio on the static torque coefficient is presented in Figure 5.15. The static torque coefficient of the rotors with outside opening is increased lineally with the increase of the opening ratio as a whole, except the rotor with 0.12 opening ratio. Thus, the static torque coefficient of the rotor with outside opening can be predicted through the equation of a line. But the static torque coefficient of the rotors with inside opening does not increase with the increase of the opening ratio. The static torque coefficients of the rotors with 0.24, 0.72 and 0.84 opening ratio are even lower than that of the rotor with zero opening ratio. There are two bumps in the curve of inside opening. It seems that maximum static torque coefficient locates between the ranges of opening ratio from 0.48 to 0.6.

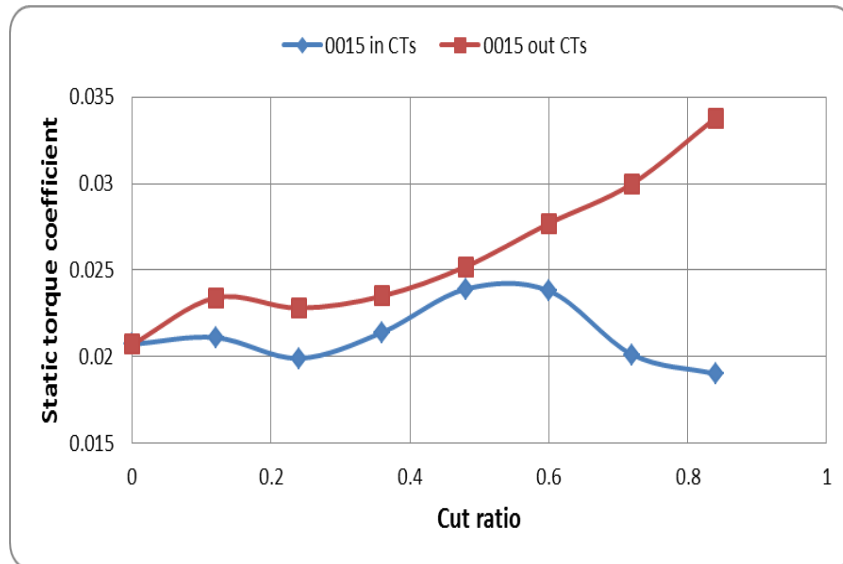


Figure 5.15 Effect of the opening ratio and location on the CTs

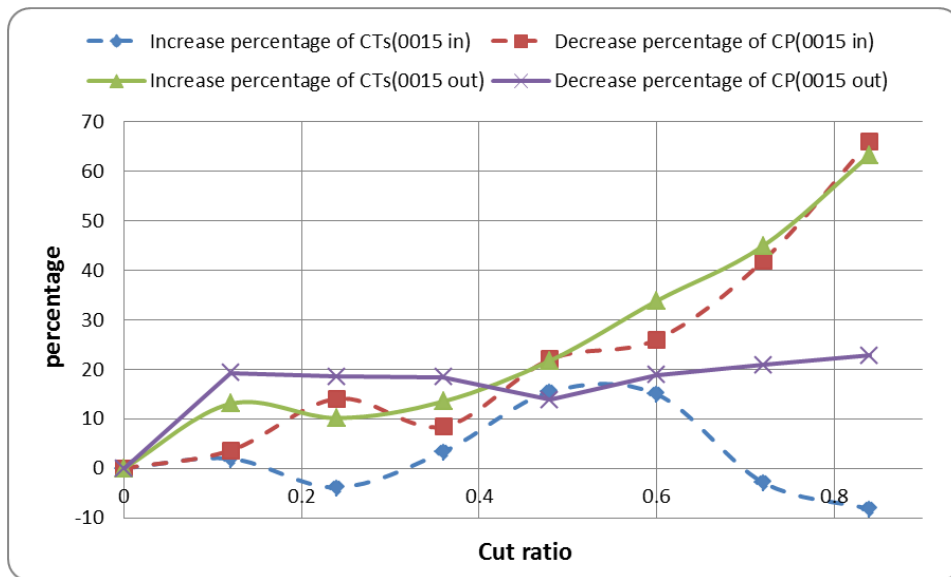


Figure 5.16 The increase percentage of CTs and decrease percentage of CP

In order to select the optimal opening ratio, the increase percentage of the static torque coefficient and decrease percentage of the power coefficient are shown in Figure 5.16. For the rotors with outside opening, the decrease percentage of power coefficient for all the rotors is less than 20%. And the increase percentage of the static torque coefficient is roughly lined with the opening ratio. Different from the rotors with inside opening, the increase percentage of the static torque for all of the rotors is less than 20%. And the decreased power coefficient is lined with the increasing of the opening ratio. Thus, it seems that the rotor with outside opening has more potential than the rotor with inside opening from the point of to gain higher static torque coefficient. However, the rotor with inside opening has more potential than the rotor with outside opening from the point of to gain higher power output and has relatively higher static torque coefficient.

## 5.8 Starting ability comparison between the Darrieus rotor with an opening and the hybrid Savonius-Darrieus rotor

So far, the increase percentage of the CTs and a decrease percentage of CP of different Darrieus rotors with an openings have been discussed in detail in the above sections. But, whether this Darrieus rotor with an opening is superior to the hybrid Savonius-Darrieus rotor has not been answered well yet. Thus, a comparison between this Darrieus with an opening and the Savonius-Darrieus hybrid rotors is conducted focusing on the decrease of CP and increase of CTs. The equation used to calculate the starting torque is presented below:

$$T = \frac{1}{2} C_{Ts} \rho A R V^2 \quad \text{Equation 5.1}$$

It is found that the starting torque not only relies on the swept area, but also on the radius of the rotor when the velocity of the wind is constant. Therefore, the starting torque of the Darrieus with an opening and Savonius-Darrieus rotor will be different even when the CTs of the above two rotors is the same.

Based on the studies of Wakui et al. (2005), the diameter ratio of the Savonius rotor to Darrieus rotor cannot exceed 0.3 or 0.38 for type A or type B configurations (Figure 2.57), respectively. If the diameter ratio between the Savonius and Darrieus rotors is larger than the ratio mentioned above, the CP will fall dramatically. According to the design parameters of the rotor investigated by Wakui, the CT increase percentage can be calculated when the Darrieus rotor integrated with the Savonius rotor.

The diameter and height of the Savonius rotor tested by Wakui are both 0.6m and 0.6m. The Darrieus rotor has 2m height and 1.6m diameter. The average CTs of the Savonius ranges from 0.11 to 0.2 based on other researchers' testing and our lab testing. Thus, the CTs increase of the Darrieus rotor is about 0.00464 and 0.008437 for the average Savonius rotor's CTs is 0.11 and 0.2. The average CTs of the Darrieus rotor ranges from the 0.0133 to 0.024 for the rotors without an opening. Hence, the Savonius rotor will increase CTs of Darrieus rotor about 34% and 35.1%.

The CP loss of most Darrieus rotors with an opening is less than 35 percent, except for the rotor with NACA 0015 airfoil when the opening ratio is larger than 0.64 and the opening is inside. For the Darrieus rotor with opening outside blades showed in Figure 5.16, it can be found that the CP loss of and CTs increase of rotor with NACA 0015 are 20 and 35 percentage when the opening ratio is 0.6. And the variety of CP is very small when the opening ratio is larger than 0.6. But the CTs will increase dramatically as the increase of the opening ratio. Thus, this Darrieus rotor is superior to the Savonius-Darrieus rotor when the opening ratio is larger than 0.6. Another issue, in fact, needs to be considered. It is that the small increase percentage of the CTs may be enough for self-starting. This issue needs further experimental testing.

## **5.9 Power coefficient equation to evaluate the Darrieus turbine with an opening**

In the previous section, the effect of the opening ratio and the opening location on

the performance of the Darrieus rotor with an opening is analyzed in 2D. In 2 dimensional spaces, inside opening and outside opening are the design parameters of the opening location. In 3 dimensional spaces, another two important design parameters need to be considered. They are the opening location along the z direction and the opening length along the z direction. The blades can be cut at the center of the blade or at the tip of the blades. And the opening length can be a quarter or half of the length of the blades. These two design parameters will affect the pressure distribution of the blade profoundly. They may increase or decrease the power coefficient. In order to evaluate the performance of the Darrieus with an opening using the 2D simulation results, one ratio is defined. This ratio is called the opening length ratio (OLR) which is the ratio of the opening length to the blade length. Thus, the power and static torque coefficient of the Darrieus with an opening can be calculated through the following equations.

$$CP = CP_0 * (1-OLR) + CP_{cut} * OLR \quad \text{Equation 5.2}$$

$$CT_s = CT_{s_0} * (1-OLR) + CT_{s_{cut}} * OLR \quad \text{Equation 5.3}$$

In the above equations,  $CP_0$  means the power coefficient of the rotor without an opening, and  $CP_{cut}$  is the power coefficient of the rotor with an opening which is selected by the users. The meaning of  $CT_{s_0}$  and  $CT_{s_{cut}}$  is similar to the meaning of  $CP_0$  and  $CP_{cut}$ .

## 5.10 Summary

This chapter numerically studied the Darrieus rotor with an opening at the blade tip. The effect of cutting ratio, cutting location and mounting location is studied through the CFD method for the rotor with symmetrical NACA 0015 airfoil and camber NACA 4415 airfoil. The effect of the center shaft is also studied in this chapter. The conclusions found in this chapter are summarized below:

- a) The effect of the mounting ratio on the CP of the Darrieus rotor without an opening is studied in this chapter. And the optimal mounting ratio of this thesis is one quarter of the chord length. This optimal mounting ratio is filled into the optimal range suggested by other authors.
- b) The center shaft has a small effect on the CP of the Darrieus rotor without an opening. The reason for the small effect of the shaft, especially at low tip speed ratio, is possible that the effect of the dynamic stall is larger than the effect of wake behind the shaft on the pressure distribution of the airfoil.
- c) A research of the Darrieus rotor with an opening is carried out for the NACA 4415 airfoil firstly, it is found that the optimal cutting ratio is 0.12 when the cutting location is on the inside edge and the range of the cutting ratio is from 0 to 0.36. The CP loss percentage and CT increase percentage of the rotor with 0.36 cutting ratio and outside opening is about 17 and 20 compared with the rotor with zero cutting ratio, respectively.
- d) Then, the research of the Darrieus rotor with an opening is also conducted for NACA 0015 airfoil, the optimal rotor is the one with a cutting ratio of 0.48

when the cutting location is inside. The CP loss percentage and CT percentage increase of this rotor is 0.22 and 0.15 compared to the rotor with zero cutting ratio, respectively. The optimal rotor for the rotor with outside opening is the rotor with 0.8 cutting ratio. The CP loss percentage and CT percentage increase of this rotor is 0.22 and 0.70 compared to the rotor with zero cutting ratio, respectively.

- e) A remarkable finding in this chapter is that the opening at the tip can improve the CTs of the Darrieus rotor. The CTs increase percentage of some rotors can reach about 70% compared to the Darrieus rotor without an opening.
- f) Another remarkable finding is that the CP loss percentage of most Darrieus rotors with an opening is less than the CP loss of the Savonius-Darrieus rotor which is about 30. Thus, the Darrieus rotor with an opening has great potential in real field applications.



# CHAPTER 6 THE DARRIEUS ROTOR WITH TWO SETS OF BLADES

## 6.1 Introduction

Two kinds of starting ability improvement methods are investigated and evaluated in the Chapter 3 and Chapter 5. In this chapter, the third starting ability improvement method for the Darrieus rotor is studied. As mentioned in the review, few researchers stated that the Darrieus rotor with several sets of blades has a potential to improve the starting ability and power coefficient. However, the research of the Darrieus rotor with several sets of blades is limited and inadequate. This statement needs to be further investigated. Thus, the CFD investigation about the Darrieus rotor with two sets of blades is conducted in the following sections to evaluate the starting ability and power improvement of the Darrieus rotor with two sets of blades.

## 6.2 Geometry parameters of the investigated rotors

The design geometry parameters of the rotor with two sets of blades are the distance between the two sets of blades, the chord length of the two sets of blades and the offset angle between two sets of blades. The distance between the two sets of blades is calculated by the subtraction of radius of outer blades ( $r_{out}$ ) and radius of inner blades ( $r_{in}$ ). And the chord length of the outer blades and inner blades is defined as

$c_{out}$  and  $c_{in}$ . The offset angle ( $\eta$ ) between two sets of blades is defined as positive when outer blades move ahead. All those geometry parameters will be illustrated in Figure 6.1.

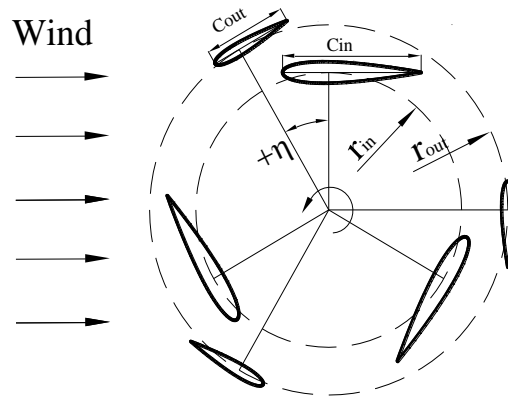


Figure 6.1 Geometry of rotor with two sets of blades

Table 6.1 Dimensions and abbreviations of the tested rotors

	<i>AB25</i>	<i>AB50</i>	<i>BB25</i>	<i>BB50</i>	<i>BB100</i>
<i>Section type(in)</i>	airfoil	airfoil	airfoil	airfoil	airfoil
<i>Section type(out)</i>	arc	arc	airfoil	airfoil	airfoil
$r_{in}(m)$	1.21875	1.1875	1.21875	1.1875	1.1
$r_{out}(m)$	1.28125	1.3125	1.28125	1.3125	1.4
$c_{in}(m)$	0.25	0.25	0.25	0.25	0.223
$c_{out}(m)$	0.25	0.25	0.25	0.25	0.284
$\eta$ (Degree)	0	0	0	0	0

Table 6.1 Dimensions and abbreviations of the tested rotors (continued)

	<b><i>BB200</i></b>	<b><i>BBOP100</i></b>	<b><i>BBOP200</i></b>	<b><i>BBON100</i></b>	<b><i>BBON200</i></b>
<b><i>Section type(in)</i></b>	airfoil	airfoil	airfoil	airfoil	airfoil
<b><i>Section type(out)</i></b>	airfoil	airfoil	airfoil	airfoil	airfoil
<b><i>r<sub>in</sub>(m)</i></b>	1	1.1	1	1.1	1
<b><i>r<sub>out</sub>(m)</i></b>	1.5	1.4	1.5	1.4	1.5
<b><i>c<sub>in</sub>(m)</i></b>	0.208	0.223	0.208	0.223	0.208
<b><i>c<sub>out</sub>(m)</i></b>	0.3125	0.284	0.3125	0.284	0.3125
<b><i>η(Degree)</i></b>	0	20	20	-20	-20

Different combinations of the design parameters were investigated to find the effect of the distance between two sets of blades, the effect of the offset angle and chord length. Moreover, the outer airfoil was replaced with an arc to check the feasibility of the arc utilization. The arcs used have the same length and size as the chord length of the airfoil and the radius of outer blades. Detailed dimensions and abbreviation of the simulated rotors with two sets of blades are listed in Table 6.1. The character ‘A’ in the abbreviation means that blade section is an arc. The character ‘B’ indicates that blade section is NACA 0015 airfoil. The character ‘O’ means that certain offset angles exist between two sets of blades. And the character ‘P’ and ‘N’ represent positive and negative of the offset angle, respectively. The index number after the character is the distance ratio of the distance between two blades to the average

radius of two sets of blades.

### **6.3 The effect of distance between two sets of blades**

The effect of the distance between two sets of blades was evaluated through the comparison of power output curves and values of static torque coefficient for all the cases with different distance. The power output curves of the rotors with two sets of blades were compared with the curve of the rotor with one set of blades whose section is NACA 0015 airfoil. This comparison is presented in Figure 6.2. It is clearly found that the power curves of rotors with arc blades are the lowest among rotors with two sets of blades. It seems that the increasing of distance ratio has negative impact on the power output for the rotors with arc blades. The reason of using the arc is that the fabrication cost of the arc is cheaper than that of the airfoil. However, the simulated results showed that the way of utilization of arc instead of airfoil is impracticable from the power output point of view.

For the rotors with two sets of blades which have airfoil sections, the increasing of the distance ratio has a positive impact on the power output in the beginning. And this positive impact began to disappear when the distance ratio is larger than 50 percentages. The power output began to decrease slightly with the increase of the distance ratio when the distance ratio is larger than 50%. The maximum power is presented in the case of BB50. The maximum power output of the case of BB50 is 2022 which is 9.7% less than the power output of the rotor with a single set of blades which is NACA 0015 section. And the loss value of power output for the case of BB100 and BB200 is about 15.4% and 16.96% compared to the rotor with NACA

0015 airfoil.

In fact, those values are acceptable compared with the loss value of the hybrid Savonius-Darrieus rotor. However, the loss value of the case of BB25 is about 33.9%. And this value is not acceptable for the real application. It is important to point out that the working range of rotor with two sets of blades will also be narrowed compared with the rotor with a single set of blades. It means that the rotor with two sets of blades works at lower rotational speed which means lower noise and bigger size of generator. Low level of noise is beneficial for the utilization in an urban area. A slightly large generator will not have great impact on the installation process due to the vertical axis design.

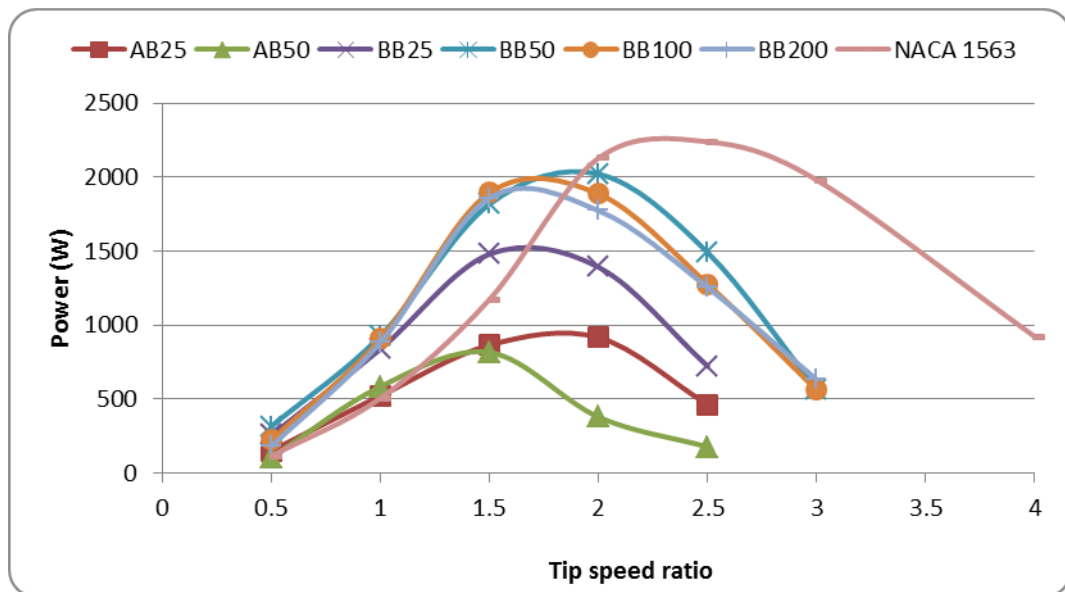


Figure 6.2 Power output of the rotors with two sets of blades for different distance ratios

We have found that the loss of the power output is acceptable in the previous

paragraphs. The best candidate is BB50 from the higher power output point of view. And BB100 and BB200 are also receivable compared with the hybrid Saovnius-Darrieus rotor. Another important issue which is the CTs should be discussed in details to give a right evaluation the practicability of the rotors with two sets of blades. Thus, the values of CTs of rotors with two sets of blade and one set of blade are compared in Figure 6.3.

As stated in the previous, the power output values of the case of AB25, AB50 and BB25 are too low to apply in the real field. Moreover, the CTs values of the case of AB25, AB50 and BB50 are drastically smaller than that of the rotor with NACA 1563 airfoil. The value of CTs will increase significantly with the rise of the distance ratio. The CTs value of the case BB50 is the same level as the CTs value of the case with NACA 1563. Thus, the case BB50 is unacceptable for the real application due to less power output. The CTs values of the case of BB100 and BB200 are extraordinarily higher than that of the case with NACA 1563. Those values are, at least, twice higher than that of the case with NACA 1563. Thus, it is recommended that the case BB100 and BB200 can be used to improve the starting ability of the H-Darrieus rotor under the circumstances of relatively low power output.

It is important to know that the radius of the case used for comparison with one set of blades is 1.25m. This value is the average of the inner radius and outer radius. It may be a little inconvincible to using this average radius. Thus, the loss percentage of the maximum power and increase percentage of CTs were corrected in Table 6.2 using the maximum outer radius which is 1.5m. For the case of BB100 and BB200, the loss of power and increase of the CTs is still acceptable.

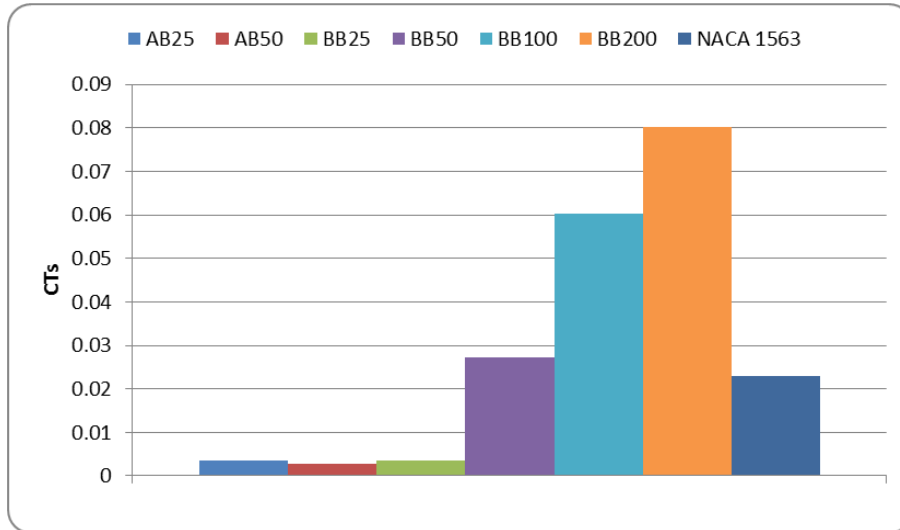


Figure 6.3 CTs of rotors with two sets of blades

Table 6.2 The loss percentage of CP and increase percentage of CTs

	<i>NACA 1563</i>	<i>BB25</i>	<i>BB50</i>	<i>BB100</i>	<i>BB200</i>
<i>Maximum power(W)</i>	2240	1480	2022	1895	1860
<i>Loss percentage</i>		33.9	9.7	15.4	16.96
<i>Corrected percentage</i>		40.68	11.64	18.48	20.352
<i>Average CTs</i>	0.023	0.0034	0.0272	0.06	0.08
<i>Increase percentage</i>		-85	18.2	160.8	247.8
<i>Corrected percentage</i>		-122.4	12.64	111.7	172.08

#### 6.4 The effect of the offset angle between two sets of blades

We have found that the case BB50, case BB100 and case BB200 are acceptable for

the real application. Thus, we want to conduct a further investigation on this type of rotor. In the above paragraphs, two sets of blades are placed parallel to each other. A reasonable question will be raised about how it will be if the two sets of blades are not placed parallel. It means that there will be a certain offset angle between the two sets of blades. And the chord length value of inner airfoil is the same as the outer airfoil in the above paragraphs; another question will be raised about how it will be if the chord length values of the inner and out airfoil are different. That is the reason why we simulated the cases which are named BBOP100, BBOP200, BBON100 and BBON200.

Although there are only four cases to answer the questions addressed above, those four cases are used to find a path. The simulated results of those four cases are presented in Figure 6.5, Figure 6.5 and Table 6.3. The power output loss values of the rotors with zero offset angle and same inner and outer chord length range from 9.7 to 16.96 without correction.

However, the value of the rotors with nonzero offset angle and different inner and outer chord length ranges from 15.8 to 19 without correction. It is found that the offset angle and different inner and outer chord length of the blade have a negative impact on power output compared with zero offset angle and same inner and outer chord length. And this negative impact is also found for the values of CTs. As addressed before, there are only four cases simulated in this part. It is possible that the rotors with another value of the offset angle and value of chord length may have higher power output and CTs. Thus, there are still many kinds of combinations needed to be simulated in the future.

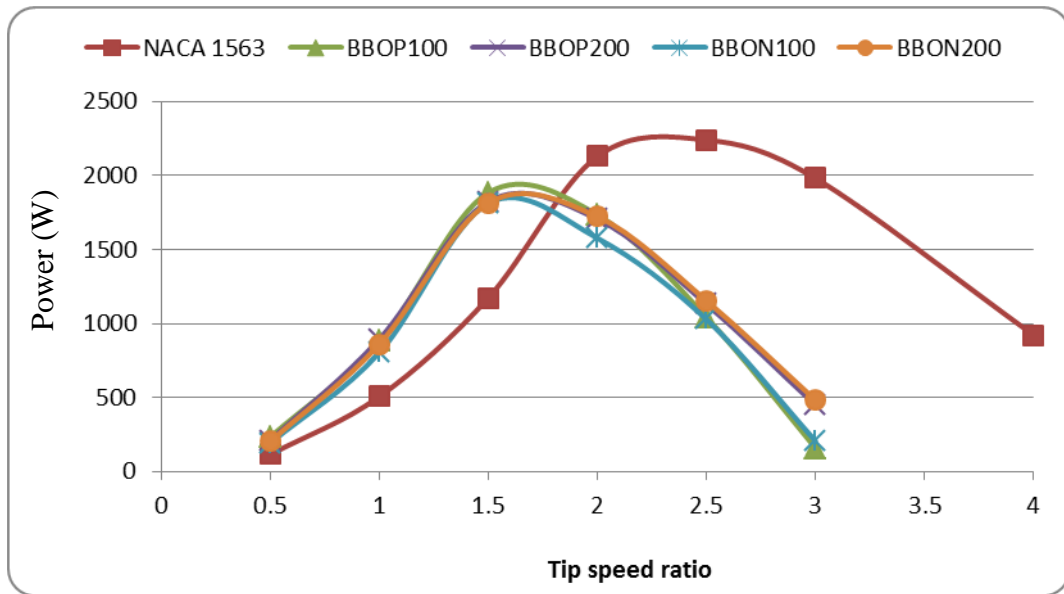


Figure 6.4 Power output curves of the rotor for different offset angle

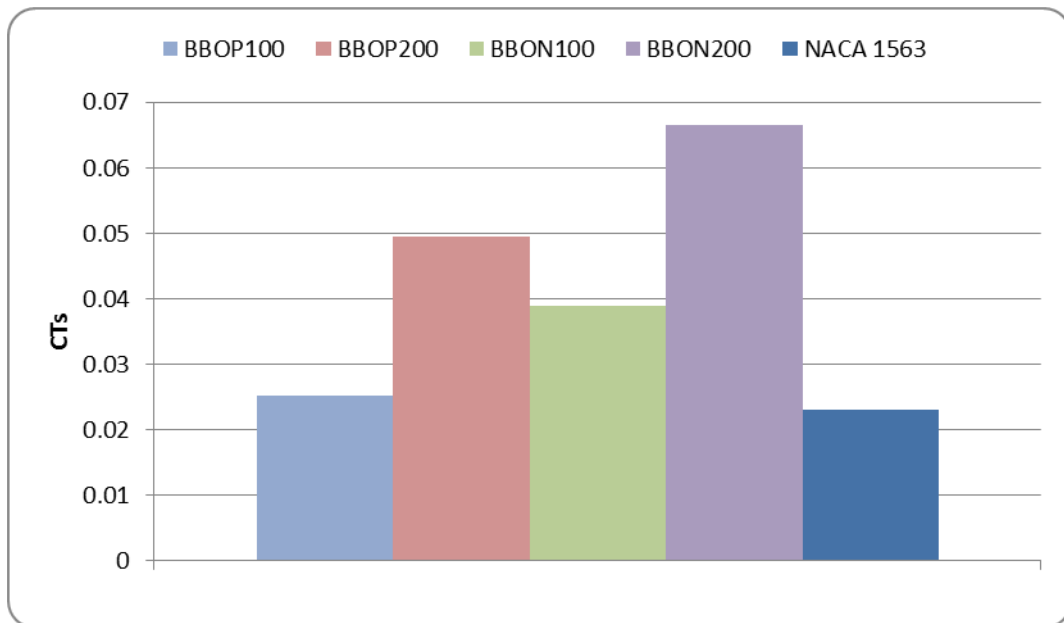


Figure 6.5 CTs values of the rotor for different offset angle

Table 6.3 The loss percentage of power and increase percentage of CTs

	<i>NACA 1563</i>	<i>BBOP100</i>	<i>BBOP200</i>	<i>BBON100</i>	<i>BBON200</i>
<i>Maximum power (W)</i>	2240	1885	1825	1814	1814
<i>Loss percentage</i>		15.8	18.6	19	19
<i>Corrected loss percentage</i>		19	22.2	22.8	22.8
<i>Average CTs</i>	0.023	0.0252	0.0494	0.0389	0.0666
<i>Increase percentage</i>		9.5	114.7	69	189.5
<i>Corrected increase percentage</i>		6.6	79.7	48	131.6

## 6.5 Summary

The effects of the distance and offset angle between two sets of blades on the CTs and CP are investigated through the CFD simulation in this chapter. Moreover, the rotors with different chord length of inner and outer airfoil were also investigated. To summarize, the following conclusions can be drawn:

- a) One of the interesting conclusions found in this chapter is that the CP of the rotors with two sets of blades is generally lower than that of the rotor with one set of blades. This conclusion is different from the statement in literature which stated that the two sets of the blades can improve the CP of the Darrieus rotor.

- b) The usage of the two sets of blades does increase the CTs of the Darrieus rotor. The maximum CTs increase percentage is about 131.6 when the CP loss is 22.8. This significant increase of the CTs makes the Darrieus rotors can start itself easily. It seems that the Darrieus rotor with two sets of blades is better than the Savonius-Darrieus rotor in terms of increase of the CTs and loss of the CP.
- c) Another interesting conclusion is that the offset angle between two sets of blades has a smaller effect on the CP and CTs of the Darrieus rotor with two sets of blades when the chord length of the inner airfoil and outer airfoil is different.

Generally, the usage two sets of blades will improve the CTs of the Darrieus rotor, but suffers the decrease of the CP. And the Darrieus rotor with two sets of blades is superior to the hybrid Savonius-Darrieus rotor in terms of CTs improvement and CP loss. Thus, the Darrieus rotor with two sets of blades is a good method to improve the starting ability of the Darrieus rotor.



# **CHAPTER 7 A NOVEL AIRFOIL OPTIMAL DESIGN PROCESS FOR THE DARRIEUS ROTOR**

## **7.1 Introduction**

The aim of this chapter is to improve the CP of the Darrieus rotor through an optimal airfoil design method proposed by the author. The right airfoil may not only improve the CP of the Darrieus rotor, but also the starting ability of the Darrieus rotor. Hence, an optimal airfoil design process is presented in an effort to gain high CP of the Darrieus rotor. Two NACA airfoil families are studied in this chapter. They are NACA 4-digit-series family and NACA 4-digit-modified-series family.

The purpose of the investigation of NACA 4-digit-series family is to evaluate the prediction ability of the CFD method. And the purpose of the investigation of NACA 4-digit-series family investigation is to validate the efficiency of the optimal airfoil design method created by the author.

The NACA 4-digit-series has only one design parameter. Thus, one factor selection method was combined with the automatic CFD design process.

In terms of NACA 4-digit-modified series family, it has three design parameters. Hence, orthogonal method was used firstly to integrate with the automatic CFD process. Then, one factor selection method based on the conclusions gained from the orthogonal method. Thus, there are two steps of the design of the NACA 4-digit-modified series family. And these two steps are the core of the novel airfoil optimal

design process.

## 7.2 Introduction of the NACA 4-digit-series and NACA 4-digit-modified-series

The airfoil selection research mainly focuses on the NACA 4-digit-series and NACA 4-digit-modified-series airfoils, especially on the latter one. These two families are symmetric airfoils. NACA 4-digit-series airfoils are the most popular airfoils for the Darrieus. The NACA 4-digit-series airfoils are designated by 4-digit number of the form NACA 00 XX. The first two digits mean a symmetric airfoil. The second two digits indicate the thickness-chord ratio. The thickness and chord length are defined as  $t$  and  $c$ , respectively. Thus, the thickness-chord ratio is the only input parameter of the NACA 4-digit-series airfoils. The equation of NACA 4-digit-series airfoils are listed below:

$$\frac{y}{c} = a_0 \left(\frac{x}{c}\right)^{1/2} + a_1 \left(\frac{x}{c}\right) + a_2 \left(\frac{x}{c}\right)^2 + a_3 \left(\frac{x}{c}\right)^3 + a_4 \left(\frac{x}{c}\right)^4 \quad \text{Equation 7.1}$$

The constant in the equation for  $t/c = 0.2$  was calculated from the following boundary conditions:

Maximum ordinate:

$$\frac{x}{c} = 0.3 \quad \frac{y}{c} = 0.1 \quad \frac{dy}{dx} = 0 \quad \text{Equation 7.2}$$

Ordinate at trailing edge:

$$\frac{x}{c} = 1.0 \qquad \frac{y}{c} = 0.002 \qquad \text{Equation 7.3}$$

Magnitude of trailing-edge angle:

$$\frac{x}{c} = 1.0 \qquad \left| \frac{dy}{dx} \right| = 0.234 \qquad \text{Equation 7.4}$$

Nose shape:

$$\frac{x}{c} = 0.1 \qquad \frac{y}{c} = 0.078 \qquad \text{Equation 7.5}$$

Thus, the constants meeting these boundary conditions are calculated below:

$$a_0 = 0.2969 \quad a_1 = -0.1260 \quad a_2 = -0.3516$$

$$a_3 = 0.2843 \quad a_4 = -0.10015$$

The ordinates of the other airfoils in this family are obtained by multiplying  $(t/c)/0.2$  to the ordinates of airfoil with thickness-chord ratio of 0.2.

It is not sufficient to select the airfoil which has only one design parameter. Thus, the NACA 4-digit-modified-series airfoils which have three design parameters were introduced to study the effect of thickness-chord ratio, leading-edge-radius and maximum thickness in tenths of chord aft of the leading edge on the performance of the Darrieus. The designation of NACA 4-digit-modified-series airfoils is a NACA 4-digit adds in a dash and a 2 digit number, for example NACA 0015-63. The meaning of the first four digits is the same as the 4-digit-series airfoils. The first number after dash means an index number of leading-edge index, and the second number is the location of maximum thickness in tenths of chord aft of the leading

edge.

The equation of NACA 4-modified-digit-series airfoils is described below:

Ordinates from leading edge to maximum thickness:

$$\frac{y}{c} = a_0 \left(\frac{x}{c}\right)^{1/2} + a_1 \left(\frac{x}{c}\right) + a_2 \left(\frac{x}{c}\right)^2 + a_3 \left(\frac{x}{c}\right)^3 \quad \text{Equation 7.6}$$

Ordinates from the maximum thickness to trailing edge:

$$\frac{y}{c} = d_0 + d_1 \left(1 - \frac{x}{c}\right) + d_2 \left(1 - \frac{x}{c}\right)^2 + d_3 \left(1 - \frac{x}{c}\right)^3 \quad \text{Equation 7.7}$$

The constant in the equation for  $t/c = 0.2$  were calculated from the following boundary conditions:

Maximum ordinate:

$$\frac{x}{c} = m \quad \frac{y}{c} = 0.1 \quad \frac{dy}{dx} = 0 \quad \text{Equation 7.8}$$

Leading-edge radius:

$$\frac{x}{c} = 0 \quad R = \frac{a_0^2}{2} \quad \text{Equation 7.9}$$

Radius of curvature at maximum thickness:

$$\frac{x}{c} = m \quad R = \frac{(1-m)^2}{2d_1(1-m) - 0.588} \quad \text{Equation 7.10}$$

Ordinate at trailing-edge:

$$\frac{x}{c} = 1.0 \quad \frac{y}{c} = d_0 = 0.002 \quad \text{Equation 7.11}$$

Magnitude of trailing-edge angle:

$$\frac{x}{c} = 1.0 \qquad \frac{dy}{dx} = d_1 = f(m) \qquad \text{Equation 7.12}$$

Table 7.1 The relationship between values of  $d_1$  and values of  $m$

$m$	$d_1$
0.2	0.2
0.3	0.234
0.4	0.315
0.5	0.465
0.6	0.700

Table 7.2 The relationship between leading-edge index number and values of  $a_0$

Leading-edge index number	$a_0$
0	0
6	0.2969
9	0.514246

The values of  $d_1$  were chosen according to Stack and Von Doenhoff (1997) to avoid reversals of curvature. The relationship between values of  $d_1$  and values of  $m$  is

given in Table 7.1 The leading-edge index which is proportion to  $a_0$  was assigned to the leading edge arbitrarily. This proportion is presented in Table 7.2. Based on the equations of the NACA 4-modified-digit-series, a code compiled by the MATLAB programming language was written to generate the ordination of the NACA 4-modified-digit-series airfoils. The ordination was used as the input file of the mesh generation process mentioned in the section of methodology.

### **7.3 One factor selection for NACA 4-digit-series**

The thickness-chord ratio is the only design parameters related to the NACA 4-digit-series airfoils. Therefore, the effect of the thickness-chord ratio on the performance of the rotor was studied through the CFD simulation. The studied thickness-chord ratios are 0.15, 0.18, 0.21 and 0.24.

The simulated results were presented in Figure 7.1. It is clear that the maximum power coefficient is increased as the decrease of the thickness-chord ratio. This conclusion is the same as the conclusion gained by Migliore et al. (Migliore and Fritschen 1982). Three different thickness-chord ratios were compared by Migliore et al. They are 0.12, 0.15 and 0.18. That is the reason why NACA 0012 and 0015 were widely used for Darreius rotors (South and Rangi 1972, Templin 1974, Sheldahl and Sandia National Labs. 1981) built previously.

And the purpose to use the NACA 0015 airfoil is to improve the structural strength of the rotors. This simulation results again validate the prediction ability of the CFD simulation. The change of the CTs varies linearly with the thickness-chord ratio. The

larger the thickness-chord ratio is, the higher the CTs are. And the CTs of the rotor can be interpreted through the linear equation easily roughly.

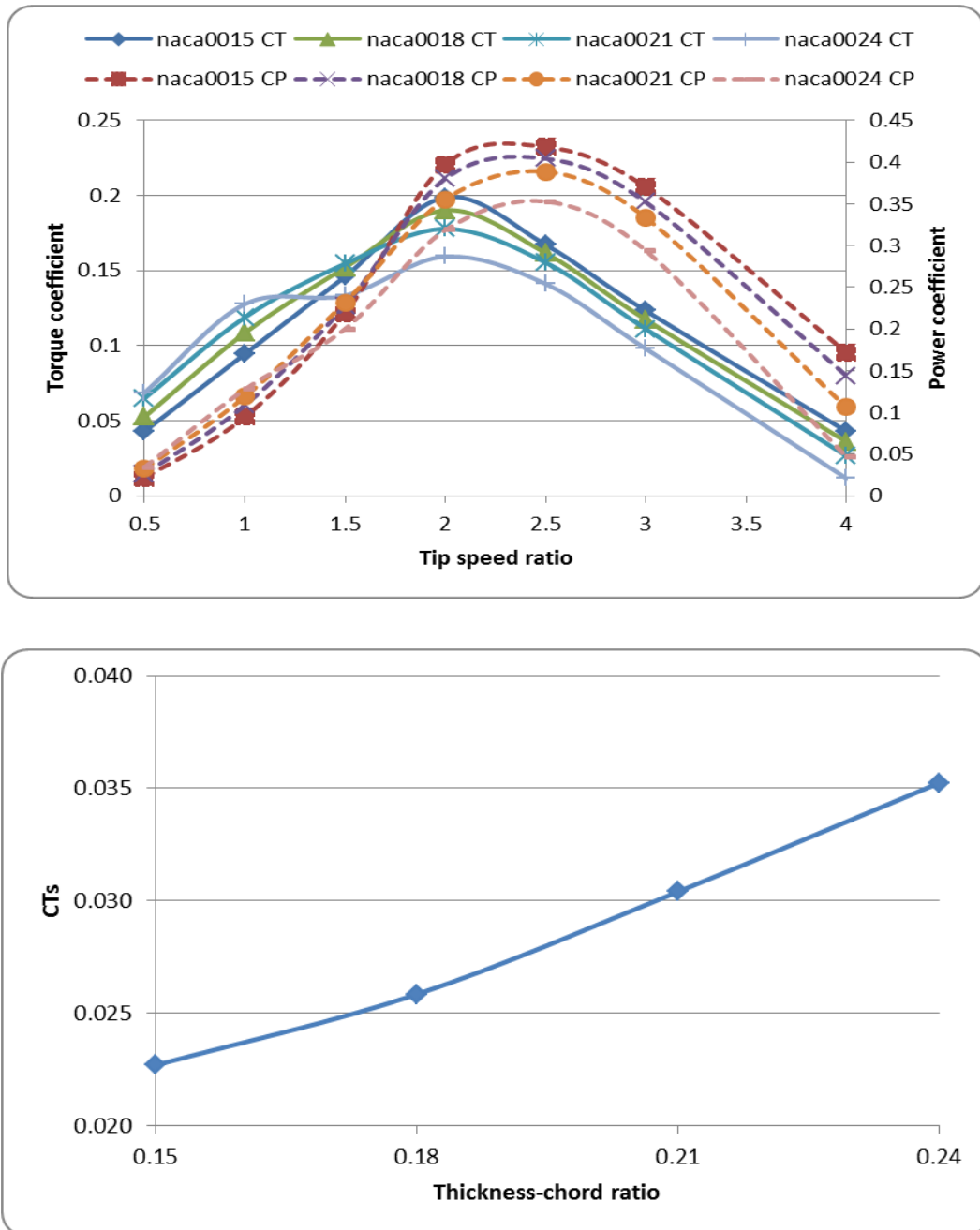


Figure 7.1 Effect of the thickness-chord ratio on the performance of the rotor

## **7.4 A novel airfoil optimal design process**

In this section, a novel airfoil optimal design process will be presented. This novel airfoil optimal design process has two steps.

In the first step, the orthogonal algorithm together with the automatic CFD analysis process mentioned in Chapter 4 is used to evaluate the impact weight of each design parameter.

In the second step, one factor optimal method based on the impact weight found in the first step is used to work with the automatic CFD analysis process to further optimize the airfoil.

This novel airfoil optimal design process will be presented in the following sections in detail.

### **7.4.1 Selection using the orthogonal method for NACA 4-modified-digit-series**

NACA 4-modified-digit-series airfoils have three design parameters which will affect the performance of the Darrieus. In the previous section, the effect of these three parameters was investigated through the variation of one design parameters at a time. However, this one dimension selection method may be gain wrong conclusions when the design parameters have interaction.

The full factorial design method can find the effect of all factor's combinations, but it will cost many efforts to evaluate the impact of each factor for the case with massive number of factors and levels. The design parameters are called factors. And

the numbers needed to be evaluated of each parameter are called levels.

For the NACA 4-modified-digit-series airfoils, there are three factors. They are thickness-chord ratio, leading-edge index number and the maximum thickness in tenths of chord aft of the leading edge.

Table 7.3 The factors and levels investigated

Factors		Levels	1	2	3	4
		Thickness-chord ratio	Factor A	15	18	21
Leading-edge number	Factor B	0	3	6	9	
Maximum thickness in tenths of chord	Factor C	2	3	4	5	

The thickness-chord ratio ranges from 0 to 1. The leading-edge number ranges from 0 to 9. And the maximum thickness in tenths of chord aft of the leading edge ranges from 0 to 1. The levels of thickness-chord ratio are selected based on the section 4.6.1. 0.12 thickness-chord ratio is not selected due to the structure consideration mentioned by Migliore et al. (Migliore and Fritschen 1982). The levels and factors were listed in Table 7.3.

Although four levels were selected for each factor, 64 combinations need to be investigated to find the impact of each parameter. One combination needs about 36 hours to get the performance curve with 7 points and CTs. Consequently, 64 combinations need 2304 hours and 3.2 months to finish the calculation.

Table 7.4 Orthogonal list  $L_{16}(4^5)$

Column No. Test No.	1	2	3	4	5
1	1(15)	1(0)	1(2)	1	1
2	1(15)	2(3)	2(3)	2	2
3	1(15)	3(6)	3(4)	3	3
4	1(15)	4(9)	4(5)	4	4
5	2(18)	1(0)	2(3)	3	4
6	2(18)	2(3)	1(2)	4	3
7	2(18)	3(6)	4(5)	1	2
8	2(18)	4(9)	3(4)	2	1
9	3(21)	1(0)	3(4)	4	2
10	3(21)	2(3)	4(5)	3	1
11	3(21)	3(6)	1(2)	2	4
12	3(21)	4(9)	2(3)	1	3
13	4(24)	1(0)	4(5)	2	3
14	4(24)	2(3)	3(4)	1	4
15	4(24)	3(6)	2(3)	4	1
16	4(24)	4(9)	1(2)	3	2

In order to save time and expense, the orthogonal experimental design method is adopted to investigate the impact of the each factor as comprehensively as possible.

The orthogonal experimental design is a method which uses part of the combinations to evaluate the impact of the each factor.

An orthogonal list  $L_{16}(4^5)$  is used due to four levels and three factors to be investigated. The orthogonal list  $L_{16}(4^5)$  presented in Table 7.4 is the list used for selection of 4 levels and five factors. The levels of each factor for the airfoil were also bracketed in Table 7.4. The last two columns were not used because three factors were considered. Thus, 16 cases were built with 16 different airfoils. These airfoils are NACA 1502, NACA 1533, NACA 1564, NACA 1595, NACA 1803, NACA 1832, NACA 1865, NACA 1894, NACA 1832, NACA 1865, NACA 1894, NACA 2104, NACA 2135, NACA 2162, NACA 2193, NACA 2405, NACA 2434, NACA 2463 and NACA 2492. All the cases were built and simulated through the automatic CFD analysis process mentioned in the previous section.

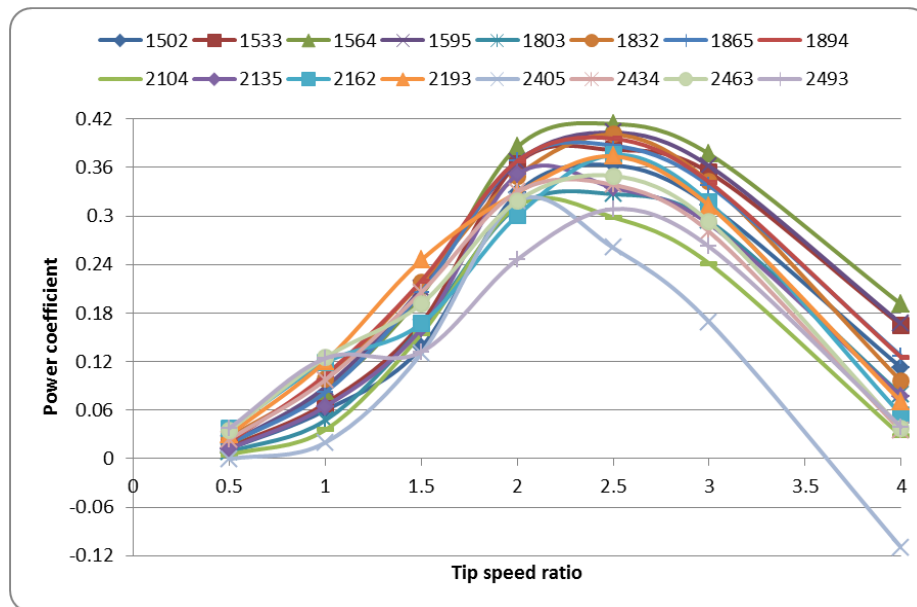


Figure 7.2 The power curves of all cases

The power coefficient curves of the 16 rotors with different airfoils are depicted in

Figure 7.2. Based on this figure, the rotor with NACA 1564 airfoil has the highest power coefficient, especially when the TSR range is larger than 2. The power curve of the rotor with NACA 2493 airfoil is the lowest, especially when the TSR range is larger than 2. Through this comparison, the effect of different factors cannot be found easily.

Thus, the impact of different factors on maximum power coefficient was analyzed through Table 7.5. The lattices of Table 7.5 between the first row to sixteenth and first column to third column are the same as the corresponding lattices of Table 7.4. The last column of Table 7.5 lists the maximum power coefficient of each corresponding case.  $K_1$  includes three numbers. The first number represents the sum of the power coefficient for level 1 and factor A. The second number represents the sum of the power coefficient for level 1 and factor B. The third number represents the sum of the power coefficient for level 1 and factor C. The calculation of the three numbers of  $K_2$  is similar as that of  $K_1$ . The only difference is that  $K_2$  calculates the sum of power coefficient of level 2 for three factors.

The first number of  $\kappa_1$  is the average of the power coefficient for level 1 and factor A. The second number of  $\kappa_1$  is the average of the power coefficient for level 1 and factor B. The third number of  $\kappa_1$  is the average of the power coefficient for level 1 and factor C. The difference between the  $\kappa_1$  and  $\kappa_2$  is the same as the difference between  $K_1$  and  $K_2$ .

In the end, there will be three columns of  $\kappa_1$ ,  $\kappa_2$ ,  $\kappa_3$  and  $\kappa_4$  related to three different factors. For each column, the difference between  $\max(\kappa_i)$  and  $\min(\kappa_i)$  is calculated

in the penultimate row of Table 7.5. This difference reveals the impact weight of different factors. In the last row of Table 7.5, the optimum level for different factors was presented. Based on the analysis, it is found that among the impact weight of three factors, the thickness-chord ratio occupies first place; leading-edge number comes second. Maximum thickness in tenths of chord has the smallest impact on the power coefficient. The optimal level of the factor A, factor B and factor C is 1, 3 and 3. The corresponding airfoil is NACA 0015-64 airfoil. This airfoil is one of the tested airfoils. And the maximum power comparison of the 16 cases presented in Figure 7.3 pointed that the rotor with NACA 0015-64 has the best power coefficient..

Table 7.5 The maximum CP results of the orthogonal method

<i>Test No.</i> \ <i>Column No.</i>	<i>1</i> <i>A</i>	<i>2</i> <i>B</i>	<i>3</i> <i>C</i>	<i>Maximum power</i>
<i>1</i>	1(15)	1(0)	1(2)	0.362775
<i>2</i>	1(15)	2(3)	2(3)	0.38175
<i>3</i>	1(15)	3(6)	3(4)	0.413975
<i>4</i>	1(15)	4(9)	4(5)	0.4033
<i>5</i>	2(18)	1(0)	2(3)	0.327225
<i>6</i>	2(18)	2(3)	1(2)	0.400825
<i>7</i>	2(18)	3(6)	4(5)	0.38725
<i>8</i>	2(18)	4(9)	3(4)	0.39585
<i>9</i>	3(21)	1(0)	3(4)	0.31264
<i>10</i>	3(21)	2(3)	4(5)	0.35136
<i>11</i>	3(21)	3(6)	1(2)	0.37565

Table 7.5 The maximum CP results of the orthogonal method (continued)

<i>Test No.</i> \ <i>Column No.</i>	<i>1</i> <i>A</i>	<i>2</i> <i>B</i>	<i>3</i> <i>C</i>	<i>Maximum power</i>
<i>12</i>	3(21)	4(9)	2(3)	0.374
<i>13</i>	4(24)	1(0)	4(5)	0.31856
<i>14</i>	4(24)	2(3)	3(4)	0.338725
<i>15</i>	4(24)	3(6)	2(3)	0.34975
<i>16</i>	4(24)	4(9)	1(2)	0.308675
$K_1$	1.5618	1.3212	1.447925	
$K_2$	1.51115	1.47266	1.432725	
$K_3$	1.41365	1.526625	1.46119	
$K_4$	1.31571	1.481825	1.46047	
$\kappa_1$	0.39045	0.3303	0.361981	
$\kappa_2$	0.377788	0.368165	0.358181	
$\kappa_3$	0.353413	0.381656	0.365298	
$\kappa_4$	0.328928	0.370456	0.365118	
$Max(\kappa_i)-Min(\kappa_i)$	0.061522	0.051356	0.007117	
<i>Optimal level</i>	A1	B3	C3	

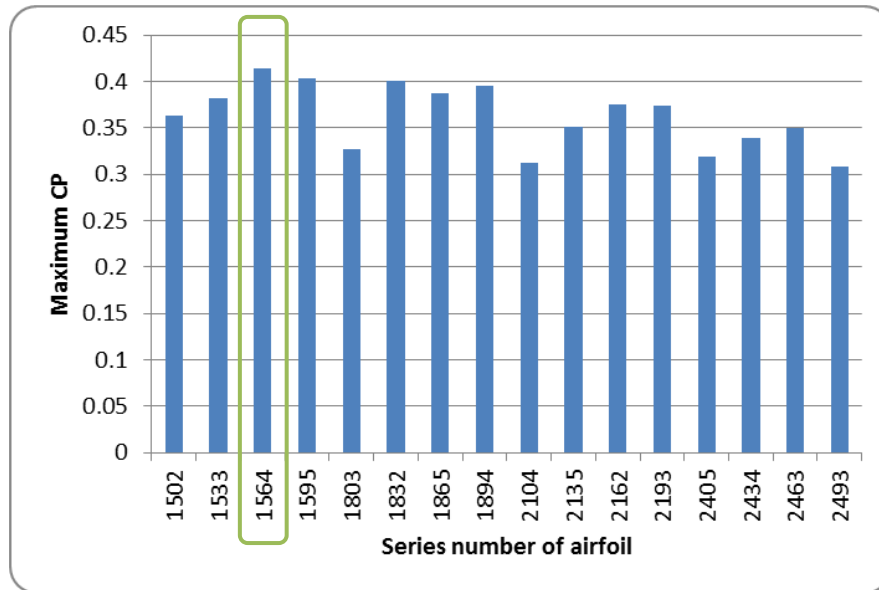


Figure 7.3 Maximum power coefficient for 16 different cases

The similar analysis method is adapted to the CTs of rotors. The analysis results are listed in Table 7.6. It is found that the thickness-chord ratio occupies the first place among the impact weight of three factors; Maximum thickness in tenths of chord comes second. Leading-edge number has the smallest impact on the CTs.

The optimal level of the factor A, factor B and factor C is 4, 4 and 1. The corresponding airfoil is NACA 0024-92. This airfoil is not covered in the list of orthogonal method. The simulated airfoils which are close to the optimal airfoil are NACA 0024-93 airfoil and NACA 0024-63 airfoil. From Figure 7.4, the CTs of the rotors with NACA 0024-93 and NACA 0024-63 airfoil is higher than those of the other cases. Hence, the conclusion gained from the analysis table offers valuable guidance for the selection of the airfoils.

Table 7.6 The CTs results of the orthogonal method

<i>Test No.</i> \ <i>Column No.</i>	<i>I</i> <i>A</i>	<i>2</i> <i>B</i>	<i>3</i> <i>C</i>	<i>CTs</i>
<i>1</i>	1(15)	1(0)	1(2)	0.02089
<i>2</i>	1(15)	2(3)	2(3)	0.0196
<i>3</i>	1(15)	3(6)	3(4)	0.01743
<i>4</i>	1(15)	4(9)	4(5)	0.01586
<i>5</i>	2(18)	1(0)	2(3)	0.01749
<i>6</i>	2(18)	2(3)	1(2)	0.03052
<i>7</i>	2(18)	3(6)	4(5)	0.01363
<i>8</i>	2(18)	4(9)	3(4)	0.02234
<i>9</i>	3(21)	1(0)	3(4)	0.01122
<i>10</i>	3(21)	2(3)	4(5)	0.01107
<i>11</i>	3(21)	3(6)	1(2)	0.02985
<i>12</i>	3(21)	4(9)	2(3)	0.02863
<i>13</i>	4(24)	1(0)	4(5)	-0.0002
<i>14</i>	4(24)	2(3)	3(4)	0.02673
<i>15</i>	4(24)	3(6)	2(3)	0.03715
<i>16</i>	4(24)	4(9)	1(2)	0.03261
$K_1$	0.07378	0.0494	0.11387	
$K_2$	0.08398	0.08792	0.10287	
$K_3$	0.08077	0.09806	0.07772	

Table 7.6 The CTs results of the orthogonal method (continued)

<i>Column No.</i>	<i>1</i>	<i>2</i>	<i>3</i>	<i>CTs</i>
<i>Test No.</i>	<i>A</i>	<i>B</i>	<i>C</i>	
$K_4$	0.09629	0.09944	0.04036	
$\kappa_1$	0.018445	0.01235	0.028468	
$\kappa_2$	0.020995	0.02198	0.025718	
$\kappa_3$	0.020193	0.024515	0.01943	
$\kappa_4$	0.024073	0.02486	0.01009	
$Max(\kappa_i)-Min(\kappa_i)$	0.005628	0.01251	0.018378	
<i>Optimal level</i>	A4	B4	C1	

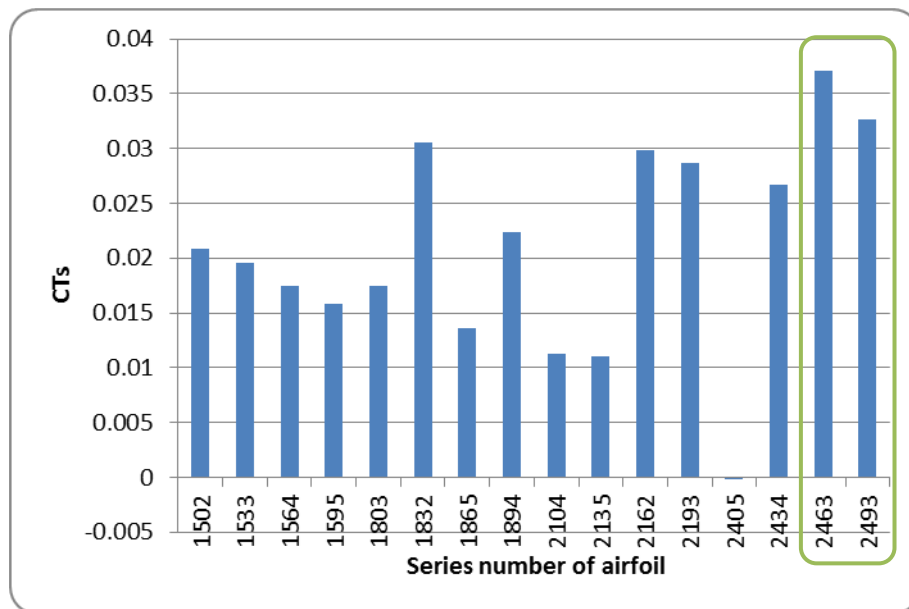


Figure 7.4 Static torque coefficient for 16 different cases

#### **7.4.2 Selection method changes one factor each time based on the orthogonal method for NACA 4-modified-digit-series**

Based on the analysis of the orthogonal method, it is found that the change of the airfoil's thickness-chord ratio has the greatest impact on the performance of the Darrieus rotor. And the impact effect of the maximum thickness in tenths of chord is the lowest among the three factors. The NACA 0015-64 has proven to be the best airfoil for the Darrieus rotor using the orthogonal method. However, the orthogonal method can only offer the weight of the different factors and there are still infinite combinations of the three factors.

Thus, the selection method which changes one factor each time was conducted based on the conclusions gained from the orthogonal method. They are a selection which changes the maximum thickness in tenths of chord, a selection which changes of the thickness-chord ratio and selection which changes of the leading-edge number. Through those selections, the effect of the each factor can be demonstrated well from the considering the effect of only one factor point of view. And those selections to some extent are the extension of orthogonal method.

For the cases of change of maximum thickness in tenths of chord, the thickness-chord ratio is 0.15 and the leading-edge number is 6 to follow the conclusions of the orthogonal method. For the cases of changing the leading-edge number, the thickness-chord ratio is 15% and maximum thickness in tenths of chord is 3, which should be 4 to conform to the conclusion of orthogonal method. The reason why the case with 30% of chord is used is that the effect of the maximum thickness in tenths

of chord is the lowest, and we want to investigate more different combinations. In the end, the effect of the thickness-chord ratio was studied when the leading-edge number is 6 and the maximum thickness in tenths of chord is 3 or 4.

#### 7.4.2.1 Maximum thickness in tenths of chord

The effect of the maximum thickness in tenths of chord is described in Figure 7.5 and Table 7.7. This effect of the maximum thickness in tenths of chord is limited in the area where the thickness-chord ratio is 0.15 and the leading-edge number is 6. The lowest power curve seems to be the curve of the rotor with NACA 0015-63 airfoil. When TSR is less than 2.5, the highest power curve is the curve of the rotor with NACA 0015-62 airfoil. At the range of TSR from 2.5 to 4, the highest power curve is the curve of the rotor with NACA 0015-64 airfoil. From Table 7.7, the highest CP does not occur for the rotor with NACA 0015-64 which is the best candidate of the selection of orthogonal method. The best option for this one dimensional selection may be the rotor with NACA 0015-62.

Table 7.7 The maximum and average CP for maximum thickness in tenths of chord

	maximum CP	Average CP
NACA 0015-62	0.41655	0.257
NACA 0015-63	0.4045	0.232
NACA 0015-64	0.41075	0.252
NACA 0015-65	0.39875	0.234

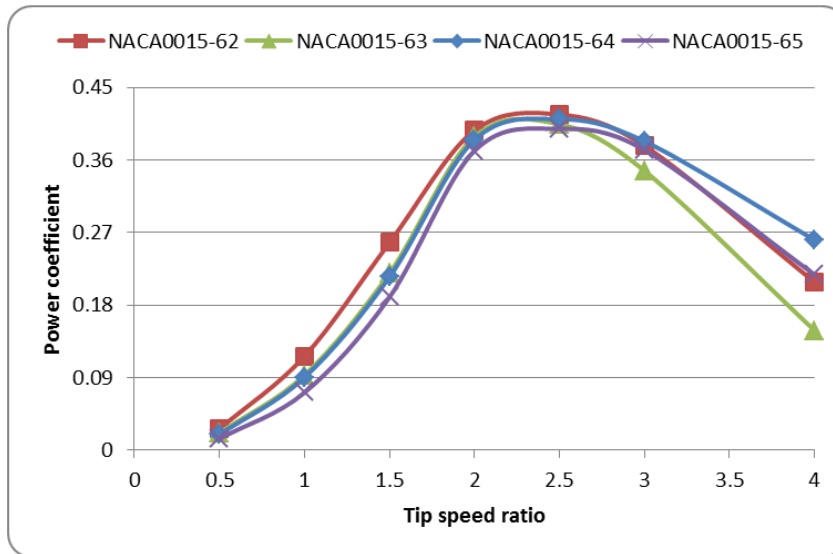


Figure 7.5 The effect of the maximum thickness in tenths of chord

It should be pointed out that the orthogonal method is some kind of global optimization method and the orthogonal method only considers part of the combinations of the whole solution space.

Thus, it is not surprising the best candidate of the orthogonal method may not be the best candidate of the one dimensional selection. To put it another way, the orthogonal method does offer the valuable guidance for the one dimensional selection because the difference between the best candidate of the orthogonal method and the best candidate of this one dimensional selection is fairly small.

This small difference conformed to the conclusion gained with the orthogonal method which indicates that the impact weight of the maximum thickness in tenths of chord is the smallest. Thus, the results of the one dimensional selection proved that this one dimensional selection is worthy. In the end, the maximum CP does not vary linearly with the maximum thickness in tenths of chord when the thickness-

chord ratio is 0.15 and the leading-edge number is 6.

#### 7.4.2.2 Leading-edge number

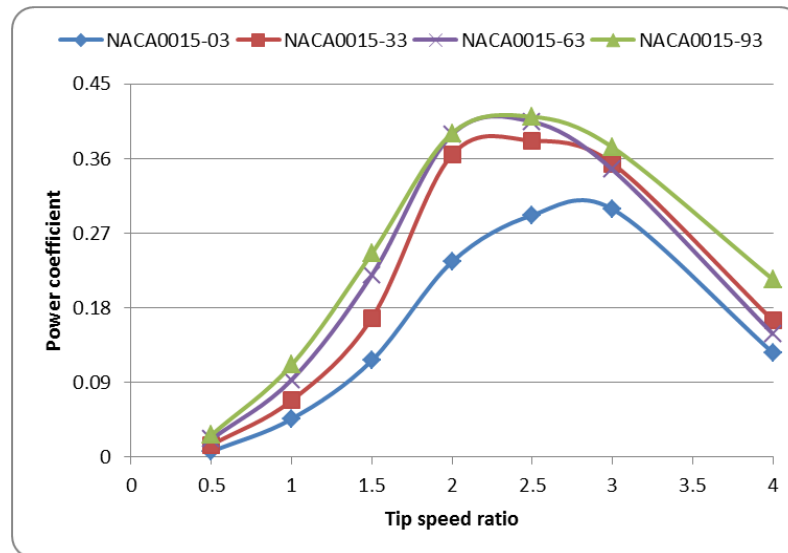


Figure 7.6 Effect of the leading-edge number

The effect of the leading-edge number presented in Figure 7.6 is very obvious. With the increase of the leading-edge number, the maximum CP is increased. The power coefficient curve of the rotor with leading-edge number zero is significantly lower than that of other rotors. In the orthogonal method, we found that the leading-edge number is the second most influential factor. And these one dimensional simulation results proved the reliability of this conclusion.

#### 7.4.2.3 Thickness-chord ratio

As discussed in the orthogonal method, the thickness-chord ratio has the greatest

impact on the power coefficient of rotors. Thus, the effect of the thickness-chord ratio was studied when the leading-edge number is 6 and the maximum thickness in tenths of chord is 4. From Figure 7.7, it is found that the power coefficient is not improved as the decrease of the thickness-chord ratio. This conclusion is not the same as the conclusion gained for the NACA 4-digit-series airfoils. The power coefficient of the rotor with NACA 0018-64 is significantly higher than that of other rotors especially when the TSR is larger than 2. It is important to state that the power coefficient of the rotor is not only dependent on the thickness-chord ratio of airfoils.

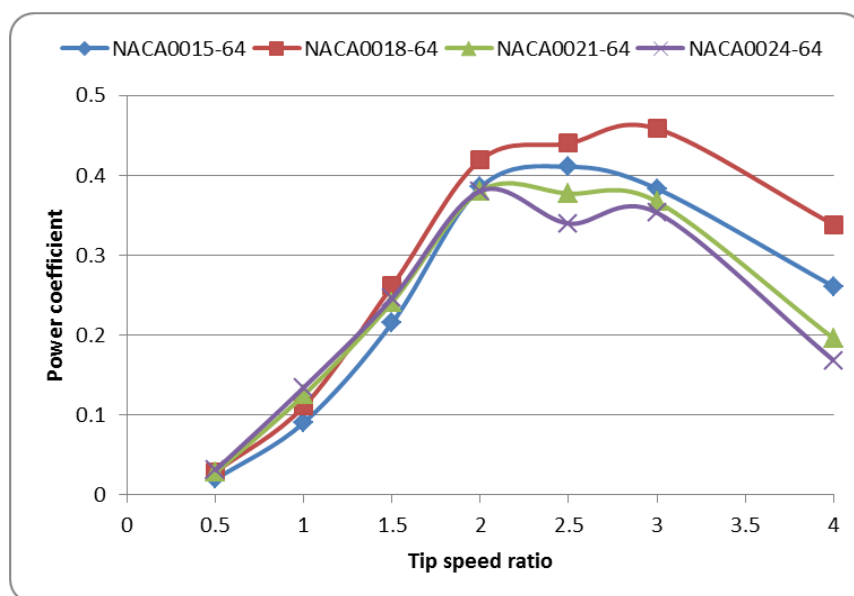


Figure 7.7 Effect of Thickness-chord ratio

The three factors of the airfoils together determine the power coefficient and interact with each other. The optimal airfoil in the selection of NACA 4-digit-series airfoils is NACA 0015. The optimal rotor in the selection of maximum thickness in tenths of chord is a rotor with NACA 0015-64. The optimal rotor in the selection of thickness-chord ratios is a rotor with NACA 0018-64. The maximum power of the rotor with

NACA 0015 is 0.397. The maximum power coefficient of the rotor with NACA 0015-64 is 0.41655. And the maximum power coefficient of the rotor with NACA 0018-64 is 0.4585 which is about 15.5% and 10% higher than the CP value of the rotor with NACA 0015 and NACA 0015-62. Thus, the selection method combined the orthogonal method and one dimensional method proved to be fairly efficient to find the optimal airfoil for the Darrieus rotor. Although, this combination screens out one of the airfoils which can be used for the Darrieus rotor, a further filtration needs to be carried out to search the entire solution domain.

## **7.5 Summary**

The aim of this chapter is to improve the CP of the Darrieus rotor through the novel airfoil optimal design process. Two airfoil families are studied in this chapter. They are the NACA 4-digit-series family and the NACA 4-digit-modified-series family. In a summary, the following conclusions are obtained:

- a) One factor selection algorithm is combined with the automatic CFD analysis process to optimal design of the NACA 4-digit-series family because this airfoil family has only one design parameter. The CFD analysis results show that the maximum power coefficient is increased as the increase of the thickness-chord ratio. This conclusion is the same as the conclusion gained by other researchers. This again proves that the CFD simulation strategies selected in Chapter 4 are reliable.
- b) A novel airfoil optimal design process is established in this chapter for

the NACA 4-digit-modified-series family because this airfoil family has three design parameters. This novel optimal design process not only can find the impact weight of each design parameters, but also found an optimal airfoil whose CP is 9.8% higher than that of the Darrieus rotor with NACA 0015 airfoil which is commonly used by most researchers.

- c) The novel airfoil optimal design process also found that among the impact weight of three factors on the power coefficient, the thickness-chord ratio occupies first place; leading-edge number comes second. Maximum thickness in tenths of chord has the smallest impact on the power coefficient.
- d) This novel airfoil optimal design process can also be used for the optimal design of the airfoil with many design parameters.

In general, this novel optimal design process not only can find the impact weight of each design parameters, but also found an optimal airfoil which can be used for to improve the CP of the Darrieus rotor. And this novel optimal design process lays down the foundation of the multiple-parameter airfoil design process for the Darrieus rotor. Through the multiple-parameters airfoil design process, the optimal airfoil design will not be extended to a large number of airfoils and will help the development of the airfoil design.

## CHAPTER 8 SUMMARY AND FUTURE WORKS

### 8.1 Summary of this thesis

The aim of this thesis is to improve the starting ability and the power coefficient of the Darrieus rotor. The logical relationship between chapters of this thesis and contributions of each chapter are summarized below:

- a) In chapter 2, a comprehensive review to find the methods which can improve the starting ability and CP of the Darrieus rotor. After review, three methods are proposed to improve the starting ability of the Darrieus rotor. One method is proposed to improve the CP of the Darrieus rotor. This chapter also offers a valuable information about the evolution of the VAWTs, the research focus of the VAWTs and the research insufficiency of the VAWTs.
- b) In chapter 3, CFD simulation and wind tunnel test are used to study the first starting ability improvement method (two-stage Savonius rotor). CFD simulation is conducted firstly for the one-stage Savonius rotor. And it is found that the CFD simulation is not suitable for the two-stage Savonius rotor due to the complicated the geometry of this rotor. Thus, wind tunnel test is conducted for the research about the two-stage rotor. The effects of the stage, blade number, gap rate, phase shift angle on the starting ability (CTs) and CP is evaluated in this chapter. It presents a detailed investigation of the two-stage Savonius rotor with two and three blades. And the starting ability of

this two-stage Savonius is also well evaluated. This wind tunnel test also enriches the understanding of the two-stage Savonius rotor with two and three blades.

- c) In chapter 4, CFD simulation processes and strategies are discussed to find the right CFD simulation process and strategies for the study of second and third starting ability improvement methods and the study of a novel airfoil optimal design process. The discussion of the CFD simulation processes assigns the different CFD simulation processes to the different starting ability improvement methods and CP improvement methods. And the discussion of the CFD strategies finds the right and efficient CFD strategies for the CFD simulation of the Darrieus rotor. None of such comprehensive discussion has been found before. It is useful not only for the researches conducted in the following chapter, but also for someone who want to use the CFD to simulate the Darrieus rotor.
- d) Based on CFD simulation discussion in Chapter 4, Chapter 5 presents the simulation of the second starting ability improvement method of the Darrieus rotor (the Darrieus rotor with an opening at blade tip). This method cannot be found in the published literatures and is a new method proposed by the author. The opening at the blade tip can improve the starting ability of the Darrieus rotor when the CP loss is acceptable. However, the opening ratio and opening location has a different effect on the starting torque and CP. And this paper gives a detailed study about the effect of the opening ratio and opening location on the CTs and CP. This will offer a reference for the real design of

this kind of Darrieus rotor. In addition, this new kind of Darrieus rotor gives a new form or type of the Darrieus rotor

- e) Based on CFD simulation discussion in Chapter 4, Chapter 6 presents the simulation of the third starting ability improvement method of the Darrieus rotor (the Darrieus rotor with two sets of blades). Few researchers have been conducted for this kind of Darrieus rotor. And they claimed that several sets of blades will improve the starting ability and the CP of the Darrieus rotor. However, a detailed CFD study shows that two sets of blade can improve the starting ability of the Darrieus rotor, but will reduce the CP of the Darrieus rotor. The study of the distance and offset angle between two sets of blades evaluates the effects of those design parameters which has never been studied carefully.
- f) Based on CFD simulation discussion in Chapter 4, Chapter 7 introduces the establishment of the novel airfoil optimal design process to improve the CP of the Darrieus rotor. The novel airfoil optimal design process has two steps. The first step is to evaluate the impact weight of the each design parameter. Then, one factor design based on the impact weight found in the first step is used to further study the airfoil in the second step. By doing this, not only is the impact weight of each design parameter found, but also one optimal airfoil is found. This novel airfoil optimal design process not only extended the Darrieus rotor airfoil design from one-factors to three factors, but also laid down the fundamentals of the parametric airfoil design process for Darrieus rotors.

## 8.2 Future work

### **Research work about the Savonius rotor:**

The method combined with the CFD and GA selection needs to be adopted for the one-stage rotor without the block which will eliminate the omnidirectional ability.

The method of the combination of the CFD and GA selection is used only for the 2D geometry design of one-stage rotor current with augmented device, especially for the design of the blade profile. It also can be extended to the 3D geometry design which will consider the effect from the z direction. This will take account into the effect of the aspect ratio and the effect of the helix and twist. After the simulation through the CFD and GA selection, the related experiment should be conducted to validate the simulated results. The researches about the augmentation devices and the interaction of rotors seem not sufficient.

The research of the two-stage Savonius rotor is studied independently. The interaction between the two-stage Savonius rotor and the Darrieus rotor is needed to be evaluated in the future.

### **Research work about the Darrieus rotor:**

In this thesis, two airfoil sections were used for the rotors with an opening at the blade tip. One airfoil section was used for the rotors with two sets of blades. And the airfoil selection is only focused on the NACA 4-digit-series and NACA 4-digit-modified-series. In fact, there are still many kinds of airfoil series needing to be investigated for the rotors with an opening at the blade tip, rotors with two sets of

blades and rotors with one set of blades. One of original aims is this thesis is to parameterize the airfoil with several factors considering the effect of the flaps and slots and find the best candidate using the optimum selection method for the power generation of the VAWTs.

The aerodynamic mechanics of the Darrieus rotor with opening and two sets of blades should be studied to understand the effects of the design parameters on the performance of these two kinds of vertical axis wind turbine.

**A real 1.5kW vertical axis wind turbine:**

A real 1.5kW Darreius rotor has been established. The real power coefficient of the 1.5kW VAWTs will be recoded in the future (Appendix A).



# **APPENDIX A THE CONSTRUCTION OF AN 1.5kW DARRIEUS ROTOR**

## **Appendix A 1. Introduction**

In this chapter, an experimental model, 1.5kW Darrieus rotor with an opening simulated in Chapter 5 and the optimal airfoil found in Chapter 7, is constructed to investigate the effectiveness of the opening and the actual performance of the Darrieus rotor with the optimal NACA 0018-64 airfoil in the future. The construction and design process of this model 1.5kW VAWT is also described in detail. This offers some suggestions for the further improvement of this micro Darrieus rotor.

In our renewable energy research group, four members were engaged in this project. Professor HongXing Yang is in charge of the management of the whole project. Professor ChengZhi Lou is in charge of the design of the electrical system.

The tower is designed and checked by a professor of the CSE. Jan Kumbernuss who was a PhD student focused on the design of the magnetic bearing and central column. And I focused on the design of the blades and struts and contact with the manufacturers.

In fact, most of the time Jan Kumbernuss and I worked together and shared the different opinions.

## **Appendix A 2. Construction of the blades and their components**

### **A 2.1 Construction of the blades**

There are four questions in developing the blades of the rotor. The first one is that which airfoil will use for this rotor. The second one is which method was used to build the blades. The third one is how to decide the dimensions of the blades components. In addition, the final question is what material was used for the blades. The aim of the blade design is to minimize the bending force and offset distance from the central line of the blades. The first question is answered in Chapter 4. The airfoil used for this real 1.5kW lift-type Darrieus rotor is the NACA 0018-64 airfoil section. This airfoil section has been proved to be the best candidate in Chapter 4.

Generally, there are two kinds of method to solve the problem of how to build the straight blades of the rotor. One is the wing method used in the aircraft industry. Another one is the method widely adopted by many research groups and small VAWT companies. These two methods will be described in details and the three questions will be answered in the following section. The method used in the aircraft industry is the method of the wing construction. Most of the wings of the airplane were constructed through the ribs, spars and skin. These ribs and spars were shown in Figure 0.1.

The ribs have the same outline as the selected airfoil section and have some slots through which the spars can be passed. The spars chain all the ribs and fix the ribs with the screws or snap rings. In order to manufacture the ribs and spars, the size of

the ribs and spars must be confirmed firstly. The main parameters of the ribs are the thickness and the size of the slots. And the main parameters of the spars are the width and length. The thickness is the only parameter of the skin surface. In order to minimize the bending force, the blade's installation points of the struts must be decided together with the thickness of the ribs, spars and skin surface. The blade installation ratio is defined as the ratio of the length between the installation points to the center of the blade to the half-length of the blade.

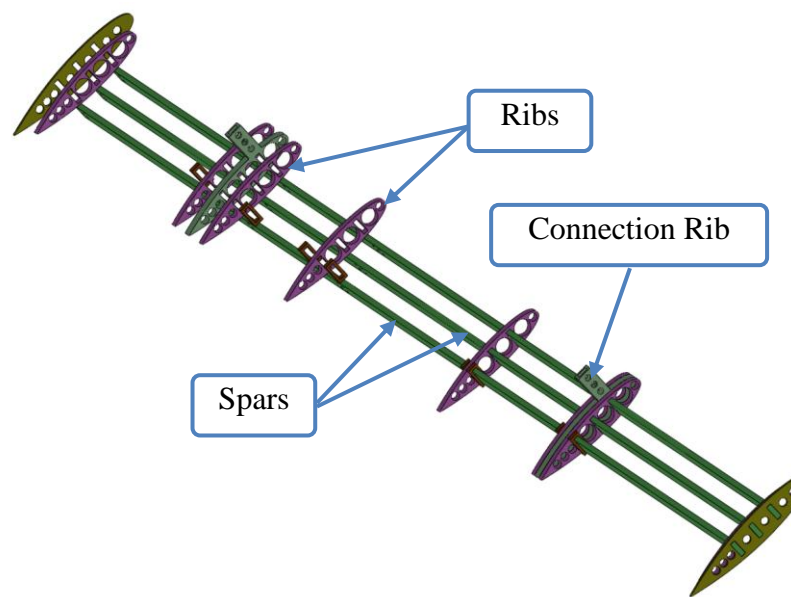


Figure 0.1 Ribs and spars of the rotor blades (Appendix A)

From what it looks like, the thicker the spars and skin surface are smaller the offset distance is. However, the simulation of the Abques program shows that the thinner the spars and the skin surface area, the smaller the offset distance is. The simulated results show that the structure with 1mm thickness of the spars, 0.5 mm skin surface, and 1mm thickness of the ribs and 0.56 of blade installation ratio is strong enough to resist the bending force caused by the centrifugal force of the blades when the blade

material is Aluminum 6061-T6. The rivets are used to connect the skin surface, ribs and spars. The ribs and spars are designed as stampings to easily mass production. The skin surface has the pre-made slots to form the opening of the blades. The opening is located at the center of the blades. All this design is presented in Figure 0.2.

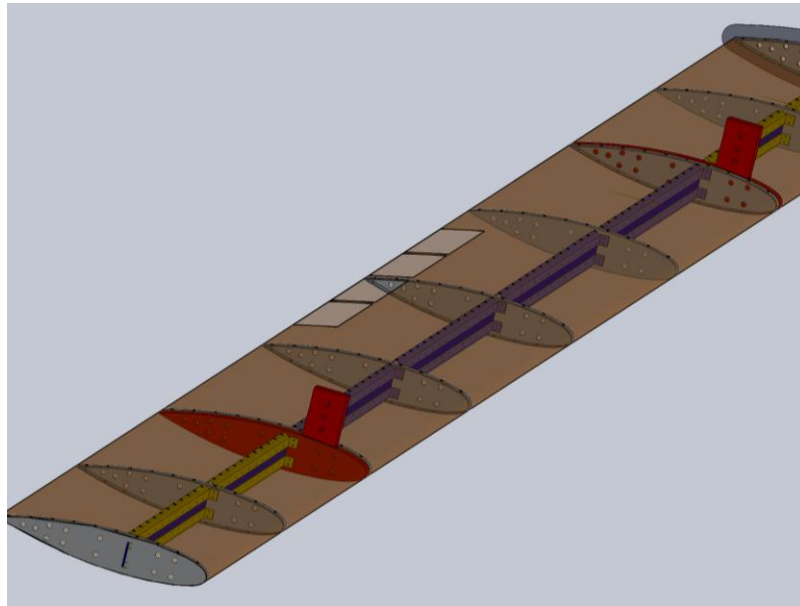


Figure 0.2 The blade design of the wing method (Appendix A)

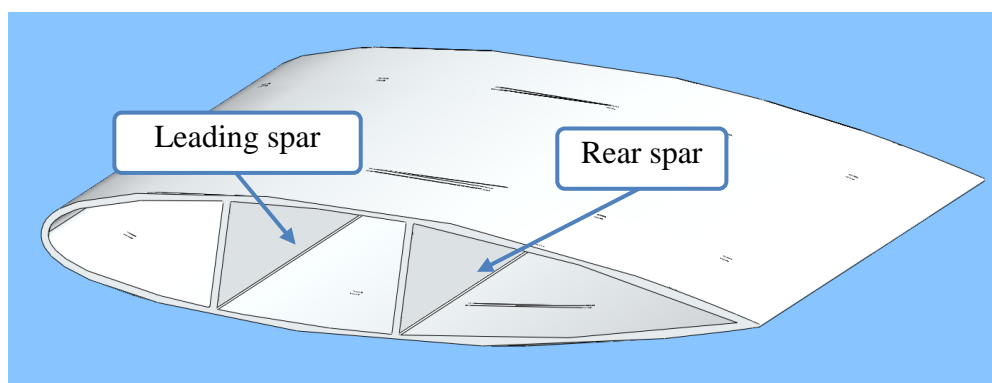


Figure 0.3 The extrusion of the blades (Appendix A)

The size of airfoil chord length of the airfoil will not be limited using this method. However, it is difficult to make sure the blade cross section fits the designed airfoil curve precisely. Thus, this method can be used for the blades of the large Darrieus rotors.

The second method to build the rotor blades is extrusion which creates objects of a fixed, cross-sectional profile. The material is drawn or pushed through a mold of the desirable cross-section profile. The greatest advantage of this process is in building the complicated cross-section profile. And this method can be used for mass production. The cross-section of the extrusion is presented in Figure 0.3

Two spars were used to improve the strength of the blades. Based on the analysis in the wing method, the thickness of the blades and the spars should be 0.8 mm and 1mm. And the blade installation ratio is 0.56.

The extrusion method is limited by the chord length and the thickness of the airfoil. For the chord length of 250mm, the minimum thickness which the manufacturer can offer is 2.5mm. This value is about 3 times higher than the suggested value. The curve profile error and measuring straightness error of the blades cannot be controlled easily.

A further analysis proved that the blades with 2.5mm spar and 2.5mm skin surface are strong enough to withstand the centrifugal force generated at the rotational speed of 500rpm with consideration of the wind load when the material is Aluminum 6061-T6. This analysis results are presented in Figure 0.4. The maximum offset distance (displacement) is only 7mm at rotational speed 500RPM. Thus, the blades were extruded based on the dimensions above.

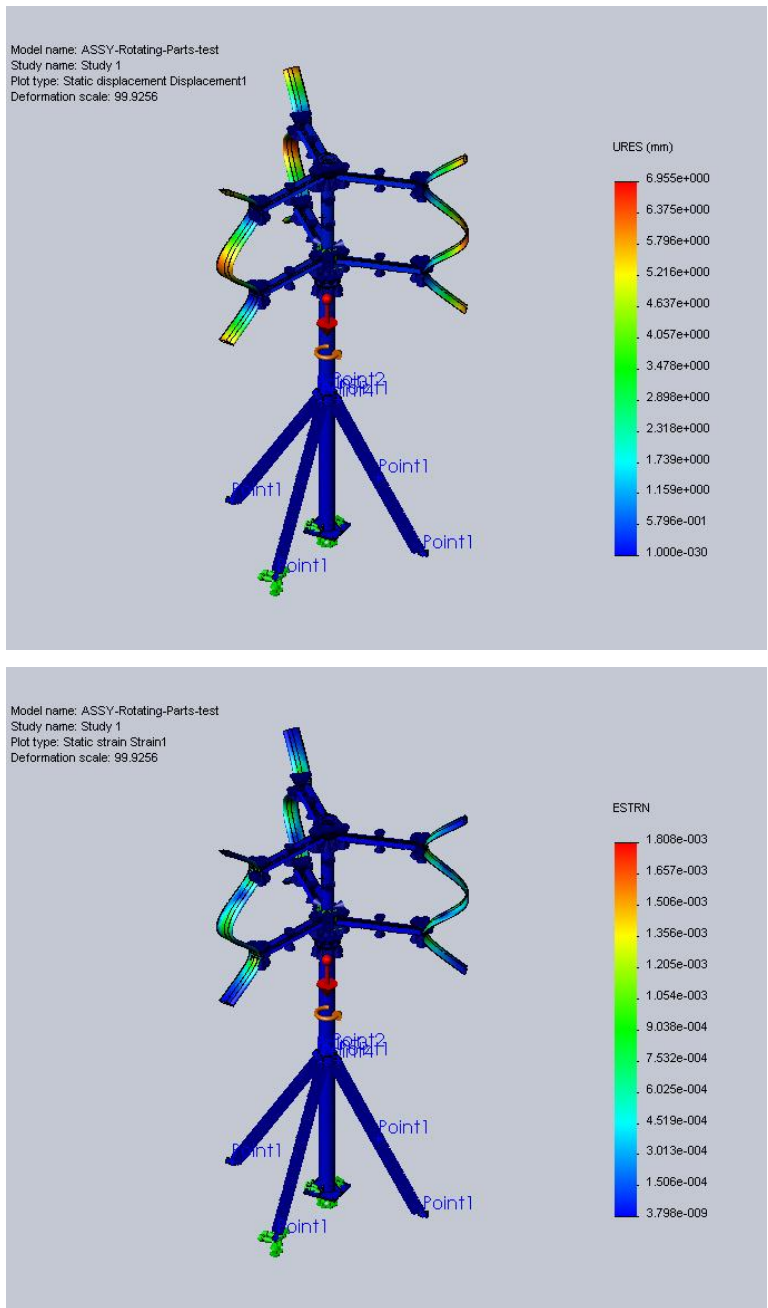


Figure 0.4 The strain and displacement analysis (Appendix A)

A further analysis proved that the blades with 2.5mm spar and 2.5mm skin surface are strong enough to withstand the centrifugal force generated at the rotational speed of 500rpm with consideration of the wind load when the material is Aluminum 6061-

T6. This analysis results are presented in Figure 0.4. The maximum offset distance (displacement) is only 7mm at rotational speed 500RPM. Thus, the blades were extruded based on the dimensions above.

The extruded blades were presented in Figure 0.5. And a relatively reliable way and cost saving way was used to check the curve profile error of the manufactured blades. The CAD file of the airfoil cross-section was printed and compared to the sample of the extruded blade. This comparison is shown in Figure 0.6. Generally, the curves of the extruded blades fit well with the curves of design airfoil except a small difference happens at the training edge of the airfoil. This difference is about 0.6% of the chord length. It is reasonable to accept such a small error. After the extrusion of the blades, the openings and holes for installation of the blades were made in the factory.

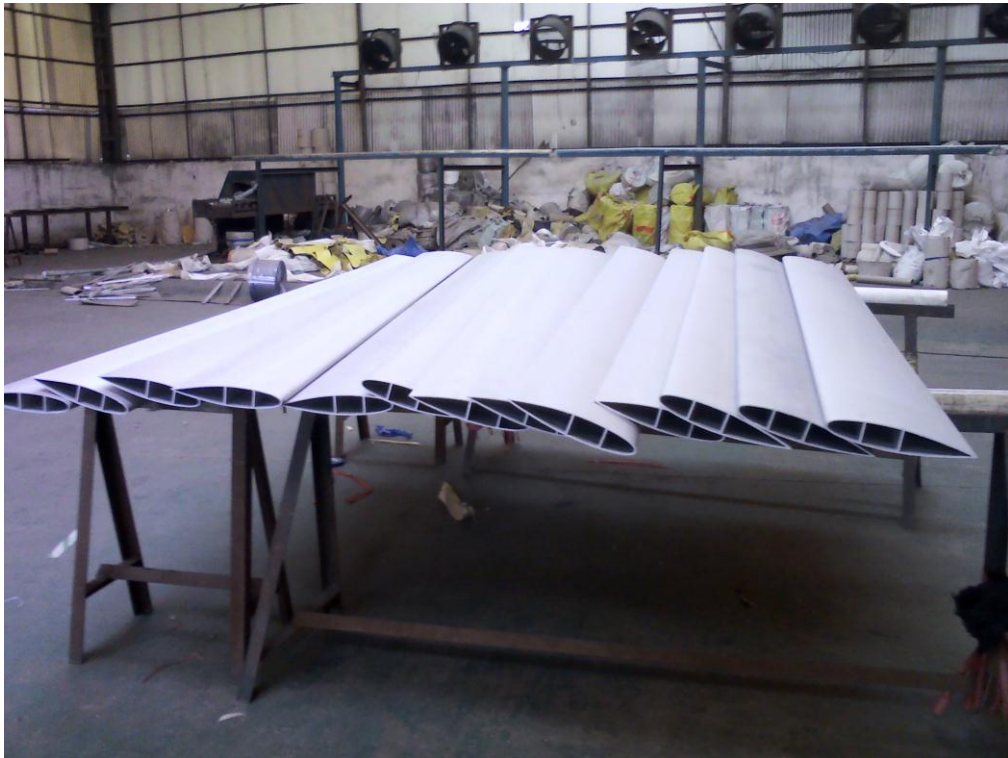


Figure 0.5 The extruded blades in the factory (Appendix A)

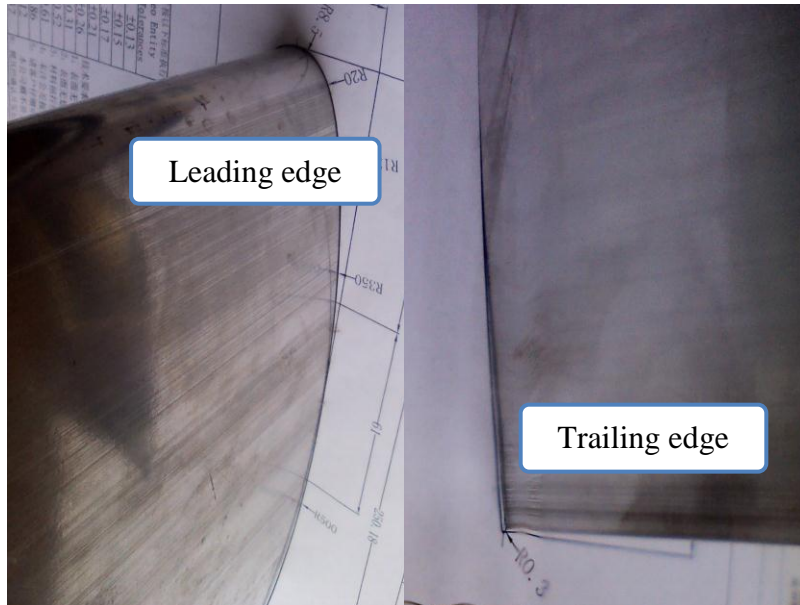


Figure 0.6 Comparison between the real airfoil profile to the designed airfoil profile  
(Appendix A)

## A 2.2 Construction of the components related to the blades

There are three components related to the blades. They are endplates at the top and bottom of the blades, the connection ribs and several small L connectors. The endplates were used to reduce the air circulation from the high pressure side to the low pressure side at wing tips. Thus, the wingtip drag can be reduced. Those endplates were wire cut in the factory. The cross-section of those endplates is about 5mm bigger than that of the NACA 0018-64 airfoil.

The connection ribs were used to connect the blades with the struts. One side of the connection rib is an empty airfoil which allows the blades to fit in. The endplates and blades were connected using the small L connectors which are installed by the rivets. The detailed information of these components was shown in Figure 0.7. All the

components which are presented in Figure 0.8 were pre-assembled in the factory to make sure all components fit well with each other.

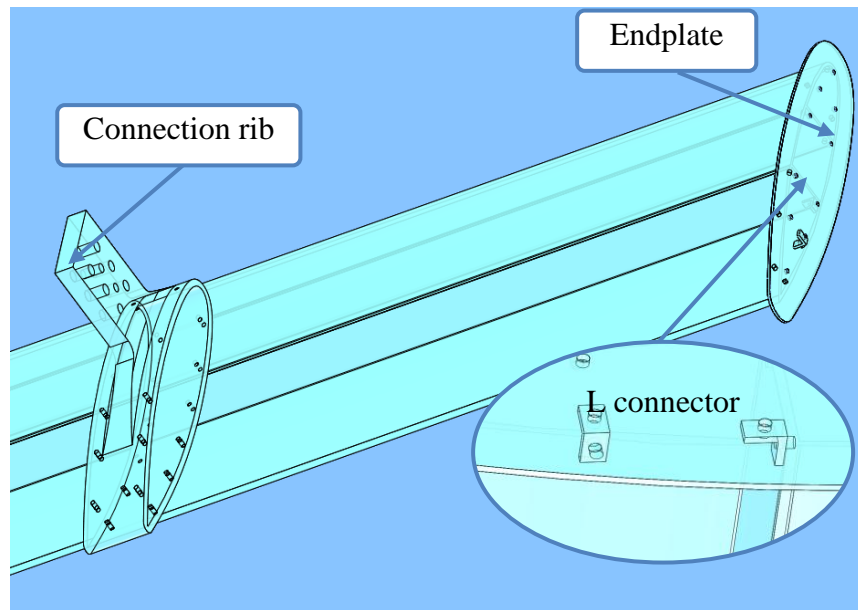


Figure 0.7 Components related to the blades (Appendix A)

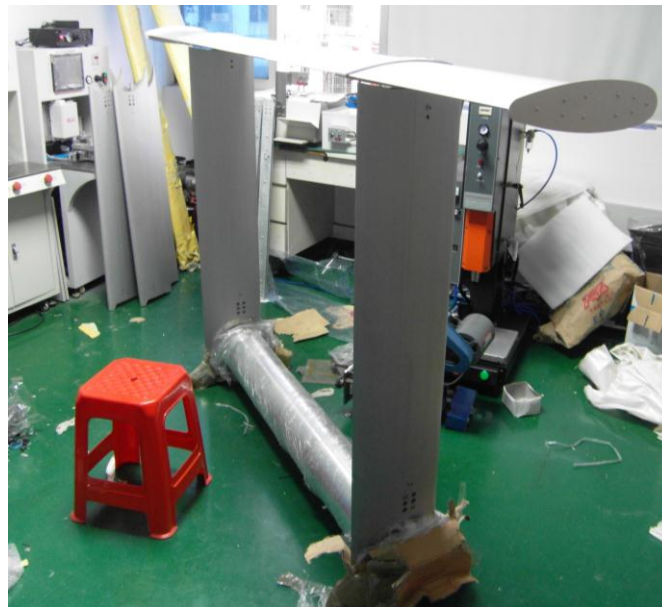


Figure 0.8 Pre-assembly of blades in the factory (Appendix A)

### Appendix A 3. Design of the struts

The choice of the struts will affect the stability and structure of the system. The struts of the Darrieus can be inclined or horizontal struts which are presented in Figure 0.9. Most of H-Darrieus used the horizontal struts. In fact, the usage of the inclined struts not only reduces the length of the central column, but may also increase the stability of the system. However, the strut system used in our project is the horizontal strut system due to a special design of the bearing system. The bearing system of this 1.5 H-Darrieus rotor consists of two ball bearings and one magnetic bearing. Two ball bearings were limited the movement in the horizontal plane. And the magnetic bearing is used to lift and withstand the weight of the rotor. Thus, the generator is placed on the top of the central column. And the magnetic bearing is placed on top of the tower. The final structure of the H-Darrieus is the same as the depiction on the right of Figure 0.9.

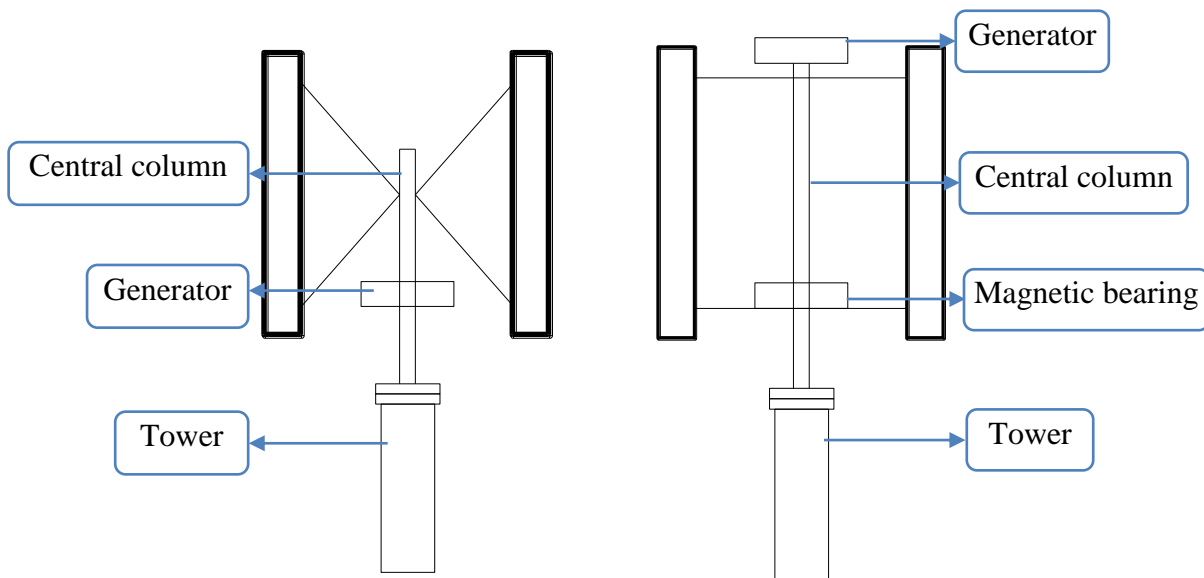


Figure 0.9 Inclined and horizontal struts (Appendix A)

The horizontal struts of this H-Darrieus rotor is composed of three parts. They are strut1-1, strut1-2 and strut1-3. Strut1-2 locates at the center of the two pieces of strut1-1. The length of the strut1-2 is a little shorter than the length of the strut1-1 to fit the connection rib into the space created from two pieces of strut1-1. The cross-section profile of the strut1-3 is same as the blades. The purpose of the using strut1-3 is to reduce the drag force generated by the horizontal struts. Figure 0.10 shows the three parts of the strut in details. Strut1-3 is transparent in Figure 0.10. One of the strut1-1 is also presented transparently in the small ellipse. Some tapping holes were made to connect the strut1-1 with strut1-2.

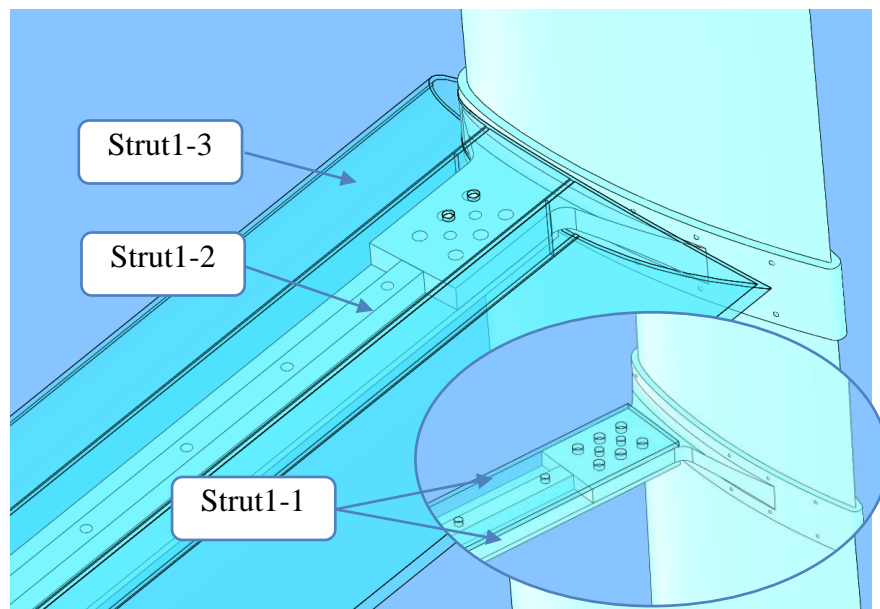


Figure 0.10 Three parts of the struts (Appendix A)

#### **Appendix A 4. Magnetic bearing and the central column**

As mentioned in the design of the struts, a special design was adopted for the bearing

system of this H-Darrieus. The magnetic bearing was used to withstand the force at Z direction. This magnetic bearing is made up upper and lower disk. The surface area of the upper disk is larger than that of the lower disk. Thus, the upper disk can cover on top of the lower disk. There are many slots in the upper and lower disk. These slots will be filled up with many small rectangular magnets.

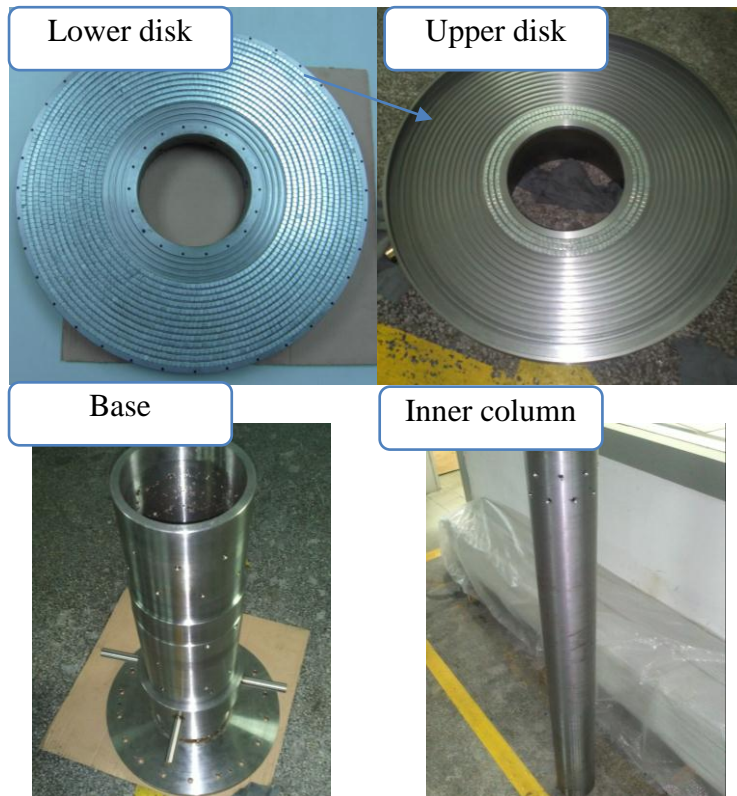


Figure 0.11 Lower disk, upper disk, base and center column (Appendix A)

The arrangement of the small magnets is very special. The detailed information can be found in the paper or dissertation written by Jan Kumbernuss. The lower and upper disk is presented in Figure 0.11. The location of the upper and lower magnetic bearing and the settlement of the main components are in Figure 0.12.

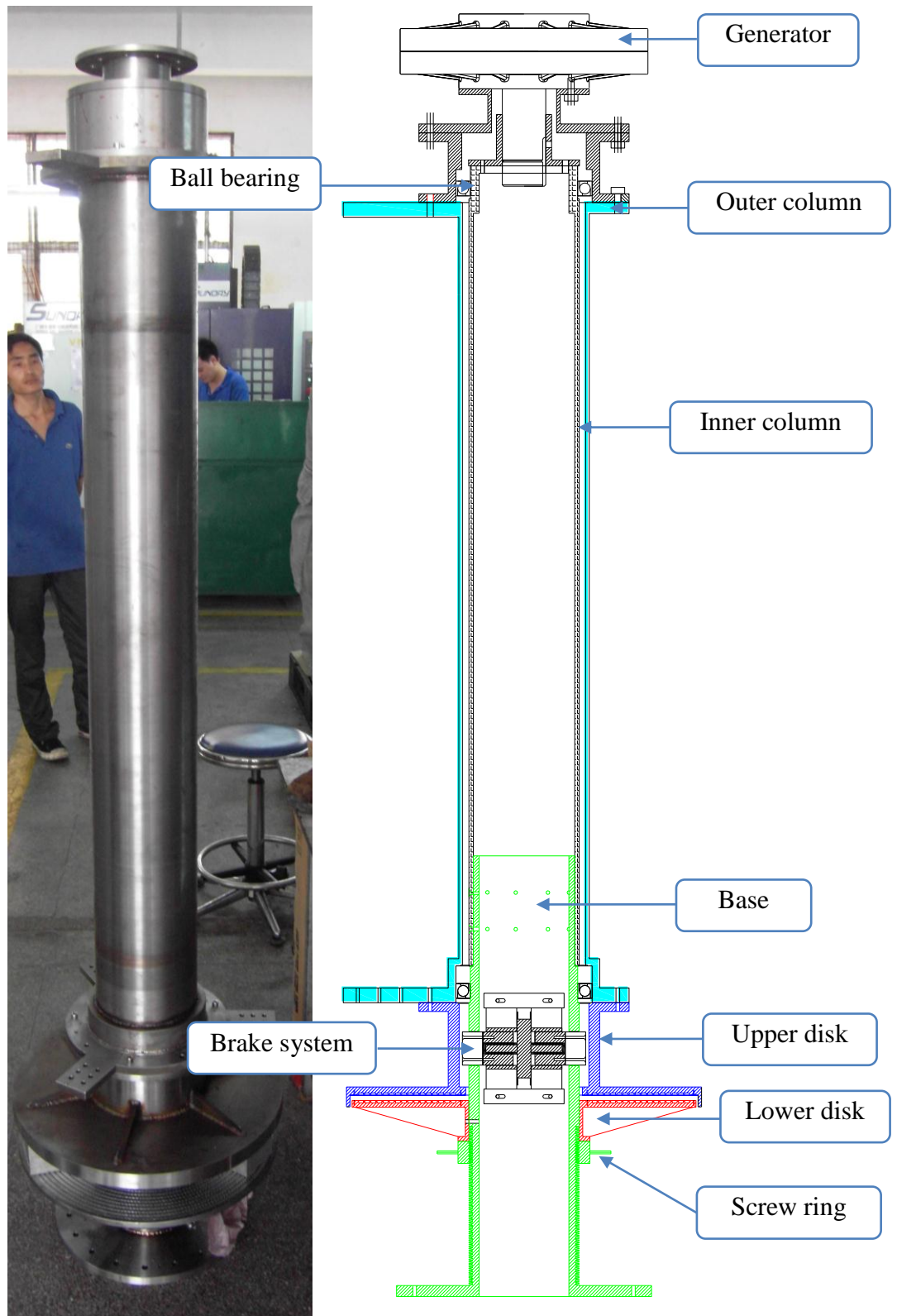


Figure 0.12 The settlement of main components (Appendix A)

. The main components except the blades are lower disk, upper disk, inner column, outer column, brake system and base. The outer column is filled with cyan color and the inner column is marked by black color. The lower disk and base is marked with red and green respectively. The order of installation is that the lower disk is mounted on the base firstly. The upper disk is put above the lower disk. Then, the inner column is fitted and fixed on top of the base through several screws. Following this, the outer column is installed through the inner column from top to bottom. Finally, a generator is placed on top of the rotors

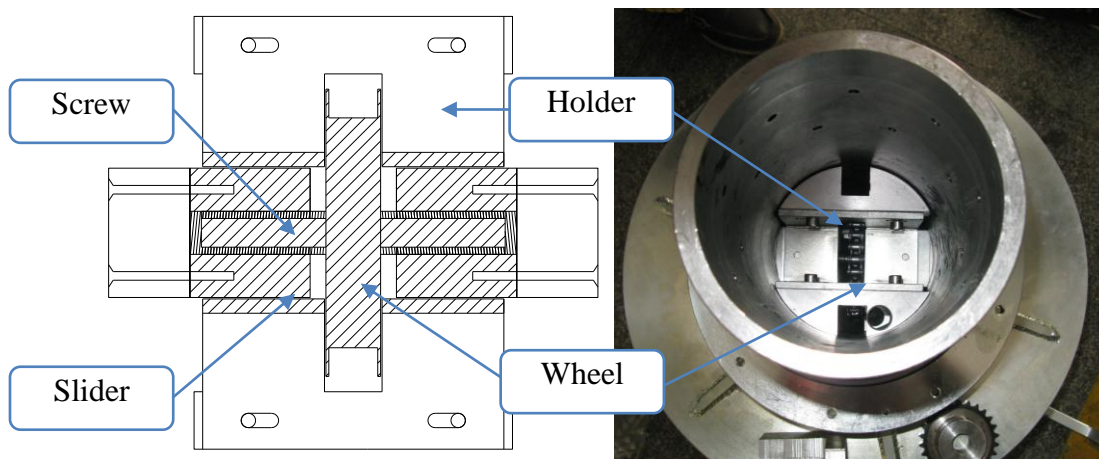


Figure 0.13 The braking system of the H-Darrieus (Appendix A)

The braking system is comprised of three parts, the holder, wheel and sliders. The holder is used to fix the brake system at the right place which is the center of the upper disk. A chain turns the wheel to drive two sliders. There are two short screws welded to the two sides of the wheel. When the chain turns the wheel, the sliders will contraction or expand based on the direction of wheel's rotation. When the sliders expand, the brake linings attached on the sliders will contact with the inner surface of the upper disk to reduce the rotational speed of the rotors. In case of something

wrong with the brake, the screw ring on the base can be lowered down to repair the brake system.

## **Appendix A 5. Selection of the generator**

In fact, the starting ability of the rotor is highly dependent on the starting torque of the generator. Few journal papers have discussed the starting torque requirement of the generator. The H-Darrieus needs to overcome the torque generated by the friction of the bearing and the starting torque of the generator. Wu et al. (2000) conducted direct-drive permanent Magnet Generator for wind turbines. They found that the peak cogging torque of a rotor 20kW nominal power with an outer-rotor direct-drive permanent magnet generator is 5.8 Nm. And the hysteresis torque is 8.4 Nm. Thus, the total starting torque of this rotor is about 16.2 Nm which includes 2Nm caused by the bearing and seal friction. However, the starting torque of this generator is much higher. An axial flux permanent-magnet synchronous generator (AFPMSG) (Chan and Lai 2007) is adopted to reduce the starting torque of the VAWTs system. The cogging torque is eliminated from the coreless design.

The AFPMSG adopted in this project has 1.5kW nominal power and is an outer-rotor design. This generator is presented in Figure 0.14. The shaft of this generator is connected to the inner column. And the outer disk is connected to outer column. The tested starting torque of a 1.5kW generator brought from the JingJiang Fields wind Power Equipment Co., Ltd is only 0.2 Nm. And the efficiency is about 0.88 according to the data offered by the company. This small starting torque allows the H-Darrieus to start very easily. And the on-site testing also showed that this H-

Darrieus can be started to turn when the wind speed is around 1.5m/s. One reason for this low wind speed starting is the lower starting torque of the generator.

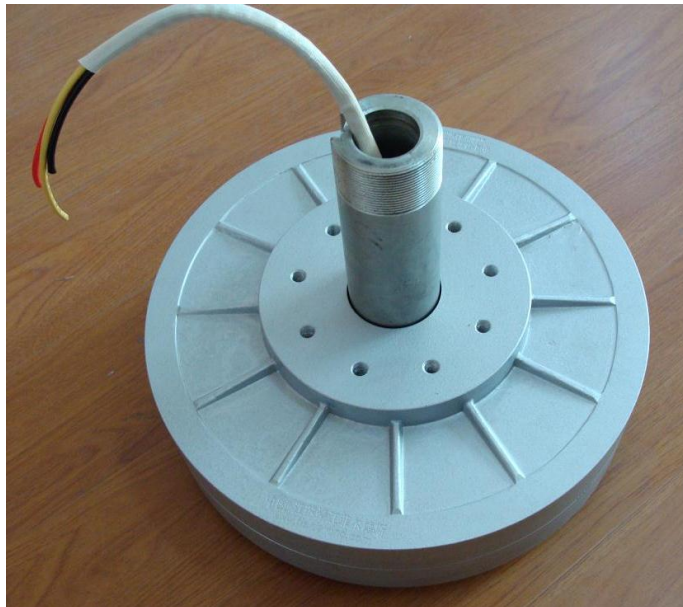


Figure 0.14 An outer-rotor axial flux permanent-magnet synchronous generator

(Appendix A)

Another issue related to the selection of the generator is the match of power curves between the rotors and generator. The power curve of the Darrieus was estimated based on the simulated results. And the power curve of the generator is gained from the manufacturer. The match of the power curves is shown in Figure 0.15. Generally, these two curves match fairly well when the rotational speed is about 210 RPM at which two curves intersect. After 210 RPM, the power curves of the wind turbine increased faster than the power curves of the generator due to the third-order relationship between the wind power and the wind speed. Based on the match of curves, the optimal rotational speed of the H-Darrieus should be 210 RPM which is highlighted through the red line in Figure 0.15. However, the estimated optimal

rotational speed is about 230 RPM which is highlighted through the blue line in Figure 0.15 when the wind speed is 11 m/s. Thus, a small mismatch between the generator and Darrieus exists. But, it should be pointed out that the power curve of the Darrieus is totally estimated through the simulation results. In order to find the real match results, the real power curve of the H-Darrieus should be determined.

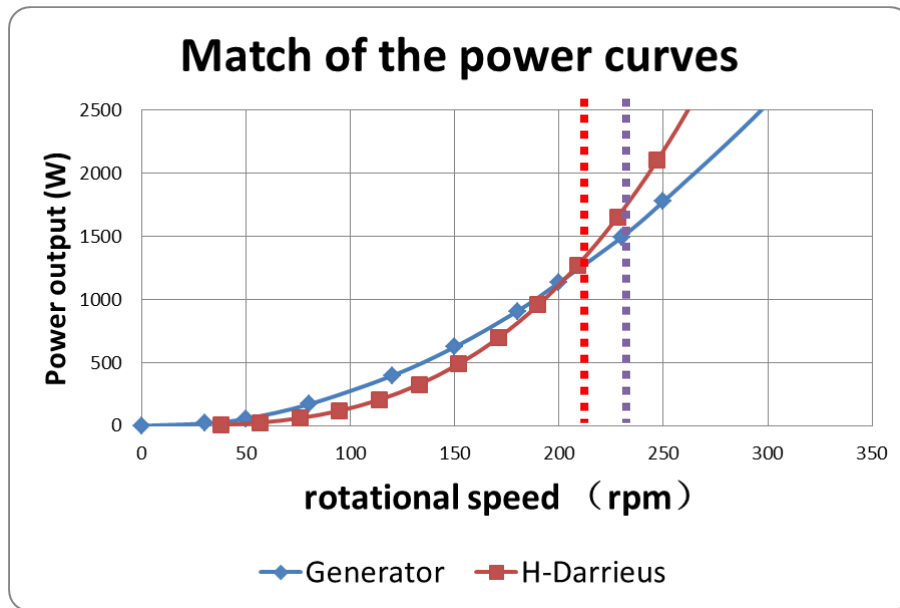


Figure 0.15 Match of the power curves (Appendix A)

## Appendix A 6. On-site installation

All the components mentioned above, tower, inverter and controller were well packed and delivered to the site. The tower is installed first. Four cables were used to enforce the strength and stability of the tower. An 8m scaffold was erected beside the tower to lift the Darrieus rotor on top of the tower. The Darrieus rotor without the blades was assembled on the ground. And this Darrieus rotor without the blades was

lifted using a pulley and connected to the tower by 16 stainless screws. After that, three blade sets which include two struts and one blade were installed one by one on the ground. Then, three blade sets will be lifted and connected to the central column one by one. Figure 0.16, Figure 0.17 and Figure 0.18 demonstrate the process mentioned above.



Figure 0.16 Installed site (Appendix A)

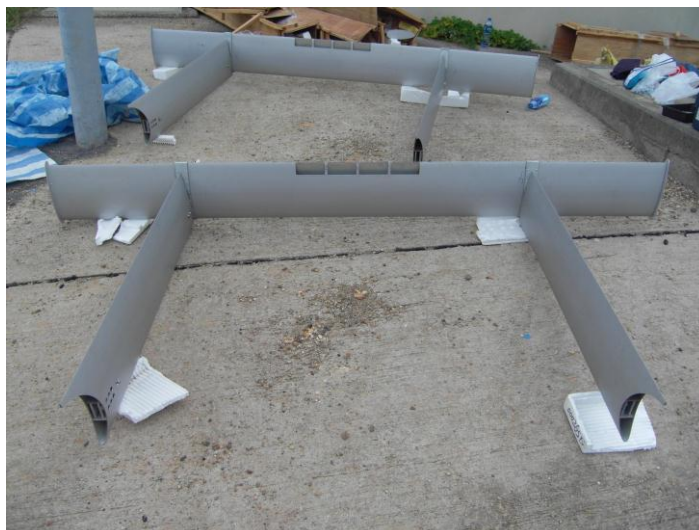


Figure 0.17 One blade set (Appendix A)



Figure 0.18 The finished installation (Appendix A)

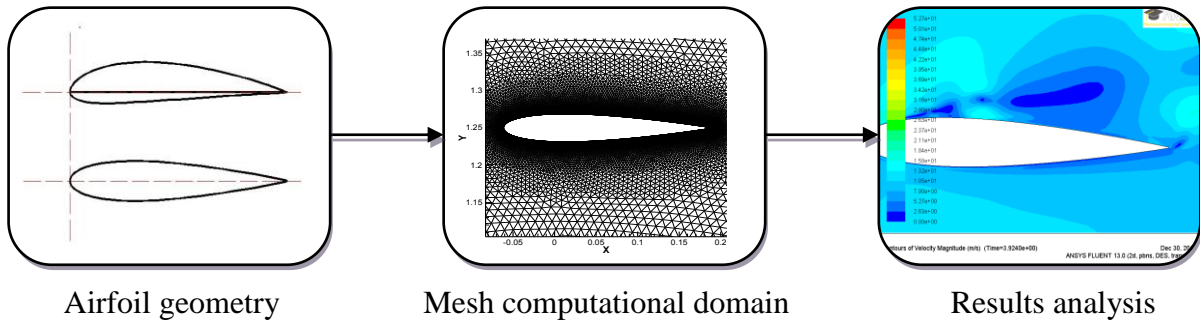
A brief construction and installation of a 1.5 kW H-Darrieus with the openings at the blade tip and magnetic bearing has been presented in this chapter. It looks like quite easy. In fact, we faced and solved a lot of problems and challenges for this one year project. Now, this rotor is under test on site. There are still some problems about the data collection system. Thus, we cannot present more information about the rotor's performance now. The real performance of this Darrieus rotor will be presented in the future.

## **Appendix A 7. Summary of the design and construction process**

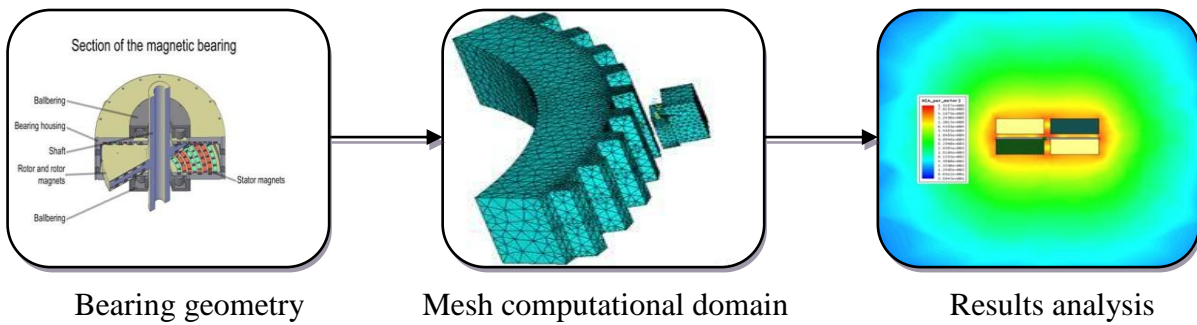
In this section, five main design and construction processes will be presented to give

a summary of the design and construction process of 1.5kW H-Darrieus rotor. The erection of a real H-Darrieus is a process covered several disciplines.

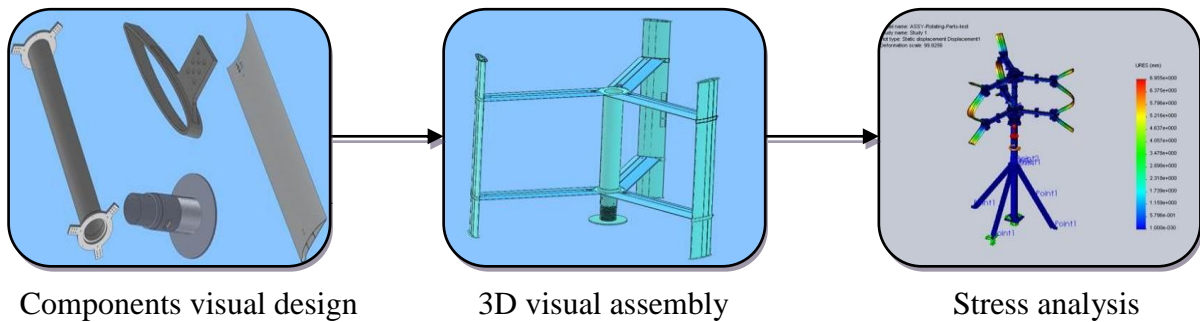
### Process of airfoil design



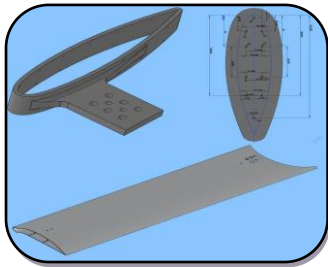
### Process of magnetic bearing design



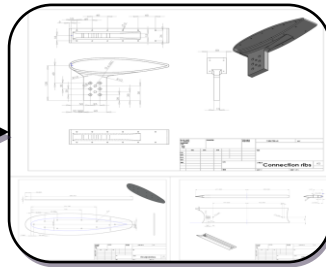
### Process of 3D visual design



### Process of stress analysis



Components visual design



2D CAD files

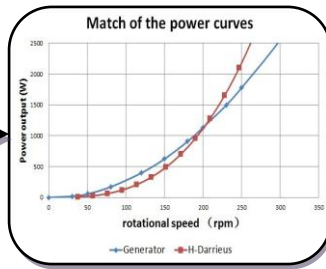


Real components

### Process of the installation



Assembly of the wind turbine



Match of power curves



Record of power



## **APPENDIX B APPLICATION OF VAWT FOR DEVELOPING A VERTICAL AXIS WATER TURBINE**

From Chapter 3 to Chapter 7, all research focused on the vertical axis wind turbine, actually, on the vertical axis wind turbine working at open condition. In fact, some researchers have conducted some investigations on the vertical axis wind turbine working in the half open condition or confined condition. It seems that the Betz limits in the open condition can be broken in the half open condition or confined condition. And, it is an interesting topic to study the vertical axis wind turbine in the half open condition or confined condition. The mechanics and working principle of the vertical axis wind turbine in the open condition may suitable or unsuitable for the vertical axis wind turbine in the confined condition. Coincidentally, there is an opportunity to apply the vertical axis wind turbine principle in developing small hydro turbines for water pipelines in urban areas. Thus, an exploratory research of the vertical axis water turbine working in confined condition is conducted in this chapter. The aim of the utilization of the vertical axis water turbine in water pipelines and adaptability of different vertical axis water turbines will be addressed in the following paragraphs.

### **Appendix B 1. Introduction**

Water plays a vital role in the proper functioning of the Earth's ecosystems and most of our daily water supply is offered by the water utilities which have to ensure the

safe and clean water supply for local residents. Modern water utilities, however, are facing several challenges because many urban water pipelines installed during the rapid urban growth period after the World War II are now suffering from rapid deterioration (Brothers 2003). The major challenges involve how to early warn and control water leakage, how to efficiently control and detect water quality, how to manage the pressure distribution along the pipeline, how to maintain and renew the pipeline and how to optimize design and operation of water distribution network. A large number of technologies and prediction models have been developed to deal with the challenges mentioned above during the past a few decades.

In terms of water leaking control, Rajani and Klenier (2001) and Kleiner and Rajani (2001) summarized the physically and statistically based models for structural deterioration prediction of water mains through model description, critique and data requirements. However, all these prediction models need a lot of data with different types.

For example, the Frost load model (Rajani and Zhan 1996) requires continuous freezing index, soil properties, thermal gradient at the freezing front, frost depth and other related variables. Based on the co-author's (Camarinopoulos et al. 1996, Camarinopoulos et al. 1996, Camarinopoulos et al. 1999) publications of the Hadzilacos (2000) models, factors such as traffic load, frost load, earth load, pipe working and surge pressure, temperature change, internal and external pipe diameter and corrosion coefficients, bursting strength, tensile strength, maximum external load and fracture toughness have been taken into consideration in their probabilistic framework. Therefore, Rajani and Kleiner claimed that even the best physical

analysis model is good only under the circumstance that relevant data are available for its implementation.

Water quality is another rising issue. The United States Environmental Protection Agency (EPA) claimed that microbes, chemicals, and pathogens are still such a concern that even EPA has set standards for about 90 contaminants. Levin et al. (2002) suggests that we need better, more efficient and sensitive monitoring tools and strategies, especially to assess microbial risks and groundwater contamination.

Most of these technologies and models are based on many types of data, enough detection nodes and synchronous and continuous data gained at one node for the analysis, inspection and prediction of the water leakage and quality so that water utilities need to install a lot of different types and quantities of sensors along pipelines to gain the different data for leaking and contamination inspections at different locations.

Till now, most of the sensors are powered by batteries. However, the fact mentioned by Younis and Akkaya (2008) is that it is envisioned that monitoring network always need hundreds of nodes that operate on small batteries. According to Yang et al. (2002), the operation period per battery charge is only 21 days when an aqueous sensor network was applied to measure environmental parameters of interest for the lake or drinking water reservoir. Power supply to the data acquisition systems, especially the magneto elastic transmitter and sensor interface board, is usually off. Hence, they proposed to obtain power supply from the environment, such as thermo-electric and mechanical power.

A real wireless sensor network was used by Stoianov et al. (2006) to monitor the

Boston city's water supply. Many sensors relied on battery operation due to the fact that many of the sensor locations do not have access to local utility grid power. Even using lossless data compression algorithms, the battery life (6V 12Ah battery) is about 50-62 days. They claimed that the major challenge in developing the wireless monitoring system (Stoianov et al. 2007) is how to balance the conflict between long distance, communication, bandwidth, local data processing and the constraints for low-power consumption.

Therefore, more and more studies have focused on how to provide power to the monitoring sensor networks which are the essential for the modern water mains management technologies and methods, especially for the sensors which have no access to grid power and need to offer continuous monitoring. Thus, a new type of power supply system is proposed, which harvests a little hydropower from the pipeline for power supply to the data acquisition systems. This paper reports the development details of the micro hydropower system including CFD simulation and experiments.

There are four main parts in this section. The first part gives a general review of the current power supply system to the pipeline monitoring system and a basic concept of our hydropower system. The second part presents the design methodology for the development of the hydropower system. The third part describes the evolution of our hydropower system. And the last part summaries our hydropower system and discusses some of the contributions and insufficiencies of the research.

## **Appendix B 2. Review of the current power supply to the pipeline monitoring system**

Generally, the researchers of the power supply to the pipeline can be classified into two categories—low power consumption methods and power generation from the ambient environment.

### **B 2.1 Low power consumption methods**

Low power consumption methods mean using some of the technologies to reduce the power consumption of the monitoring system. Min et al. (2001) presented a technological overview for low-energy distributed micro sensors such as the power aware computation/communication component technology, system partitioning, low-energy signaling and networking and a power aware software. Chi et al. (2003) achieved lower power required by the combination of the hardware monitoring and profiling software. Younis and Akkaya (2008) summarized the various nodes positioning strategies to meet the wireless networks' requirements at limited energy. However, these low power consumption methods can only finite prolong the life of the monitoring networks. That is the reason why power harvesting researches have attracted more and more attention recently.

### **B 2.2 Power generated from the ambient environment**

There are four major types of power harvesting methods. First is the solar energy

harvest. A solar-aware routing was developed by Voigt et al. (2003), they claimed that this system only suits for small networks. Niyato et al. (2007) presented a approach combining the solar power with a game-theoretic approach to optimal energy management. Dondi et al. (2008) focused on the maximizing the harvester's efficiency in transferring energy from the solar panel to the energy storing device. However, they claimed that the energy harvesting process under varying light irradiance conditions is certainly one of the major design challenges. And some sensors may be located at the position which is surrounded by the trees and buildings.

The second power harvesting method bases itself on ambient vibration energy using the active materials such as piezoelectric, ferroelectric and magnetostrictive, etc. Xia et al. (2006) developed a self-power wireless sensor system using MEMS piezoelectric micro power generator. The power generated by this system is 0.173mW. Metzger et al. (2007) designed a vibration energy scavenging system that powers monitoring devices for the truck transportation environment. The designed system generates 0.73  $\mu$ W of power. Renno et al. (2009) utilized a circuit including an inductor and a resistor to optimize the vibration energy harvesting. The maximum power output observed is 70 $\mu$ W. It is obvious that the vibration harvesting power is very small. And the conversion from the vibration energy into electrical energy is available only when the frequency of the converter meets the frequency of the vibration (Pobering and Schwesinger 2008). Furthermore, the vibration harvesting systems are expensive systems due to their fabrication process (Vullers et al. 2009).

Thermal energy harvesting is the third methods. Semiconductor thin films were used to build a small compact thermoelectric generator by Stordeur and Stark (1997). The

power output is 60 $\mu$ W when the temperature difference is 20 K. Ten thermopiles were fabricated by Kishi et al. (1999) using the sintered BiTe. Pure poly-Si and poly-Si70%Ge30% were tested by Stasser to optimize thermal design and reduce the generator's total electrical resistance (Strasser et al. 2004). They claimed that poly-Si thermo-electric generator which is sized to 1cm<sup>2</sup> can produce about 1 $\mu$ W and voltage of 5V at the temperature difference 5K.

A flexible thermo-electric power generation system using the thermo-electric materials of the Cu-Ni was developed by Itoigawa et al (2005). The output power is 4.1  $\mu$ W K<sup>-2</sup> per thermocouple. A passive configuration (Sodano et al. 2007) which removes the system heat through the conduction was used for the thermal electric generators. The testing results indicated that the ability of quick battery recharge is enhanced by using this passive configuration.

To further improve the efficiency of the thermo-electric devices, Researches are paying more and more attention to nanostructured thermo-electric materials. Minnich et al. (2009) described the current research and future prospects of bulk nanostructured thermo-electric materials and claimed that bulk nanostructured materials is the most promise for commercial use due to mass production and compatibility with the existing thermo-electric device.

Generally, the efficiency rate of thermo-electric generators is ranged from five to ten percent (Amatya and Ram 2010). The reason for the poor efficiency rates is that it is difficult to guarantee the heat travel across the generator easily and satisfy the requirement of both low thermal conductivity and high thermal resistance.

The energy harvesting approaches mentioned above have some of the obvious

disadvantages. The first one is that the power output is relatively low, such as the vibration and thermo-electric energy. Another is that the above three power harvesting methods are highly dependent on the surrounding condition. And most of monitoring nodes were placed underground. That is the reason why some researchers proposed the hybrid power harvesting methods (Li et al. 2008).

### **Appendix B 3. Hydropower harvest inside the pipeline**

In order to offer sufficient and safe power for the monitoring system, abundant hydropower inside pipeline seems very attractive. The superfluous water head or small part of kinetic hydropower inside pipeline can satisfy the power requirement of the monitoring system. But the challenge of using hydropower is to select a water turbine which can suit for the requirements of the water pipeline condition, especially for the underground and urban cities condition. The requirements are listed below:

The average water velocity in the pipe is 1.5m/s.

Although some superfluous water head may exist in the water pipeline, the water turbine cannot consume a lot of water head to make sure drinking water can overcome friction of water loss and can be delivered safely to the end user.

In most of time, space for the installation is very limited in the underground condition and urban cities. Therefore, pathway of the water flow cannot be altered.

The system does not have any underlying dangers that may affect water quality

There are many kinds of conventional water turbines which work at different water head and flow rate, such as Francis, Kaplan, Bulb and Pelton turbine. And the efficiency of those water turbines normally ranges from 75 to 95 percent based on the size of hydro turbine generator aggregate.

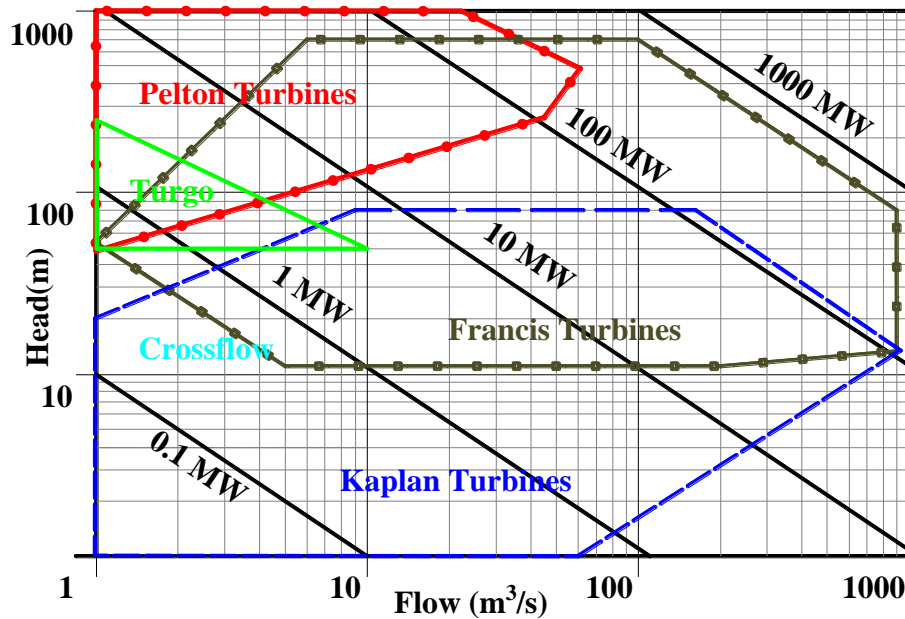


Figure 0.1 Turbine application chart (Appendix B)

According to Figure 0.1, Kaplan turbine looks like a promising turbine for the water pipeline because it can work at low flow rate and low water head condition. But a Kaplan turbine will alter the pathway of the water flow and cannot be well integrated with pipeline. Ampair's UW100 pichydro turbine which is a kind of bulb turbine was proposed by Saftner et al. (2008) to generate the power for the wireless sensors.

Although this kind of water turbine will not change the pathway of the water flow, the generator and some electrical components were immersed in the drinking water. Any improper waterproofing of this system will contaminate the drinking water. And

the loss of the water head of this system also needs to be well evaluated. Thus Water Supplies Department (WSD) of the Hong Kong SAR Government has commissioned the Hong Kong Polytechnic University to develop a hydro turbine for pipeline applications which must satisfy the requirements mentioned above.

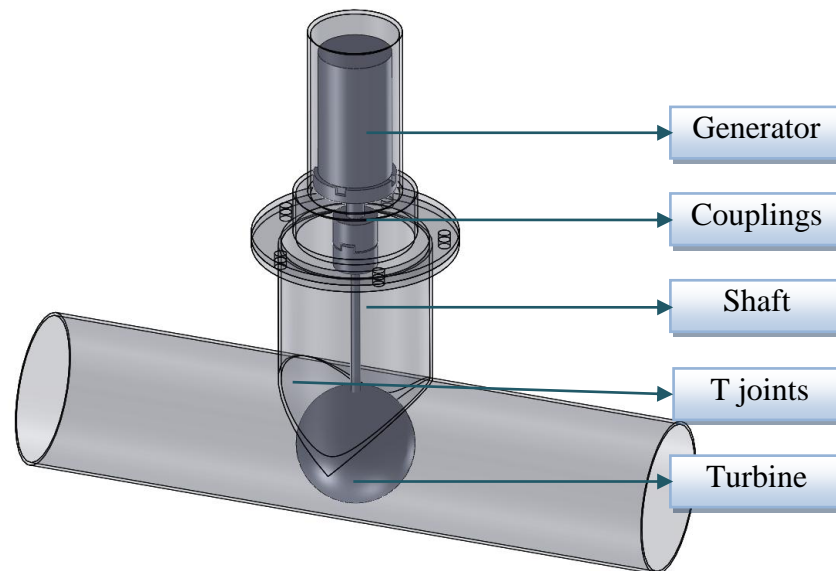


Figure 0.2 The proposed system for the water pipeline (Appendix B)

A vertical axis water turbine system shown in Figure 0.2 was proposed to satisfy the requirements. By using such turbine, the pathway of the water will not change, the electrical parts can be arranged outside of the water pipe, and there are some of ready-made tubular T joints which can be used directly on the pipeline.

After searching the existing vertical axis turbines, lots of the research focused on the application of the vertical axis turbines in the open air or water condition (Islam et al. 2008, Kirke and Lazauskas 2011, Kjellin et al. 2011). A few researchers have turned their interest to develop the vertical axis turbine used in the half (Ponta and Dutt

2000, Furukawa et al. 2010, Kirke 2011) confined condition due to the fact that the Betz limitation can be broken.

Several journal papers have been published about the vertical axis water turbine working in a complete confined condition. One company named Lucid Energy(Energy) developed a lift-type vertical axis water turbine for the big water pipeline recently. Figure 0.3 shows this kind of lift-type vertical axis water turbine. And this system is only developed for the pipelines which is bigger than 24 inches.

Therefore, the fact is that there is very little information about the vertical axis water turbine used in a confined condition, especially for the small pipelines. Thus, in this chapter, we want to develop the vertical axis water turbine for 100mm pipeline to convert as much energy as possible when the average water velocity is 1.5m/s and the water head drop is less than 5 m.

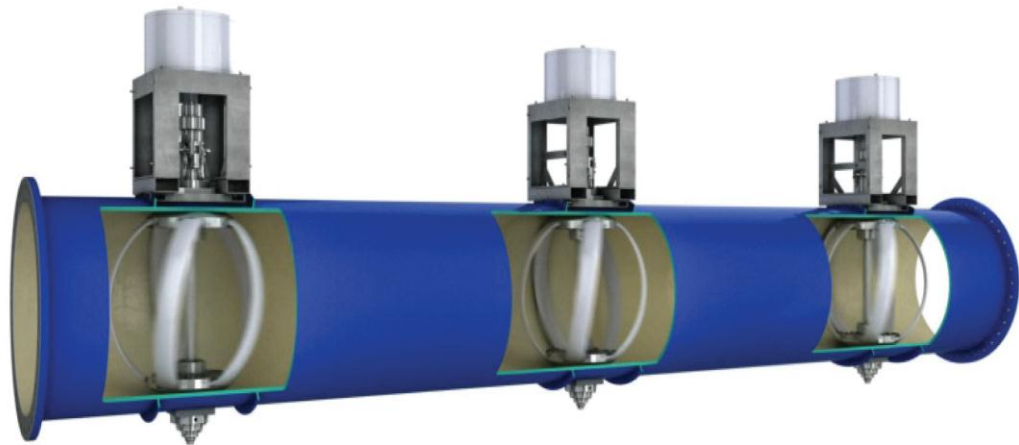


Figure 0.3 LucidEnergy lift-type turbines from LucidEnergy (Appendix B)

## **Appendix B 4. Design methodology**

### **B 4.1 Design process**

Due to the development of the CFD, the modern fluid mechanical design is changed from pure experimental design to simulation-based design supplemented by experimental test. This design process is described in Figure 0.4, which can be divided into two stages.

In the first stage, the proposed water turbine was made by using the CAD software, and then the CAD model was imported into the CFD software to simulate different water turbines' performance under different working conditions. After that, the simulation results were compared to the design aims to check whether the performance of the proposed model can meet the design aims. If the performance of the proposed model cannot meet the design aims, then the first two processes were repeated till the performance of the proposed turbine achieves the design aims.

Once the simulated performance of the proposed model was close to the design aims, the testing stage was launched. If the performance of the proposed model cannot meet the design aims, the first and second stage will be repeated until the model meets the requirements. There are mainly two purposes of the experiments, i.e. to ensure that the proposed models meet the design requirements, and to find whether the simulation is really instructive and the difference between the experimental results and simulation results.

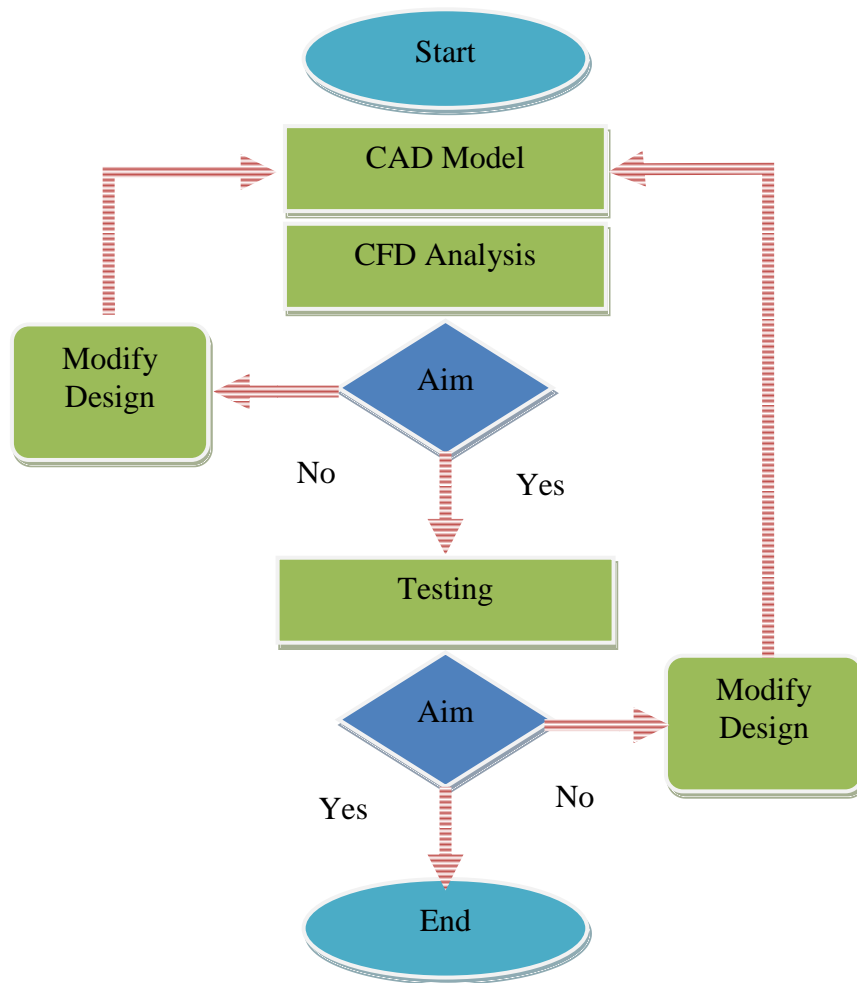


Figure 0.4 Design methodology of the hydropower system (Appendix B)

#### B 4.2 CFD settings

The design and prediction capacity of the CFD has been confirmed to be effective and instructive in many areas, such as fluid machinery, aerospace and atmospheric environment and other fields. The CFD method also has been widely used in the design of the vertical axis wind turbine (D'Alessandro et al. 2010, Mohamed et al. 2011, Raciti Castelli et al. 2011). In this section, the ANSYS CFD package, which is

considered to be one of the best fluid design software packages nowadays, is applied to simulate the vertical axis water turbine. To calculate the unsteady flow field, the sliding mesh method was adopted. The computational domain was divided into internal and external parts. The face between the internal and external domain is defined as an interface which allows the flow properties to transport through the interface. A simple algorithm was used to solve the Navier-Stokes equations. The enhanced wall treatment was chosen for the near-wall region to resolve the viscous layer and the  $Y^+$  of the turbine blades should be close to 1. The whole computational domain was decomposed by 1.5 million unstructured tetrahedral meshes.

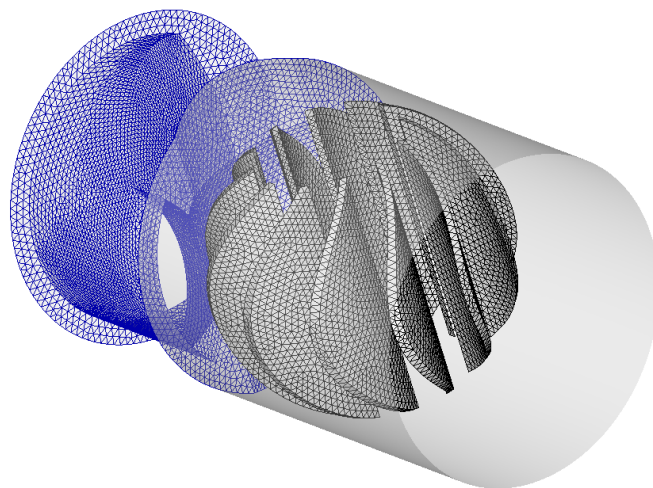


Figure 0.5 Mesh of the simulated models (Appendix B)

The mesh of the final design is presented in Figure 0.5. Although the mesh number remains a controversial issue, the degree of the mesh number was considered well enough for such a small computational domain to make an investigation of the grid-dependence unnecessary. And the computational time of such one case is about one day using a desktop computer with Intel Core2 Quad CPU Q9550 @ 2.83 GHZ 2.83

GHZ processor. It means that we need four days to get one turbine's power coefficient curve at four different rotational speeds. That is why some simulations of the water turbines only have one or two power coefficient points.

It is unfortunate that none of turbulence model can be applied to all the problems. The choice of the turbulence model depends mainly on the considerations such as the physics encompassed in the flow, the required level of accuracy, the available computational resources, and the amount of time available for the simulation. Taking into account the available computing resources, the number of the design models and relatively shorter design cycles, a two-equation model is chosen to approach the Reynolds-averaged Navier-Stokes equations. The most commonly used turbulence models is the  $\kappa - \varepsilon$  turbulence model, and the realizable  $\kappa - \varepsilon$  model is likely to be superior to the standard  $\kappa - \varepsilon$  and RNG  $\kappa - \varepsilon$  models for flows involving rotations, boundary layers under strong adverse pressure gradients, separation, and recirculation. Another kind of the two-equation turbulence models is the  $\kappa - \omega$  models. Among the  $\kappa - \omega$  models, the SST  $\kappa - \omega$  model is more reliable and accurate than the standard  $\kappa - \omega$  model due to the additional features added into the SST  $\kappa - \omega$  model (FLUENT 2009).

According to the above analysis, the SST  $\kappa - \omega$  model and realizable  $\kappa - \varepsilon$  model were adopted to simulate the initial case. The default values in Fluent are used for all the constant values of the SST  $\kappa - \omega$  and realizable  $\kappa - \varepsilon$  model. Velocity inlet was used for the inlet of pipeline. The velocity of the flow is 1.5m/s according to the datum provided by the Water Supply Department of the Hong Kong SAR Government. The outlet of pipelines is the pressure outlet boundaries of the model. It

is found that there is no significant difference between the simulation results of the two models over a large number of time steps. Therefore, we selected the realizable  $\kappa - \varepsilon$  model to simulate all the subsequent design models.

In order to calculate the power output, the torque coefficient of the water turbine is monitored. The average torque coefficient will be calculated until the torque coefficient shows a periodic variation. To evaluate the pressure drop caused by the water turbine, the monitoring point of the inlet pressure and outlet pressure were placed upstream 4 times and downstream 8 times diameter of the pipeline, respectively.

#### **B 4.3 Prototypes and Experiment setup**

The simulated water turbine was fabricated by a Computer Numerical Control (CNC) machine using stainless steel which will not contaminate drinking water and has enough strength. The prototype water turbine was installed into a lab testing system as shown in Figure 0.6 to measure the real performance of the developed turbine.

The testing system is mainly composed of a water tank of  $1.6\text{m}^3$ , a circulation pump, valves and sensors in a circulation loop. The pump is assumed to operate at 50% of its full capacity during the 8-10 hours final acceptance test. A 37kW pump produces 82m water head at  $81\text{m}^3/\text{h}$  (equivalent to  $2.8\text{m/s}$  in a 100mm pipe) to simulate the real water pipeline conditions. A variable speed drive will control the revolution speed of the pump. Several valves were used to regulate the water pressure and flow rate.



Figure 0.6 CNC turbine models (Appendix B)

There are also several sensors used to monitor the flow rate, temperatures and pressures inside the pipe. The flow meter was placed far away from the water turbine. The inlet and outlet pressure sensors were installed upstream 5 times and downstream 4 times diameter of the pipeline, respectively, due to the limited space in I the lab. If 5m water head is consumed totally, the estimated power is  $\alpha \times 384.8$  W, where  $\alpha$  is the block ratio which is defined as the ratio between the turbine's diameter and the diameter of the pipeline. If the water turbine is well designed, it will produce at least 80w when the assumptive system efficiency is 0.3 and  $\alpha$  is 0.7. The following equation is used to estimate the potential power generation of the

water turbine:

$$P = \rho g \left( z_1 + \frac{p_1}{\rho g} + \frac{v_1^2}{2g} - z_2 - \frac{p_2}{\rho g} - \frac{v_2^2}{2g} \right) Q \quad \text{Equation 0.1}$$

Therefore, a micro permanent magnet power generator (FF-50W) was used due to the propriety of low starting torque and zero cogging design whose rated power output is 50W and maximum output can reach 100W. In addition, the generator winding would be customized finally after testing the system performance, such that the output voltage at the maximum power point can match the battery charging voltage, which is around 28V. The main components of the system are presented in Figure 0.7.

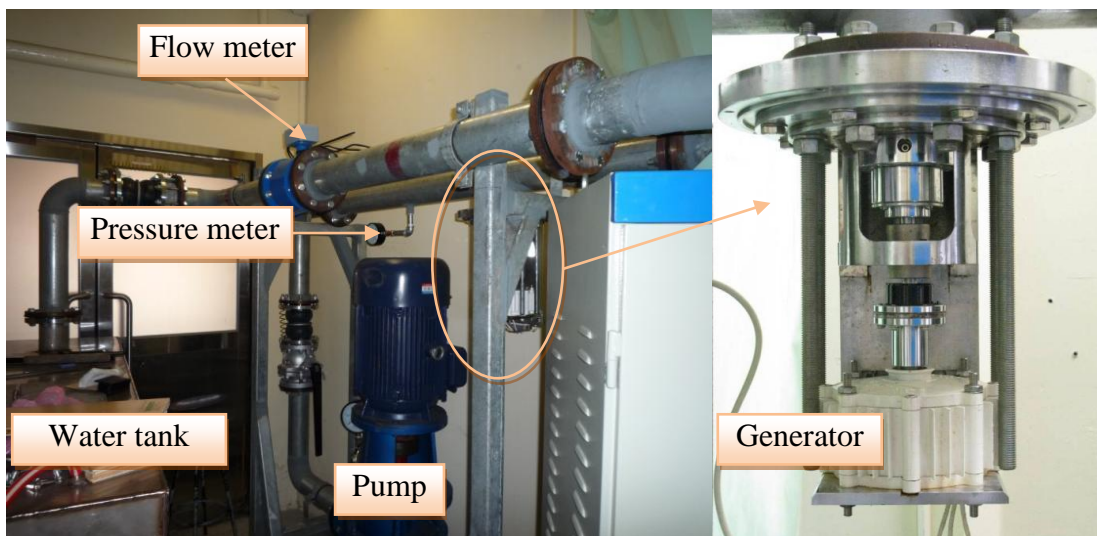


Figure 0.7 Whole testing rig (Appendix B)

## Appendix B 5. Experimental and simulation results of the three evolutions of hydropower system

### B 5.1 First generation of the hydropower system

According to literature survey, there are very few reports about the vertical axis water turbine working in a confined condition (Antheaume et al. 2008, Kirke 2011). Thus, there is little reference which can be found for this project. Therefore, at the initial design stage, different spherical drag and lift-type water turbines which are mainly based on the vertical axis wind and water turbines were proposed and simulated using the CFD software. The airfoil used was the NACA 4415 airfoil which is considered as a promising airfoil for the Darrieus rotor (Kirke 1998). The drag-type turbine was a conventional Savonius rotor with three blades and zero overlap. Some of the proposed models (left) and real models (right) are shown in Figure 0.8.

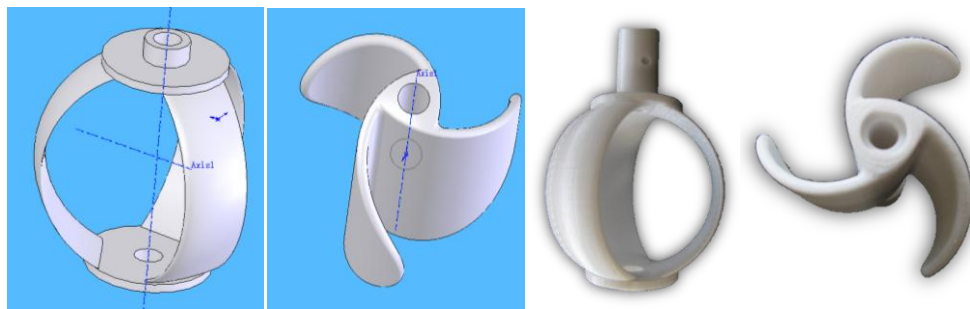
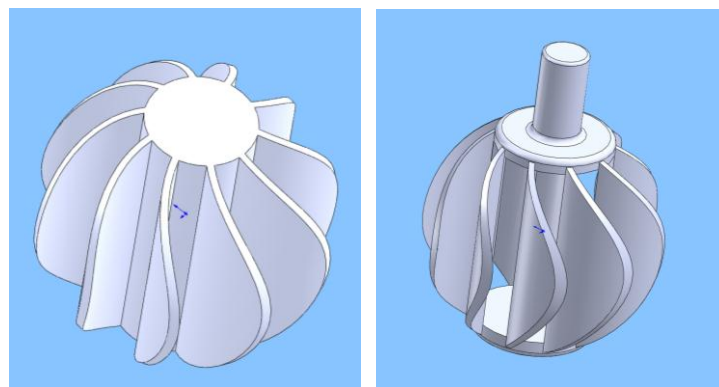


Figure 0.8 Initial proposed designs (Appendix B)

The design parameters of the lift-type turbines are their chord length and blade number. The rotor size and blade number are the design parameters of the solid drag-

type turbines. The diameter of the hollow circular cylinder is the design parameters of the hollow drag-type turbines. Figure 0.9 shows the difference between the solid and hollow turbines. All the results of simulated and testing cases were numbered. A letter S will be added before the simulated case number. Similarly, a letter T means testing. If one case was simulated and tested, both S and T will be used in the case number.



(a) Solid turbine

(b) Hollow turbine

Figure 0.9 The solid and hollow drag-type turbines (Appendix B)

Table 0.1 shows the simulation results of the four different lift-type vertical water turbines at different rotational speeds. In order to improve the self-start ability, the lift-type turbine with high solidity was used. The rotational speeds of the lift-type turbines were initially decided according to the principle of the high solidity vertical axis wind turbine in open conditions. The higher solidity, the sharper the power curve is (Paraschivoiu 2002). In other words, the maximum power point of the turbine is close to lower tip speed ratio (TSR). Thus, the evaluated TSR for the turbine ranged from 0 to 4. The interval between the two TSR points was 0.4.

Table 0.1 Simulation and testing results of lift-type model at 1.5m/s: (Appendix B)

Influence of chord length and blade number on the turbine performance

	<i>Case No.</i>	<i>Blade No.</i>	<i>Chord length/solidity (mm)</i>	<i>Angular speed/TSR (rad/s)</i>	<i>Power output(W)</i>	<i>Pressure drop(pa)</i>
<i>Simulated Lift turbine Diameter (66mm)</i>	S1	3	24/1.09	18.75/0.4	0.65	1101
				37.5/0.8	1.86	682
				56.25/1.2	3.14	1001
				75/1.6	1.28	915
	S2	3	32/1.45	18.75/0.4	0.48	749
				37.5/0.8	1.568	927
				56.25/1.2	0.22	*
				75/1.6	0.027	2495
	S3	5	16/1.21	37.5/0.8	1.4	3025
				56.25/1.2	1.65	3342
	S4	6	24/2.18	37.5/0.8	1.14	2223
				56.25/1.2	2.06	2560
<i>Testing result</i>	T1-S1	3	24/1.09	*	0	*
	T2-S2	3	32/1.45	*	0	*

The power coefficient is negative when the TSR is larger than 2.5. Therefore, the TSR of most of the simulation cases is less than 2.5. The TSR is defined as:

$$\lambda = \frac{\omega * r}{v} \quad \text{Equation 0.2}$$

where  $v$  is the water velocity,  $\omega$  is angular speed and  $r$  is the radius of the turbine.

The solidity is expressed as:

$$\sigma = \frac{N * c}{D} \quad \text{Equation 0.3}$$

where  $N$  is the blade number of the turbine,  $c$  is the chord length of the airfoil and the  $D$  is the diameter of the rotor.

The comparison between the Case S1 and Case S2 shows that the chord length influence on the turbine performance is obvious. The conclusion drawn from the comparison is the same as that of a vertical axis wind turbine under the open condition. The higher solidity, the sharper the power curve is. The reason why the working principle is the same between a wind turbine and a water turbine is that the rotor blockage value is not big enough to influence the working principle of the vertical axis turbine under the open condition.

The comparison of the Case S3 and Case S4 shows the blade number influence on the turbine performance. The power output of the Case S3 and Case S4 is much lower than that of the Case S1. However, the pressure drop of the Case S3 and Case S4 is much sharper than the Case S1 and Case S2, although the pressure drop of the Case S2 is not shown at angular speed 56.25 rad/s because the datum was lost one year ago due to the damaged of a hard disk.

The Case S1 and Case S2 were fabricated and installed in the pipeline to measure their real power outputs. The last two rows in Table 0.1 show the test results of the

Case S1 and Case S2. Zero power output is predictable when the Case S1 and Case S2 were used to drive the 50W power generator. The optimum TSR of the drag-type turbines is about 0.8 under the open condition. Thus, the angular speeds of the drag-type turbines can be chosen when the TSR is close to 0.8.

Table 0.2 Simulation and testing results of drag type models at 1.5m/s: influence of rotor size on the turbine performance (Appendix B)

	<i>Case No.</i>	<i>Blade No.</i>	<i>Rotor size (mm)</i>	<i>Angular speed (rad/s)/TSR</i>	<i>Power output (W)</i>	<i>Pressure drop (pa)</i>
<i>Simulated Drag Turbine (solid)</i>	S5	3	66	37.5/0.825	0.543	1551
	S6	3	86	22.5/0.645	3.8	6777
				30/0.86	4.28	7030
				37.5/1.075	4.2	7268
	S7	3	95	22.5/0.7125	10.64	*
30/0.95				12.34	*	
37.5/1.1875				13.59	*	
45/1.425				14.49	*	
<i>Test result</i>	T3-S6	3	86	*	0	0

Table 0.2 shows the influence of the rotor size on the power output of the solid drag-type turbines. It is obvious that the power output increases with the increase of the rotor size. The highest power rate is 14.49W for the Case S7. The power rate

increase could be probably attributed to several factors. The power output is in direct proportion to the sweep area of the turbine under the open condition. It seems that this principle is applicable to confined condition. However, the power changes non-linear along the sweep area. A small change in the sweep area could cause big changes of power output. The second factor is the blockage ratio which is only used under the confined conditions. Water flow can skirt around the turbine in the open condition, but it can only act on the water turbine directly due to the limitation of the pipe wall, thus generating more thrust force.

Table 0.3 Simulation and testing results of drag type models at 1.5m/s: influence of blade number on the turbine performance (Appendix B)

	<i>Case No.</i>	<i>Blade No.</i>	<i>Rotor size (mm)</i>	<i>Angular speed (rad/s)/TSR</i>	<i>Power output (W)</i>	<i>Pressure drop (pa)</i>
<i>Simulated Drag Turbine (Solid)</i>	S8	3	66	37.5/0.825	0.543	1551
	S9	5	66	18.75/0.4125	1.875	7829
				28.125/0.618	3.9375	8173
				37.5/0.825	0.85	*
	S10	10	66	150.33	3.67	7752
				22.5/0.495	4.63	7344
				30/0.66	5.24	7086
				37.5/0.825	4.8	6833

The influence of the blade number on the power output of the solid drag-type

turbines is presented in Table 0.3. It is clear that the more blades a turbine has the more power it can generate. The maximum power output is only 5.24 W when ten blades are adopted for the solid drag-type turbine working at 30 rad/s.

Under the open condition, the power coefficient will decrease with the increase of the blade number. However, it is opposite in the confined condition. The reason for this increase may be that the numbers of advancing blades which generate the thrust forces is increased in the confined condition. And the drag force produced by the returning blades is reduced due to the smooth pass of the incoming flows.

Table 0.4 Simulation and testing results of drag type models at 1.5m/s: influence of diameter of the center hollow on the turbine performance (Appendix B)

	<i>Case No.</i>	<i>Blade No.</i>	<i>Diameter of hollow circular cylinder (mm)</i>	<i>Rotor size (mm)</i>	<i>Angular speed (rad/s)/TSR</i>	<i>Power output (W)</i>	<i>Water head loss(m)</i>
<i>Simulated Drag Turbine (Hollow)</i>	S11	10	20	92	15/0.46	3.06E-04	14
					30/0.92	9.65E-05	14
	S12	10	30	92	15/0.46	2.92E-04	9.77
					30/0.92	1.01E-04	9.932
					40/1.22	-3.31E-05	*
					50/1.53	-1.69E-04	*
S13	10	40	92	15/0.46	1.01E-04	7	
				30/0.92	-2.59E-04	7.32	

Three turbines with different diameters of the hollow circular cylinder were presented in Table 0.4. It is found that the power output is almost close to zero when the water velocity is 1.5m/s and the pressure drop is very high. One possible reason, which is responsible for this phenomenon of lower power output and high pressure consumption, is that the angular speed of the rotor is evaluated improperly. The optimum rotational speed of this hollow rotor with multiple blades may be much lower than the rotational speed of estimation. Hence, this rotor is working under off-design condition which causes turbulence flow in and around the turbines. Another reason may be that this type of turbine is not suitable for this design condition.

The comparison of Table 0.1 ,Table 0.2, Table 0.3 and Table 0.4 shows that the power output of the drag-type turbine is generally higher than that of the lift-type turbines and the same for the pressure drop in a confined condition except for the hollow drag-type turbines, which indicates that the solid drag type especially ones with more blades and larger diameter, is more suitable than the lift-type in a confined space. Although the power output of the first generation of the hydropower generators is sufficient for the power of the monitoring sensors, there is still a lot of room for improvement due to the pressure drop of the initial proposed turbine which is much lower than the allowed pressure head consumption of 5m. Further modification is necessary for the drag-type turbines so as to generate more power.

## **B 5.2 Second generation of the hydropower system**

Based on the conclusions drawn from the development of the first generation turbines, more attention was paid to the drag-type turbines with more blades and

larger size on their second generation as more water head can be consumed to have more power output. According to the working principle of the drag-type rotor, it is obvious that the returning blades of the drag type turbine create most of the resistance force. If we can install a block inside the pipeline to surround the returning blades, the water flow will not attack the returning blades directly. At the same time, part of the water head energy is converted into kinetic energy due to narrowing the water flow channel. The returning blades, advanced blades and some blocks are shown in Figure 0.10.

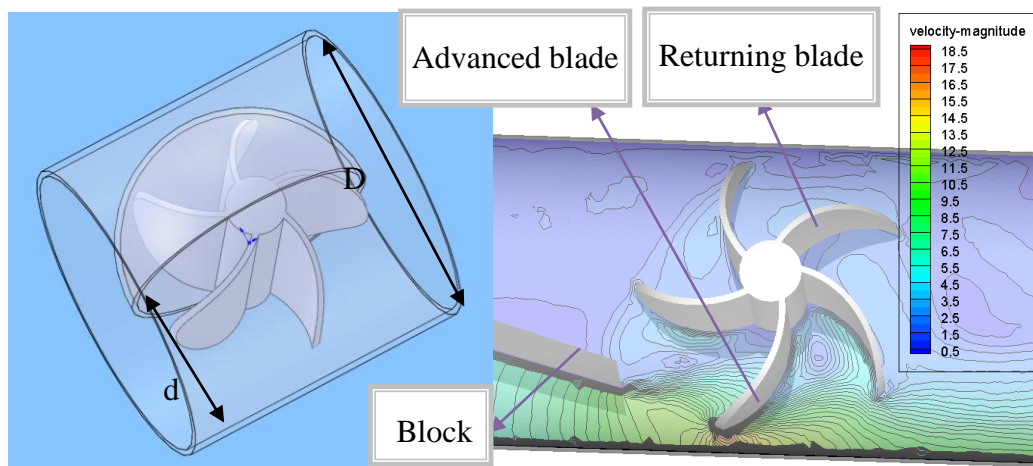


Figure 0.10 The working principle of the drag-type turbine (Appendix B)

Therefore, four types of blocks were designed for solid drag-type turbines. Figure 0.11 shows the four types of blocks according to the sequence of the evolution. In order to install the block through the T joints, the size and type of the blocks are limited. The vertical block is the first proposed block which can be inserted directly into the pipeline through a T joint. The second block which is a long slanted block needs to be divided into three pieces for installation. Hence, the installation process of the second block is relatively complex. Thus, the third block which is a short

slanted block was developed to replace the second block. The last block is a slanted block with an eye-shaped opening. The definition of the block ratio which is shown in Table 0.5, Table 0.6, Table 0.7 and Table 0.8 is the same for the vertical, long slanted and short slanted blocks. The block ratio is defined as  $d/D$  which is presented in Figure 0.11. The block ratio of the eye shaped block is defined as the ratio of the outlet area for inlet area. The angular speed of the simulated turbines was evaluated based on the first generation turbine.



(1) Vertical block

(2) Long slanted block



(3) Short slanted block

(4) Eye shaped block

Figure 0.11 Four forms of block (Appendix B)

The simulation results of vertical and slanted blocks are listed in Table 0.5. And the

testing results are presented in Table 0.6. Case S14 and Case S15 were compared to investigate the blades number influence on the turbine performance when the blockage ratio is 0.5. It is found that power output of Case S14 is less than that of Case S15 when the vertical block is combined with solid turbine. The maximum power output of Case S14 is 10.6Wm, which seems that the principle (more blades for more power) is suitable for the vertical block when the block ratio is 0.5. The corresponding tested turbine is the Case T5 which has zero power output.

More tested Cases with vertical block were listed in Table 0.6. It is clear that with the increase of the blockage ratio the power output will increase. The maximum power output and pressure drop are 13.4W and 3.75m when the blade number is six and block ratio 0.9. As the power output is much less, and the aim and the vertical block cannot converge all the water flow, second block was developed and simulated. Based on the testing results of the vertical block, the simulation of second block was focused on the high block ratio. Although simulation results show the maximum power output is 67.69 at block ratio 0.8, the testing result is only 11.8W. And it is a little complex to install the long slanted block through the T joints. Thus the short slanted block was built and tested. It seems that the power output of the short slanted block is close to that of long slanted block.

Three blocks mentioned above have a common disadvantage. It is that the offset between the flow pathway and the turbine's advanced blade will increase when the blockage ratio increases. Thus the fourth generation block was developed. Through this block, the flow can act directly on the turbine's advanced blades. Figure 0.11 illustrates this improvement clearly. The eye shaped block was manufactured and

tested without the simulation. From Table 0.6, the maximum power of the slanted eye shaped block can reach 32.2W. This is a significant improvement. And the more water head was consumed. The optimum block ratio is 0.9.

Table 0.5 Simulation results of drag type models at 1.5m/s (Appendix B)

	<i>Case No.</i>	<i>Blade No.</i>	<i>Block type block ratio</i>	<i>Rotor diameter (mm)</i>	<i>Angular speed (rad/s)</i>	<i>Power output (W)</i>	<i>Pressure drop (pa)</i>
<i>Simulated Results of Drag Turbine (solid) + Vertical Block or Long slanted block</i>	S14	5	Vertical block 0.5	86	37.5	2.2	4007
					56.25	10.6	5726
	S15	10	Vertical block 0.5	86	15	3.67	*
					22.5	4.63	*
					30	5.24	7305
					37.5	4.8	6994
	S16	5	Long slanted block 0.6	86	30	12.56	36829
					40	13.77	36339
					50	12.29	36004
	S17	5	Long slanted block 0.8	92	30	55.15	84523
40					64.68	85176	
50					67.69	80875	
S18	6	Long slanted block 0.8	92	37.5	59.79	87623	
S19	10	Long slanted block 0.8	92	40	64.43	85329	

Table 0.6 testing results of drag type models at 1.5 m/s (Appendix B)

	<i>Case No.</i>	<i>Blade No.</i>	<i>Block type</i>	<i>Rotor diameter (mm)</i>	<i>Max Power output (W)</i>	<i>Pressure drop (m)</i>
<i>Testing results</i>  <i>Drag Turbine (solid)</i> + <i>Four kinds of blocks</i>	T4	3	Vertical block 0.5	86	0	*
	T5-S14	5	Vertical block 0.5	86	0	*
	T6	5	Vertical block 0.7	86	0	*
	T7	5	Vertical block 0.8	86	1.9	2.24
	T8	6	Vertical block 0.7	86	1.1	2.11
	T9	6	Vertical block 0.8	86	4.0	2.37
	T10	6	Vertical block 0.9	86	13.4	3.75
	T11-S17	5	Long slanted block 0.8	92	11.8	*
	T12	5	Long slanted block 0.9	92	0	*
	T13	5	Short slanted block 0.8	92	12	*
	T14	5	Slanted block with eye-shaped opening 0.9	92	24.8	5.6
	T15	6	Slanted block with eye-shaped opening 0.8	92	6.1	3.36
	T16	6	Slanted block with eye-shaped opening 0.85	92	26.2	4.75
	T17	6	Slanted block with eye-shaped opening 0.9	92	32.2	5.82
	T16	6	Slanted block with eye-shaped opening 0.95	92	26.6	10.41

Table 0.7 Testing results of drag type models with long slanted block (Appendix B)

	Case No.	Blade No.	Block type	Rotor diameter (mm)	Flow rate (m/s)	RPM	Load (ohm)	Voltage (V)	Power (W)	Input pressure (m)
Testing results Drag Turbine (solid) + Long slanted block	T11	5	long slanted block 80%	92	1.66	691	No load	87.0	0.0	40
					1.66	325	100	34.0	10.9	40
					1.66	206	60	23.0	8.3	40
					1.66	171	40	16.0	5.6	40
					1.92	840	No load	108.0	0.0	45
					1.92	612	200	69.0	22.8	45
					1.92	379	80	42.0	21.0	45
					1.92	348	60	33.4	17.4	45
					1.92	282	40	25.6	14.8	45
					2.58	1207	No load	154.0	0.0	40
					2.58	840	100	90.8	82.6	40
					2.58	765	80	84.0	84.0	40
					1.90	754	No load	68.0	0.0	40
					1.90	509	200	44.0	9.1	40
					1.90	420	100	36.0	13.3	40
					1.90	404	80	35.0	14.7	40
					1.90	265	40	27.2	17.4	40
1.90	257	20	20.2	17.8	40					

Table 0.8 Testing results of drag type models with short slanted block (Appendix B)

	Case No.	Blade No.	Block type	Rotor diameter (mm)	Flow rate (m/s)	RPM	Load (ohm)	Voltage (V)	Power (W)	Input pressure (m)
Testing results Drag Turbine (solid) + Short slanted block	T13	5	short slanted block 80%	92	1.58	703	No load	89.0	0.0	40
					1.58	461	200	50.6	12.1	40
					1.58	357	100	36.9	11.8	40
					1.58	286	80	30.5	10.7	40
					1.58	249	60	25.2	9.6	40
					1.58	166	40	16.8	6.2	40
					1.58	102	20	8.0	2.4	40
					1.91	912	No load	112.0	0.0	44
					1.91	691	200	75.0	27.8	44
					1.91	498	100	51.0	25.0	44
					1.91	433	80	44.8	24.2	44
					1.91	351	60	36.5	21.5	44
					2.51	1280	No load	158.0	0.0	44
					2.51	1020	200	115.0	66.7	44
					2.51	884	100	95.0	84.6	44
					2.51	840	80	86.7	92.8	44
					2.51	357	20	31.0	46.5	44

### B 5.3 Third generation of the hydropower system

In fact, the power output from the above turbine is enough to supply the monitoring system. However, there is still much room for improvement according to our estimation. Till now, we conclude that the solid drag turbine can produce the highest power in the first generation. And the slanted eye shaped block has been proved to be the best block in the second generation.

It seems that we have tried a lot of design combinations of the solid turbines and blocks. The only combination which we did not try is the combination of the hollow turbine and the block due to the zero power output of the hollow drag type turbines in the first generation.

Thus, simulation cases of such combination were created. The cases include two types of combinations which are presented in Figure 0.12. One is the combination of the long slanted block and hollow drag type turbine. Another one is the combination of the slanted eye shaped block and hollow drag type turbine.

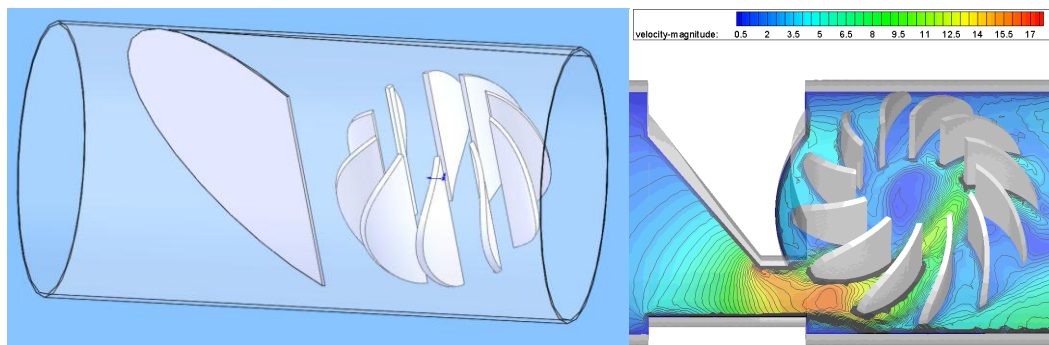


Figure 0.12 Two different combinations (Appendix B)

Table 0.9 Simulation results of drag type models (Appendix B)

<i>Simulated Results of Drag Turbine (hollow) + Long slanted block or slanted eye shaped block</i>	<i>Case No.</i>	<i>Blade No.</i>	<i>Block type</i>	<i>Diameter of hollow circular cylinder (mm)</i>	<i>Rotor size</i>	<i>Angular speed (rad/s)</i>	<i>Power output (W)</i>	<i>Pressure drop (pa)</i>
	S20	10	Long slanted block 0.8	20	92	40	99	72787
	S21	10	Long slanted block 0.8	30	92	40	116.3	74739
	S22	10	Long slanted block 0.8	45	92	40	127.5	75647
	S23	12	Slanted block with eye- shaped opening 0.9	45	92	40	226.8	124337
	S24	12	Slanted block with eye- shaped opening 0.9	55	92	40	215.3	124369
	S25	15	Slanted block with eye- shaped opening 0.9	45	92	40	228	122469
	S26	18	Slanted block with eye- shaped opening 0.9	45	92	40	221	122642

Table 0.9 shows the simulation results. The power output of the Case S22 is twice higher than that of the Case S19 which produces the highest power in the second generation. The only difference between the two cases is the turbine's hollow structure. The simulation results indicate that the optimum diameter of the hollow circular cylinder is close to 45mm. From the conclusion of the second generation development, the best block is the slanted eye shaped turbine. Thus, the hollow turbines were used together with a slanted eye shaped block.

Case S23 and Case S24 show the influence of the turbine diameter with a hollow circular cylinder. Only two kinds of diameters were investigated of the slanted eye shaped block due to time consideration and some indications given from the simulation of the long slanted block system. The influence of blade number can be found through the comparison among Case S24, Case S25 and Case S26. The simulation results show that the optimum blade number is close to 15. In fact, the difference of the simulation power output between the 12-blade turbine and 15-blade turbine is only 2W.

Although the combination of the hollow turbine and slanted eye shaped block provides a significant improvement of power output, the water head loss is close to 12m, which is not acceptable. In order to validate the conclusion about the blade number influence, the turbines with a large blade number difference were developed. The test results presented in Table 0.10 are very inspiring. The maximum power output of this combination reached 88.2W and the consumed water head is within the 5m limit. The optimum blade number of the tested turbines is 12, which has also validated the conclusion drawn from the simulation results, although the power

output and pressure drop from the simulation are much higher than those of the test results.

Table 0.10 Testing results of drag type models (Appendix B)

<i>Tested Results of Drag Turbine (hollow) + Slanted Eye Shaped Block</i>	<i>Case No.</i>	<i>Blade No.</i>	<i>Block type</i>	<i>Diameter of hollow circular cylinder (mm)</i>	<i>Rotor size (mm)</i>	<i>Angular speed (rad/s)</i>	<i>Power output (W)</i>	<i>Pressure drop (m)</i>
	T17	8	Slanted block with eye-shaped opening 0.9	45	92	66	66.4	4.48
	T18-S23	12	Slanted block with eye-shaped opening 0.9	45	92	74	88.2	4.85
	T19	24	Slanted block with eye-shaped opening 0.9	45	92	63	67.4	4.43

#### B 5.4 Summary of three generations

A summary of the typical vertical axis water system is presented in Table 0.11. The power output is increased significantly from zero to 88.2 W during the one-year experiment test and CFD simulation. The typical designs of the different generations are listed below. The combination of the hollow drag type turbine and the slanted eye shaped block not only can produce the estimated power to supply the monitoring system, but also satisfy the power supply requirements. The eye shaped block and hollow turbine can be inserted easily through the T joints in the pipeline. The power output and pressure drop can be controlled through the adjustment of the blockage

ratio, which makes the system readily suitable to the different requirements.

Table 0.11 Summary of the development of hydropower turbine (Appendix B)

Drag type turbine design		Max Power (W)	Head drop (m)
1st Gen: 5-blade solid turbine (Ø86mm) + vertical half block		0	0
1st Gen: 5-blade solid turbine (Ø92mm) + 80% short slanted block		12.0	N/A
2rd Gen: 6-blade solid turbine (Ø92mm) + 90% slanted eye shaped block		32.2	5.82
3th Gen: 12-blade (Ø92mm) hollow turbine+ 90% slanted eye-shaped block		88.2	4.85

Although the simulated and testing results demonstrate large quantitative difference, the trends and variations of the simulated results are consistent with that of the testing results from the qualitative point of view. Both the simulation and test results show that the rotor with hollow shaft and short slanted block can generate much more power than the others. The simulation results do offer important theoretical guidance for the design of a real model. The possible reason for the difference is that the energy losses caused by water flow friction and various mechanical frictions were not considered in the simulations, and the mismatch between the turbine's

power curve and generator's power curve may exist. Besides, the simulated models and water pipe are not exactly the same as the tested models and water pipe in shape. In addition, the effect of the CFD settings on the simulation results is not investigated profoundly due to the high cost of computational effort and the limitation of design time.

### **B 5.5 Conclusion**

An inline vertical axis water turbine is developed in this chapter for power supply of water pipeline data monitoring systems. This turbine system is designed for a 100mm pipeline. The expected power output is larger than 80 W when water velocity is 1.5m/s and pressure drop is less than 5m. After simulating and testing more than 20 different kinds of water turbines under various working conditions, the combination of the vertical axis water turbine with a hollow shaft and short slanted eye shaped block was proved to be the best for generating the highest amount of power output which is 88.2W.



Figure 0.13 The hydropower system is running on the site (Appendix B)

Further improvement can still be made for this novel inline vertical axis water turbine although the final design can meet the expectations under certain limitation. The design parameters which need to be further investigated can be the tilted angle of the turbine blades, foil of turbine blades and the hollow shapes of the turbines. Lastly, the simulated and testing results offer valuable insight into hydropower harvest inside the water pipeline of different sizes, although the system developed in this chapter focused on the 100mm pipeline. Some of the turbines of the first and second generations may also be adopted when the power supply demanding is low.

Several final systems have been installed at designated areas in Hong Kong for the purpose of further on-site investigation. One of these systems is presented in Figure 0.13. The measured value of the on-site power output is very close to the tested value in laboratory

## **B 5.6 Discussion**

All the simulated and testing results demonstrate that the difference between the simulation and testing results is significant. It can be explained through the following reasons. The first one is the power loss caused by mechanical friction. The second one is the mismatch between the turbine's power curve and generator's power curve. The third one is that the simulated models are not exactly the same to the test models in shape. Although the simulation results diverge from the test results, the simulation results do offer important theory guidance for the real model design. Both the simulation and test results show that the rotor with hollow shaft and short slanted block generates higher power than the others. There are also some of insufficiencies

in this section. The first one is that some of datum is missing which is marked using the asterisk. The second one is that different types of turbines should use different types of torque meter to measure the torque precisely. However, we used a 50w generator to replace the torque meter due to the limitation of the funding and time.

### **B 5.7 Acknowledgements**

The work described in this section was supported by the Water Supplies Department and the Inter-Faculty Research Grant of The Hong Kong Polytechnic University (Project No.: G-YG08). The PolyU Technology & Consultancy Company Limited provided a lot of laboratory testing support to the project.



# APPENDIX C (AWARD and PATNET)

## PATENT

知識產權署專利註冊處  
Patents Registry  
Intellectual Property Department



香港特別行政區政府  
The Government of the Hong Kong  
Special Administrative Region

---

### 批予短期專利證明書

《專利條例》(第 514 章)

### CERTIFICATE OF GRANT OF SHORT-TERM PATENT

Patents Ordinance (Chapter 514)

茲證明下述短期專利在今日批予:

*I hereby certify that a short-term patent with the following particulars has been granted today:*

專利所有人姓名或名稱及地址 **Name and Address of Proprietor:**

香港特別行政區政府  
香港

The Government of HKSAR  
Water Supplies Department  
48/F Immigration Tower  
7 Gloucester Road, Wanchai  
HONG KONG

香港理工大學  
香港

The Hong Kong Polytechnic University  
The Hong Kong Polytechnic University  
Hung Hom, Kowloon  
HONG KONG

專利編號 **Patent No.:** HK1150355

申請編號 **Application No.:** 11107929.8

發明名稱 **Title of Invention:**

內聯閉式水力發電系統

AN INLINE HYDROELECTRIC GENERATING SYSTEM IN CONFINED  
CONDITION

**短期專利有效期 (在符合續期的規定下) Term of Short-term Patent (subject to renewal):**

由 01.08.2011 起計 8 年

Eight years commencing on 01.08.2011

日期：2011 年 12 月 2 日

Date: 2 December, 2011

專利註冊處處長張錦輝  
Peter K.F. Cheung  
Registrar of Patents

註： 1. 短期專利的有效期最長為 8 年，由提交專利申請的日期起計。專利所有人須遵照《專利條例》及《專利(一般)規則》的規定，繳付訂明的續期費，維持專利有效。繳付續期費時，須一併遞交指明的專利續期表格。  
Note: The term of a short-term patent is up to a maximum of 8 years from the date of filing of the patent application. The proprietor shall pay the prescribed renewal fees in accordance with the Patents Ordinance and the Patents (General) Rules to keep the patent in force. Fees should be accompanied by the specified patent renewal form.

《專利條例》第 126(2)條規定，如欲在短期專利的申請的提交日期起計的第 4 年屆滿後將短期專利再維持有效 4 年，須在該第 4 年的屆滿前 3 個月內繳付續期費。凡批予專利日期是在自該專利的申請的提交日期起計的第 4 年屆滿之後，則根據《專利條例》第 126(3)條，續期費須在批予日期起計的 3 個月內繳付。

Under section 126(2) of the Patents Ordinance, to keep the short-term patent in force for a further 4 years after the expiry of the 4th year from the date of filing of the application for the patent, the renewal fee shall be paid within the 3 months ending with the expiry of the 4th year. Where the date of grant of the patent occurs after the expiry of the 4th year from the date of filing of the application, the payment of renewal fee shall be made within 3 months from the date of grant in accordance with section 126(3) of the Patents Ordinance.

如專利註冊處在上述期限內沒有收到有關表格及續期費，則在期限屆滿後 6 個月內繳付的續期費，必須連同訂明的逾期附加費一併繳交。如專利註冊處未能在訂明期限內收到有關費用，專利便會停止有效。If the form and fee are not lodged with the Patents Registry within the above-mentioned period, any renewal fee paid within the period of 6 months after the end of that expiry shall be accompanied by the prescribed additional fee for late payment. If no fee is received within the prescribed period, the patent will cease to have effect.

2. 本專利的擁有權如有改變，或所有人的姓名/名稱及/或地址/送達地址改變，必須立刻向專利註冊處處長申請更改註冊。  
Upon any change of ownership of this patent, or change of name and/or address/address for service of the proprietor, application should AT ONCE be made to the Registrar of Patents to register the change.

3. 專利註冊處處長在批予短期專利前並無就發明的可享專利性進行實質審查。請參閱香港特別行政區知識產權署網站的“短期專利”一節 ([http://www.ipd.gov.hk/chi/intellectual\\_property/patents/short\\_term\\_patents.htm](http://www.ipd.gov.hk/chi/intellectual_property/patents/short_term_patents.htm)) 內的進一步資料。

The grant of a short-term patent does not follow a substantive examination of its patentability by the Registrar of Patents. For further information, please refer to the section “Short-term patents” of the website of Intellectual Property Department Hong Kong SAR ([http://www.ipd.gov.hk/eng/intellectual\\_property/patents/short\\_term\\_patents.htm](http://www.ipd.gov.hk/eng/intellectual_property/patents/short_term_patents.htm)).

# DIPLÔME

**G**inventions  
Geneva

## SALON INTERNATIONAL DES INVENTIONS GENÈVE

Après examen, le Jury International a décidé

de remettre à: Prof. Hong-Xing YANG, Mr. Jian CHEN & Dr. Lin LU

pour l'invention: Système d'exploitation d'énergie hydraulique pour utilisation dans les tuyaux à eau douce



MÉDAILLE D'ARGENT  
SILVER MEDAL  
SILBERMEDAILLE

Genève, le 20 avril 2012

Le Président du Jury: David Tajji /

Le Président du Salon: Jean-Luc Vincent

# HKIE AWARD

**HKIE** THE HONG KONG  
INSTITUTION OF ENGINEERS  
香港工程師學會

卓越工程巡禮  
Engineering Week 2013

工程創意大獎  
Innovation Award for the  
Engineering Industry



Technology Category

*Certificate of Merits*

**Ir Prof YANG Hong Xing**

*Principal Innovator*

An Inline Hydroelectric Generating System in  
Confined Condition for Urban Water Pipelines

## REFERENCE

- Afungchui, D., B. Kamoun, A. Helali and A. Ben Djemaa (2010). The unsteady pressure field and the aerodynamic performances of a Savonius rotor based on the discrete vortex method. *Renewable Energy* 35(1): 307-313.
- Akwa, J. V., G. Alves da Silva Júnior and A. P. Petry (2012). Discussion on the verification of the overlap ratio influence on performance coefficients of a Savonius wind rotor using computational fluid dynamics. *Renewable Energy* 38(1): 141-149.
- Aldos, T. (1984). Savonius rotor using swinging blades as an augmentation system. *Wind Engineering* 8: 214-220.
- Aldoss, T. and M. Kotb (1988). Theoretical calculations of the flow field around a Savonius rotor. *Wind Engineering* 12(3): 194-203.
- Aldoss, T. K. and Y. S. H. Najjar (1987). The performance of two savonius rotors running side by side. *wind Engineering* 11(2): 79-88.
- Alexander, A. (1978). Wind tunnel corrections for Savonius rotors. NASA STI/Recon Technical Report A 79: 40127.
- Altan, B. D. and M. Atilgan (2008). An experimental and numerical study on the improvement of the performance of Savonius wind rotor. *Energy Conversion and Management* 49(12): 3425-3432.
- Altan, B. D., M. Atilgan and A. Özdamar (2008). An experimental study on improvement of a Savonius rotor performance with curtaining. *Experimental Thermal and Fluid Science* 32(8): 1673-1678.
- Amatya, R. and R. Ram (2010). Solar thermoelectric generator for micropower applications. *Journal of electronic materials* 39(9): 1735-1740.
- Amet, E., T. Maitre, C. Pellone and J. L. Achard (2009). 2D Numerical Simulations of Blade-Vortex Interaction in a Darrieus Turbine. *Journal of Fluids Engineering-Transactions of the Asme* 131(11).
- Antheaume, S., T. Maitre and J. L. Achard (2008). Hydraulic Darrieus turbines efficiency for free fluid flow conditions versus power farms conditions. *Renewable Energy* 33(10): 2186-2198.
- Armstrong, S. and S. Tullis (2011). Power performance of canted blades for a vertical axis wind turbine. *Journal of Renewable and Sustainable Energy* 3(1).
- Ashwill, T. D. (1992). Measured data for the Sandia 34-meter vertical axis wind turbine, Sandia National Laboratories.
- Ashwill, T. D., T. M. Leonard, S. N. Laboratories and U. S. D. o. Energy (1986). Developments in blade shape design for a Darrieus vertical axis wind turbine, Sandia National Laboratories.

- Bach, v. G. (1931). Untersuchungen über Savonius-Rotoren und verwandte Stromungsmaschinen. *Forsch auf dem Gebiete des Ingenieurwesens* 2(6): 218-231.
- Baker, J. (1983). Features to aid or enable self starting of fixed pitch low solidity vertical axis wind turbines. *Journal of Wind Engineering and Industrial Aerodynamics* 15(1): 369-380.
- Banks, A., J. Vincent and C. Anyakoha (2007). A review of particle swarm optimization. Part I: background and development. *Natural Computing* 6(4): 467-484.
- Bargsten, C. J. and M. T. Gibson (2011). *NASA Innovation in Aeronautics: Select Technologies That Have Shaped Modern Aviation*, National Aeronautics and Space Administration: 1-68.
- Barlow, J. B., W. H. Rae and A. Pope (1999). *Low Speed Wind Tunnel Testing*, John Wiley and Sons, Inc.
- Benghrib, D., A. Ahram and L. Bchir (1998). Description of the vortex formation on a Savonius rotor in a water channel. *Comptes Rendus de l'Academie des Sciences Series IIB Mechanics Physics Astronomy* 326(8): 495-500.
- Bergeles, G. and N. Athanassiadis (1982). On the flow field around a Savonius rotor. *Wind Engineering* 6: 140-148.
- Bernad, S. I., A. Georgescu, S. Georgescu and R. F. Resiga (2008). Numerical Investigations of the Unsteady Flow in the Achard Turbine. *Fma'08: Proceedings of the 6th Iasme/Wseas International Conference on Fluid Mechanics and Aerodynamics*: 59-65.
- Blackwell, B. F., R. F. Sheldahl, L. V. Feltz, S. Laboratory, U. S. E. Research and D. Administration (1977). *Wind tunnel performance data for two-and three-bucket Savonius rotors*, Sandia Laboratories.
- Blanch, M. (2002). Wind energy technologies for use in the built environment. *Wind Engineering* 26(3): 125-143.
- Bowden, G. and S. McAleese (1984). The properties of isolated and coupled Savonius rotors. *Wind Engineering* 8: 271-288.
- Bravo, R., S. Tullis and S. Ziada (2007). Performance testing of a small vertical-axis wind turbine. In *21st Canadian Congress of Applied Mechanics CANCAM*.
- Brothers, K. (2003). A practical approach to water loss reduction. *Water* 21: 54-55.
- Brownlee, B. G. (1988). A vortex model for the vertical axis wind turbine. Master of Science, Texas Tech University.
- Camarinopoulos, L., A. Chatzoulis, S. Frontistou-Yanas and V. Kalidromitis (1999). Assessment of the time-dependent structural reliability of buried water mains. *Reliability Engineering and Safety* 65(1): 41-53.
- Camarinopoulos, L., A. Chatzoulis, S. Frontistou-Yannas and V. Kallidromitis, Eds. (1996). *Structural reliability of water mains. Probabilistic Safety Assessment and*

Management '96, ESREL-PSAM III. New York, Springer.

Camarinopoulos, L., G. Pampoukis and N. Preston, Eds. (1996). Reliability of a water supply network. Probabilistic safety assessment and management '96, ESREL-PSAM III. New York, Springer.

Carr, L. W. (1985). Dynamic stall progress in analysis and prediction. AIAA, Atmospheric Flight Mechanics Conference, 12 th, Snowmass, CO.

Castelli, M. R. and E. Benini (2012). Effect of Blade Inclination Angle on a Darrieus Wind Turbine. *Journal of turbomachinery* 134: 031016.

Chan, T. F. and L. L. Lai (2007). An axial-flux permanent-magnet synchronous generator for a direct-coupled wind-turbine system. *Ieee Transactions on Energy Conversion* 22(1): 86-94.

Chauvin, A. and D. Benghrib (1989). Drag and lift coefficients evolution of a Savonius rotor. *Experiments in Fluids* 8(1): 118-120.

Chi, E., A. M. Salem, R. I. Bahar and R. Weiss (2003). Combining software and hardware monitoring for improved power and performance tuning, IEEE.

Claessens, M. (2006). The design and testing of airfoils for application in small vertical axis wind turbines. Master of Science Thesis.

Conti, J. and P. Holtberg (2011). The International Energy Outlook 2011. Washington, DC, U.S. Energy Information Administration: 301.

D'Alessandro, V., S. Montelpare, R. Ricci and A. Secchiaroli (2010). Unsteady Aerodynamics of a Savonius wind rotor: a new computational approach for the simulation of energy performance. *Energy* 35(8): 3349-3363.

Dixon, K. (2008). The Near Wake Structure of a vertical axis wind turbine-Including the Development of a 3D Unsteady Free-Wake Panel Method for VAWTs. Master of Science Thesis, Delft University of Technology.

Dondi, D., A. Bertacchini, D. Brunelli, L. Larcher and L. Benini (2008). Modeling and optimization of a solar energy harvester system for self-powered wireless sensor networks. *Industrial Electronics, IEEE Transactions on* 55(7): 2759-2766.

Energy, L. How it works. Retrieved 04-13, 2012, from <http://www.lucidenergy.com/how-it-works/>.

Ferreira, C. J. S., H. Bijl, G. van Bussel and G. van Kuik (2007). Simulating dynamic stall in a 2D VAWT: Modeling strategy, verification and validation with particle image Velocimetry data - art. no. 012023. *Science of Making Torque from Wind* 75: 12023-12023.

Ferreira, C. J. S., G. J. W. van Bussel and G. A. M. van Kuik (2006). Wind tunnel hotwire measurements, flow visualization and thrust measurement of a VAWT in skew. *Journal of solar energy engineering* 128: 487.

Fiedler, A. (2009). The effects of blade pitch and mount point offset on vertical axis

- wind turbine performance. Master of Applied Science, McMaster University.
- Fiedler, A. J. and S. Tullis (2009). Blade offset and pitch effects on a high solidity vertical axis wind turbine. *Wind Engineering* 33(3): 237-246.
- Fleming, P. and S. Probert (1982). A proposed, three-sail, savonius-type wind-rotor. *Applied Energy* 12(4): 327-331.
- FLUENT, A. (2009). 12.0/12.1 Documentation Users Guide Manual. ,Ansys Inc.
- FLUENT, A. (2009). 12.0/12.1 Documentation Users Guide Manual. Ansys Inc.
- FLUENT, A. (2009). FLUENT, A. 12.0/12.1 Documentation Users Guide Manual, Ansys Inc. Users Guide Manual, Ansys Inc.
- Fujisawa, N. (1996). Velocity measurements and numerical calculations of flow fields in and around Savonius rotors. *Journal of Wind Engineering and Industrial Aerodynamics* 59(1): 39-50.
- Fujisawa, N. and F. Gotoh (1992). Visualization study of the flow in and around a Savonius rotor. *Experiments in Fluids* 12(6): 407-412.
- Fujisawa, N. and H. Shirai (1987). Experimental investigation on the unsteady flow field around a Savonius rotor at the maximum power performance. *Wind Engineering* 11(4): 195-206.
- Furukawa, A., S. Watanabe, D. Matsushita and K. Okuma (2010). Development of ducted Darrieus turbine for low head hydropower utilization. *Current Applied Physics* 10: S128-S132.
- Gavalda, J., J. Massons and F. Diaz (1991). Drag and Lift coefficients of the Savonius Wind Machine. *Wind Engineering* 15(5): 240-246.
- Gorban', A. N., A. M. Gorlov and V. M. Silantyev (2001). Limits of the turbine efficiency for free fluid flow. *Journal of Energy Resources Technology-Transactions of the Asme* 123(4): 311-317.
- Gorlov, A. (1998). Development of the helical reaction hydraulic turbine. Washington,DC, Northeastern Univ., Boston, MA (United States): 59.
- Grinspan, A., P. Suresh Kumar, U. Saha, P. Mahanta, D. Ratna Rao and G. Veda Bhanu (2001). Design, Development and Testing Of Savonius Wind Turbine Rotor with Twisted Blades. *Proceedings of 28th National Conference on Fluid Mechanics and Fluid Power*: 428-431.
- Gupta, R. and A. Biswas (2010). Computational fluid dynamics analysis of a twisted three-bladed H-Darrieus rotor. *Journal of Renewable and Sustainable Energy* 2(4).
- Hadzilacos, T., D. Kalles, N. Preston, P. Melbourne, L. Camarinopoulos, M. Eimermacher, V. Kallidromitis, S. Frondistou-Yannas and S. Saegrov (2000). UtilNets: a water mains rehabilitation decision-support system. *Computers, Environment and Urban Systems* 24(3): 215-232.
- Hamada, K., T. Smith, N. Durrani, N. Qin and R. Howell (2008). Unsteady flow

- simulation and dynamic stall around vertical axis wind turbine blades. 46th AIAA Aerospace Sciences Meeting and Exhibit.
- Hayashi, T., Y. Li and Y. Hara (2005). Wind tunnel tests on a different phase three-stage Savonius rotor. *JSME International Journal Series B* 48(1): 9-16.
- Healy, J. V. (1978). The influence of blade camber on the output of vertical-axis wind turbines. *Wind Engineering* 2: 146-155.
- Hestnes, A. G. (1999). Building integration of solar energy systems. *Solar Energy* 67(4): 181-187.
- Howell, R., N. Qin, J. Edwards and N. Durrani (2010). Wind tunnel and numerical study of a small vertical axis wind turbine. *Renewable Energy* 35(2): 412-422.
- Irabu, K. and J. N. Roy (2007). Characteristics of wind power on Savonius rotor using a guide-box tunnel. *Experimental Thermal and Fluid Science* 32(2): 580-586.
- Islam, M., M. R. Amin, D. S. K. Ting and A. Fartaj (2008). A New Airfoil for the Supporting Struts of Smaller-capacity Straight-Bladed VAWT, American Institute of Aeronautics and Astronautics, 1801 Alexander Bell Drive, Suite 500, Reston, VA, 20191-4344, USA.
- Islam, M., M. R. Amin, D. S. K. Ting and A. Fartaj (2008). Performance Analysis of a Smaller-capacity Straight-bladed VAWT with Prospective Airfoils, American Institute of Aeronautics and Astronautics, 1801 Alexander Bell Drive, Suite 500, Reston, VA, 20191-4344, USA.
- Islam, M., D. S. K. Ting and A. Fartaj (2007). Desirable airfoil features for smaller-capacity straight-bladed vawt. *Wind Engineering* 31(3): 165-196.
- Islam, M., D. S. K. Ting and A. Fartaj (2008). Aerodynamic models for Darrieus-type straight-bladed vertical axis wind turbines. *Renewable & Sustainable Energy Reviews* 12(4): 1087-1109.
- Islam, M., D. S. K. Ting and A. Fartaj (2008). Aerodynamic models for Darrieus-type straight-bladed vertical axis wind turbines. *Renewable and Sustainable Energy Reviews* 12(4): 1087-1109.
- Itoigawa, K., H. Ueno, M. Shiozaki, T. Toriyama and S. Sugiyama (2005). Fabrication of flexible thermopile generator. *Journal of Micromechanics and Microengineering* 15: S233.
- Jones, B. (1997, Thu Jul 3 09:59:14 EDT 1997). Viscous Grid Spacing Calculator. Retrieved 10th, May, 2011, from <http://geolab.larc.nasa.gov/APPS/YPlus/>.
- Kamoji, M., S. Kedare and S. Prabhu (2008). Experimental investigations on single stage, two stage and three stage conventional Savonius rotor. *International Journal of Energy Research* 32(10): 877-895.
- Kamoji, M., S. Kedare and S. Prabhu (2009). Performance tests on helical Savonius rotors. *Renewable Energy* 34(3): 521-529.

- Khan, M. H. (1978). Model and prototype performance characteristics of Savonius rotor windmill. *Wind Engineering* 2: 75-85.
- Kiho, S., M. Shiono and K. Suzuki (1996). The power generation from tidal currents by Darrieus turbine. *Renewable Energy* 9(1): 1242-1245.
- Kirke, B. K. (1998). Evaluation of Self-starting Vertical Axis Wind Turbines for Stand-alone Application. Doctor of Philosophy PhD, Griffith University Gold Coast Campus.
- Kirke, B. K. (1998). Evaluation of self-starting vertical axis wind turbines for stand-alone applications, Griffith University.
- Kirke, B. K. (2011). Tests on ducted and bare helical and straight blade Darrieus hydrokinetic turbines. *Renewable Energy* 36(11): 3013-3022.
- Kirke, B. K. and L. Lazauskas (2011). Limitations of fixed pitch Darrieus hydrokinetic turbines and the challenge of variable pitch. *Renewable Energy* 36(3): 893-897.
- Kishi, M., H. Nemoto, T. Hamao, M. Yamamoto, S. Sudou, M. Mandai and S. Yamamoto (1999). Micro thermoelectric modules and their application to wristwatches as an energy source, IEEE.
- Kjellin, J., F. Bülow, S. Eriksson, P. Deglaire, M. Leijon and H. Bernhoff (2011). Power coefficient measurement on a 12 kW straight bladed vertical axis wind turbine. *Renewable Energy* 36(11): 3050-3053.
- Kleiner, Y. and B. Rajani (2001). Comprehensive review of structural deterioration of water mains: statistical models. *Urban Water* 3(3): 131-150.
- Klimas, P. C. and M. H. Worstell (1981). Effects of blade preset pitch/offset on curved-blade Darrieus vertical axis wind turbine performance, Sandia National Labs., Albuquerque, NM (USA).
- Kulfan, B. M. (2008). Universal parametric geometry representation method. *Journal of Aircraft* 45(1): 142-158.
- Kyozuka, Y. (2008). An experimental study on the Darrieus-Savonius turbine for the tidal current power generation. *Journal of Fluid Science and Technology* 3(3): 439-449.
- Lain, S. and C. Osorio (2010). Simulation and evaluation of a straight-bladed Darrieus-type cross flow marine turbine. *Journal of Scientific & Industrial Research* 69(12): 906-912.
- Levin, R. B., P. R. Epstein, T. E. Ford, W. Harrington, E. Olson and E. G. Reichard (2002). US drinking water challenges in the twenty-first century. *Environmental Health Perspectives* 110(Supplement 1): 43.
- Li, Q. Y., S. L. Wu, F. B. Peng and G. J. Li (1983). A study on aerodynamics of vertical axis windmill with double blades. *Solar World Congress, Proc. ISES 8th Biennial Congress. Perth, WA*: 2360-2364.

- Li, Y. and S. M. Calisal (2010). Three-dimensional effects and arm effects on modeling a vertical axis tidal current turbine. *Renewable Energy* 35(10): 2325-2334.
- Li, Y., H. Yu, B. Su and Y. Shang (2008). Hybrid micropower source for wireless sensor network. *Sensors Journal, IEEE* 8(6): 678-681.
- Littlefair, P. (1998). Passive solar urban design: ensuring the penetration of solar energy into the city. *Renewable and Sustainable Energy Reviews* 2(3): 303-326.
- Ljungstrom, O. (1982). Wind turbine of cross-flow type, US Patent 4,329,116.
- Maskell, E., C (1965). A Theory of the Blockage Effects on Bluff Bodies and Stalled Wings in a Closed Wind Tunnel. London, ARC R&M 3400.
- McLaren, K. W. (2011). A numerical and experimental study of unsteady loading of high solidity vertical axis wind turbines.
- Mertens, S., G. van Kuik and G. van Bussel (2003). Performance of an H-Darrieus in the skewed flow on a roof. *Journal of solar energy engineering* 125: 433.
- Metzger, C., F. Michahelles and E. Fleisch (2007). Ambient energy scavenging for sensor-equipped RFID tags in the cold chain. *Smart Sensing and Context*: 255-269.
- Migliore, P. and J. Fritschen (1982). Darrieus wind-turbine airfoil configurations. NASA STI/Recon Technical Report N 83: 21600.
- Migliore, P. G. (1983). Comparison of NACA 6-series and 4-digit airfoils for Darrieus wind turbines. *Journal of Energy* 7: 291.
- Min, R., M. Bhardwaj, C. Seong-Hwan, E. Shih, A. Sinha, A. Wang and A. Chandrakasan (2001). Low-power wireless sensor networks. *VLSI Design, 2001. Fourteenth International Conference on*.
- Minnich, A. J., M. Dresselhaus, Z. Ren and G. Chen (2009). Bulk nanostructured thermoelectric materials: current research and future prospects. *Energy Environ. Sci.* 2(5): 466-479.
- Modi, V. and M. Fernando (1989). On the performance of the Savonius wind turbine. *Journal of solar energy engineering* 111: 71.
- Mohamed, M., G. Janiga, E. Pap and D. Thévenin (2011). Optimal blade shape of a modified Savonius turbine using an obstacle shielding the returning blade. *Energy Conversion and Management* 52(1): 236-242.
- Mohamed, M. H., G. Janiga, E. Pap and D. Thévenin (2011). Multi-objective optimization of the airfoil shape of Wells turbine used for wave energy conversion. *Energy* 36(1): 438-446.
- MORAN, W. (1977). Giromill wind tunnel test and analysis, volume 2. Technical discussion[Final Report, Jun. 1976- Oct. 1977].
- Morcos, V. and O. Abdel-Hafez (1996). Testing of an arrow-head vertical-axis wind turbine model. *Renewable Energy* 7(3): 223-231.

- Murai, Y., T. Nakada, T. Suzuki and F. Yamamoto (2007). Particle tracking velocimetry applied to estimate the pressure field around a Savonius turbine. *Measurement Science and Technology* 18: 2491.
- Nakajima, M., S. Iio and T. Ikeda (2008). Performance of Double-step Savonius Rotor for Environmentally Friendly Hydraulic Turbine. *Journal of Fluid Science and Technology* 3(3): 410-419.
- Nema, P., R. K. Nema and S. Rangnekar (2009). A current and future state of art development of hybrid energy system using wind and PV-solar: A review. *Renewable and Sustainable Energy Reviews* 13(8): 2096-2103.
- Nemoto, Y., A. Anzai and I. Ushiyama (2003). A Study of the Twisted Sweeney-Type Wind Turbine. *Wind Engineering* 27(4): 317-321.
- Newman, B. (1974). Measurements on Savonius rotor with variable gap.
- Niyato, D., E. Hossain, M. M. Rashid and V. K. Bhargava (2007). Wireless sensor networks with energy harvesting technologies: a game-theoretic approach to optimal energy management. *Wireless Communications, IEEE* 14(4): 90-96.
- Ogawa, T. (1984). Theoretical study on the flow about Savonius rotor. *Journal of Fluids Engineering* 106: 85.
- OGAWA, T. and H. YOSHIDA (1986). The effects of a deflecting plate and rotor end plates on performances of Savonius-type wind turbine. *Bulletin of the JSME* 29(253): 2115-2121.
- Oler, J., J. Strickland, B. Im and G. Graham (1983). Dynamic stall regulation of the Darrieus turbine, Sandia National Laboratories.
- Paraschivoiu, I. (2002). *Wind Turbine Design-With Emphasis on Darrieus Concept* Polytechnic International Press.
- Paraschivoiu, I. (2002). *Wind turbine design: with emphasis on Darrieus concept*, Presses inter Polytechnique.
- Peacock, A. D., D. Jenkins, M. Ahadzi, A. Berry and S. Turan (2008). Micro wind turbines in the UK domestic sector. *Energy and Buildings* 40(7): 1324-1333.
- Perez-Lombard, L., J. Ortiz and C. Pout (2008). A review on buildings energy consumption information. *Energy and Buildings* 40(3): 394-398.
- Pobering, S. and N. Schwesinger (2008). Power supply for wireless sensor systems. *Sensors*, 2008 IEEE.
- Ponta, F. and G. S. Dutt (2000). An improved vertical-axis water-current turbine incorporating a channelling device. *Renewable Energy* 20(2): 223-241.
- Pope, A. and J. Harper, J (1966). *Low speed wind tunnel testing*. New York, John Wiley& Sons.
- Raciti Castelli, M., A. Englaro and E. Benini (2011). The Darrieus wind turbine: Proposal for a new performance prediction model based on CFD. *Energy*.

- Rajani, B. and Y. Kleiner (2001). Comprehensive review of structural deterioration of water mains: physically based models. *Urban Water* 3(3): 151-164.
- Rajani, B. and C. Zhan (1996). On the estimation of frost loads. *Canadian geotechnical journal* 33(4): 629-641.
- Renno, J. M., M. F. Daqaq and D. J. Inman (2009). On the optimal energy harvesting from a vibration source. *Journal of Sound and Vibration* 320(1-2): 386-405.
- Reupke, P. and S. D. Probert (1991). Slatted-blade Savonius Wind-Rotors. *Applied Energy* 40: 65-75.
- Ross, I. J. (2010). *Wind Tunnel Blockage Corrections: An Application to Vertical-Axis Wind Turbines*.
- Sabzevari, A. (1977). Performance characteristics of concentrator-augmented Savonius wind rotors. *Wind Engineering* 1: 198-206.
- Saftner, D. A., R. D. Hryciw, R. A. Green, J. P. Lynch and R. L. Michalowski (2008). The Use of Wireless Sensors in Geotechnical Field Applications. *Proceeding of the 15th Annual Great Lakes Geotechnical/Geoenvironmental Conference*. Indianapolis, IN.
- Saha, U. and M. J. Rajkumar (2006). On the performance analysis of Savonius rotor with twisted blades. *Renewable Energy* 31(11): 1776-1788.
- Savonius, S. J. (1931). The S-rotor and its Applications. *Mechanical Engineering* 53(5): 333-337.
- SAWADA, T., M. NAKMURA and S. KAMAI (1986). Blade force measurement and flow visualization of Savonius rotors. *Bulletin of JSME* 29(253): 2095-2100.
- Scheurich, F., T. M. Fletcher and R. E. Brown (2010). The influence of blade curvature and helical blade twist on the performance of a vertical-axis wind turbine.
- Shankar, P. (1975). Design, Fabrication and Preliminary Testing of NAL's 1 kw Vertical Axis Wind Turbine. Bangalore, India, National Aerospace Laboratories.
- Shankar, P. (1979). Development of vertical axis wind turbines, Indian Academy of Sciences.
- Sharp, D. J. and D. A. Taylor (1985). The aerodynamic performance of the vee type vertical axis wind turbine. *Proc. 7th BWEA conf*: 155-159.
- Sheldahl, R. E. and A. Sandia National Labs., NM. Aerothermodynamics Div (1981). Comparison of field and wind tunnel Darrieus wind turbine data, Sandia National Labs., Albuquerque, NM. Aerothermodynamics Div.
- Shigetomi, A., Y. Murai, Y. Tasaka and Y. Takeda (2011). Interactive flow field around two Savonius turbines. *Renewable Energy* 36(2): 536-545.
- Shiono, M., K. Suzuki and S. Kiho (2002). Output characteristics of Darrieus water turbine with helical blades for tidal current generations. *Proceedings of the Twelfth (2002) International Offshore and Polar Engineering Conference*, Kitakyushu, Japan.

- Sim ão Ferreira, C. (2009). The near wake of the VAWT: 2D and 3D views of the VAWT aerodynamics, PhD Thesis, Technische Universiteit Delft, The Netherlands.
- Simonds, M. H. and A. Bodek (1964). Performance test of a Savonius rotor. Quebec, Canada, Brace Research Institute, McGill University.
- Sivapalan, S. and S. Sivasegaram (1980). Direction-independent concentration augmentation of power in a resistance-type wind rotor. *Wind Engineering* 4: 134-141.
- Sivasegaram, S. (1978). An experimental investigation of a class of resistance-type, direction-independent wind turbines. *Energy* 3(1): 23-30.
- Sivasegaram, S. (1978). Secondary parameters affecting the performance of resistance-type vertical-axis wind rotors. *Wind Engineering* 2: 49-58.
- Sivasegaram, S. (1979). Concentration augmentation of power in a Savonius-type wind rotor. *Wind Engineering* 3: 52-61.
- Sivasegaram, S. (1981). Wind tunnel tests on slow-running vertical-axis wind-rotors. *Sadhana* 4(3): 395-404.
- Sivasegaram, S. and S. Sivapalan (1983). Augmentation of power in slow-running vertical-axis wind rotors using multiple vanes. *Wind Engineering* 7: 12-19.
- Sobieczky, H. (1998). Parametric airfoils and wings. *Notes on Numerical Fluid Mechanics* 68: 71-88.
- Sodano, H. A., G. E. Simmers, R. Dereux and D. J. Inman (2007). Recharging batteries using energy harvested from thermal gradients. *Journal of Intelligent Material Systems and Structures* 18(1): 3-10.
- South, P. and R. Rangi (1972). A Wind Tunnel Investigation of a 14 Ft. Diameter Vertical Axis Windmill, National Aeronautical Establishment, Low Speed Aerodynamics Section.
- Stoianov, I., L. Nachman, S. Madden, T. Tokmouline and M. Csail (2007). PIPENET: A wireless sensor network for pipeline monitoring. *ACM/IEEE International Conference on Information Processing in Sensor Networks*. (MIT) Cambridge, Massachusetts, USA: 264-273.
- Stoianov, I., L. Nachman, A. Whittle, S. Madden and R. Kling (2006). Sensor networks for monitoring water supply and sewer systems: Lessons from Boston. *Proceeding of the 8th Annual Water Distribution System Analysis Symposium*. Cincinnati, OH: 1-17.
- Stordeur, M. and I. Stark (1997). Low power thermoelectric generator-self-sufficient energy supply for micro systems, *IEEE*.
- Strasser, M., R. Aigner, C. Lauterbach, T. Sturm, M. Franosch and G. Wachutka (2004). Micromachined CMOS thermoelectric generators as on-chip power supply. *Sensors and Actuators A: Physical* 114(2): 362-370.
- Strickland, J. H. (1975). The Darrieus Turbine: A Performance Prediction Model

- Using Multiple Streamtubes. New Mexico, Sandia Laboratories: 1-38.
- Strickland, J. H., B. T. Webster and T. Nguyen (1979). Vortex Model of the Darrieus Turbine - Analytical and Experimental-Study. *Journal of Fluids Engineering-Transactions of the Asme* 101(4): 500-505.
- Talay, T. A. (1975). *Introduction to the Aerodynamics of Flight*, Scientific and Technical Information Office, National Aeronautics and Space Administration.
- Tanaka, H. (1997). A comparative study of GA and orthogonal experimental design. *Evolutionary Computation, 1997.*, IEEE International Conference on, IEEE.
- Templin, R. J. (1974). *Aerodynamic Performance Theory for the NRC Vertical-Axis Wind Turbine*. OTTAWA, Canada, National Research Council Canada: 29.
- USHIYAMA, I., H. NAGAI and J. SHINODA (1986). Experimentally determining the optimum design configuration for Savonius rotors. *Bulletin of JSME* 29(258): 4130-4138.
- Van Dusen, E. and R. Kirchhoff (1978). A two dimensional vortex sheet model of a Savonius Rotor. *Fluids Engineering in Advanced Energy Systems*.
- Vance, W. (1973). *Vertical axis wind rotors: Status and potential California*, NASA.
- Voigt, T., H. Ritter and J. Schiller (2003). *Solar-aware routing in wireless sensor networks*, Springer.
- Vullers, R., R. van Schaijk, I. Doms, C. Van Hoof and R. Mertens (2009). Micropower energy harvesting. *Solid-State Electronics* 53(7): 684-693.
- Wakui, T., Y. Tanzawa, T. Hashizume and T. Nagao (2005). Hybrid configuration of Darrieus and Savonius rotors for stand-alone wind turbine-generator systems. *Electrical Engineering in Japan* 150(4): 13-22.
- Wang, L., L. Zhang and N. Zeng (2007). A potential flow 2-D vortex panel model: Applications to vertical axis straight blade tidal turbine. *Energy Conversion and Management* 48(2): 454-461.
- Wilson, R. E., P. B. S. Lissaman and S. N. Walker (1976). *Aerodynamic Performance of Wind Turbines Oregon State Univ., Corvallis (USA)*: 170.
- Worstell, M. H. (1978). *Aerodynamic performance of the 17 meter diameter darrieus wind turbine*. . Albuquerque, NM, Sandia Laboratories. 87185.
- Wu, W., V. S. Ramsden, T. Crawford and G. Hill (2000). A low-speed, high-torque, direct-drive permanent magnet generator for wind turbines. *Ias 2000 - Conference Record of the 2000 Ieee Industry Applications Conference, Vols 1-5*: 147-154.
- Xia, R., C. Farm, W. Choi and S. G. Kim (2006). Self-powered wireless sensor system using MEMS piezoelectric micro power generator, IEEE.
- Yang, H., L. Lu and W. Zhou (2007). A novel optimization sizing model for hybrid solar-wind power generation system. *Solar Energy* 81(1): 76-84.

Yang, X., K. G. Ong, W. R. Dreschel, K. Zeng, C. S. Mungle and C. A. Grimes (2002). Design of a wireless sensor network for long-term, in-situ monitoring of an aqueous environment. *Sensors* 2(11): 455-472.

Younis, M. and K. Akkaya (2008). Strategies and techniques for node placement in wireless sensor networks: A survey. *Ad Hoc Networks* 6(4): 621-655.

Zanette, J., A. Tourabi and D. Imbault (2010). A design methodology for cross flow water turbines. *Renewable Energy* 35(5): 997-1009.